

Uncertainty and Sensitivity Analysis of Computational Simulations of Industrial Jet Flows

FRANCISCO-JAVIER GRANADOS-ORTIZ

A thesis submitted in partial fulfilment of the requirements
of the University of Greenwich for the degree of
Doctor of Philosophy

December 2016

First of all, I have to admit that I simply did the easiest part to successfully complete my PhD degree: to study hard, to work hard and to write this manuscript whilst receiving a grant to cover all my needs. The hardest part had to be endured by my family, in particular by my parents, Francisco & Carmen.

Since the beginning of my university studies (and undoubtedly before) they have been supporting me and covering all the costs related to my education, despite the fact of our humble incomes. I will never forget the day I saw my mother crying because she was aware that I was truly on the way to receive an engineering degree, as well as recalling how proud her parents (my deceased loved maternal grandparents, Antonio & Antonia) would feel about this. I feel, hence, very happy to have shared this research experience with my paternal grandparents, specially with my lovely grandfather, Ramón, who sadly passed away recently. They all made a huge sacrifice during really hard times to rear my parents and to make this opportunity possible in life for me.

Another very special warm dedication goes to my lovely girlfriend, and now fiancée, Elia. Thank you for leaving everything behind and starting this adventure with me. Thank you for all your love, passion and trust. You made every single day special, no mattered how hard it was. You were always there and I feel blessed to marry you.

DECLARATION

I certify that this work has not been accepted in substance for any degree, and is not concurrently being submitted for any degree other than that of Doctor of Philosophy, being studied at the University of Greenwich. I also declare that this work is the result of my own investigations except where otherwise identified by references and that I have not plagiarised the work of others.

Author: Francisco-Javier Granados-Ortiz

Supervisor: Prof. Choi-Hong Lai

Second supervisor: Prof. Koulis Pericleous

FRANCISCO-JAVIER GRANADOS-ORTIZ

December 2016

ACKNOWLEDGEMENTS

I would like to acknowledge my supervisors Prof. Choi-Hong Lai and Prof. Koulis Pericleous for giving me the opportunity to come to the University of Greenwich, and to this amazing city of London, to experience possibly the best years of my entire life, thanks to the *Marie Curie Initial Training Networks (ITN) AeroTraNet 2* of the European Community's Seventh Framework Programme (FP7) under contract number PITN-GA-2012-317142. This project has been such an amazing experience that gave me the chance to grow not only academically, but also personally. It was great to share office with Dr. André Ribeiro, Shih-Hau Tan, Dr. Yang Hai, Serife Arif, Kokulan Natkulam and Mani Santhanakrishnan, as well as great chats with Dr. Tim Tilford, Giorgio Zorzi, Georgios Tournloukis, Christopher Beckwith, Ivars Krastins, Andrejs Tucs and William Carter.

From a collaborative perspective, I would also like to express my sincere gratitude to Dr. Joaquín Ortega-Casanova, from the University of Málaga. He demonstrated to be not only a very professional researcher, but also a great person, becoming a very good friend of mine. He provided me tireless support and supervision in the development of the uncertainty study on the CFD simulations of the swirling impinging jet, and the opportunity to go on two secondments at the University of Málaga. It was also great to host you at University of Greenwich to work together for a month.

Regarding AeroTraNet 2, I am very pleased to thank Carlos Pérez Arroyo and his supervisor Dr. Guillaume Puigt (CERFACS), the time invested in discussions on their CFD simulations with *elsA* of the under-expanded jets and all the related data provided, as well as one of the most fruitful secondments I did during this research. I specially would like to thank Tobias Ansaldi & Prof. Christophe Airiau from IMFT for the scientific collaboration involving uncertainty quantification on PSE simulations with *Pasteq* and the very fruitful secondment I did at their facilities. It has also been amazing to share knowledge, opinions and experiences with Dr. Shreyas Bidadi and with Elena Miguel-Nicio, Mohsin Khalil & Dr. Mario Felli from INSEAN (during my secondment in Rome and scientific collaboration in optimising the BOS facility set-up), and Lior Gefen & Prof. Roberto Camussi from University of Roma Tre (with the great discussions about acoustic-hydrodynamic separation with wavelets during my secondment at their facilities in Rome), to Daniel Guariglia & Dr. Christophe Schram (with discussions about experimental uncertainty, courses and "informal lessons on experimental fluid dynamics" and the secondment at your facilities at von Karman Institute for Fluid Dynamics), with the colleagues at the University of Leicester, Dr. Aldo Rona, Dr. Edward Hall, Danilo Di Stefano & Alessandro Mancini (very funny moments that made the project even more special!), the Alstom Power/General Electric Power UK people (Ilaria de Dominicis, Sarah Davis and Mark Willetts) and Airbus people (Alessandro Savarese).

Also, I would like to express my gratitude for the interesting conversations I had in person and in further email exchanges with Dr. Francesco Montomoli (Imperial College) on polynomial chaos and applications, Dr. Paul Constantine (Colorado School of Mines) on UQ methods and best practices, with Prof. Pierre Sagaut (Université Pierre et Marie Curie) about polynomial chaos and Kriging, Dr. Marc Montagnac (CERFACS) about surrogate-based methods and Dr. Jeroen Witteveen (Center for Mathematics and Computer Science, CWI) on Stochastic Collocation for swirling jets, who sadly passed away.

ABSTRACT

The main purpose of this thesis has been to improve the deterministic computational simulations of two industrial problems with a stochastic approach. For this purpose, uncertainty quantification and global sensitivity analysis have been carried out in two industrial jet flows with different objectives.

First, an impinging swirling air jet for heat transfer purposes is generated by an axisymmetric rotating pipe. Despite that many mechanisms to generate swirling jets for heat transfer can be found in literature, there is no application with rotating pipes. To develop such study, two Computational Fluid Dynamic (CFD) simulations are carried out in FLUENT (*Simulation 1* for the rotating pipe to generate the swirling flow and *Simulation 2* for its impingement on a heated flat plate) in order to compare this heat transfer mechanism with others available in literature. Once the simulations are validated, experimental uncertainties are taken into account in the simulation by means of the Stochastic Collocation Method, as to provide measures of uncertainty is typical in experimental studies but also relevant in CFD. Moreover, as this Uncertainty Quantification (UQ) method requires to run *Simulation 1* several times, mathematical models are also investigated for the outflow turbulent and velocity profiles to reduce the complexity and time invested in the analysis. The simulated results show that this swirling mechanism can significantly beat others in literature, specially by increasing the angular velocity in small nozzle-to-plate distances, increasing the heat transfer at the stagnation point. This is the only mechanism that provides such increase in short nozzle-to-plate distances. The investigated models were also implemented in User Defined Functions (UDF) introducing negligible errors in the simulations.

Second, a framework is presented for the propagation of uncertainties in the computational research of under-expanded jets. For this aim, experimental and turbulence uncertainty is input to the CFD simulations of the jet flow and its impact is accounted and apportioned (UQ and sensitivity analysis) by means of generalised Polynomial Chaos and Kriging surrogates. The results show that some interesting parts in the computational domain suffer significant variations due to the input uncertainty. In addition to this, the last part of the framework is the stability analysis by the Parabolised Stability Equations (PSE). Stochastic Collocation is used to demonstrate that the impact of experimental and turbulence uncertainty can be linked to PSE in this framework, despite the fact that the PSE do not include them in their formulation.

Contents

List of Figures	ix
List of Tables	xv
1 Introduction	1
1.1 The Importance of Computational Fluid Dynamics and Stochastic Analysis	1
1.1.1 Industrial Interest in UQ and SA	5
1.2 Stochastic CFD Analysis in Jet Flows: Aims and Objectives	6
1.2.1 CFD Simulations and UQ for Incompressible Swirling Impinging Jet Flows with Heat Transfer Purposes.	7
1.2.2 Framework for Uncertainty Propagation in Aircraft Under-expanded Jet Flows.	8
1.3 Outline of the Thesis	10
1.4 Summary	11
2 Mathematical Preliminaries	12
2.1 An Overview of Uncertainty Quantification	13
2.1.1 Sources of uncertainty	13
2.1.2 Probabilistic vs Non-Probabilistic	13
2.1.3 Non-Probabilistic Methods for Uncertainty Quantification	14
2.1.4 Probabilistic Methods for Uncertainty Quantification	16
2.2 An Overview of Sensitivity Analysis	33
2.3 Conclusions and Critique on the Different Probabilistic UQ Methods	39
2.4 Some Model Case Studies	41
2.4.1 Applying Uncertainty Quantification to a Damped Sinusoidal Func- tion with Mach Effect Resemblance	41
2.4.2 Comparison of Global Sensitivity Analysis Methods	46
2.5 Current Research Trends and Needs in the Field	47
2.6 Summary	49

3	A Swirling Flow Generated by a Rotating Pipe for Heat Transfer by Impingement Under Uncertainty. Part I: CFD Modelling	50
3.1	Introduction and Motivation	51
3.1.1	Literature Review	52
3.1.2	Methodology and Challenges	54
3.2	Setting-Up the CFD Simulations	56
3.2.1	Simulation 1: CFD Simulations of a Fully-Developed Turbulent Flow in a Rotating Pipe.	56
3.2.2	Grid uncertainty	64
3.2.3	Simulation 2: CFD Simulations of the Heat Transfer to a Heated Solid Flat Plate from an Impinging Swirling Jet	66
3.3	Coupling the Two-Step CFD Simulations	69
3.4	Proposed Mathematical Models for the Dimensionless Profiles From the Rotating pipe	71
3.5	Comparison and Discussion of Results	80
3.6	Conclusions	85
 4	 A Swirling Flow Generated by a Rotating Pipe for Heat Transfer by Impingement Under Uncertainty. Part II: Uncertainty Quantification	 87
4.1	Introduction and Motivation for Uncertainty Quantification	88
4.1.1	Methodology and Challenges	88
4.2	Uncertainty Quantification	91
4.2.1	Stochastic Collocation Method and Sources of Uncertainty	91
4.3	Coupling the Two-Step CFD Simulations For UQ purposes	92
4.4	Uncertainty Quantification Results of the Two-Step CFD Simulation	96
4.4.1	Simulation 1. Uncertainty Quantification on the Fully-developed Turbulent Swirling Flow Generated by the Rotation of a Pipe	96
4.4.2	Simulation 2. Uncertainty Quantification on the Impinging Swirling Jet for Heat Transfer: Boundary Conditions Imposed from Simulation 1.	98
4.4.3	Simulation 2. Uncertainty Quantification on the Impinging Swirling Jet for Heat Transfer: Use of Models for Outputs from Simulation 1.	105
4.5	Conclusions	106
 5	 A Framework for Uncertainty Propagation in Under-expanded Single Jet Simulations	 109
5.1	Introduction and Motivation	110
5.2	Literature Review	110
5.2.1	Methodology and Challenges	113
5.3	CFD simulations	115

5.3.1	Numerical formulation	115
5.3.2	Simulation set-up	115
5.3.3	Mesh generation	116
5.4	Uncertainty Quantification on 3D RANS simulations	118
5.4.1	Tests and Prescription of Uncertainties	119
5.4.2	Uncertainty Quantification Methods: Generalised Polynomial Chaos and Kriging Surrogates	120
5.4.3	Comparison and Discussion of Uncertainty Quantification Results .	122
5.5	Global Sensitivity Analysis by Means of Generalised Polynomial Chaos and Kriging Surrogates	129
5.5.1	Comparison and Discussion of Global Sensitivity Analysis Results .	131
5.6	Uncertainty Quantification on Parabolised Stability Equations (PSE) Applied to Stability Analysis	133
5.6.1	Results from Uncertainty Quantification on PSE from a Stochastic CFD Base-flow	136
5.7	Conclusions	137
6	Conclusions and Suggested Future Work	141
6.1	CFD Simulations and UQ for Incompressible Swirling Impinging Jet Flows with Heat Transfer Purposes.	141
6.1.1	Conclusions and Contribution to Knowledge	141
6.1.2	Suggested future work	143
6.2	Framework for Uncertainty Propagation in Aircraft Under-expanded Jet Flows Research	144
6.2.1	Conclusions and Contribution to Knowledge	144
6.2.2	Suggested Future Work	145
6.3	Dissemination of Work to Date	146
	Bibliography	148
	Appendix A User-Defined Functions to Implement the Models	167
	Appendix B Models for the Fitting Coefficients	170

List of Figures

1.1	Classification of the most normally used methods in turbulence simulations. <i>Image taken from J.P. Laval's slides from 'International Master on Turbulence' at University of Lille (France).</i>	2
1.2	Sketch of propagation of uncertainties in a mathematical model.	5
1.3	Impact of UQ for decision-making in engineering practice. <i>Image taken from Luis Crespo's slides from 'NASA Langley's UQ Challenge' presentation (2015).</i>	7
1.4	Sketch of <i>Simulation 1 & 2</i>	8
1.5	Detail of a) shock-cell patterns in aircraft and missiles [33], and b) Kelvin-Helmholtz instabilities [179].	9
1.6	Sketch of the uncertainty propagation through experiments, CFD simulations and PSE equations.	10
2.1	Comparison of sampling techniques. Image created with several images from https://people.sc.fsu.edu/~jburkardt	19
2.2	Monomials for integration of polynomials of order P_p [30].	26
2.3	Smolyak construction for $P_p = 2$ and $N_\xi = 2$. It can be noticed that with the lower triangular set of rules the grid can be constructed without the upper ones. <i>Image from [30] with minor modifications.</i>	28
2.4	Clenshaw-Curtis Smolyak's nested Sparse Grids for different levels of accuracy.	28
2.5	Clenshaw-Curtis tensor grid construction.	29
2.6	Solution of the PDE.	42
2.7	(a) Experimental results from Andre Benoit's PhD thesis[8] and CFD simulations performed at CERFACS with the Onera's <i>elsA</i> solver. (b) Analytical solution of the prescribed PDE in Eq. (2.63) at $t = 2.125$	43
3.1	Sketch of the swirling flow generator by a rotating pipe. The flow enters the pipe with a uniform profile and swirlless, and leaves the pipe as turbulent fully-developed with swirl.	57

3.2	Sketch of <i>Simulation 1</i> & 2. Note that the x and r axis are the same in practice and with origin in the axisymmetry axis, but for the sake of avoiding confusion in the following plots and data tables, r is used in <i>Simulation 1</i> and x for <i>Simulation 2</i>	57
3.3	Computational grid for the pipe.	58
3.4	Detail of the evolution of the axial velocity profile along the pipe and boundary conditions imposed. The red colour scale stands for the radial distance with the maximum exit velocity and the blue colour scale stands for the lowest.	59
3.5	a) Plot of the axial velocity profiles of the fully-developed turbulent swirling flow for several turbulence models and validation with Imao et al [101]. b) Zoom of the boundary layer. $Re = 20000$ and $S = 1$	64
3.6	a) Plot of the azimuthal velocity profiles of the fully-developed turbulent swirling flow for several turbulence models and validation with Imao et al [101]. b) Zoom of the boundary layer. $Re = 20000$ and $S = 1$. U_r stands for the solid rigid body rotational velocity $U_r = \Omega R$	65
3.7	Plot of the errors of relevant parameters of the simulation for several turbulence models, with respect to the minimum value of the error (the RSM linear enh.). The error measure is the euclidean norm.	65
3.8	Grid Convergence Index to quantify the discretization errors and Richardson Extrapolation. The iterations per minute and the corresponding error are also included in the figure for each grid.	66
3.9	Computational grid for the CFD simulations of the impinging jet and boundary conditions imposed. H_{bc} stands for the height of the upper boundary condition, that can be different than H . The size of the pipe wall is kept fixed at a length D	67
3.10	Validation of the turbulent model for $H/D = 2$. The different configurations of the SST $k - \omega$ turbulence model correspond to conf. 1: with transitional flow (old model in FLUENT version 6.3), conf. 2: with Low Reynolds correction, conf. 3: without Low Reynolds correction, conf. 4: Transition SST with the Production Kato-Launder option and conf. 4: Transition SST with the Production Limiter option. The chosen option was SST $k - \omega$ with the Production Kato-Launder option.	68
3.11	Graphs of the friction factor on the plate (left), turbulent intensity (centre) and Nusselt number (right).	68
3.12	Velocity contour plots made dimensionless with the mean velocity U . $Re = 23000$, $S = 1$ and $H/D = 5$	69
3.13	Effect of the position of the upper boundary condition in the Nusselt number.	70
3.14	The two possibilities: by using the CFD profiles at the exit of the nozzle to impose, or by modelling them.	71

3.15	Axial and azimuthal velocity profiles from CFD and tested mathematical models.	73
3.16	Dimensionless kinetic energy profile and tested mathematical models.	74
3.17	Viscosity ratio profile and tested mathematical models.	75
3.18	Axial and azimuthal velocity profiles from CFD and mathematical model fits with prediction bounds.	78
3.19	Dimensionless kinetic energy profile from CFD simulations and mathematical model fits with prediction bounds.	78
3.20	Turbulent viscosity ratio profile from CFD simulations and mathematical model fits with prediction bounds.	79
3.21	A comparison between the use of <i>Simulation 1</i> and the models as inlet boundary conditions. $Re = 23000$, $S = 1$ and $H/D = 5$	80
3.22	Comparison of Nusselt at stagnation point and various swirl numbers with other existing data in literature, with different swirl generation mechanisms for a) $H/D = 2.5$, and b) $H/D = 10$. In the legends, <i>exp</i> and <i>CFD</i> stands for experimental and computational, respectively.	80
3.23	a) Evolution of the optimal Nu_0 with $Re = 23000$, and different Ω and H/D . b) Correlation fit $\Omega - H/D$	84
4.1	Sketch of <i>Simulation 1</i> & 2. Note that the x and r axis are the same in practice and with origin in the axisymmetry axis, but for the sake of avoiding confusion in the following plots and data tables, r is used in <i>Simulation 1</i> and x for <i>Simulation 2</i>	93
4.2	(●) Axial velocity profile from CFD. (*) Azimutal velocity profile from CFD. (- -) Mathematical models for the Clenshaw-Curtis sparse grid with level 2 of accuracy. Each plot corresponds to a deterministic run and its fit.	94
4.3	(●) Turbulent kinetic energy profile from CFD. (- -) Mathematical models for the Clenshaw-Curtis sparse grid with level 2 of accuracy. Each plot corresponds to a deterministic run and its fit.	95
4.4	(●) Turbulent kinetic energy profile from CFD. (- -) Mathematical models for the Clenshaw-Curtis sparse grid with level 2 of accuracy. Each plot corresponds to a deterministic run and its fit.	95
4.5	Dimensionless profiles from CFD and their models for (a) axial and azimuthal velocity, (b) turbulent kinetic energy and (c) turbulent viscosity ratio, for optimisation purposes in [85], where S was varied from 0 up to 1.5.	97
4.6	Radial distribution of the axial (○) and azimuthal (□) dimensionless velocity profiles at the exit of the pipe for the level 4 of the C-C Sparse Grid.	99
4.7	Radial distribution of the Turbulent Kinetic Energy, k , and the Turbulent Viscosity Ratio, β , at the exit of the pipe for the level 4 of the C-C Sparse Grid.	99

4.8	Computational grid for <i>Simulation 2</i> and boundary conditions imposed. Note that D is the diameter of the pipe but D is also the length of the wall pipe in the computational domain.	100
4.9	Evolution of the stochastic mean of the Nusselt number along the plate \pm its stochastic standard deviation for level 4 of the C-C sparse grid.	102
4.10	Sampling with $N_s = 2000$ samples.	103
4.11	PDFs for Nu_0 (left) and Nu_{avg} (right). The greater the N_s , the better the uniformity in the PDF. However, as the problem under study has a notable linearity, since a low number of samples the shape of the PDF is not changing anymore.	103
4.12	Sampling with $N_s = 4556$ samples.	104
4.13	PDFs for Nu_0 (left) and Nu_{avg} (right) when sampling the normal probabilistic distributions.	104
4.14	Comparison between Nusselts when using the CFD profiles and models for the inlet boundary conditions.	106
5.1	Shock-cell pattern [33].	112
5.2	a) Generation of Kelvin-Helmholtz instabilities (<i>Image from [165]</i>). b) Detail of shear-layer Kelvin-Helmholtz instabilities in a round jet (<i>Image from [122]</i>).	112
5.3	Sketch of the uncertainty propagation through experiments, CFD simulations and PSE equations.	113
5.4	Mesh cuts representing every fourth cells in the plane (a) $z/D = 0$ and the plane (b) $x/D = 0$. <i>Image courtesy of CERFACS</i>	116
5.5	Mach number profile relative error of the deterministic base case at the centreline for (a) different azimuthal discretizations, where each line represents the number of azimuthal nodes, and (b) different axial discretizations, where each line represents the starting position where the mesh is uniform. The refined mesh has been used as converged solution. <i>Image courtesy of CERFACS</i>	117
5.6	CFD RANS simulation of the Mach number from the deterministic base case of the under-expanded jet in <i>elsA</i> . <i>Image courtesy of CERFACS</i>	118
5.7	CFD RANS simulations of the deterministic base case of the under-expanded jet in <i>elsA</i> . The shown parameters are (a) the dimensionless axial velocity profile, $v_x^* = v_x/c_{ref}$, (b) dimensionless radial velocity profile, $v_r^* = v_r/c_{ref}$ and (c) dimensionless static pressure, $p^* = \frac{P}{\gamma_{ref} p_{ref}}$, with $\gamma = 1.4$ the specific heat ratio, $p_{ref} = 98000 Pa$ the reference pressure and $c_{ref} = 340.26 m/s$ the reference speed of sound.	118

5.8	Mach number profile of the deterministic base case at the axis for different R_t inlet values in a (a) general and a (b) detailed view. Experimental \times , $R_t = 0.022$ \square , $R_t = 0.22$ \circ , $R_t = 2.2$ \triangle , $R_t = 22$ ∇ , $R_t = 220$ \diamond , $R_t = 2200$ \circlearrowright . Results by <i>elsA</i> software, run at CERFACS facilities.	120
5.9	R_t profile of the deterministic base case at the axis for different R_t inlet values in a (a) general and a (b) detailed view. $R_t = 0.022$ \square , $R_t = 0.22$ \circ , $R_t = 2.2$ \triangle , $R_t = 22$ ∇ , $R_t = 220$ \diamond , $R_t = 2200$ \circlearrowright . Results by <i>elsA</i> software, run at CERFACS facilities.	120
5.10	Axial velocity profile of the deterministic base case at the axis for different R_t inlet values in a (a) general and a (b)&(c) detailed view. Experimental \times , $R_t = 0.022$ \square , $R_t = 0.22$ \circ , $R_t = 2.2$ \triangle , $R_t = 22$ ∇ , $R_t = 220$ \diamond , $R_t = 2200$ \circlearrowright . Results by <i>elsA</i> software, run at CERFACS facilities	121
5.11	Examples of Kriging surrogates at several x/D distances on data sets with challenging shape. The blue points correspond to the deterministic CFD solutions from the fourth level of accuracy in the Clenshaw-Curtis sparse grid. In the plots Cp_s stands for the coefficient of variation for p_s ($\pm 5\%$).	123
5.12	Evolution of the v_x^* stochastic means (a) and standard deviations (b) along the lipline for LHS on Kriging surrogates with different number of samples, N_s , and its comparison with gPC results. Even for a small number of samples, LHS is undergoing very good convergence.	124
5.13	Evolution of the Mach stochastic means (a) and standard deviations (b) along the centreline for LHS on Kriging surrogates for different number of samples and its comparison with gPC results. Even for a small number of samples, LHS is undergoing very good convergence.	125
5.14	Evolution of (a) Mach stochastic standard deviation for different P and levels of the sparse grid and (b) a zoom of the hardest part in the convergence analysis. These results are compared with Kriging surrogates sampled by means of LHS with $N_s = 2000$	126
5.15	Contour plots of v_x^* (a) stochastic mean and (b) variance by means of LHS on KG surrogates. Contour plots of the absolute error between (c) stochastic mean and (d) variance between KG and gPC methods.	127
5.16	Contour plots of v_r^* (a) stochastic mean and (b) variance by means of LHS on KG surrogates. Contour plots of the absolute error between (c) stochastic mean and (d) variance between KG and gPC methods.	128
5.17	Contour plots of p^* (a) stochastic mean and (b) variance by means of LHS on KG surrogates. Contour plots of the absolute error between (c) stochastic mean and (d) variance between KG and gPC methods.	129
5.18	Stochastic mean and standard deviation envelopes with gPC for (a) Mach along centreline and (b) dimensionless axial velocity, v_x^* along the lipline.	130

5.19	Validation of computations with the Mach number along the centreline. The green dots are the deterministic evaluations required for the fourth level of accuracy of the Clenshaw-Curtis sparse grid.	131
5.20	Sensitivity indices contour plots by means of Kriging for p^* . a) and b) are the first-order sensitivities and c) the higher-order interaction.	132
5.21	Sensitivity indices contour plots by means of gPC for p^* . a) and b) are the first-order sensitivities and c) the higher-order interaction.	133
5.22	Contribution to the total variance of a) stagnation pressure, b) laminar to turbulent viscosity ratio and c) their interaction, for v_x^*	134
5.23	Contribution to the total variance of a) stagnation pressure, b) laminar to turbulent viscosity ratio and c) their interaction, for v_r^*	135
5.24	Contribution to the total variance of a) stagnation pressure, b) laminar to turbulent viscosity ratio and c) their interaction, for p^*	136
5.25	Impact of input uncertainties on $\alpha(x)$ for $St = 0.4$. The real part, α_r , is related to the spatial wavelength of the instabilities and the imaginary part, α_i is related to the growth rate.	137
B.1	Models for the $\frac{v_z}{U}$ coefficients.	172
B.2	Models for the $\frac{v_r}{U_r}$ coefficients.	172
B.3	Models for the $\frac{k}{U^2}$ coefficients.	173
B.4	Models for the β coefficients.	173

List of Tables

2.1	Correspondence of the type of Wiener–Askey polynomial chaos to the type of random inputs ($N \geq 0$ is a finite integer) [258].	23
2.2	Comparison of stochastic means with sampling methods in the test case at the point $x = 4.25$ and with $t = 2.125$	44
2.3	Comparison of stochastic variances with sampling methods in the test case at the point $x = 4.25$ and with $t = 2.125$	45
2.4	Comparison of stochastic collocation and generalised Polynomial chaos for the stochastic mean on the test case at the point $x = 4.25$ and with $t = 2.125$. The number of collocation points for level 2, 3, 4 and 5 are 13, 29, 65 and 145 respectively. Obviously, for higher values of P , the mean from gPC is the same as it is the first term of the expansion.	45
2.5	Comparison of stochastic collocation and generalised Polynomial chaos for the stochastic variance in the test case at the point $x = 4.25$ and with $t = 2.125$. The number of collocation points for level 2, 3, 4, 5 and 6 are 13, 29, 65, 145 and 321 respectively.	45
2.6	Comparison of sensitivity analysis results by means of sampling (Jansen Sobol indices with Latin Hypercube Sampling and 5000 samples), generalised Polynomial Chaos (gPC with $P = 4$ and 145 samples) and exact values. 47	47
3.1	Fitting coefficients of the discarded mathematical models for the axial and azimuthal dimensionless velocity profiles.	73
3.2	Fitting coefficients of the discarded mathematical models for the kinetic energy dimensionless profile. $k/U^{2(3)}$ does not appear because the search was not possible.	74
3.3	Fitting coefficients of the discarded mathematical models for the turbulent viscosity profile.	75
3.4	Fitting coefficients of the dimensionless profiles for the deterministic base case. 77	77
3.5	Goodness fitting of the dimensionless profiles for the deterministic base case. 79	79

4.1	Stochastic means of the friction factor (λ), turbulent intensity (I), dimensionless axial (v_z/U) and azimuthal (v_t/U) velocity at $r/R = 0.5$, at the exit of the rotating pipe.	98
4.2	Stochastic variances of the friction factor (λ), turbulent intensity (I), dimensionless axial (v_z/U) and azimuthal (v_t/U) velocity at $r/R = 0.5$, at the exit of the rotating pipe.	98
4.3	Stochastic means of the Nusselt number at the stagnation point and its average value along the flat plate.	101
4.4	Stochastic variance of the Nusselt number at the stagnation point and its average value along the flat plate.	101
4.5	Stochastic means of the Nusselt number at the stagnation point and its average value along the flat plate for the two different input uncertainties tested on the construction of the surrogate.	104
4.6	Stochastic variance of the Nusselt number at the stagnation point and its average value along the flat plate for the two different input uncertainties tested on the construction of the surrogate.	105
4.7	Stochastic means of the Nusselt number case at the stagnation point and its average value along the flat plate. Relative error (in %) between the CFD and model input results.	106
4.8	Stochastic variances of the Nusselt number case at the stagnation point and its average value along the flat plate. Relative error (in %) between the CFD and model input results.	106
B.1	Goodness of the fitting for the coefficients of the models.	174

Chapter 1

Introduction

In industry, it is decisive to achieve the best performance of a product in order to have the best position in market. To reach this goal, advanced techniques in Uncertainty Quantification (UQ) and Sensitivity Analysis (SA) can be quite useful if properly applied to computational simulations. This thesis aims to analyse how the impact of these techniques can benefit to two industrial jet flow designs: an impinging swirling jet for heat transfer and a multidisciplinary framework for aircraft under-expanded jets. Both problems deal with certain multi-step research issues where the propagation of uncertainties is of high interest.

Regarding the under-expanded jet, its investigation has taken place within the *FP7 European Commission Marie Curie Action AeroTraNet 2*, in collaboration with several partners across Europe, where contact with computational, experimental and analytical fluid dynamics experts has been possible and their comments were certainly useful to investigate this type of jet flow.

In this chapter, the main concepts and definitions of the thesis in the uncertainty context will be explained. The chapter starts introducing the importance of Computational Fluid Dynamics (CFD) and stochastic analysis in Section 1.1, where also the current industrial interest on this field is addressed. Later, the jet flow problems must to be introduced. In Section 1.2, the aims and objectives of the jet flow investigations in this thesis are explained, and the methodology is also briefly addressed. The chapter ends with an outline of the thesis.

1.1 The Importance of Computational Fluid Dynamics and Stochastic Analysis

With the present technology it is possible to perform numerical simulations of events taking place in real life and governed by complex physics. In the field of fluid dynamics, this is particularly challenging since many ‘features’ have to be taken into account in order to develop reliable simulations: compressibility, turbulence, viscosity, etc. Sometimes also the

1.1 The Importance of Computational Fluid Dynamics and Stochastic Analysis

so-called fluid-structure interaction, that takes into account not only the performance of the flow but also the interactions with the physical body, which must be simulated as well.

For a long time, scientists and engineers from both industry and academia have developed the best algorithms and models (especially a key aspect in turbulence modelling) in order to perform reliable numerical results for the so-called Navier-Stokes equations [45, 229], which govern the physics of flows. This area of research is the well-known Computational Fluid Dynamics (CFD).

For this task, there are several possibilities available with increasing importance of numerics and decreasing model dependence, thanks also to the increasingly available computational resources: from Reynolds-Average Navier-Stokes (RANS) to Direct Numerical Simulations (DNS). RANS are time-averaged equations of motion for fluid flows that let modelling turbulence by decomposing quantities into its time-averaged and fluctuating part. On the contrary, DNS allows to solve directly the Navier-Stokes equations for turbulent flows not requiring any turbulent model, as depicted in Fig. 1.1.

One of the key aspects of the CFD simulations is that they are, generally, a cheaper option

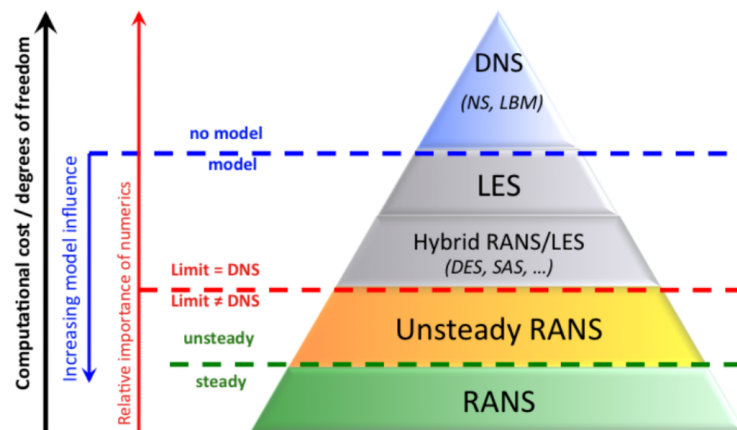


Figure 1.1 Classification of the most normally used methods in turbulence simulations. *Image taken from J.P. Laval's slides from 'International Master on Turbulence' at University of Lille (France).*

for product design and development than experiments. If an engineer wants to test the performance of an experimental facility or measure the risk in particular new conditions (imagine a nuclear reactor) not taken into account in early stages of the design, to undertake such a task can be expensive (you may need to build several prototypes) and even dangerous (if conditions are extreme). For this reason, CFD simulations are a powerful tool in fields like optimisation [223, 85], aerospace & aerodynamics industry [150, 84], fire safety modelling [228], heat transfer [177] or nuclear energy [144], amongst many others. Much effort has

1.1 The Importance of Computational Fluid Dynamics and Stochastic Analysis

been spent to develop the above mentioned techniques, leading to the most reliable simulations for decision-making purposes.

Despite these relevant advances in the field, recently, a new discussion has appeared. It is a regular practice in CFD to analyse the scenario performance of fluids by undertaking simulations with fixed parameters in the set-up configuration. However, this can often be an incomplete approach. When a classic code is used to mimic the physics of a flow, it does not take into account the associated error and uncertainties such as geometrical adaptation, grid uncertainty, domain size, numerical convergence, manufacturing tolerances or uncertainty of the measurement devices. Not taking into account these inaccuracies can result to misleading or incomplete engineering conclusions. This gives rise to the need of providing extra accuracy metrics in CFD, as most experimentalists do.

Before going into details on this, it is important to explain the meaning and differences between uncertainty and error. According to [170], where these concepts are put into work in a modelling and simulation environment, *error* is defined as a recognisable inaccuracy in any phase or activity of modelling and simulation that is not due to lack of knowledge. That is, the inaccuracy is identifiable or knowable upon examination; and therefore not caused by lack of knowledge. In their paper, it is also distinguished between errors that result from *acknowledged sources*, such as mathematical modelling approximations or finite arithmetic precision in computers, and *unacknowledged sources* not recognised by the analyst, such as computer programming errors.

Regarding uncertainty, it is important to also differentiate between this concept and risk. In [59], *uncertainty* is referred to as the stochastic behaviour of any physical phenomenon that causes the indefiniteness of outcomes meaning the expected and actual outcomes are never the same. The variation could have a negative, positive or no impact on the overall performance. On the contrary, *risk* is defined as a special case of uncertainty where the outcomes of a specific event or a number of events have a negative effect on the overall performance. Other interesting definitions in literature of these two terms state that risk is defined as something unknown but with measurable probability, while uncertainty has unknowns in its formulation but with no measurable probability.

Within the definition of uncertainty, it was earlier expressed this term with the label ‘stochastic’. In this thesis, uncertainty is playing a role in *costly simulations*¹ with random inputs. In this context, as *stochastic* one has to understand any simulation which has inherent random variables in its performance. Thus, it contains random elements which make the output unpredictable.

Uncertainty is often distinguished as aleatoric or epistemic. *Aleatoric uncertainty* (also known as statistical uncertainty) is considered as inherent to the natural stochasticity in

¹The term ‘costly’ will be often addressed in this thesis, and it means that a run takes a long time, typically hours or days.

1.1 The Importance of Computational Fluid Dynamics and Stochastic Analysis

a physical quantity. This source of uncertainty is generally quantified by a probability or frequency distribution when sufficient information is available [170]. On the other hand, epistemic uncertainty (also known as systematic uncertainty) rises from the lack of knowledge. It is commonly referred to as incomplete inherent variability of which not enough is known to accurately approximate the uncertainty through a form such as a density function [199].

When simulating the physics of a problem, boundary conditions and geometries are imposed, neglecting any variability or inaccurate description that can be noted in the real-life performance. This leads to the statement that, if an accurate description is desired, these problems cannot be carried on a deterministic framework but a stochastic one. Therefore, it is necessary to model input uncertainties according to a realistic stochastic behaviour provided by probabilistic distributions from experiments. This is often unavailable and, initially, modellers themselves used to provide the assessment of input uncertainties as well as the study of this propagation, as this was not considered a main activity in former research in the field, being the main objective to compute the nominal values [123]. Nowadays, with formal methods it has been demonstrated that there is a dependence of the output with the selected input uncertainties [253] and it is recommended to have a reliable modelling for the parameters. This is particularly important for correlated inputs, as in these cases to neglect the correlation in the uncertainty propagation leads to very misleading results.

Uncertainty Quantification (UQ) is about determining how likely the outputs of a model (numerical or otherwise) are when the inputs are not precisely defined. Once the input uncertainties are modelled, it is necessary to find an appropriate UQ methodology. This process can be summarised as depicted in Fig. 1.2. There is a mathematical model represented as a function $\hat{y}(\xi, x)$, of the random variables $\xi_1, \xi_2, \dots, \xi_{N_\xi}$, with N_ξ the dimension of the random input space. These variables can represent a large variety of parameters in a problem, like temperatures, flow rate, pressure, etc. Then, when their variation is modelled by probabilistic functions based on their own performance, the objective is to extract information of the imprecision or variation in the output of $\hat{y}(\xi, x)$, being x the spatial coordinate for instance. Among the possibilities, one has for instance, to extract the probabilistic distribution of an output y_k (i) or to get the standard deviation as uncertainty measure to plot envelopes (ii). Another important study that can be extended from UQ is Sensitivity Analysis (SA). According to [205], this is the study of *how uncertainty in the output of a model (numerical or otherwise) can be apportioned to different sources of uncertainty in the model input*. In fact, ideally, SA and UQ should be run in a row, with uncertainty analysis usually preceding sensitivity analysis. This mathematical approach undoubtedly helps to rank the most influential random inputs and provides decision-making solutions. Also, understanding the sensitivity of model output to input parameter uncertainty can guide field data-collection activities [162] and can be exploited to direct experimental work in order to reduce uncertainty

1.1 The Importance of Computational Fluid Dynamics and Stochastic Analysis

in identified influential parameters, neglecting the non-influential ones [216]. In Chapter 2, UQ and SA methods are extensively described.

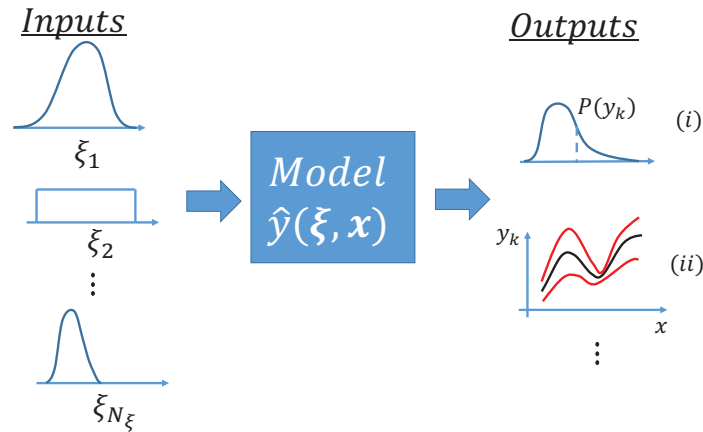


Figure 1.2 Sketch of propagation of uncertainties in a mathematical model.

1.1.1 Industrial Interest in UQ and SA

The stochastic analysis in CFD simulations is an increasingly important fact in industry. Here are several quotes [31] from relevant company leaders giving evidence of the importance of adding the sources of uncertainty to simulations:

“The **future of fluids** is analysis, modelling and simulation”. *Edward Whalen, The Boeing Company.*

“**Many noisy factors** and variables affect the final performance achieved by the vehicle. [...] It is essential that engineers are therefore able to understand and quantify the impact these uncertainties might have on the performance”. *Andy Richardson, Head of Simulation, Jaguar and Land Rover product development.*

“The term ‘uncertainty’ is unquestionable fraught with misunderstanding. I would prefer the phrase ‘**how confident I am?**’, the reciprocal of uncertainty”. *Prof. Michael Rawlins, Chair, National Institute of Clinical Excellence.*

“All the time, multi-million pound decisions are made using weather forecasts that contain uncertainty; in energy trading to predict future energy demands or by local councils deciding when to grit roads, for example. If you know the **potential cost or damage**, you can work out when it pays to take action”. *Prof. Leonard Smith, Director of Centre for Analysis of*

1.2 Stochastic CFD Analysis in Jet Flows: Aims and Objectives

Time Series, London School of Economics.

Similarly, a more synthesized and useful view can be extracted from the following bullet-points presented by Prof. Gianluca Iaccarino at the von Karman Institute Lecture series in Uncertainty Quantification (2014), where he pointed out the key-facts of UQ&SA in CFD related problems:

- Uncertainty is everywhere and everybody can notice it in daily events.
- UQ is an essential part of validation.
- It can provide a rigorous measure of confidence.
- It indicates priorities and supports decision making.
- It quantifies robust design/optimization and margins of safety or risk.

And the usefulness of the full analysis can even be further interpreted. With a proper uncertainty analysis it is possible to detect the so-called *Black Swans*. These are rare events, that could happen and have severe consequences. The deterministic models are unable to predict them, since they take place in variability from the tails of the input probabilistic distributions [158]. This is a useful concept in engineering performance. To illustrate the meaning of good engineering practice, in Fig. 1.3 are shown the possible case scenarios, according to Dr. Luis Crespo, senior researcher at the NASA Langley Research Center. In such diagram, it would be reasonable to think that, with a wishful thinking (pretending to ignore the risk with a bad engineering practice) and with not enough information to measure the impact, one could end with a negligence outcome. It is therefore important to invest efforts in reducing uncertainty and increase the knowledge to avoid, if possible, an unknown-unknown scenario (it is not even known what is unknown) leading to *Black Swans*, or at least be able to measure the impact reliably by exploration. These conclusions are showing the necessity of developing stochastic analysis in our case scenarios, exposing that a deterministic approach would have several limitations neglecting the impact of randomness. The specific addressed problems are described in the following section.

1.2 Stochastic CFD Analysis in Jet Flows: Aims and Objectives

In Section 1.1, the general goal of this piece of work has been put into context: development of computational studies accounting the existing uncertainties for a correct and complete modelling, avoiding such a big lack in literature of neglecting the inherent non-deterministic

1.2 Stochastic CFD Analysis in Jet Flows: Aims and Objectives

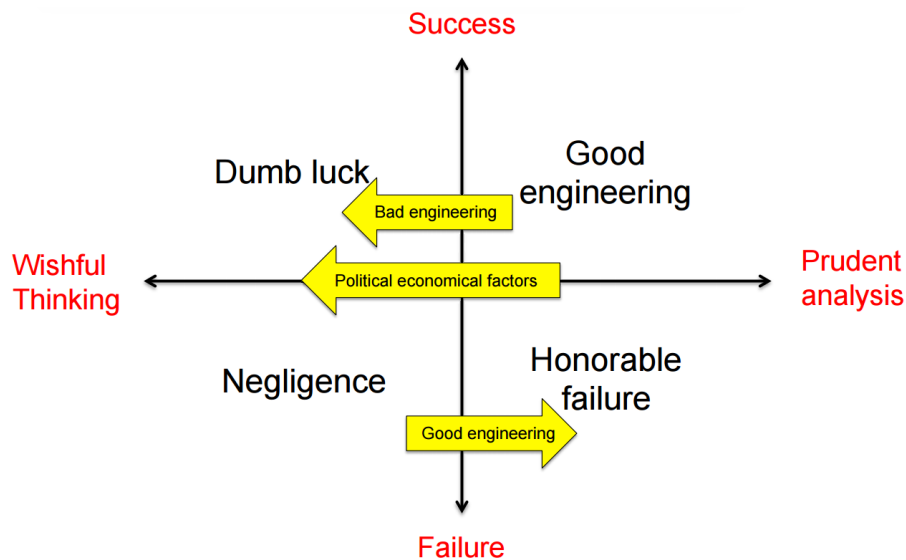


Figure 1.3 Impact of UQ for decision-making in engineering practice. Image taken from Luis Crespo's slides from 'NASA Langley's UQ Challenge' presentation (2015).

contributions. Due to the fact that in this thesis two different jet flow problems are addressed, it is important to clearly differentiate the specific objectives and procedures for each, in order to avoid any confusion. This is the purpose of this section in the introductory chapter.

1.2.1 CFD Simulations and UQ for Incompressible Swirling Impinging Jet Flows with Heat Transfer Purposes.

Objective: The main scope of this study is to provide a different impinging jet heat transfer mechanism by means of the addition of swirl to a jet flow by a rotating pipe. The methodology of this analysis is threefold.

On one hand, a CFD numerical simulation is done through deterministic **2D steady Reynolds-Averaged Navier-Stokes (RANS) simulations in FLUENT** for a swirling flow generated by a rotating pipe (*Simulation 1*) and used in heat transfer by impingement (*Simulation 2*). This swirl generation mechanism has never been addressed before to create impinging jet flows, and researchers used to rely on other devices. This study demonstrates some goodness in comparison with them. In addition, the way the two simulations are coupled can be considered novel too, since there is no literature on similar problems and normally the swirl flow that exits the nozzle is characterised already and it is not previously computed.

On the other hand, as discussed in previous sections, a deterministic analysis is not fully descriptive, so then a **quantification of the impact of input experimental uncertainties** is added to the original formulation, by means of the Stochastic Collocation method.

Moreover, **mathematical models are suggested and tested** for velocity and turbulence

1.2 Stochastic CFD Analysis in Jet Flows: Aims and Objectives

profiles at the exit of the pipe, in order to make a more efficient (from the computational cost side) uncertainty quantification. A sketch of the problem case scenario is shown in Fig. 1.4. A formal literature review and extensive explanation of the problem is done in Chapters 3 and 4.

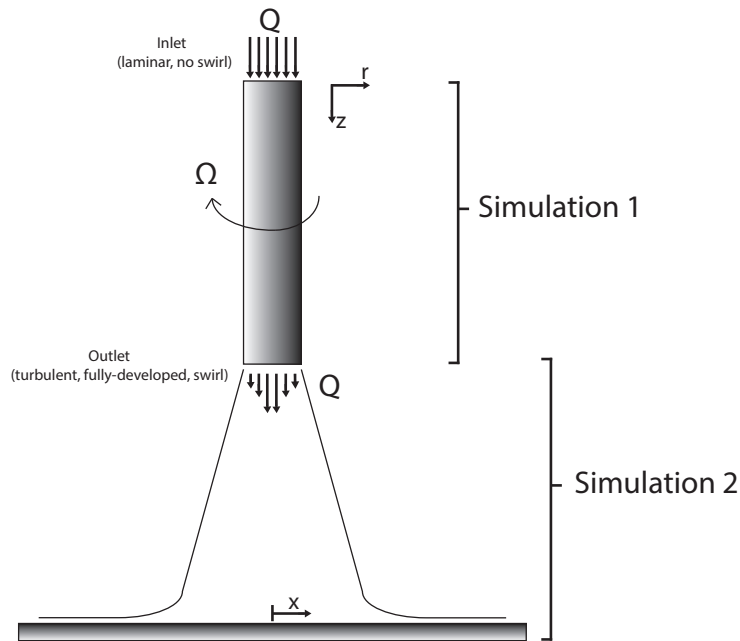


Figure 1.4 Sketch of *Simulation 1* & *2*.

1.2.2 Framework for Uncertainty Propagation in Aircraft Under-expanded Jet Flows.

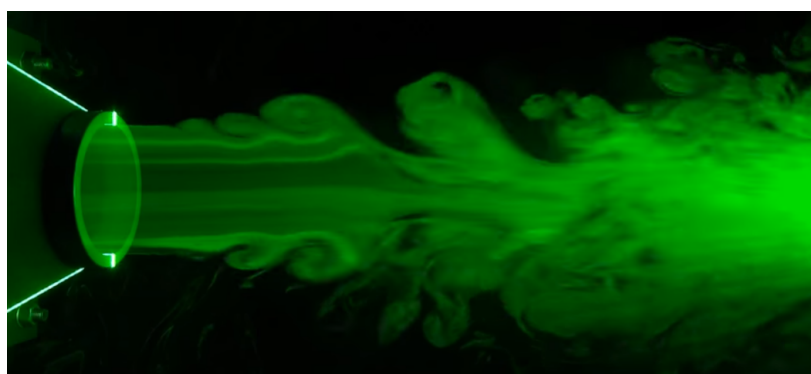
Objective: To develop and test a framework for propagation of uncertainties in the computational design of under-expanded jets, with special interest in CFD simulations run within the *FP7 AeroTraNet 2 Marie Curie Action*, with the objective of providing a stochastic approach for the deterministic analysis developed in the project.

Such framework begins with the experiments, from which uncertainty is taken into account for next design phases. The following stage in the framework involves inputting uncertainty in the numerical injection of turbulence in conjunction with the experimental one, **to develop Non-Intrusive UQ on 3D steady RANS simulations by generalised Polynomial Chaos (gPC) and Kriging surrogates**, in order to understand how the input uncertainties affect simulations of an under-expanded single jet with shock-cells (a detail of shock-cells can be seen in Fig. 1.5.a). Secondly, a **sensitivity analysis** is conducted to quantify the impact of each uncertainty contribution in the simulated jet plume. Results show that some interesting

1.2 Stochastic CFD Analysis in Jet Flows: Aims and Objectives



(a)



(b)

Figure 1.5 Detail of a) shock-cell patterns in aircraft and missiles [33], and b) Kelvin-Helmholtz instabilities [179].

areas of the CFD simulation of the jet are sensitive to the combination of input uncertainties. The last part of the framework is about **using the stochastic base-flow from UQ on RANS to develop a quantification of uncertainties through Parabolised Stability Equations (PSE) on Kelvin-Helmholtz instability features** (Fig. 1.5.b). This framework represents, to knowledge of the author, the only way to assess the propagation of experimental and turbulence model uncertainties through PSE. These results show that stability features can be sensitive to input uncertainties in jet designs, which can help to understand how the noise emission is being affected and can guide to future more robust developments in aircraft industry. A sketch of the framework is shown in Fig. 1.6. A formal literature review and extensive explanation of the problem is carried out in Chapter 5.

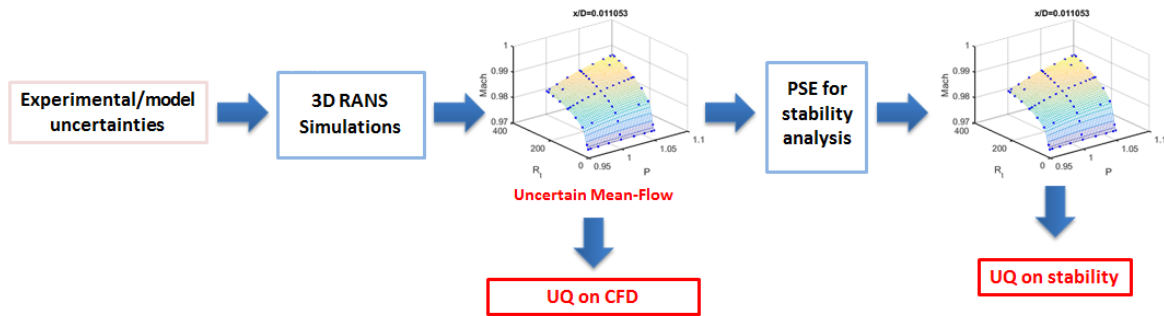


Figure 1.6 Sketch of the uncertainty propagation through experiments, CFD simulations and PSE equations.

1.3 Outline of the Thesis

The PhD thesis is broken down in seven chapters and two appendices in order to follow a coherent storyline as follows.

In **Chapter 1**, an introduction to the importance of stochastic analysis instead of deterministic for industry is given. Also, the two problems covered in this thesis are briefly described.

In **Chapter 2**, the mathematical methods utilised in this thesis for the data analysis are explained, as well as other related methods not put to work here. For testing and criticism purposes, the methods for uncertainty and sensitivity analysis are employed on two test problems. This also set a starting point for the following more advanced engineering problems.

After introducing the objectives and methods in this thesis, the first engineering problem is presented in Chapters 3 and 4. In **Chapter 3**, the Reynolds-Averaged Navier-Stokes simulations for the generation of the swirling turbulent flow (*Simulation 1*) and the heat transfer by impingement on a heated flat plate (*Simulation 2*) are developed. A literature review is also included regarding the state-of-the-art in relation to our heat transfer mechanism. In this chapter, the comparison with other existing swirling flow mechanisms is presented, as well as suggested models for the outflow profiles in (*Simulation 1*) is also presented. This will be an useful tool for the following chapter.

In **Chapter 4**, an account of experimental uncertainties is carried out, in order to evaluate how they can be affecting the CFD simulation for a more complete analysis, contrary to the standard deterministic approach. The outflow profiles are utilised here to demonstrate their advantage to avoid re-run (*Simulation 1*) each time that a new collocation point is required for the Stochastic Collocation method.

The second and last problem is the framework for propagation of uncertainties in the computational design of under-expanded jets, presented in **Chapter 5**. For this objective, experimental and turbulence uncertainty is input in the RANS simulations of the jet flow and

its impact is accounted and apportioned by means of the so-called generalised Polynomial Chaos and sampled Kriging surrogates. In addition to this, the last part of the framework is the stability analysis by the namely Parabolised Stability Equations (PSE). Stochastic Collocation is used to demonstrate that the impact of experimental and turbulence uncertainty can be linked to PSE with this framework, despite the fact that PSE does not include them in their formulation.

In **Chapter 6**, conclusions from both analysis are given, as well as suggestions for future work. The disseminated work to date is also shown here.

In addition to the aforementioned chapters, the last part of the thesis consist of two appendices: **Appendix A**, which contains the User-Defined Function script coded in *C* for the turbulent and velocity profiles, and **Appendix B**, which contains the models for the fitting coefficients of the profiles.

1.4 Summary

In this introductory chapter, the main motivation and objectives of this thesis were described. The chapter started addressing the importance of Computational Fluid Dynamics (CFD) and stochastic analysis in Section 1.1, where other relevant concepts such as risk, types of uncertainty, acknowledge& unacknowledge errors, stochastic, *Black Swans*, Uncertainty Quantification (UQ) and Sensitivity Analysis (SA) have been defined. There, it was also discussed the viewpoint of UQ&SA in industrial practice, showing also evidence in daily events, validation purposes, support in decision making and quantify robustness. In Section 1.2, the aims and objectives of the jet flow investigations are explained.

In the investigation of the swirling jet flow for heat transfer, it has been said that the main scope of this study is to provide a different impinging jet heat transfer mechanism by means of the addition of swirl to a jet flow by a rotating pipe. To this aim, CFD simulations, a quantification of uncertainties and mathematical models are the main steps in the suggested methodology.

The second research topic is to develop a framework for uncertainty propagation in simulations of an under-expanded jet flow. It has been enlighten the use of generalised Polynomial Chaos expansions and Kriging surrogates to achieve this goal, applying them to the CFD simulations. For the Parabolised Stability Equations, Stochastic Collocation has been the chosen method because of the easier implementation. The last chapter of the introduction just break down the content of this thesis.

In the next chapter useful mathematical tools will be discussed and applied to some test cases. To understand these existing methods in literature is a must before their application to complex engineering problems.

Chapter 2

Mathematical Preliminaries

Unfortunately, CFD simulations usually are computationally expensive. As the non-intrusive quantification of uncertainties is expensive itself, by requiring several model evaluations, this makes important to find an efficient way to address uncertainty in problems were it was not imaginable before. This chapter aims to describe the existing methods for an efficient analysis, as well as to point out the advantages with respect to other classical approaches. As mentioned in the introductory chapter, Uncertainty Quantification (UQ) is about determining how likely the outputs of a model (numerical or otherwise) are when the inputs are not precisely defined. This type of input for a model is referred to variables which have associated uncertainty, and therefore need a specific modelling in order to explore the new stochastic input space by advanced methods. This process hence requires firstly to identify the input uncertainties and then the choice of a suitable approach, which will be also decided based on the modelling of the input uncertainty and the desired statistical information as outputs.

In Section 2.1 the types of uncertainty and probabilistic/non-probabilistic methods are discussed. In this section, probabilistic methods are the recommended ones because of the more complete information that they provide, so these will receive a more sounded discussion and application to test cases in Section 2.4. In Section 2.2, an overview of sensitivity analysis is developed, highlighting also the methods in this thesis. An additional section of high interest is 2.3, where conclusions and a critique on the methods is developed, followed by examples of application in Section 2.4.

2.1 An Overview of Uncertainty Quantification

2.1.1 Sources of uncertainty

The sources of uncertainty can be classified in three different types: inherent, predictive and parametric.

Inherent uncertainty: It is associated to an intrinsic stochastic behaviour in nature. In [188] is defined as "processes or quantities that are inherently stochastic arise from the unavoidable unpredictability". Despite makes sense to distinguish this type of uncertainty, some authors place it in the *parametric* uncertainty group as *aleatoric parametric* uncertainty [199]. A good example of this type of uncertainty can be turbulence.

Predictive uncertainty: When developing a model, some assumptions are done. It is impossible (or at least inefficient) to produce a model that takes into account all the complexity. This remind us the famous quote "All models are wrong, but some are useful" by George E. P. Box. Moreover, it is sometimes difficult for the designer to choose the correct model for the case scenario if several are available. This leads to the concept of *model-form uncertainty* [199]. This is a common type of uncertainty in turbulence modelling in CFD.

Parametric uncertainty: When trying to mimic the physics, models require input parameters. These are often treated as deterministic, but in most case scenarios, true physics present some randomness. The uncertainty associated to these parameters is the so-called parametric uncertainty. This is the most common source of uncertainty in UQ studies in literature.

Another differentiation must be done between aleatoric and epistemic uncertainty. *Aleatoric* uncertainty (also known as statistical uncertainty), as commented above, is considered as inherent to the natural stochasticity in a physical quantity. On the other hand, *epistemic* uncertainty (also known as systematic uncertainty) rises from the lack of knowledge. It is then assumed that this uncertainty could be reduced by adding extra information. As illustrative example, if no errors are present and the epistemic uncertainty can be reduced to zero, the remaining uncertainty that would be present would be the aleatoric one [124]. Often, it is not easy to identify if underlying uncertainties are either aleatoric or epistemic, and this classification is responsibility of the analyst.

2.1.2 Probabilistic vs Non-Probabilistic

With the available prior knowledge, a decision has to be made in terms of dealing with uncertainty under a probabilistic or non-probabilistic framework.

2.1 An Overview of Uncertainty Quantification

In non-probabilistic methods, uncertainty is modelled from its model parameter error bounds. This requires just minor knowledge about input uncertainty, and a not so accurate measure of the input variability is taken into consideration, since a broad estimate is used. This makes the non-probabilistic approaches most valuable in early design stages, whereas the probabilistic approach remains indispensable in later stages [155].

There are a number of arguments used in support of the claim that probability is a coherent approach to uncertainty, of which Cox's theorem [48] is undoubtedly the most well known [41]. Such theorem states that *any measure of belief is isomorphic to a probability measure*.

A nice summary in [155] states that the probabilistic concept can be designated as a most valuable solution strategy when three conditions are met simultaneously: (1) trustworthy probabilistic information on the non-determinism is available, (2) a probabilistic description of the simulated non-deterministic behaviour is desired, and (3) the computational constraints are not too tight. In the probabilistic approach, a more detailed (statistical) analysis is developed since step one, as the input uncertainty will be modelled as probabilistic distributions. And if desired, not only statistical moments but also output probabilistic distributions of quantities of interest can be computed.

2.1.3 Non-Probabilistic Methods for Uncertainty Quantification

Despite the fact that non-probabilistic methods are out of the scope of this thesis, some descriptions will be here given for the readers. The main feature in non-probabilistic methods is that they rely on error bounds for the inputs, and probabilistic information is fully omitted in input prescription, as well as global effects. However, the following methods can be found in literature to be useful especially for early design stages.

Interval Analysis

This method aims to provide a description of the range of variability of the outputs of a model when inputs are described by intervals. The interval analysis is easy to implement and intuitive, but it provides maximal error bounds that can be quite large [239]. There are several publications that provide some mathematical foundations of the arithmetic theory approach for this method as [6, 23, 132] and applications such as [54, 197]. This method provides an estimate of the variability of the parameters, but it neglects how these vary in the error bound. Hence, this method is recommended when there is only few knowledge about that behaviour.

Fuzzy Analysis

An improvement of Interval Analysis is the application of Fuzzy Analysis. Fuzzy sets were firstly introduced by [262] to deal with indefiniteness and ambiguity in knowledge. The main advantage of this method is that this approach is capable of describing linguistic and vague information mathematically in a non-probabilistic way. This method plays an interesting role in cases where there is no real but predictable data, what can certainly happen often in real-life applications. To put this in context, examples of uncertainty that fuzzy analysis deal with can be statements like ‘the distance is one or two miles’ or ‘the project will last five or six years’.

This method introduces a function called *membership function*, which describes the degree of membership to the fuzzy set [156]. Formal descriptions of this method are not to be developed here, but the reader is suggested to see [262, 52, 263]. Interesting applications of this method can also be found in [155, 50, 116, 241].

Sensitivity Analysis for Error Propagation

The theory of propagation of errors has been widely used as a measure of variation in many works [234, 209, 243]. The role of sensitivity analysis in error propagation is to give a measure about how the output variables are changing when the inputs are varied. That is, to measure the rate as a local approach. In practice, its value can be associated to a first-order term which indicates the significance of each input to the variation in the output. Mathematically, this sensitivity ratio between the k -th output y_k and the i -th input x_i can be expressed as:

$$S_{ik} = \frac{\partial y_k}{\partial x_i}. \quad (2.1)$$

Taking into account the variation associated to each parameter, $\delta \xi_i$ and an independent relation between the inputs, the output error, δy_k , can be given by

$$\delta y_k = \sum_{i=1}^{N_\xi} S_{ik} \delta \xi_i, \quad (2.2)$$

with $k = 1, 2, \dots, N_y$, being N_y the number of output variables and N_ξ the number of inputs. To obtain the sensitivity derivatives is not always straightforward. It does happen often that an analytical calculation is not possible, being necessary to obtain the derivatives computationally. Some interesting options for the computation in [188] can be:

- **Finite Difference.** This computation is well-known and straightforward, but the size of the perturbation has to be controlled to avoid noticeable errors. In CFD applications, this approach requires several runs, for each variable, perturbed and non-perturbed,

2.1 An Overview of Uncertainty Quantification

what is expensive. And this has to be repeated at each point of the computational domain if contours are desired.

- **Complex Variable Formulation.** This approach deals with the output modelling locally by means of a complex Taylor expansion. If the complex perturbation is small enough, the expansion can be considered lineal, being the slope an approximation to the sensitivity derivative.
- **Sensitivity Equation Method.** This method requires to differentiate the model equations and then discretise and solve the new underlying equations. It is often referred to as ‘direct’ method. It is a fast approach, but has the drawback of modifying the original equations.
- **Discrete Adjoint Method.** The popular adjoint approach deals with the computation of the sensitivity derivative by creating a minimisation problem. Its computational cost is more reduced than in finite difference and it has the great advantage of computing the exact value of the derivatives [13].

The main drawback of these non-probabilistic sensitivity-based methods is that they are a local approach, being necessary a probabilistic formulation for a global analysis (as it will be discussed later in this chapter).

2.1.4 Probabilistic Methods for Uncertainty Quantification

Once the input uncertainties are statistically modelled as first step in the probabilistic approach, it is necessary to find an appropriate UQ method for the propagation of uncertainties. These methods can be either intrusive or non-intrusive. The latter are chosen in this thesis since they do not require to code inside the solver and can deal with any model as a black-box. In this thesis, there are several UQ studies on computational simulations, with FLUENT (swirling jet flows), *elsA* (under-expanded jets) and *Pasteq* (jet stability analysis), as well as on the test cases. To carry out an intrusive approach with each of them would be time consuming, complicated and the codes could not be recycled for all these three solvers. Next, popular probabilistic methods will be described.

Sampling Methods

Sampling methods are a very reliable non-intrusive technique, since they deal with the solver/model as a black-box, simply requiring many model evaluations to construct the desired output statistical information. Undoubtedly, the namely Monte-Carlo simulations [152] are a very popular and well established sampling method. This well-known method is

2.1 An Overview of Uncertainty Quantification

generally described by representing the solution of a problem as a parameter of a hypothetical population, and using a random sequence of numbers to construct a sample of the population, from which statistical estimates of the parameter can be obtained [89]. In other words, the objective is to compute the i -th statistical moments, $\mu(\mathbf{x}, \xi)_i^y$, of the output, y , based on a random sampling on the input uncertainties, in order to obtain enough output data to develop an accurate statistical analysis.

Let us consider the differential operator on an output of interest of a stationary problem, $y(\mathbf{x}, \xi(\eta))$ as

$$\mathcal{L}(\mathbf{x}, \xi(\eta); y(\mathbf{x}, \xi(\eta))) = \mathcal{Q}(\mathbf{x}, \xi(\eta)), \quad (2.3)$$

with \mathcal{L} and \mathcal{Q} differential operators on $\mathcal{D} \times \Xi$, where $\mathbf{x} \in \mathcal{D} \subset \mathbb{R}^d$, $d \in \{1, 2, 3\}$. η denotes events in the complete probabilistic space $(\hat{\Omega}, \hat{\mathcal{F}}, \hat{P})$, with $\hat{\mathcal{F}} \subset 2^{\hat{\Omega}}$ the σ -algebra of subsets of $\hat{\Omega}$ and \hat{P} a probability measure. $\Xi \subset \mathbb{R}^{N_\xi}$, is the stochastic space on which the random variables $\xi(\eta)$ are defined and N_ξ stands for the number of random variables, which defines the order of the stochastic space.

The objective is to find, by random sampling, the i -th statistical moments, $\mu(\mathbf{x}, \xi)_i^y$, of the output, y , by

$$\mu(\mathbf{x}, \xi)_i^y = \int_{\Xi} y(\mathbf{x}, \xi)^i f_\xi(\xi) d\xi, \quad (2.4)$$

with $f_\xi(\xi)$ standing for the density function $f_\xi : \xi \mapsto \mathbb{R}_+$. In many applications, to only compute the statistical moments is not enough and incomplete information of the variable of interest is given. The reason is that two very different probabilistic distributions can have, e.g., the same mean and standard deviation. Therefore, this can be misleading when further information is required, such as finding out whether the solution is multimodal or not. Consequently, the probabilistic distribution of $y(\mathbf{x}, \xi)$ is often also sought and by sampling techniques the output distributions can be easily generated.

There is a huge amount of work on the application of the Monte-Carlo technique. Some examples can be found in [168, 216, 59, 68]. The Monte-Carlo approach basically consists in a random sampling, since it is based on the idea of generating random points with values of the input parameters to sample the stochastic space evaluating the model. As many data points are inputs for the model, it produces many output points for each output variable under study. From this data, useful statistical information can be found such as means, variance, standard deviation, build probabilistic distributions of the outputs, etc. The more points, the better, since the more the input stochastic space is sampled and therefore the statistical moments are reliable. This can be described as a seek of convergence, since the statistical moments must not significantly change when more points are added to the sampling campaign. Despite of the popularity of the method, the weakest fact of this approach is the

2.1 An Overview of Uncertainty Quantification

randomness and the large number of samples (usually) required to achieve convergence in non-linear problems. This essentially affects to the stratification of the samples: because of the random nature, it can happen to have points clustering and vice versa, affecting the convergence. As the convergence of the Monte-Carlo method is of order $O(1/\sqrt{N_s})$, with N_s the number of samples, in order to reduce the size and increase the efficiency, some other sampling techniques are available in literature.

Very popular ones are Latin Hypercube (LHS) [93], quasi-random Halton [64], Hammersley [187] and Sobol sequences [29], that are often referred to as Quasi-Random Monte-Carlo and low-discrepancy sequences. An illustration of the distribution of samples with the different methods can be seen in Fig. 2.1. These sampling techniques optimise the sampling by taking also into account previous positions of the samples in the stochastic space (hence, they are not entirely random), and the convergence can be essentially considered as a $O(1/N_s)$ [15].

LHS differs from Monte-Carlo in the fact that the sampling is more stratified. The range of each variable ξ_i is exhaustively divided into N_{int} disjoint intervals of equal probability and one value is selected at random from each interval. The N_{int} values thus obtained for ξ_1 are paired at random without replacement with the N_{int} values obtained for ξ_2 . These N_{int} pairs are combined in a random manner without replacement with the N_{int} values of ξ_3 to form N_{int} triples. This process is continued until a set of N_{int} N_ξ -tuples is formed [93]. When Monte-Carlo or LHS methods are deployed, one has to set an initial budget for the Design of Experiment (DoE), which must be developed taking into account different number of samples to compare their performance. Then, when a larger/smaller number of samples is required to perform a convergence analysis, LHS does not solve the Monte-Carlo's drawback of unintentional "clustering/holey" with the increase that takes place if the previous samples are kept. Moreover, in a LHS, to join two or more different sample campaigns would lead to a new sample without the initial LHS stratification property. This is something that sequences solve, keeping the former samples in its place (nested). An example is shown in Fig. 2.1 for Sobol sequences, where one can see that when increasing the number of samples, one can keep the former ones with a nested approach. Moreover, it is observed a sampling that is distributed following a repetitive pattern (giving the name of sequence). The type of pattern is different for each method, but the convergence rate is the same in practice.

In the analysis presented in this thesis, as LHS and sequences convergence rate is pretty similar, if the model or solver evaluations are not expensive (it is the case when sampling surrogate models), it is not a crucial thing and Monte-Carlo and LHS are still a very powerful and recommended sampling method. Good examples of application of LHS can be found in [84, 39, 171].

2.1 An Overview of Uncertainty Quantification

It is important to remark that these improvements are only noticed for moderate dimensions of the stochastic space, as for high dimensional problems these sampling techniques behave similarly to Monte-Carlo (which is dimension independent).

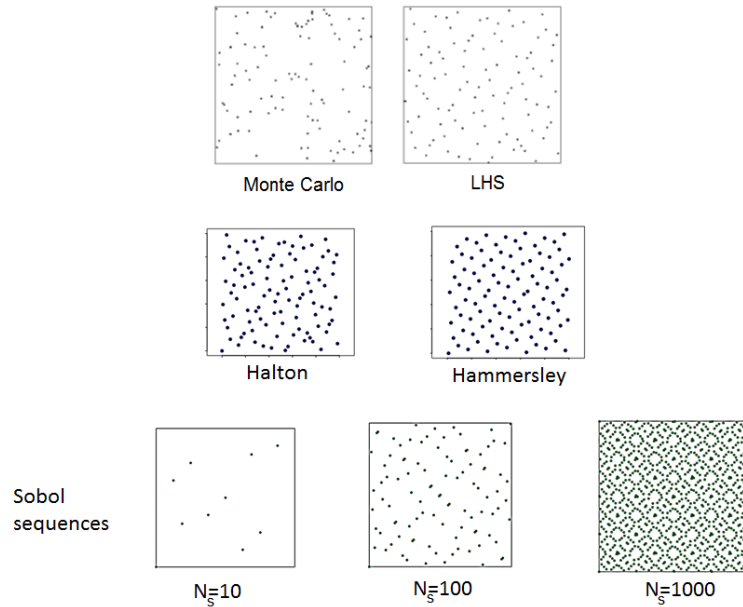


Figure 2.1 Comparison of sampling techniques. Image created with several images from <https://people.sc.fsu.edu/~jburkardt>

Stochastic Collocation Method (SCM)

Sampling based methods are, as aforementioned, a good choice for UQ. However, they usually require a large number of model evaluations (thousand of them). This is an enormous disadvantage when performing UQ in CFD, as each model evaluation takes too long, being in most cases unaffordable. To overcome this drawback, Stochastic Collocation Method (SCM) [149] can be implemented. This method allows to calculate the statistical moments of the output, $\mu(\mathbf{x}, \xi)_i^y$ in Eq. (2.4), by dedicated quadrature rules on grid points.

The non-intrusive Stochastic Collocation Method (SCM) was developed by Mathelin and Hussaini [149] at NASA to improve the high costs of other UQ methods. SCM outperforms sampling methods especially for low dimensions in the stochastic space, being an acceptable method for up to 5 uncertain inputs in most cases. When the dimension is high, the computational cost leads to the so-called *Curse of Dimensionality* [22, 56], as the number of collocation points to evaluate increases exponentially and it is preferable to look at other methods.

2.1 An Overview of Uncertainty Quantification

SCM undergoes convergence when the input uncertainty is modelled by uniform probabilistic distributions. When implementing the algorithm, special attention must be paid on the probabilistic density function of the random variables $\xi \in \Xi$, as we have to perform a mathematical transformation from the physical random variable space to an artificial stochastic space, known as α -domain or α -space (Eq. (2.5)), and this depends on how the probabilistic distributions are chosen. This transformation is a difference with respect to other UQ methods as the stochastic space $\hat{\alpha}$ is defined according to the appropriate domain of Lagrange interpolating polynomials in $[-1, 1]$ ¹. It is hence interesting to observe that, for each collocation point, the CFD problem is solved deterministically and the solution can be reconstructed by \hat{y}^{SC} as

$$\hat{\alpha} = \mathcal{S}(\xi), \quad (2.5)$$

$$\hat{y}^{SC}(\mathbf{x}, \hat{\alpha}) \simeq \sum_{j=1}^{N_q} y_j(\mathbf{x}) l_j(\mathcal{S}^{-1}(\hat{\alpha})) = \sum_{j=1}^{N_q} y_j(\mathbf{x}) l_j(\hat{\alpha}), \quad (2.6)$$

where $y_j(\mathbf{x})$ are the deterministic solutions from $y(\mathbf{x}, \xi_j)$ now transformed into $y(\mathbf{x}, \hat{\alpha}_j)$, N_q the number of collocation points and l_j the Lagrange interpolation polynomials defined in the new stochastic space. Note that $\mathcal{S}^{-1}(\hat{\alpha})$ denotes the inverse mathematical transformation to $\hat{\alpha} \in \Gamma$. The integral of Eq. (2.4) can now be approximated as

$$\mu(\mathbf{x}, \hat{\alpha})_i^{\hat{y}^{SC}} = \sum_{j=1}^{N_q} y_j(\mathbf{x})^i \int_{\Gamma} l_j(\hat{\alpha}) f_{\xi}(\hat{\alpha}) J(\hat{\alpha}) d\hat{\alpha}, \quad (2.7)$$

where $J(\hat{\alpha})$ the Jacobian of the differential transformation. The integral of Eq. (2.4) can now be numerically computed by quadrature:

$$\mu(\mathbf{x}, \hat{\alpha})_i^{\hat{y}^{SC}} \simeq \sum_{j=1}^{N_q} y_j(\mathbf{x})^i \sum_{k=1}^{N_q} l_j(\hat{\alpha}_k) f_{\xi}(\hat{\alpha}_k) J(\hat{\alpha}_k) z_k, \quad (2.8)$$

with z_k and $\hat{\alpha}_k$ standing for the quadrature weights and points respectively. Both the quadrature and collocation points can be chosen to coincide. Moreover, Lagrange interpolating polynomials are defined in the transformed space with the property of $l_i(\hat{\alpha}_j) = \delta_{ij}$ for $i, j = [1, 2, \dots, N_q]$, which states that at collocation points the values of y and \hat{y} coincides. Therefore, with these assumptions, the integral from Eq. (4.2) above can be finally rewritten as, *i.e.* for an uniform probabilistic input defined in $[-1, 1]$, as

$$\mu(\mathbf{x}, \hat{\alpha})_i^{\hat{y}^{SC}} \simeq \frac{1}{2} \sum_{j=1}^{N_q} y_j(\mathbf{x})^i z_j. \quad (2.9)$$

¹It is interesting to point out that in several papers [149] [139], $\hat{\alpha}$ is referred to as an artificial stochastic space, but the space is in fact Γ , as $\hat{\alpha} \in \Gamma$. In this work, we are going to refer to Γ as the α -space in order to be consistent with the existing notation in literature.

SCM has been successfully used in many applications such as elliptic partial differential equations with random input data [16], supersonic aircraft jets [84] or cardiovascular research [208]. Another advantage of using SCM is that the response can be approximated (Eq. (2.6)) and sampling techniques can be applied on it. Proceeding this way, statistical information such as the probabilistic distributions of the outputs, which were missed when focusing only on the statistical moments, can now be generated. An extension of this method for non-uniform random inputs is the Probabilistic Collocation Method (PCM)[139]. As the data analysis in this work is mostly related to uniform probabilistic inputs, and in such case both PCM and SCM coincide, the method is not going to be discussed here. For further information, the reader is suggested to see [139, 138, 255, 25].

Non-Intrusive Polynomial Chaos

The approach presented in this section is the Polynomial Chaos method. This method was developed to solve Stochastic Differential and Partial Equations (SDE and SPDE, respectively) [225]. It was firstly introduced by Wiener [251], in order to model through Hermite polynomials stochastic processes with gaussian random variables. Lately, Xiu & Karniadakis extended the original version of Wiener to a wider family of basis functions leading to the known concept of generalised Polynomial Chaos (gPC) [258]. It is also known as Askey-Chaos, due to the fact that is formed by the complete set of orthogonal polynomials from the Askey scheme [14]. The objective of such extension is that for non-gaussian random inputs, the convergence of the Hermite-chaos is low, and in some cases, disastrous.

Polynomial Chaos is a spectral method and as such, an important advantage is that one may decompose a random representation into deterministic and stochastic components as

$$\hat{y}^{gPC}(\mathbf{x}, \xi) = \sum_{j=0}^{\infty} y_{m_j}(\mathbf{x}) \Psi_j(\xi), \quad (2.10)$$

where y_{m_j} are the deterministic coefficients (also called modal coefficients) with \mathbf{x} the spatial coordinates and $\Psi_j(\xi)$ is the orthogonal base (constructed using the well-known three term recurrence relation), in a tensor-like form by 1-D products of the orthogonal polynomials, satisfying the orthogonality relation

$$\langle \Psi_i, \Psi_j \rangle = \langle \Psi_i^2 \rangle \delta_{ij}, \quad (2.11)$$

with δ_{ij} the Kronecker delta function and $\langle \cdot, \cdot \rangle$ the inner product. For instance, in Legendre-chaos, by applying the three-term relation it can be generated the firsts five Legendre polynomials as

$$\Psi_0(\xi) = 1, \quad (2.12)$$

2.1 An Overview of Uncertainty Quantification

$$\Psi_1(\xi) = \xi, \quad (2.13)$$

$$\Psi_2(\xi) = \frac{1}{2}(3\xi^2 - 1), \quad (2.14)$$

$$\Psi_3(\xi) = \frac{1}{2}(5\xi^3 - 3\xi), \quad (2.15)$$

$$\Psi_4(\xi) = \frac{1}{8}(35\xi^4 - 30\xi^2 + 3), \quad (2.16)$$

$$\Psi_5(\xi) = \frac{1}{8}(63\xi^5 - 70\xi^3 + 15\xi). \quad (2.17)$$

In Eq. (2.10), the expansion has infinite terms. For practical reasons, this expansion has to be truncated accounting $N_t - 1$ terms, with

$$N_t = \frac{(N_\xi + P)!}{N_\xi! P!} \quad (2.18)$$

and P standing for the maximum order of the expansion. So that, the chaos expansion is finally expressed as

$$\hat{y}^{gPC}(\mathbf{x}, \xi) = \sum_{j=0}^{N_t-1} y_{m_j}(\mathbf{x}) \Psi_j(\xi). \quad (2.19)$$

In the following, it will get rid of \mathbf{x} and ξ just for sake of notation. Polynomial Chaos can be either an intrusive or non-intrusive approach. In this thesis it is only implemented as non-intrusive, due to the fact that it takes into account the solver as a black-box not requiring to code inside each CFD software. The deterministic coefficients, y_{m_j} , are computed as

$$y_{m_j} = \frac{\langle y, \Psi_j \rangle}{\langle \Psi_j^2 \rangle}. \quad (2.20)$$

The evaluation of Eq. (2.20) is in fact the computation of the multidimensional integral over the domain $\hat{\Omega}$, on which deterministic simulations of y from the CFD solver are required under prescription of the collocation scheme. Moreover, this inner product is based on the measure of weights according to the choice of the orthogonal polynomials Ψ , as the weight function is in fact the probabilistic distribution function. Thus, it is necessary to compute two integrals in Eq. (2.20). Focusing on the numerator, the inner product integral is

$$\langle y, \Psi_j \rangle = \int_{\Xi} y(\mathbf{x}, \xi) \Psi_j(\xi) f_\xi(\xi) d\xi, \quad (2.21)$$

which has to be numerically solved, being intended to compute by quadrature techniques the expression

2.1 An Overview of Uncertainty Quantification

$$\langle y, \Psi_j \rangle \simeq \sum_{j=1}^{N_q} y_j(\mathbf{x})^i \sum_{k=1}^{N_q} \Psi_j(\xi_k) f_{\xi}(\xi_k) J(\xi_k) z_k, \quad (2.22)$$

with z_k and ξ_k standing for the quadrature weights and points in the discretisation respectively. Similarly, the denominator in Eq. (2.20) can be written as

$$\langle \Psi_j, \Psi_j \rangle = \int_{\Xi} \Psi_j(\xi) \Psi_j(\xi) f_{\xi}(\xi) d\xi, \quad (2.23)$$

and it is not compulsory to solve the integral by quadrature techniques, since it can be tabulated due to the properties of orthogonal polynomials.

With gPC, depending on the random input distribution, different polynomial basis functions must be chosen. The recommended choice can be seen in Table 2.1.

Table 2.1 Correspondence of the type of Wiener–Askey polynomial chaos to the type of random inputs ($N \geq 0$ is a finite integer) [258].

	Random inputs	Wiener-Askey chaos	Support
Continuous	Gaussian	Hermite-chaos	$(-\infty, +\infty)$
	Gamma	Laguerre-chaos	$[0, +\infty]$
	Beta	Jacobi-chaos	$[a, b]$
	Uniform	Legendre-chaos	$[a, b]$
Discrete	Poisson	Charlier-chaos	$\{0, 1, 2, \dots\}$
	Binomial	Krawtchouk-chaos	$\{0, 1, \dots, N\}$
	Negative binomial	Meixner-chaos	$\{0, 1, 2, \dots\}$
	Hypergeometric	Hahn-chaos	$\{0, 1, \dots, N\}$

Once the coefficients are computed, the mean and the variance can be found by

$$\mathbb{E}(\hat{y}^{gPC}) = \langle y \rangle = y_{m_0}, \quad (2.24)$$

$$\mathbb{V}(\hat{y}^{gPC}) = \left\langle (y - \mathbb{E}(\hat{y}^{gPC}))^2 \right\rangle = \sum_{j=1}^{N_t-1} y_{m_j}^2 \langle \Psi_j^2 \rangle. \quad (2.25)$$

Polynomial Chaos has been a popular method in the recent years with many successful applications in literature [43, 142, 58]. An advantage of gPC that cannot be found in SCM is that sensitivity analysis is straightforward (costless in fact) from the uncertainty analysis. This will be further discussed in Section 2.2.

Numerical Integration by Quadrature

For both Non-Intrusive Polynomial Chaos and Stochastic Collocation, the choice of collocation points is a very important matter. The aim of the data analysis is to compute the statistics of the outcomes, *i.e.* the mean and variance as

$$\mathbb{E}(y) = \int_{\Xi} y(\mathbf{x}, \xi) f_{\xi}(\xi) d\xi, \quad (2.26)$$

$$\mathbb{V}(y) = \int_{\Xi} (y(\mathbf{x}, \xi) - \mathbb{E}(y))^2 f_{\xi}(\xi) d\xi. \quad (2.27)$$

These integrals can be computed by using quadrature rules, as explained in the previous subsections. It is hence intuitive to think that it is possible to perform such task with any of the well-known available possibilities.

Newton-Cotes formulas are a very popular method in academic degree studies. Examples of this formula are the Simpson or trapezoidal rules. The most relevant feature of these methods is that the chosen nodes for the numerical integration are equidistant. The polynomial exactness of the formula is $N_q - 1$, being N_q the number of points. Despite their easy construction, these methods have the drawback of being numerically unstable for large number of points [119] and non-nested. By nested, it is referred to a quadrature rule with a grid that satisfies $\Gamma^l \subset \Gamma^{l+1}$, being l the desired level of accuracy in the integration. In other words, the number of grid points has to be included in the next sets generated when increasing the accuracy (the number of nodes). This is an important fact, since only the new points have to be solved with the CFD software, using this way previous simulations.

Gaussian quadrature is also a very popular and effective method for numerical integration. This rule generates the quadrature points and weights in order to maximise the accuracy of the integration (maximises the order of the polynomial to be exactly integrated). The polynomial exactness of the method is greater than the one present in Newton-Cotes formulas, being $2N_q + 1$. For the case of the unit weight function, the abscissas are the zeroes of the Legendre polynomials and the weights are computed by integrating the associated Lagrange polynomials [77]. However, these classic gaussian formulas are in general not nested either. Patterson [185, 77] iterated Kronrod's scheme [120] recursively and obtained a sequence of nested quadrature formulas with maximal degree of exactness, leading to the so-called Gauss-Patterson rule.

Clenshaw-Curtis rules [40] are also a very reliable choice for our quadrature purposes. They use non-equidistant abscissas given by the zeros of the Chebyshev polynomials defined

2.1 An Overview of Uncertainty Quantification

in $[-1, 1]$

$$\xi_i^{(j)} = \cos \frac{j\pi}{N_q}. \quad (2.28)$$

The Clenshaw-Curtis rule is nested and the polynomial degree of exactness is $N_q - 1$. A good property of this formula is that the abscissas at the boundary can be included in the collocation grid, which is a property not always available for other rules.

In the extension to multiple dimensions, if tensor grids built by a tensor product are chosen for numerical integration, the computational cost would be very high, especially when N_ξ is not low, since many simulations would be required and the problem of the *Curse of Dimensionality* would be present. To overcome this problem, a very efficient alternative is the use of sparse grids. As in a tensor-like construction many "useless" grid points are generated, a good approach is to test different levels of accuracy in a sparse grid set. By accuracy it is referred to how close to the exact value the calculation of the statistical moments is. Remember that in uncertainty quantification, the practical target is to give evidence about how confident on the performance one can be, as a consequence of the variability in the input data. That is to say, how much one can trust in the performance under uncertainty. Therefore, if the method is very accurate, this leads to the possibility of measuring with precision by simulations the confidence in our real-life fluid dynamics design. If this can be made also at a reasonable cost, even better. Sparse grids are a good alternative that combine a computationally cheaper approach than tensor grids, but accurate. This method is explained next.

Use of Sparse Grids for Quadrature

When performing an uncertainty analysis on CFD simulations, as each collocation point prescribes a particular CFD simulation, it is very useful to reduce the analysis to the lowest number as possible of collocation points, but yet keeping a desired accuracy. This is often referred to as the available computational budget, that is the answer to the question of *how many model evaluations can we afford?*

Sparse grids are built under the so-called Smolyak construction [219]. The main idea behind this approach is to construct a multidimensional grid based on linear combinations of the tensor product interpolants, building this way a coarser grid. Once the collocation points and weights are computed, the integrals can be solved by quadrature and convergence can be checked. If the function is relatively smooth, a quick convergence is expected by means of this approach.

2.1 An Overview of Uncertainty Quantification

For the sake of clarity, the linear combination will be better explained with examples ². Let assume that a sparse grid to exactly integrate all monomials up to order five is desired for a 2D case. As can be seen in Fig. 2.2, a rule that could integrate up to fifth order would need to capture the monomials shown in blue. However, if a tensor grid is constructed, one would be also generating the monomials in red. It is hence clear that with a full tensor product one would require to compute (many) nodes that are not affecting at all to the accuracy. With a sparse grid construction, we would need only those in blue.

7	y^7	xy^7	x^2y^7	x^3y^7	x^4y^7	x^5y^7	x^6y^7	x^7y^7
6	y^6	xy^6	x^2y^6	x^3y^6	x^4y^6	x^5y^6	x^6y^6	x^7y^6
5	y^5	xy^5	x^2y^5	x^3y^5	x^4y^5	x^5y^5	x^6y^5	x^7y^5
4	y^4	xy^4	x^2y^4	x^3y^4	x^4y^4	x^5y^4	x^6y^4	x^7y^4
3	y^3	xy^3	x^2y^3	x^3y^3	x^4y^3	x^5y^3	x^6y^3	x^7y^3
2	y^2	xy^2	x^2y^2	x^3y^2	x^4y^2	x^5y^2	x^6y^2	x^7y^2
1	y	xy	x^2y	x^3y	x^4	x^5y	x^6y	x^7y
0	1	x	x^2	x^3	x^4	x^5	x^6	x^7
P_p	0	1	2	3	4	5	6	7

Figure 2.2 Monomials for integration of polynomials of order P_p [30].

Another important property that we can get from the sparse grids is the nested rule. As mentioned already, a grid will be nested if satisfies $\Gamma^l \subset \Gamma^{l+1}$, being l the desired level of accuracy in the integration. Let illustrate this with an example.

Suppose that it is desired to integrate up to first order in a 2D problem. This would require a lineal combination of 1, x and y , avoiding xy . Let Θ represent a family of 1D quadrature rules in $[0, 1]$, so that $\Theta(l)$ can integrate polynomials of degree l exactly. As $l = 1$ and with each 1D quadrature rule containing 2 points; instead of using the tensor product rule $\Theta(1, 1) = \Theta_x(1) \otimes \Theta_y(1)$ that requires four points, could be tried the following combination of three rules

$$\mathcal{A}(l = 1, N_\xi = 2) = \Theta(1, 0) + \Theta(0, 1) - \Theta(0, 0). \quad (2.29)$$

This combination requires only three points. Suppose now that the 1D rules are nested, so the second rule includes the point used in the first rule, the third rule includes the two points in the second and so on. For this example, one might have

$$\Theta(0, 0) = a f(0, 0), \quad (2.30)$$

²The examples presented in this section are mainly extrated from [30] and [5], combined in a coherent way and extended to explain the construction as clear as possible, since it is less straightforward to follow from the available formal mathematical descriptions in literature.

2.1 An Overview of Uncertainty Quantification

$$\Theta(1, 0) = b f(0, 0) + c f(1, 0), \quad (2.31)$$

$$\Theta(0, 1) = d f(0, 0) + e f(0, 1), \quad (2.32)$$

where a, b, c, d and e are appropriate weights. If we compute the three quadrature rules as separate computations, and then combine the numeric results, the computation does indeed require five function evaluations. But if we take advantage of the nesting, we can get the same result as with a tensor grid by substituting in Eq. (2.29)

$$\mathcal{A}(l = 1, N_\xi = 2) = (b + d - a) f(0, 0) + c f(1, 0) + e f(0, 1). \quad (2.33)$$

Now we only need three function evaluations, and have a rule precise for the constants and linears. This is the basic idea of Smolyak sparse grids, to combine the low-order rules in order to achieve a desired accuracy in the integration while saving the cost of evaluating useless points that do not contribute to the precision. Smolyak also developed a general formula [218] for the integral \mathcal{A} of a function with sparse grid construction as a weighted sum of N_ξ -dimensional product rules

$$\mathcal{A}(l, N_\xi) = \sum_{l - N_\xi + 1 \leq |\mathbf{l}| \leq l} (-1)^{l - |\mathbf{l}|} \binom{N_\xi - 1}{l - |\mathbf{l}|} \left(\Theta^{l_1} \otimes \dots \otimes \Theta^{l_{N_\xi}} \right). \quad (2.34)$$

The level l sparse grid in N_ξ dimensions is formed from low order product rules (Θ), each defined by a level vector $\mathbf{l} = l_1 + \dots + l_{N_\xi}$, where l_j is the level or index of the j -th 1D rule. While the individual product rules may be anisotropic, the indexing on the sum allows the resulting grid to be isotropic, following the above mentioned procedure for the examples.

Following this methodology, one can easily construct the sparse grid for any monomials in the stochastic domain $\{\xi_1, \xi_2, \dots, \xi_{N_\xi}\}$ by following the steps presented in Fig. 2.3 for a 2D case. With this procedure, it is demonstrated that the quality of the sparse grid is the same but with less cost than directly using the 5×5 tensor grid. For the sparse grid, only combinations of 3×1 , 1×3 , 5×1 , 1×5 and 3×3 rules have been enough. The construction for this 2D case is then:

$$\mathcal{A}(l = 0, N_\xi = 2) = \Theta_{\xi_1}^0 \otimes \Theta_{\xi_2}^0, \quad (2.35)$$

$$\mathcal{A}(l = 1, N_\xi = 2) = \Theta_{\xi_1}^1 \otimes \Theta_{\xi_2}^0 + \Theta_{\xi_1}^0 \otimes \Theta_{\xi_2}^1 - \Theta_{\xi_1}^0 \otimes \Theta_{\xi_2}^0, \quad (2.36)$$

$$\mathcal{A}(l = 2, N_\xi = 2) = \Theta_{\xi_1}^2 \otimes \Theta_{\xi_2}^0 + \Theta_{\xi_1}^1 \otimes \Theta_{\xi_2}^1 + \Theta_{\xi_1}^0 \otimes \Theta_{\xi_2}^2 - \Theta_{\xi_1}^1 \otimes \Theta_{\xi_2}^0 - \Theta_{\xi_1}^0 \otimes \Theta_{\xi_2}^1. \quad (2.37)$$

Bear in mind that, for dimensions greater than 2, the weights are not ± 1 , but they are also constructed by combinatorials. For sake of demonstrating a practical case, in Fig. 2.4 the evolution in the construction for the Clenshaw-Curtis nested rule [238] is shown up to the fourth level for $N_\xi = 2$. The sparse grids have been generated from combinations to decrease

2.1 An Overview of Uncertainty Quantification

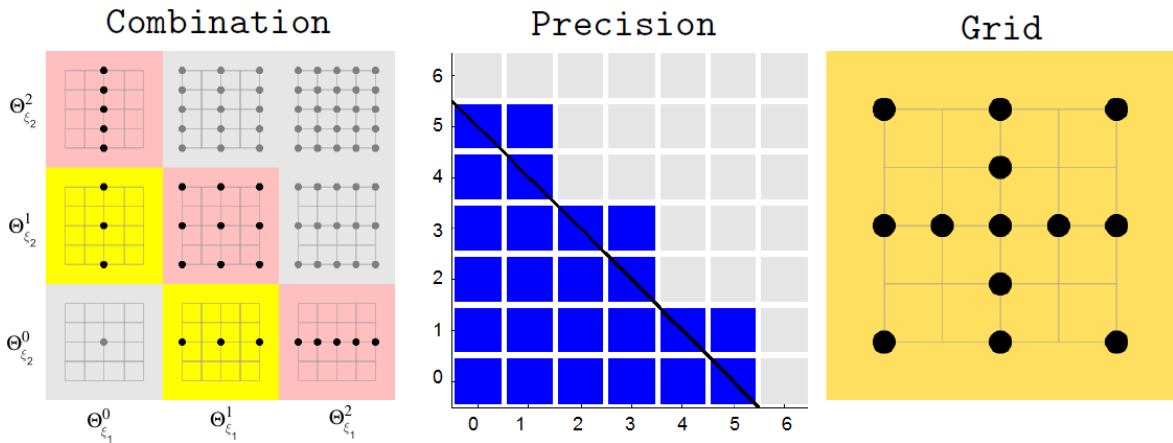


Figure 2.3 Smolyak construction for $P_p = 2$ and $N_{\xi} = 2$. It can be noticed that with the lower triangular set of rules the grid can be constructed without the upper ones. *Image from [30] with minor modifications.*

the number of points as explained for the general case, in contrast to the tensor grid shown in Fig. 2.5.

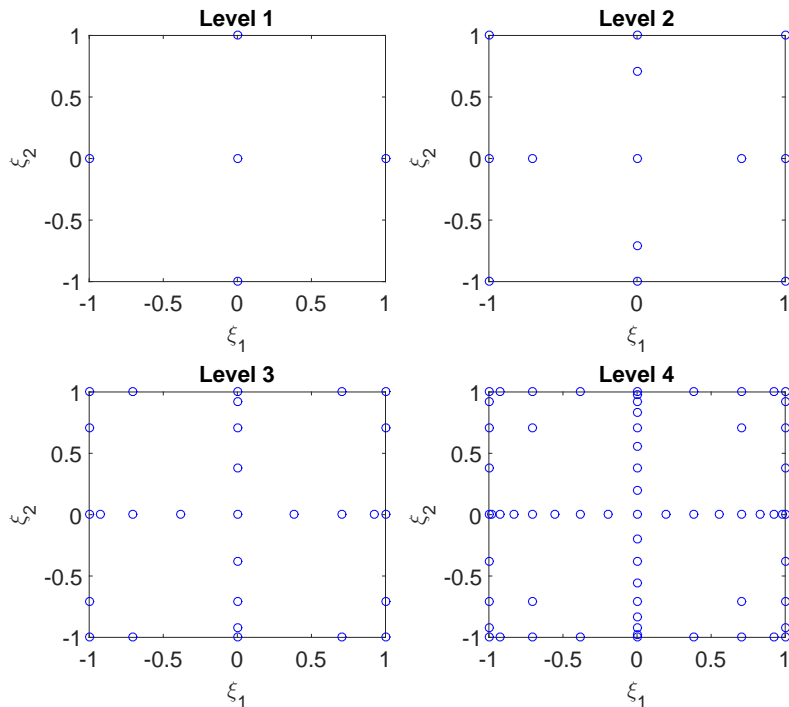


Figure 2.4 Clenshaw-Curtis Smolyak's nested Sparse Grids for different levels of accuracy.

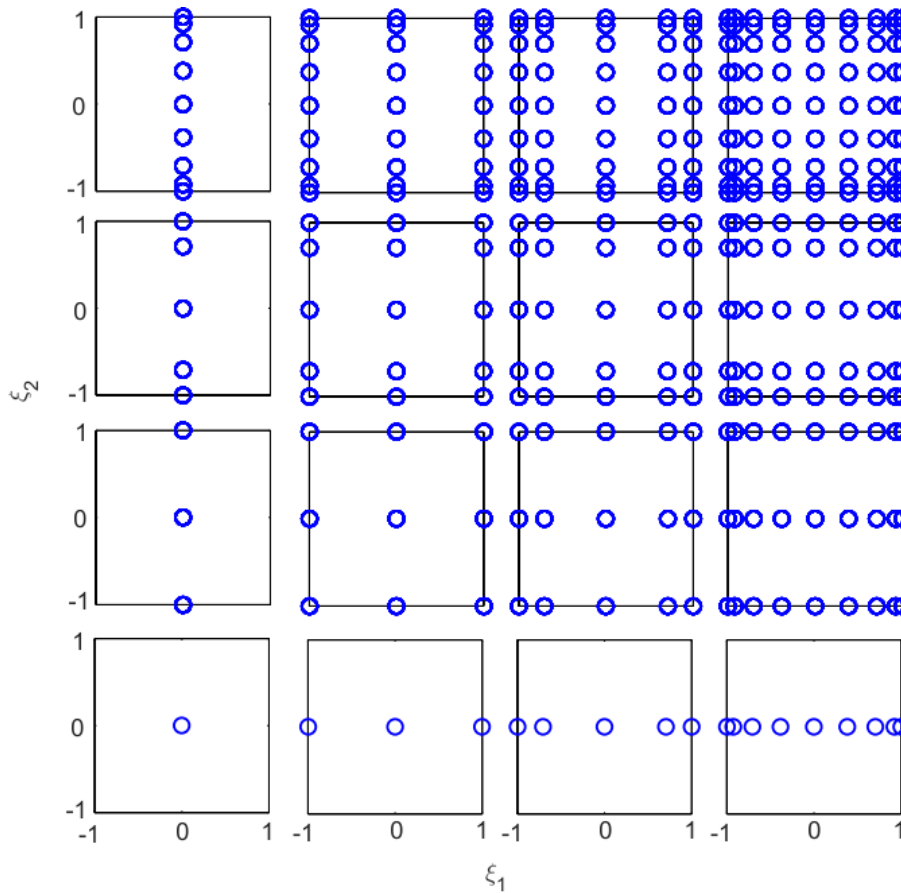


Figure 2.5 Clenshaw-Curtis tensor grid construction.

Regarding the choice of the quadrature rule for the sparse grid, there is some freedom. Depending on the distribution of the input variables, there are some recommendations. If the random parameter is uniform, Clenshaw-Curtis or Gauss-Legendre are recommended. If gaussian, Gauss-Hermite. For gamma distributed parameters, Gauss-Laguerre. And finally, for beta distributions, Gauss-Jacobi. Most of the work in this thesis has been focused on uniform probabilistic distributions, so Clenshaw-Curtis sparse grids has been the preferred choice. It is worthy to remark that an advantage of this sparse grid is that the points at the limit bounds are included, in contrast with Gauss-Legendre quadrature. Clenshaw-Curtis sparse grids are always nested, so that the level of accuracy l is always including the lowest levels. Moreover, this sparse grid is able to exactly integrate polynomials of order $P_p = 2l + 1$ or lower.

As each direction of the sparse grid can be treated differently, in some case scenarios, it might be also interesting to construct an anisotropic sparse grid. As this was not present in any purpose of the thesis, this type of sparse grid is not described here but the author suggests

to see [78, 167] for further information.

To wrap-up the use of sparse grids, it is interesting to say that they are present in many interesting applications such as data analysis [74, 125, 192] and of course uncertainty quantification [84, 116, 70, 2, 183] and sensitivity analysis [26, 84]. Despite they are a known quadrature method with successful applications in the uncertainty and sensitivity analysis field, it is not common to find it in literature and many researchers still prefer the less efficient use of full tensor rules.

Surrogate-based Uncertainty Quantification.

The use of surrogates is a popular inverse approach to expensive problems or when most of the information available is only output data. In some case scenarios, such as optimisation or UQ in CFD problems, a simulation is too costly to be repeated a large number of times for the purpose.

The term ‘costly’ stands for ‘long time run simulation’ throughout this thesis. This is the common issue in CFD involving complex physics, models and/or large simulation domains as those appearing in this manuscript. The computational efforts to model the turbulent properties and solve the discretised Navier-Stokes equations in 2D/3D domains are intensive. Sometimes, as in the study of the swirling flow to be used as impinging jet, the problem has to be split in two simulations, being even a more expensive calculation. In UQ of CFD problems, the reduction of the computational time is the greatest challenge. Some type of simulations in fluid dynamics (such as Large Eddy or Direct Numerical Simulations) usually require more than a month for each deterministic simulation in High Performance Computing centers, being uncertainty analysis discarded. In this thesis, Reynolds-Averaged Navier-Stokes equations are employed, so the computational cost of each deterministic simulation is sensitively lower, but far from being fast (around half a week with our regular computational resources). Therefore, as more than one costly simulation is required in UQ, to be able to build an almost immediate equation to generate the desired output is really helpful.

With enough information, a costless model can be found using some specific techniques or approaches. These are the nick-named *surrogates* (also known as *metamodels* or *Response Surfaces*). These models have the form

$$y(\xi) = \hat{y}(\xi) + \varepsilon(\xi), \quad (2.38)$$

with y being the exact model, \hat{y} the surrogate model and ε the difference between the surrogate and the exact formulation.

2.1 An Overview of Uncertainty Quantification

For the construction of metamodels, several possibilities are available in literature. Among them, perhaps the most popular one is the use of polynomial fits (see Appendix B for a practical example), which requires to simply model the surrogates as n order polynomials and the objective is to find the coefficients by means of inverse techniques. The problem with these techniques is that for high-dimensional non-smooth case scenarios can become too costly, and in addition to this, the algorithm implemented for the coefficient calculation could not be very robust. The reason is that some algorithms such as steepest descent or conjugate-gradient method [96] suffer a strong dependence with respect to the initial guess. Another drawback for polynomial fitting is that it is very case dependent. If a problem has a very changing behaviour, as it does happen with the Mach number evolution along the centerline (Fig. 5.11 in Chapter 5), it becomes complicated to find a global polynomial fit configuration for such non-smooth behaviour.

It is also very important to remind that from the SCM and gPC studies, one can not only make a direct computation (by numerical integration) of the statistical moments, but also to reconstruct the output with Eqs. (2.6) and (2.19). These surrogates are then at our disposal to be sampled if desired. These models have been even used for optimisation purposes [118].

Other more popular methods for surrogate modelling are Multivariate Adaptive Regression Splines (MARS), Radial Basis Functions (RBF) and Kriging.

MARS [71] are considered an extension of regression analysis. This method produces a kink in the prediction \hat{y} to create an adaptation to non-linear data sets, produced by hinge functions. A hinge function has the form $\max(0, x - \text{constant})$ or $\max(0, \text{constant} - x)$ [232]. This is one of their main advantages, in addition to their easy implementation.

RBF [28] uses the Euclidean norm to evaluate the distance between points in the interpolant

$$\hat{y}(\xi) = \sum_{i=1}^N \varsigma_i \phi(\|\xi - \xi_i\|) + \hat{f}(\xi), \quad (2.39)$$

where the constant $\varsigma \in \mathbb{R}$, $f(\xi)$ stands for a polynomial approximation and the so-called radial function ϕ can be of different types (linear, multiquadratic, cubic, gaussian or thin flat spline) [198]. RBF are a very powerful technique and have been used not only for optimisation or uncertainty analysis but also for other interesting applications such as Neural Networks for classification [164] or 3D image reconstruction [34].

Kriging surrogates have some extra features with respect to the others, as making predictions with uncertainty estimates or compensating the effects of data clustering. The selection of an appropriate surrogate method must be done taking into consideration the nature of the problem and can be also a personal preference (*i.e.* because of easier implementation).

2.1 An Overview of Uncertainty Quantification

In this thesis, due to the flexibility and robustness of the method with respect to others, as well as the possibility of generate good fits with few points, Kriging has been the preference and will be described as follows. There is some literature such as [232, 214, 63] that shows comparisons among these methods and descriptions for further interest.

Surrogate-based Uncertainty Quantification by Kriging Interpolation

Kriging (also known as Gaussian Process interpolation and in this thesis under the acronym KG) is a Machine Learning interpolation surrogate method to approximate sets of data and it has been widely used in literature, specially for tasks involving costly computational analysis that by other methods would be expensive. Examples of this are CFD optimization [128, 85], sensitivity analysis [245], topography [133] or prototyping [97].

In essence, Kriging is a two-step process: first a regression function $\hat{f}(\xi)$ is generated based on the data set, and from its residuals a Gaussian process $Z(\xi)$ is built, as can be seen in Eq. (2.40)

$$\hat{y}^{KG}(\xi) = \hat{f}(\xi) + Z(\xi) = \sum_{i=1}^k \gamma_i f_i(\xi) + Z(\xi), \quad (2.40)$$

where $f(\xi)$ stands for the $k \times 1$ vector of basis regression functions $[f_1(\xi) f_2(\xi) \dots f_k(\xi)]$ and γ_i denotes the coefficients. Depending on the regression function, Kriging can be baptised with different names. Universal Kriging defines the trend function as a multivariate polynomial, as described in Eq. (2.40). Simple Kriging refers to the use of a known constant parameter as regression function, *i.e.* $\hat{f}(\xi) = 0$. A more popular version is Ordinary Kriging, which also assumes a constant but unknown regression function $\hat{f}(\xi) = \gamma_0$. Another interesting type of Kriging interpolation is the namely Gradient-Enhanced Kriging (also referred to as Co-Kriging) [128, 90, 56, 51]. The improvements that this technique introduces is the possibility of using information of the gradient to reduce the number of samples. For Kriging interpolation, the same MATLAB toolbox [140] used by the first author in [85] has been utilised here.

The Gaussian process $Z(\xi)$ is prescribed to have mean zero and $cov(Z(\xi_i), Z(\xi'_i)) = \sigma_p^2 R_c(\theta, \xi_i, \xi'_i)$, where σ_p^2 is the process variance and $R_c(\theta, \xi_i, \xi'_i)$ is the correlation model or spatial correlation function (SCF).

In order to create an accurate Kriging surrogate it is important to pay attention to the correlation function. This function only depends on the distance between the two points ξ_i and ξ'_i , and, for the general exponential case introduced in Eq. (2.41), also on p_{KG} . The smaller the distance between two points, the higher the correlation and, hence, the more the Kriging predictor is influenced by the other. By the same token, if the distance gets bigger, the correlation drops to zero. For these reasons, it is not typically worthy to put several

2.2 An Overview of Sensitivity Analysis

data points together, as the prediction would not be influenced. Several correlations can be tried, but in the present work the generalised exponential worked very well and was the final choice.

$$R_c(\boldsymbol{\theta}, \xi_i, \xi'_i) = e^{-\theta|\xi_i - \xi'_i|^{p_{KG}}} \quad (2.41)$$

Once the Kriging surrogates are available, the sampling techniques described in Section 2.1.4 are affordable. Generally speaking, sampling techniques evaluate the models \hat{y}^{KG} for different inputs ξ , obtaining in that way the model predictions \hat{y}_i of a system

$$\hat{y}_i = \hat{y}^{KG}(\xi_i). \quad (2.42)$$

The goal of uncertainty analysis is to determine the uncertainty in \hat{y}^{KG} that results from uncertainty in the elements of ξ . These input uncertainties are represented by probabilistic distributions, on which the sampling is done for the evaluations \hat{y}_i . From the evaluations of the model, a mapping of the performance is generated, and a simple way of representing the output uncertainties can be to compute mean and variance as

$$\mathbb{E}(\hat{y}^{KG}) = \frac{1}{N_s} \sum_{i=1}^{N_s} \hat{y}_i, \quad (2.43)$$

$$\mathbb{V}(\hat{y}^{KG}) = \frac{1}{N_s - 1} \sum_{i=1}^{N_s} (\hat{y}_i - \mathbb{E}(\hat{y}^{KG}))^2. \quad (2.44)$$

It must be noticed that to compute $\mathbb{E}^{KG}(\hat{y})$ and $\mathbb{V}^{KG}(\hat{y})$ can be an incomplete representation of uncertainty in some cases, as two probabilistic distributions can have same mean and variance but very different shape.

2.2 An Overview of Sensitivity Analysis

An extension of UQ is the Sensitivity Analysis (SA) [205]. The idea when developing a SA is to apportionate the output variance. In other words, what one is trying to find is the relevance of each uncertain input factor in the variation of an output of interest. Other side benefits that one can obtain are the possibility of reducing the dimension of the problem (non-influential parameters can be fixed) and of course support decision-making (future efforts and investment should be applied to minimise output uncertainty by tackling the influential factors).

SA can be split into local or global methods. Local methods perform the sensitivity analysis by varying, commonly around a 5%, 10% or a value decided with the experience of the scientist, the nominal value of a parameter in order to see how the output changes. This deterministic approach aims to exactly calculate or estimate the first-order partial derivatives

2.2 An Overview of Sensitivity Analysis

of the model at the nominal value point. An adjoint-based approach allows not only to process models with a large number of input variables, but also to compute this sensitivity coefficient efficiently and exactly [13], contrary to the finite-difference approach which would closely estimate the derivative with higher costs.

On the other hand, the global analysis methods perform a sensitivity measurement not taking into account only the impact of the variation of one parameter, but also the higher-order effects in a wider range of the sampling. Despite of that, in literature is very common to see the use of local sensitivity analysis or OAT (One-factor-at-A-Time) methods [160]. This method has to be used very carefully, since when used, it is assumed that the model presents linearity, neglecting higher-order interactions. For further discussion between local and global methods, see [110].

There are different methods for global sensitivity analysis, such as screening method (as Morris method), Derivate-based Sensitivity Analysis or Variance-based Analysis.

In practice, Morris screening method [159] is a very popular approach. The idea of the technique is to discretise the stochastic space into several points. Then, several OAT realisations can be developed at each design point and the elementary effect of each input can be calculated. Then it is possible to determine the non-influential parameters by plotting the mean against the standard deviation of the elementary effects. Despite of the better deal with higher-order effects, this method is not providing a reliable measure for all problems. This approach is particularly recommended for a large number of input factors, as it can give an impression of what input parameters can be fixed for dimension reduction, in order to apply more reliable but computationally cost methods such as Variance-Based ones [206, 102].

Derivate-based sensitivity analysis can be seen as a less coarse version of Morris screening [103]. In the original paper by Kucherenko & Sobol [121], some interesting conclusions have been presented: (i) a link between sensitivity indices and measures based on partial derivatives is established, (ii) it is proved that small values of derivative based measures imply small values of one-dimensional total sensitivity indices, (iii) the importance criterion in Morris can be improved by using squared partial derivative rather than its absolute value and (iv) it is shown that for highly non-linear functions the ranking of important factors using derivative based importance measures may suggest false conclusions. These conclusions, may lead to better developments to develop global sensitivity analysis in high-dimensional case scenarios [102].

Other popular sensitivity measurements can be found in Regression-based methods. From a regression work, the Pearson Product Moment Correlation Coefficient, Spearman coefficient, Standardized Regression Coefficient (SRC) and Standardized Rank Regression Coefficient (SRRC) can be computed. According to [230], the Pearson Correlation Coeffi-

cient measures the usual linear correlation coefficient between the output y and a given input ξ_i (as sensitivity index strictly applied to linear models). Spearman is essentially the same as Pearson's coefficient, but using the ranks of both y and ξ_i instead of the raw values. SRC gives the strength of the correlation between y and ξ_i through a linear regression model. The reliability of the SRC strongly depends on the \hat{R}^2 (coefficient of determination) of the linear model. SRRC is used instead of SRC when \hat{R}^2 is low. In this case, the input and output variables are replaced by their ranks, and the regression is then performed entirely on these ranks. SRRC is better than SRC if the model output varies non-linearly, but monotonically with each independent variable. In [230] a comparison with other methods revealed that these regression-based coefficients encountered difficulty with non-monotonic problems, showing hence that these measures are very model-dependent, as expected.

The scientist should choose the appropriate one depending on the non-linearity, desired reliability, computational cost, dimension of the problem or the expected output, among others. There is no general framework for this, which makes important for the scientist to understand all the possibilities and drawbacks. For the purposes of this thesis, a Variance-Based Sensitivity Analysis has been chosen [205, 230]. The main reasons for the choice are:

- The input stochastic space is entirely sampled.
- Can deal with models as black-box.
- Can deal with any model: linear, non-linear, non-monotonic, etc.
- First-order and higher-order interactions can be both computed.
- Total sensitivity indices can be computed too.
- When using sampling methods, for low-dimension problems is not excessively costly and gets more accurate results than other methods in literature.
- Possibility of ranking the influence of the input factors by sensitivity indices and fixing non-influential input parameters.

This procedure is developed from the popular ANOVA High-Dimensional Model Representation (HDMR) [221] for the decomposition of the total variance. This model representation states that given a model of the form $y = y(\xi_1, \xi_2, \dots, \xi_k)$, with y a scalar, can be decomposed as

$$y = f_0^y + \sum_{i=1}^{N_\xi} f_{\xi_i}^y + \sum_{i=1, j>i}^{N_\xi} f_{\xi_{ij}}^y + \sum_{i=1, k>j>i}^{N_\xi} f_{\xi_{ijk}}^y + \dots \quad (2.45)$$

with

$$f_0^y = \mathbb{E}(y) \quad (2.46)$$

$$f_{\xi_i}^y = \mathbb{E}(y|\xi_i) - \mathbb{E}(y) \quad (2.47)$$

$$f_{\xi_{ij}}^y = \mathbb{E}(y|\xi_i, \xi_j) - f_{\xi_i} - f_{\xi_j} - \mathbb{E}(y) \quad (2.48)$$

In these equations, the multiple subscripts refer to first, second, third or higher order interactions, depending on the number of subscripts. Following the logic, the variances of the terms in Eq. (2.45) are proposed as measures of sensitivity. This leads to the decomposition of the variance shown in Eq. (2.49), and the sensitivity coefficients can be computed as in Eq. (2.50). S_i and S_{T_i} , in Eq. (2.51), are the first-order and total sensitivity index respectively.

$$\mathbb{V}(y) = \sum_{i=1}^{N_\xi} \mathbb{V}_{\xi_i} + \sum_{i=1, j>i}^{N_\xi} \mathbb{V}_{\xi_{ij}} + \sum_{i=1, k>j>i}^{N_\xi} \mathbb{V}_{\xi_{ijk}} + \dots \quad (2.49)$$

The values at the right hand side of the expression are the first and higher order contributions to the total variance. Dividing by the total variance, the sensitivities can be computed as

$$1 = \sum_{i=1}^{N_\xi} S_i + \sum_{i=1, j>i}^{N_\xi} S_{ij} + \sum_{i=1, k>j>i}^{N_\xi} S_{ijk} + \dots + S_{ijk, \dots, N_\xi}. \quad (2.50)$$

This leads to the following expression for the total sensitivity index for the i -th parameter

$$S_{T_i} = S_i + S_{ij} + S_{ijk} + \dots + S_{ijk, \dots, m}, \quad (2.51)$$

where the right hand terms are the so-called **Sobol sensitivity coefficients** [220]. The first order sensitivity coefficient is computed as

$$S_i = \frac{\mathbb{V}_{\xi_i}(\mathbb{E}_{\xi_{\sim i}}(y|\xi_i))}{\mathbb{V}(y)}, \quad (2.52)$$

where ξ_i is the i -th factor and $\xi_{\sim i}$ denotes the matrix of all factors but ξ_i . This index indicates by how much one could reduce on average the output variance if a parameter could be fixed. On the other hand, the total effect index can be computed as

$$S_{T_i} = \frac{\mathbb{E}_{\xi_{\sim i}}(\mathbb{V}_{\xi_i}(y|\xi_{\sim i}))}{\mathbb{V}(y)}. \quad (2.53)$$

S_{T_i} measures the total effect, *i.e.* first and higher order effects (interactions) of factor ξ_i . It represents a good measure to determine if a parameter is influential or not, and whether could be neglected from the model.

The use of this sensitivity technique can be seen in many fields such as solar energy [213],

wastewater treatment [215], or heat exchangers [67].

The computation of the sensitivity coefficients in the Variance-based method can be done by different ways. The two most popular approaches are Fourier Amplitude Sensitivity Test (FAST) [49, 207] and through sampling (Monte-Carlo, Latin Hypercube, etc). Both provide reliable results and a very similar computational cost. For this reason, and considering that sampling was already made for UQ purposes, the sampling one is preferred in this thesis. Being clear about the above presented idea, it is now time to introduce the two approaches developed in this thesis for global sensitivity analysis, and that have a clear connection with the previous UQ described methods: Use of gPC coefficients and Kriging surrogates. It is very important to remark that the use of two different approaches is aimed to compare results. In gPC, quadrature with sparse grids is applied to perform numerical integration, in contrast to the possibility of also generate a surrogate to sample like with Kriging, whose analysis would be substantially more costly.

Generalised Polynomial Chaos for Sensitivity Analysis

One of the interesting features of gPC is the possibility of performing sensitivity analysis straightforward after uncertainty quantification. For such task, it is not difficult to realise that there is a clear relation between Eqs. (2.25), (2.49) and (2.50). Eq. (2.25) can thus be rewritten as

$$1 = \frac{1}{\mathbb{V}(\hat{y}^{gPC})} \sum_{j=1}^{N_i-1} y_{m_j}^2 \langle \Psi_j^2 \rangle, \quad (2.54)$$

and the first and higher-order sensitivity indices can carefully be extracted from the expression above since the literal part of each monomial gives the hints of the interaction.

This approach to compute the sensitivity coefficients is **for free**. From the uncertainty analysis, all the required information is available for the sensitivity. If on the contrary we rely on the generation of a gPC surrogate, it would be necessary to perform a sampling campaign as the one to be explained in the following for Kriging surrogates.

Use of Surrogates for Sensitivity Analysis

Since the Kriging surrogates, \hat{y}^{KG} , are available from the uncertainty quantification study described in Section 2.1.4, it is now possible to compute the sensitivity indices in Eqs. (2.52) and (2.53) by means of a sampling approach.

In order to compute S_i , ξ_i has to be fixed in several points $\xi_i = \xi_i^*$ along the possible values of the random variable and then compute the mean individually for a further computation of \mathbb{V}_{ξ_i} . This would require a very large number of calculations, since the number of fixed

points has to be great enough to compute reliable statistics. A less expensive method has been coded in MATLAB by a Latin Hypercube Sampling (LHS) and following the suggested procedure in [105]. This way of computing the sensitivities is analysed in [204], comparing it with other estimators like [220, 222, 100] demonstrating very good results in different tests and concluding it as a recommended approach. Following this method, the first order sensitivity sampling Kriging surrogates, S_i^{KG} , and the total effect, S_{Ti}^{KG} , can be computed as

$$S_i^{KG} = \frac{1 - \frac{1}{2N_s} \sum_{j=1}^{N_s} (\hat{y}^{KG}(B)_j - \hat{y}^{KG}(AB^i)_j)^2}{\mathbb{V}(\hat{y}^{KG})}, \quad (2.55)$$

$$S_{Ti}^{KG} = \frac{\frac{1}{2N_s} \sum_{j=1}^{N_s} (\hat{y}^{KG}(A)_j - \hat{y}^{KG}(AB^i)_j)^2}{\mathbb{V}(\hat{y}^{KG})}. \quad (2.56)$$

In these expressions, $\hat{y}^{KG}(A)$, $\hat{y}^{KG}(B)$ and $\hat{y}^{KG}(AB)$ are model evaluated matrices, product of decomposition of the original matrices which contain the sample campaign. These two original matrices, A and B , correspond to two different independent samples on the same surrogate and random variables, with $N_s \times N_\xi$ dimensions.

Eqs (2.55) and (2.56) are built upon the original sensitivity indices shown in Eqs (2.52) and (2.53). These numerators come from the known identity

$$\mathbb{V}(y) = \mathbb{V}_{\xi_i}(\mathbb{E}_{\xi_{\sim i}}(y|\xi_i)) + \mathbb{E}_{\xi_i}(\mathbb{V}_{\xi_{\sim i}}(y|\xi_i)). \quad (2.57)$$

The first element at the right hand side of Eq (2.57) is the expected reduction in variance that would be obtained if ξ_i could be fixed. The second element at the right hand side of Eq (2.57) is the expected variance that would be left if all factors but ξ could be fixed. Hence, $\mathbb{V}_{\xi_{\sim i}}(\mathbb{E}_{\xi_i}(y|\xi_{\sim i}))$ is the expected reduction in variance that would be obtained if all factors but ξ_i could be fixed.

The aforementioned elements need to be integrated. Applying the well-known $\mathbb{V}(y) = \mathbb{E}(y^2) - \mathbb{E}^2(y)$ relation, the integral of the numerator of the first-order sensitivity index takes the form of

$$\mathbb{V}_{\xi_i}(\mathbb{E}_{\xi_{\sim i}}(y|\xi_i)) = \int \mathbb{E}_{\xi_{\sim i}}^2(y|\xi_i) d\xi_i - \left(\int \mathbb{E}_{\xi_{\sim i}}(y|\xi_i) d\xi_i \right)^2, \quad (2.58)$$

and the first integral can be rewritten and numerically computed by sampling techniques taking into account the following decomposition in $2(N_\xi - 1)$ variables

$$\begin{aligned} \mathbb{E}_{\xi_{\sim i}}^2(y|\xi_i) &= \mathbb{E}_{\xi_{\sim i}}(y|\xi_i) \mathbb{E}_{\xi_{\sim i}}(y|\xi_i) = \\ &\int \int y(\xi_1, \xi_2, \dots, \xi_i, \dots, \xi_{N_\xi}) \times y(\xi'_1, \xi'_2, \dots, \xi_i, \dots, \xi'_{N_\xi}) d\xi_{\sim i} d\xi'_{\sim i}, \end{aligned} \quad (2.59)$$

and finally the integral over $2N_\xi - 1$ variables

2.3 Conclusions and Critique on the Different Probabilistic UQ Methods

$$\int \mathbb{E}_{\xi_{\sim i}}^2(y|\xi_i)d\xi_i = \mathbb{E}_{\xi_{\sim i}}(y|\xi_i) \mathbb{E}_{\xi_{\sim i}}(y|\xi_i) = \int \int y(\xi_1, \xi_2, \dots, \xi_i, \dots, \xi_{N_\xi}) \times y(\xi'_1, \xi'_2, \dots, \xi_i, \dots, \xi'_{N_\xi}) d\xi d\xi'_{\sim i} \quad (2.60)$$

which is computed by means of the evaluations of the sampling matrices, A and B , and their resampling with replacement, AB^i and BA^i . A very similar procedure must be developed for the numerator of S_{T_i} . This improvement can be found in [105], where the numerators of the sensitivity indices are found to be best computed as

$$\mathbb{V}_{\xi_i}(\mathbb{E}_{\xi_{\sim i}}(y|\xi_i)) = \mathbb{V}(y) - \frac{1}{2N_s} \sum_{j=1}^{N_s} (y(B)_j - y(AB^i)_j)^2, \quad (2.61)$$

$$\mathbb{E}_{\xi_{\sim i}}(\mathbb{V}_{\xi_i}(y|\xi_{\sim i})) = \frac{1}{2N_s} \sum_{j=1}^{N_s} (y(A)_j - y(AB^i)_j)^2. \quad (2.62)$$

For the sake of practical clarification, the developed procedure on the surrogates is broken down as follows:

1. Generate two independent Design of Experiment with LHS: A and B .
2. For the i -th sensitivity index, only the i -th column in matrix A is swapped with the i -th column in matrix B . The new matrix is referred to as AB^i . This new version of the A matrix clearly preserves its $N_s \times N_\xi$ structure and can still be considered a sample matrix, but without the original properties of a LHS.
3. Evaluate the Kriging surrogates with the elements from the matrices A , B and AB^i .
4. Compute the sensitivity coefficients in Eq. (2.55) and (2.56). j stands for the row of the matrices.

This alternative dramatically decreases the number of model evaluations in comparison to brute force method.

2.3 Conclusions and Critique on the Different Probabilistic UQ Methods

Once several options have been introduced, one has to choose the most appropriate method for the specific purpose. Amongst the two large groups (**probabilistic** and **non-probabilistic**), the drawbacks of the non-probabilistic approach are very clear: these methods require minor knowledge on the inputs, since error bounds are used omitting details of the input/output

2.3 Conclusions and Critique on the Different Probabilistic UQ Methods

variability, but the information that they provide to the analyst is more reduced (and sometimes very misleading). This methodology is acceptable for early design stages. For a full analysis, probabilistic methods are the recommendation in literature. However, there is no perfect method, and some details make preferable either a method or another in our application:

- **Direct sampling.** Monte-Carlo, Latin Hypercube or Sobol sequences, for instance, are very popular approaches, but these have to be carefully applied. If the model is expensive (that is, each sample comes from a long time run), this approach is unaffordable. In order to use these methods, some actions must be taken such as i) find a way to reduce the computational cost of the model (use coarser meshes, lower-fidelity models, etc.) and/or ii) develop ‘artificial’ quick models to be sampled: **surrogate models**. It is important to point out that, if the problem is high-dimensional, direct sampling is as efficient as any other probabilistic method because of the dimension-independence.
- **Surrogate models.** These models have the advantage of being ‘equations’ that produce the output instantaneously. Built upon an increasingly number of deterministic simulations, it is then only necessary to control the accuracy of the surrogate, and for this purpose the **Kriging** interpolation lets compute the Root Means Square Error (RSME). Once the surrogates are available, they can be easily cost-free sampled (Monte-Carlo, LHS, etc.) and uncertainty or sensitivity analysis can be developed. Despite of their good performance, in order to obtain the statistical moments, integrals must be computed and quadrature rules in **gPC/SCM/PCM** are more accurate. However, if probabilistic distributions of the output are sought, sampling is the way.
- **Stochastic Collocation Method.** To compute the integrals by means of any quadrature rule is an efficient idea, and if a **nested** rule is chosen with **sparse grids**, convergence can be quickly found in moderate dimensions (around six or lower for a smooth problem), being a demonstrated faster approach than direct sampling. However, this method only allows the use of **uniform probabilistic** distributions.

If probabilistic distributions or histograms of the outputs are desired, surrogates by Lagrange interpolation can be generated and sampled. It does happen also for sensitivity analysis, since the surrogates need to be sampled more times than in UQ to generate the Sobol indices. With **generalised Polynomial Chaos**, sensitivity analysis can be made for free (not requiring extra sampling) after UQ.

- **Generalised Polynomial Chaos.** SCM has the advantage of needing only to control the number of collocation points to increase the accuracy. In gPC, also the order of the expansion P has to be controlled, but it is worthy to pay such price when a sensitivity analysis can be continued with no extra deterministic simulations. Simply from the UQ study. This feature made polynomial chaos a very interesting and popular approach.

The most relevant drawbacks of the method with respect to SCM are i) the achievement of convergence, since to control both P and N_q can be sometimes complicated, and ii) the requirement of computing integrals with orthogonal polynomials.

gPC can be extended to other probabilistic distributions than uniform, following the Wiener-Askey polynomial basis functions, and for these, quadrature rules can be applied for exact computations of the statistical moment integrals.

It is thus clear that the main points to take into account in order to chose the suitable approach are the **knowledge about the random inputs** (can I construct the probabilistic distributions? are they uniform/normal/etc.?), **computational budget/computational cost** (how many simulations can I afford? how long does a deterministic run take?), **intrusiveness** (is it worthy to code inside the solver?), **desired accuracy** (is precision a crucial thing for my approach? can I use approximations?), and the **desired outputs** (is the mean and variance enough? sensitivity analysis? probabilistic distributions?).

In the following section, examples of application of the discussed techniques will be presented for the sake of testing and demonstration of capabilities.

2.4 Some Model Case Studies

In this section, two test cases (a damped sinusoidal function for UQ and a benchmark model for global sensitivity analysis) are studied to show the performance of the main methods used for stochastic analysis in this thesis. The main intention is to apply the methods on very simple test cases to show the goodness of each UQ and SA methods. More advanced work on engineering applications will be lately presented in the following chapters.

2.4.1 Applying Uncertainty Quantification to a Damped Sinusoidal Function with Mach Effect Resemblance

As a first toy problem, a damped sinusoidal equation has been tested with the uncertainty quantification algorithms. This test is the exact solution of the following Partial Differential Equation (PDE):

$$\begin{aligned} \frac{\partial u}{\partial t} &= \frac{\partial^2 u}{\partial x^2} + S(x, t; A, \omega_x), \\ S(x, t; A, \omega_x) &= Ae^{-\frac{1}{2}x}(2\pi \sin(\omega_x x) \cos(2\pi t) - \sin(2\pi t) \\ &\quad ((\frac{1}{4} - \omega_x^2) \sin(\omega_x x) - \frac{1}{2} \omega_x \cos(\omega_x x))), \\ &0 < x < L; \quad t > 0, \\ u(0, t) &= 0; \quad u(x, 0) = 0; \quad u(1, t) = 0. \end{aligned} \tag{2.63}$$

The exact solution of the equation is $u_{exact} = Ae^{-\frac{1}{2}x} \sin(\omega_x x) \sin(2\pi t)$. The deterministic base values of the parameters are $A = 0.3$, $\omega_x = 3\pi$. In Fig. 2.6, the exact solution can be seen for $L = 8$ and $0 < t < 4.25$. This equation u_{exact} has been chosen for the tests with the purpose of using the UQ methods on a model with a behaviour resemblant to the Mach number in compressible jets in the presence of shock-cells (see Chapter 5). The resemblance between the shock-cell patterns and the output of the PDE is shown in Fig. 2.7.

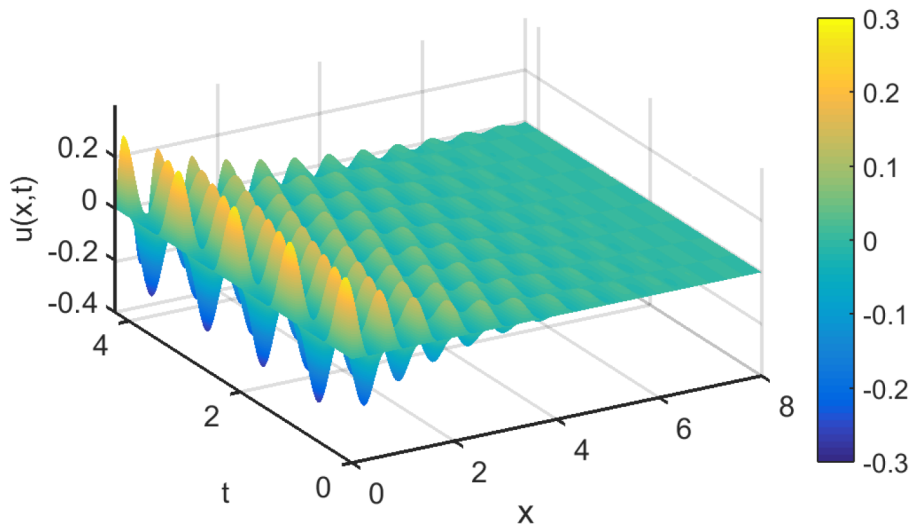
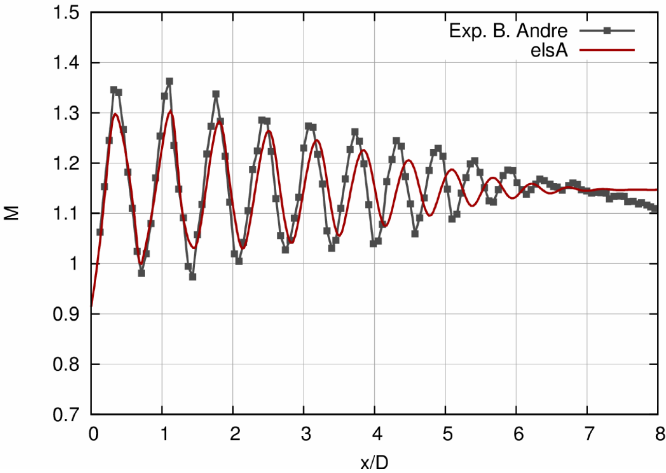


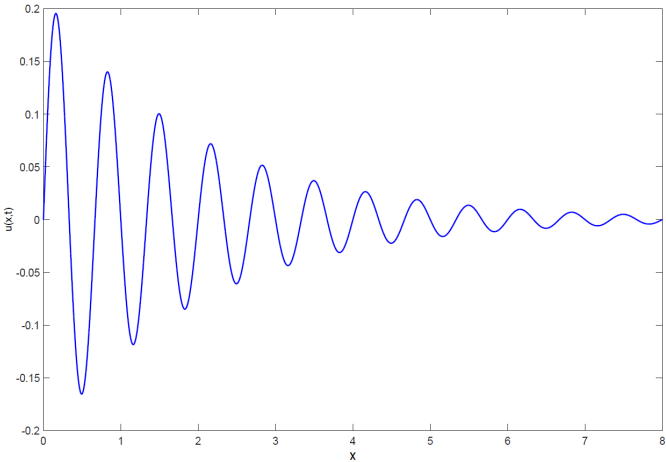
Figure 2.6 Solution of the PDE.

For the uncertainty quantification comparison, Monte-Carlo (MC), Latin Hypercube Sampling (LHS), Stochastic Collocation (SC) and generalised Polynomial Chaos (gPC) with Clenshaw-Curtis sparse grids have been tested on the exact solution of Eq. (2.63). Kriging surrogates have not been analysed here since the Matlab Kriging Toolbox [140] has been successfully earlier tested by other researchers and, as surrogates require to be sampled, the sampling is already done with MC and LHS. Moreover, in this thesis the accuracy of Kriging will be mostly controlled by the number of points in the sparse grid datasets, which will be firstly checked by SC and gPC.

In this UQ test case, the inputs are two uniform probabilistic distributions as source of uncertainty, as in the study in Chapter 5. Following this idea, both A and ω_x are varied $\pm 10\%$ and $\pm 10\%$ respectively, since they can be considered interesting as they control the amplitude and spatial shift. The parameters of interest to check the accuracy are the mean and variance in the testing, shown in Tables 2.2-2.5, for the specific performance point $(x, t) = (4.25, 2.125)$. Of course this can be extended to any point, but it is preferred to



(a)



(b)

Figure 2.7 (a) Experimental results from Andre Benoit’s PhD thesis[8] and CFD simulations performed at CERFACS with the Onera’s *elsA* solver. (b) Analytical solution of the prescribed PDE in Eq. (2.63) at $t = 2.125$.

rather focus on a point to give more exhaustive details with convergence tables. The exact computation of these statistical moments for a benchmark reference is

$$\mathbb{E}(u) = \int_{0.9-0.3}^{1.1-0.3} \int_{0.9-3\pi}^{1.1-3\pi} u_{exact}(x = 4.25, t = 2.125) f_A f_{\omega_x} d\omega_x dA = -3.400955E - 3, \quad (2.64)$$

$$\begin{aligned} \mathbb{V}(u) &= \int_{0.9-0.3}^{1.1-0.3} \int_{0.9-3\pi}^{1.1-3\pi} (u_{exact}(x = 4.25, t = 2.125) - \mathbb{E}(u))^2 f_A f_{\omega_x} d\omega_x dA = \\ &= 3.104486E - 04, \end{aligned} \quad (2.65)$$

and in the limits of the integral 0.9 and 1.1 stand for the $\pm 10\%$ of variation of the deterministic base case values of $A = 0.3$ and $\omega_x = 3\pi$.

Starting with a comparison between the two most popular sampling methods in both industry and academia, Monte-Carlo (MC) and Latin Hypercube Sampling (LHS), results can be checked in Tables 2.2 and 2.3. MC is possibly the most common practice in literature, mainly because the simplicity on developing a quick random algorithm for sampling, but its convergence is slower than LHS, as earlier discussed in 2.1.4. Actually, it can be observed that with 20000 samples, which is a large number of deterministic runs, the stochastic statistical moments in MC did not fully converge, and LHS did with few thousands. This is because of the effect of the stratification of the samples in LHS, since MC performs a random sampling. Despite of this, MC is still a very valuable approach, as there are applications such as biological models, chemical reactions or available low-cost surrogates which allow a large number of model evaluations without high computational resources. Moreover, if the dimension of the stochastic space (that is, the number of random variables) is large, the difference between LHS and MC is negligible. This is currently leading to a very interesting research trend in the *Curse of Dimensionality* [22, 56] and the so popular *Big Data*.

Table 2.2 Comparison of stochastic means with sampling methods in the test case at the point $x = 4.25$ and with $t = 2.125$.

	$N_s = 20$	$N_s = 50$	$N_s = 1000$	$N_s = 5000$	$N_s = 20000$
MC	-2.752E-03	6.645E-04	-3.019E-03	-3.040E-03	-3.352E-03
LHS	-3.662E-03	-3.514E-03	-3.398E-03	-3.407E-03	-3.401E-03

Table 2.3 Comparison of stochastic variances with sampling methods in the test case at the point $x = 4.25$ and with $t = 2.125$.

	$N_s = 20$	$N_s = 50$	$N_s = 1000$	$N_s = 5000$	$N_s = 20000$
MC	2.85E-04	3.47E-04	2.97E-04	3.14E-04	3.10E-04
LHS	3.098E-04	3.204E-04	3.130E-04	3.105E-04	3.105E-04

2.4 Some Model Case Studies

In Tables 2.4 and 2.5, Stochastic Collocation (SC) and generalised Polynomial Chaos (gPC) are compared, both using Clenshaw-Curtis sparse grids for quadrature nested rules. Taking also into account the outcome of sampling methods, it is surprising to see how quick the convergence is in the computation of the mean by the chosen quadrature rules. With only 29 samples, one can compute the exact value of the mean, and the gPC expansion is independent on the order.

However, in the computation of the stochastic variance, gPC needs some extra care, due to the fact that the order P of the expansion affects the convergence of the numerical integrals. The earliest exact computation takes place with 145 collocation points and an order of the expansion $P = 6$. But, acceptably accurate computations took place with *e. g.* 65 samples and $P = 5$. The quick convergence of SC makes it attractive, however, one has to take into account that for a latter sensitivity analysis it is better to choose gPC, since its calculation is immediate from UQ output as discussed earlier in this chapter when SC and gPC were introduced. This feature also provides to gPC of a great popularity in large-run simulation problems under uncertainty in both industry and academia. Nevertheless, this method is sometimes ‘blindly applied’ in literature, possibly driven by its popularity, not considering that SC can be an advantageous approach with uniform distributions.

Table 2.4 Comparison of stochastic collocation and generalised Polynomial chaos for the stochastic mean on the test case at the point $x = 4.25$ and with $t = 2.125$. The number of collocation points for level 2, 3, 4 and 5 are 13, 29, 65 and 145 respectively. Obviously, for higher values of P , the mean from gPC is the same as it is the first term of the expansion.

	<i>level = 2</i>	<i>level = 3</i>	<i>level = 4</i>	<i>level = 5</i>
SC	-2.711E-03	-3.401E-03	-3.401E-03	-3.401E-03
gPC	-2.711E-03	-3.401E-03	-3.401E-03	-3.401E-03

Table 2.5 Comparison of stochastic collocation and generalised Polynomial chaos for the stochastic variance in the test case at the point $x = 4.25$ and with $t = 2.125$. The number of collocation points for level 2, 3, 4, 5 and 6 are 13, 29, 65, 145 and 321 respectively.

	<i>level = 2</i>	<i>level = 3</i>	<i>level = 4</i>	<i>level = 5</i>	<i>level = 6</i>	
SC	3.147E-04	3.104E-04	3.104E-04	3.104E-04	3.104E-04	
gPC	P=2	1.292E-03	6.086E-04	4.933E-04	1.348E-04	1.348E-04
	P=3	4.443E-04	2.583E-04	2.535E-04	2.535E-04	2.535E-04
	P=4	1.074E-03	6.765E-04	3.008E-04	2.993E-04	2.993E-04
	P=5	1.129E-03	8.360E-04	3.181E-04	3.090E-04	3.090E-04
	P=6	1.211E-03	6.478E-04	2.187E-04	3.104E-04	3.103E-04

In this section has been shown the advantage of using quadrature rules with sparse grids in UQ. Now, it is time to compare them with sampling in sensitivity analysis.

2.4.2 Comparison of Global Sensitivity Analysis Methods

In this section, a comparison between global sensitivity analysis methods is carried out. For this purpose, the previously studied unsteady heat diffusion problem is not going to be taken into account, since a more intuitive analytic problem would be better to visualise the interaction between variables. The former example has no higher-order interaction, and hence only first-order indices would be computed.

Let us consider the following model as toy problem for sensitivity analysis:

$$y = 4\xi_1^2 + 3\xi_2^2 + 5\xi_1\xi_2^2 + 2.7, \quad (2.66)$$

with ξ_1 and ξ_2 uniform probabilistic distributions in $(-1, 1)$. In the next steps, the performance of sampling and gPC for global sensitivity methods is going to be compared via benchmark solution.

For the exact solution, the mean and variance are our first step, calculated by the integrals

$$\mathbb{E}(y) = \int_{-1}^1 \int_{-1}^1 y(\xi) f_{\xi}(\xi) d\xi = 5.0333, \quad (2.67)$$

$$\mathbb{V}(y) = \int_{-1}^1 \int_{-1}^1 (y(\xi) - \mathbb{E}(y))^2 f_{\xi}(\xi) d\xi = 3.888. \quad (2.68)$$

Then, the terms of the ANOVA HDMR decomposition from Eq.(2.45) are computed by

$$f_{\xi_1}^y = \mathbb{E}(y|\xi_1) - \mathbb{E}(y) = \frac{1}{2} \int_{-1}^1 y(\xi) d\xi_2 - \mathbb{E}(y) = 4\xi_1^2 + \frac{5}{3}\xi_1 + 3.7 - \mathbb{E}(y) \quad (2.69)$$

$$f_{\xi_2}^y = \mathbb{E}(y|\xi_2) - \mathbb{E}(y) = \frac{1}{2} \int_{-1}^1 y(\xi) d\xi_1 - \mathbb{E}(y) = \frac{4}{3} + 3\xi_2^2 + 2.7 - \mathbb{E}(y) \quad (2.70)$$

$$f_{\xi_1, \xi_2}^y = y(\xi) - f_{\xi_1}^y - f_{\xi_2}^y - f_{\xi_0}^y = 5\xi_1\xi_2^2 - 3.7 - \frac{5}{3}\xi_1 - \frac{4}{3} + \mathbb{E}(y), \quad (2.71)$$

and the sensitivity indices can be easily computed from their variances by means of

$$S_{\xi_1} = \frac{\mathbb{V}(f_{\xi_1}^y)}{\mathbb{V}(y)} = \frac{\int_{-1}^1 \int_{-1}^1 f_{\xi}(\xi) (f_{\xi_1}^y)^2 d\xi}{\mathbb{V}(y)} = 0.60381, \quad (2.72)$$

$$S_{\xi_2} = \frac{\mathbb{V}(f_{\xi_2}^y)}{\mathbb{V}(y)} = \frac{\int_{-1}^1 \int_{-1}^1 f_{\xi}(\xi) (f_{\xi_2}^y)^2 d\xi}{\mathbb{V}(y)} = 0.20571, \quad (2.73)$$

$$S_{\xi_1, \xi_2} = \frac{\mathbb{V}(f_{\xi_1, \xi_2}^y)}{\mathbb{V}(y)} = \frac{\int_{-1}^1 \int_{-1}^1 f_{\xi}(\xi) (f_{\xi_1, \xi_2}^y)^2 d\xi}{\mathbb{V}(y)} = 0.19047, \quad (2.74)$$

2.5 Current Research Trends and Needs in the Field

where one has to be careful with the integrands, since $f_{\xi}(\xi)$ stands for the density functions and $f_{\xi_i}^y$ are the terms of the HDMR decomposition.

In the table below it is now shown the comparison of the computation of the first-order and total sensitivity indices for each method, following the procedures already introduced earlier in this chapter. The convergence study is not shown here for sake of simplicity and it can be noticed that all the indices are pretty close to their exact value. In fact, the gPC ones coincide, demonstrating how efficient the method is with only 145 deterministic evaluations (level 5 of accuracy in the Clenshaw-Curtis sparse grid).

Global sensitivity analysis is a very valuable tool in both industry and academia. There are plenty of applications of sensitivity to reduce the number of terms in equations for modelling in chemical reactions, selection of relevant features in ground water modelling and model complexity reduction in stochastic ecological models. Moreover, as humankind is nowadays dealing with increasingly more and more data, especially in *Big Data* contexts, to be able to reduce the number of variables required to feed machine learning algorithms is a remarkable advantage to prevent overfitting and develop reliable predictions. Sensitivity analysis represents, therefore, the icing on the cake in models with stochastic behaviour.

Table 2.6 Comparison of sensitivity analysis results by means of sampling (Jansen Sobol indices with Latin Hypercube Sampling and 5000 samples), generalised Polynomial Chaos (gPC with $P = 4$ and 145 samples) and exact values.

	LHS	gPC	Exact
S_{ξ_1}	0.60778	0.60381	0.60381
S_{ξ_2}	0.22130	0.20571	0.20571
S_{ξ_1, ξ_2}	0.17883	0.1905	0.1905
$S_{\xi_1} + S_{\xi_2} + S_{\xi_1, \xi_2}$	1.0079	1	1
ST_{ξ_1}	0.78661	0.79428	0.79428
ST_{ξ_2}	0.39477	0.3962	0.3962

2.5 Current Research Trends and Needs in the Field

It is certainly an exciting moment for statisticians, data scientists and researchers who deal with statistics in their jobs, since we are currently experiencing a great impact of fields such as statistics and data handling from *Machine Learning* and *Big Data* in our lives. As earlier discussed, in *Big Data* and other high-dimensional contexts, to reduce the number of variables to input to the algorithms that extract meaningful information is a valuable advantage, as otherwise the analysis can be sometimes even infeasible.

Likewise, the reduction of dimensions is a very promising current research trend in uncertainty quantification, where *Machine Learning* algorithms are also used. To be able

2.5 Current Research Trends and Needs in the Field

to decrease the size of the stochastic space has a dramatical effect on the applications. On this topic, sampling methods are still a very useful approach, which gained popularity in the last decade in applications reducing the number of parameters, such as in biological models or chemical reactions [215]. Also, investigations in the sampling of high-dimensional analysis can be found in [66], where a geometrical sampling is developed or with surrogates in regression-based approximation techniques as in [136].

In long-time run simulations (costly simulations according to the definition earlier given in this thesis), a new constrain is that the computational budget is more reduced. This basically led to the use of the sparse grids in nested quadrature rules as discussed earlier in this section. However, to reduce the number of variables to participate is complicated and represents a big challenge. In engineering problems involving many uncertain input factors, to find a reduction of the original set is highly valuable, since at the moment uncertainty quantification, optimisation and global sensitivity analysis in such problems is typically accounting few variables, restricted by the elapsed time of the simulations. For this reason, this is a key topic of research nowadays in these fields, which suffers from the so-called *Curse of Dimensionality* [22, 56].

It is not usual to find papers on uncertainty quantification dealing with more than 5-6 variables in collocation approaches, such as in [141], where 12 variables are used, with a large number of model evaluations required. For this reason, some actions must be taken. The dimension reduction by means of Active Subspaces [46] is very interesting. This field, whose term was originally introduced by Dr. Paul Constantine, aims to obtain a reduced dimension set of features from the original one by identifying the most relevant directions in the parameter space, especially for long-run simulations. This approach has been successfully applied already to few engineering applications such as [47, 143].

In the same line, there are other studies that deal with the adaptivity of the sparse grids to high-dimensional problems [91, 192]. With this approach, it is intended to reduce the number of points in the sparse grid by starting from simple functions in each direction of the parameter space, increasing the approximation until the best is reached, adding points in the most steeped parts. This certainly decreases the number of impractical model evaluations in smooth regions, and thus the computational times. This, therefore, takes on the *Curse of Dimensionality* in a very efficient way.

To sum up, the efficient computation for costly simulations involving a large number of parameters (high-dimensional problems) is the current necessity. In fact, in recent relevant UQ conferences this was of large interest from the audience. For example, in *SIAM Conference on Uncertainty Quantification* held in Lausanne (Switzerland) last April 2016, high-dimensional analysis was one of the main interests, and the next SIAM one to be held in April 2018 in California (USA) will have the application of UQ in *Machine Learning* as one of the central topics, where surely *Big Data* will play a relevant role.

2.6 Summary

An overview of both UQ and SA has been developed in Section 2.1 and 2.2, where the types of uncertainty and probabilistic/non-probabilistic methods are discussed and the probabilistic approach is the suggested one according to literature. This decision is also obvious, since the probability theory provides a more robust framework for uncertainty management than simple vague descriptions typically found in non-probabilistic approaches such as Fuzzy or Interval analysis. For this reason, probabilistic methods received a more sounded discussion and were applied to test cases in Section 2.4.

In Section 2.3, these methods have been discussed and critically analysed, commenting their advantages and drawbacks. Lately, the methods were followed by examples of application in Section 2.4, where it is concluded that the choice of the UQ/SA approach will always be driven by the knowledge about the random inputs, computational budget/computational cost, intrusiveness, desired accuracy, and the desired outputs.

Finally, in Section 2.5 the current research trends and necessities are discussed, showing that the reduction of the number of parameter and adaptive sampling in high-dimensional problems is a very relevant topic, especially for long-time run simulations to deal with the *Curse of Dimensionality*.

In the following chapters, the methods are to be applied to realistic cases in fluid dynamics, providing a better illustration of their performance and aiming to improve the deterministic approaches by means of stochastic frameworks.

Chapter 3

A Swirling Flow Generated by a Rotating Pipe for Heat Transfer by Impingement Under Uncertainty. Part I: CFD Modelling

It is well known that impinging jets are widely used in industry for heat transfer purposes in different fields, especially in manufacturing and cooling of electronics. Due to this fact, it is interesting to understand more about the influence of possible modifications in the design. This leads to the present chapter, where computational simulations of Reynolds-Averaged Navier-Stokes (RANS) equations are used to model a swirling jet generated by the rotation of a pipe by means of the commercial software FLUENT. The computational domain has been split in two simulations: *Simulation 1*, for the flow in the rotating pipe, and *Simulation 2*, for the impinging jet implemented as inlet condition. The best turbulent model performance has been found for the Reynolds Stress turbulent Model (RSM) with swirl conditions, as the most popular and less complex eddy-viscosity turbulent models in RANS fail when simulating the swirl. However, for the impinging jet simulations, the SST $k - \omega$ turbulent model has been found the best. For coupling both problems, mathematical models for the velocity and turbulent profiles from *Simulation 1* have been also found.

In addition to this, a comparison with other popular swirl generation mechanisms from literature has been done, showing the advantages and disadvantages in the use of rotating pipes, such as the possibility of varying the swirl intensity while keeping the mean flow velocity fixed.

For sake of clarification, this chapter is presented as follows: In Section 3.2, the difficulties performing the CFD simulations and descriptions of the turbulent models are broken down for a better understanding. The mathematical models are suggested and implemented in Section 3.4. The chapter ends with a comparison with other swirl generation mechanisms

from literature in Section 3.5, and in Section 3.6 the relevant conclusions are given.

3.1 Introduction and Motivation

Swirling flows in pipes can be found in many industrial applications, such as in erosion damage reduction [257], chemical engineering [53] or dehydration systems in multi-phase flows [94]. Recent applications of this type of flows are heat transfer by impingement. In that sense, impinging jets have been extensively studied for cooling in electronic components [99, 129], surface varied plates [177] or impinging gases and flame jets [148, 236], among others.

The improvement of the existing impinging jet mechanisms has been a matter of research in literature. As result of an extensive literature search, **there is no work regarding the effect of using rotating pipes** for swirling flow generation as impinging jet flows, and this is the main motivation for the present study. The objective of this work is also to **discuss the drawbacks and advantages in comparison with other swirl flow generators**: the use of pipes with spirals or vane-type swirl generators [130], swirl strips in pipes [248], angled blades to force rotation [174, 173] and the use of tangential jets to impart the swirl [260].

When the motivation is to produce swirl in flows to improve the heat transfer as demonstrated in several papers [248, 18, 130, 174, 177, 3], it is surprising that such a simple mechanism as a rotating pipe was not previously analysed. Amongst the aforementioned available options, **to use a pipe with a forced angular velocity seems to have less complications in manufacturing and it can be affordable to any experimental lab, not requiring machining or assembly of extra complex components**. Also, there is, in principle ¹, a **great range of swirl intensity available since one only needs to increase the angular velocity of the pipe** by means of a motor. With other mechanisms, as the oriented blades or angled spirals, there is a maximum angle that cannot be surpassed. In other words, the suggested mechanism can represent a more flexible method so this supports the interest in the present novel computational study.

In this chapter, the impinging swirling jet is created by means of a rotating pipe with fully-developed condition at the outflow. The inflow velocity field is uniform with an imposed flow-rate corresponding to a Reynolds number $Re = 23000$. Due to the fact that the walls are rotating with a Swirl number, S , set to 1, the outflow is turbulent and swirling at the exit. This flow is spreading from the pipe (nozzle) and impinges on the heated flat plate located

¹Large values for the angular velocity have a remarkable impact on vortex breakdown and jet spreading angle among others, completely changing the flow physics. This is out of the scope of this thesis, and only moderated values from literature are under study.

at a dimensionless distance H/D , where H stands for the nozzle to plate distance, and D is the diameter of the pipe. The simulation of swirling flows in ducts is not straightforward in CFD. In this piece of work, Reynolds-Averaged Navier Stokes (RANS) were solved, as Direct Numerical Simulations (DNS) and Large Eddy Simulation (LES) represent a very expensive way to simulate turbulent flows, and for further uncertainty quantification studies it becomes unaffordable, since several deterministic CFD simulations are required.

3.1.1 Literature Review

There is a large amount of work regarding the experimental analysis of confined swirling flows. One of the first attempts on swirling flows was [250], showing experimentally that the flow is stabilized when the pipe is rotated about its axis. In [163], a long smooth pipe rotating about its axis was analysed and changes of the flow pattern, together with hydraulic loss within the pipe, were examined by measuring the velocity and pressure distributions across sections at various distance from the pipe entrance. In [114], the mean velocities and Reynolds stress components were preliminary studied by means of the hot wire experimental technique. A further continuation of these works on swirling flows is [101], which is the reference work for the validation of the computational results in this thesis. In this paper, an experimental study with LDV measurements was carried out in order to measure mean velocity profiles, distributions of five components of the Reynolds stress, and velocity fluctuations. This paper hence provides a more complete analysis on the turbulent properties of the swirling flow.

Regarding the computational simulations of swirling flows, there is a vast literature [98, 104, 117, 60, 80, 166] about the turbulent models to be used for confined swirling flows when the RANS equations are used, and the general viewpoint is that the RSM performs the better. However, in [117] a modified $k - \epsilon$ turbulence model is used for a swirling flow in a straight pipe, based on the improvement of the existing $k - \epsilon$ by reconsidering of the assumption of isotropic turbulence, which is analysed from the anisotropic viewpoint. Despite the modifications of turbulent models in FLUENT [69] not being considered in this work, this motivated the trial of several turbulent models in this manuscript, in order to have a deep insight and extract conclusions not only with the recommended turbulent model. In [104], a test for several types of rotating and swirling flows for a range of Reynolds numbers and swirl intensities have been studied computationally, aimed at identifying specific features that require special consideration in turbulence modeling. For this aim, several turbulent models were tried and the conclusions reveal that $k - \epsilon$ models are not appropriate when simulating swirling flows, and RSM represents a more efficient way. Similarly, in [60] can be found the comparison of two turbulence models (Re-Normalization Group RNG $k - \epsilon$ model and RSM) and their effects on modelling the developing turbulent swirling flow inside a straight

pipe arriving to the same conclusions. In [166], the turbulent swirling decay pipe flow is investigated analytically and computationally. And for the validation of results, RSM was used in FLUENT, showing a very good agreement. Other successful applications of RSM on swirling flows are shown in [80] for a swirling flow within two concentric cylinders, in [196] for the numerical flow prediction in torus reactors with swirl using FLUENT, or in [109] about highly swirling turbulent flows in cyclones, where several turbulent models were tested. For higher fidelity simulations, not intended here due to a further uncertainty quantification would be too expensive, DNS of swirling flows in pipes can be found in [169, 62, 172] and LES results in [65, 57]. A description of the turbulent models and their properties will be given in Section 3.2.

After the generation of the swirling flow, once it exits the pipe, it will impact on a flat plate for heat transfer purposes. The improvement of the heat transfer due to impinging jets has been also addressed in literature. There is a large amount of work on non-swirling impinging jets [20, 4, 87, 265, 203], and **it has been demonstrated in both experimental [248, 18, 130] and computational [174, 177, 3] studies that the addition of swirl to these jets can increase the heat transfer.**

The number of experimental studies on swirling jet flows greatly surpass the computational ones. The swirl for impinging jets can be generated by different ways, such as by means of spiral ducts (also referred to as helical generators or swirling strips), angled blades at the tip, agitation by stirrer blades (perhaps too intrusive for this purpose), use of tangential jets to impart the swirl or by rotating pipes. Some closely related works, shown for comparison and discussion in Section 3.5, are the following.

In [130] and [18] the swirl is generated by pipes with spirals and the swirl number is based on geometrical parameters as in [112], being the swirl independent of the Reynolds number. Despite the swirl devices are similar in both papers, in [18] the hub was extended with a conical tip in order to avoid a sudden expansion, that is affecting the jet and then producing such a different behaviour in the heat transfer.

Another experimental work is [20]. Here only non-swirling round jet flows are studied, but they are good for comparison with our non-swirling simulation, despite the Reynolds is slightly greater ($Re = 23700$), but with a reported uncertainty of a 2.3%.

A similar but computational work is [21], where only non-swirling flows data is available. In this paper, the turbulence model used is $V2f$ ($k - \epsilon$ is employed too, but with a very poor performance). The turbulence model has a good performance for large H/D distances, but not so good for small. No uncertainty is reported on the simulation, and the importance of this will be discussed in Chapter 4, since it is a regular missing step in CFD.

Finally, in [260] several swirl intensities are imparted by three tangential jets separated by 120 degrees. These results have been tried to be computationally simulated by other researchers in literature [231, 259].

Depending on the employed mechanism, the generated jet will have different patterns and hence, the way it spreads downstream will be different. This spreading is influential for the impinging conditions affecting the heat transfer as in the swirling jet, the degrees of jet growth, entrainment of ambient air, and jet decay are affected by the degree of swirl [18, 195] and other perturbations from generation mechanisms. In [202] has been reported that even the addition of light swirl can change significantly the behaviour of the jet. Also, in [195] in a similar configuration as in [202] it has been carried out a complete experimental characterisation of the swirling jet flow showing that the swirling flow jet generated by the rotation of a pipe has a more remarkably spreading angle than the non-swirling one (almost twice in their experiments).

Regarding the computational work in literature, especially relevant for our choice of the turbulent model for the RANS simulations of impinging jet flows with swirl, only few works can be found in literature at the moment, despite the fact that some papers on heat transfer in the rotating pipe can be found [210]. One can point out the work in [4], where the RNG $k - \epsilon$ are used for the simulations. Also, another recent paper is [7], where a RANS simulation with RNG $k - \epsilon$ is again developed for a jet flow whose swirl is generated by means of a twisted tapes via numerical approach, showing that the addition of swirl is beneficial for heat transfer. A more recent paper [106] employs the SST $k - \omega$ in FLUENT for a jet, whose swirl is again added by means of twisted tapes. In addition to these, the $V2f$ turbulence model has been applied to previous works with a relatively good match in some comparisons with swirling jet experiments [259, 21], but its performance was not always successful, especially in short H/D distances as reported in [226, 21]. This makes sense since at far distances, the swirl effect is less notable due to mixing. In any case, since $V2f$ model is not available in our commercial version of FLUENT and other methods had a good performance, it is discarded in this work.

In this thesis, the SST $k - \omega$ turbulence modelling as in [177, 174, 176, 106] has been repeated and details about the CFD set-up will be given in Section 3.2. This choice was based on the successful computational simulations achieved and also their possibility of imposing the suggested velocity and turbulent profiles at the exit of the pipe as in [177, 173, 174, 176] (see Section 3.4) by means of User-Defined Functions in FLUENT.

3.1.2 Methodology and Challenges

All along the investigation, there are several drawbacks that must be solved to finally obtain a reliable computational simulation of the mechanism, as expressed in the literature review. **The main difficulties are to find an appropriate turbulence model for both *Simulation 1* and *Simulation 2*, to couple both CFD simulations and to try to minimise the computational costs**, since this is essential for uncertainty quantification (and optimisation) in Chapter 4.

As the main scientific interest in this type of jet is an **experimental trend** (especially for fluid characterisation purposes), there are few computational papers on impinging swirling jets, as fluid characterisation by computational analysis requires very advanced computing resources such as LES or DNS. As the main objective in this work is focused on RANS, alternatives are thus investigated.

Since in literature one can only find the rotating pipe as an independent study, and impinging studies with different jet flows, an efficient way to compute the whole system has to be found and results have to be validated at each step too. The suggested framework for the simulation of the set-up is to **split in two simulations**: *Simulation 1* (generation of a swirling flow by means of a rotating pipe) and *Simulation 2* (simulation of the impingement and heat transfer). This let us try different turbulent models for each simulation in FLUENT.

In *Simulation 1*, due to the complexity in computing the swirling behaviour by common turbulence models in RANS as discussed in Section 3.1.1, the most expensive turbulence model in RANS, the **Reynolds Stress Model (RSM)**, was used. It is undoubtedly agreed in literature that it is an accurate model for this type of flows. However, for sake of curiosity and double-checking purposes, other turbulence models were tested and the results validated with the experimental results from Imao et al. [101].

Moreover, as a fully-developed flow is desired, a very long pipe should be computed. To carry on the simulation there are two options: to mesh a long pipe and simulate up to fully-developed state (this would require around 50 – 60 times the nozzle diameter, with a fine mesh for the boundary layer, requiring a large computational elapsed time) or to simply take a short piece of pipe with periodical boundary conditions. This type of condition is available in FLUENT, and it refers to the continuous use of the outflow as inflow until the velocity profile does not change anymore (fully-developed flow). For practical reasons, the short pipe steady simulation is chosen, discarding the expensive approach.

Regarding *Simulation 2*, the use of RSM turbulent model for impingement is inefficient and less computational demanding models are preferable, since the domain for this simulation is large and with a fine mesh nearby the jet spreading region to properly simulate the flow. Following the existing literature the eddy-viscosity models provided, in some case scenarios, a good performance. Concretely, in [177, 176, 173, 10] the Shear Stress Transport (SST) $k - \omega$ turbulent model has demonstrated to be accurate, and the same steps have been reproduced here. Also, another turbulent model, $V2f$, has been reported in literature with a relatively good match with swirling jet experimental results [259], but as $V2f$ model is not available in our commercial version of FLUENT, and $SST k - \omega$ performed very well in previous developed works, the choice is obvious.

As to make repeatable simulations is a must for optimisation or uncertainty analysis, and CFD is a computationally expensive way of modelling, some extra work can be done to save some computational resources. For this purpose, to find **mathematical models** for the fully-developed swirling flow (*Simulation 1*) and to include uncertain conditions in the study (as done in the following chapter), will provide a useful outcome of the analysed scenario. The models have been designed following the same practice as in [175], and which were also successfully input in CFD simulations of impinging swirling jets [177, 173, 174]. These models are a very useful tool to save computations, but one has to bear in mind that they are mere generalised fit approximations, and they are not derived from the Navier-Stokes equations or any other fluid equation. They simply play the same roll that surrogate models play in any other UQ or optimisation problem.

3.2 Setting-Up the CFD Simulations

3.2.1 Simulation 1: CFD Simulations of a Fully-Developed Turbulent Flow in a Rotating Pipe.

As described in the introduction, the swirling jet is to be produced in a separated simulation of a rotating pipe (*Simulation 1*), with an uniform non-swirling flow as inlet, in order to generate its swirl by the pipe rotation. In Fig. 3.1, the pipe problem is depicted, for which a 2D RANS simulation was developed in FLUENT. The reason of using FLUENT is simply that it is a powerful available commercial CFD software, very popular in both industry and academia and well established, with its features extensively documented in the FLUENT User's Guide [69].

The flow under study goes out of the pipe fully-developed, what requires to have a long enough pipe length. In order to avoid such an expensive simulation, a piece of pipe has been simulated instead with periodic boundary conditions, where a mass-flow rate is imposed according to the desired Reynolds number $Re = \frac{4\rho Q}{\pi D\mu} = 23000$ and under rotating conditions set by the unity Swirl number $S = \frac{\Omega D}{2U} = \frac{\pi D^3 \Omega}{8Q} = 1$, where ρ is the density of the fluid, Q the volume-flow rate, U the inflow velocity, μ is the dynamic viscosity, D the diameter of the pipe and Ω the angular velocity of rotation of the pipe. The impinging jet is air with Prandtl number $Pr = 0.71$.

One of the biggest issues when simulating a flow is the choice of the turbulence model. The $k - \omega$ and $k - \epsilon$ turbulent models have been widely used in CFD RANS simulations with very good agreement with experimental results in many problems and there is a vast literature with practical applications. But under some circumstances, these models can not accurately simulate the physical behaviour of fluids. The simulation of a swirling flow is a particular application where simple turbulence models fail, meaning with simple to those

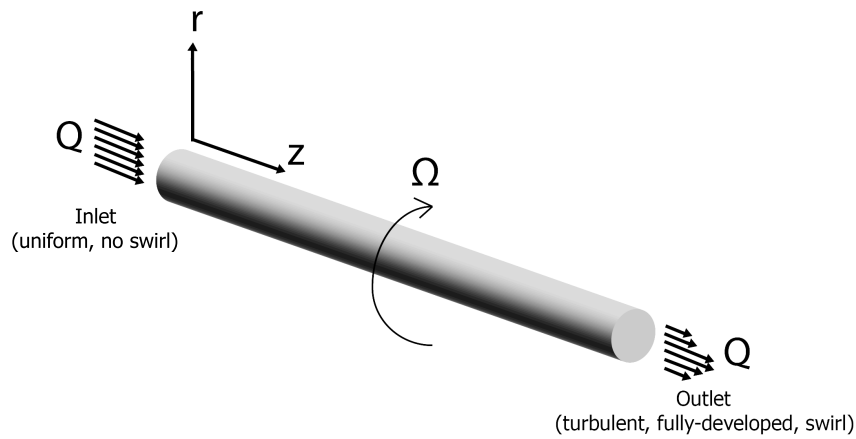


Figure 3.1 Sketch of the swirling flow generator by a rotating pipe. The flow enters the pipe with a uniform profile and swirless, and leaves the pipe as turbulent fully-developed with swirl.

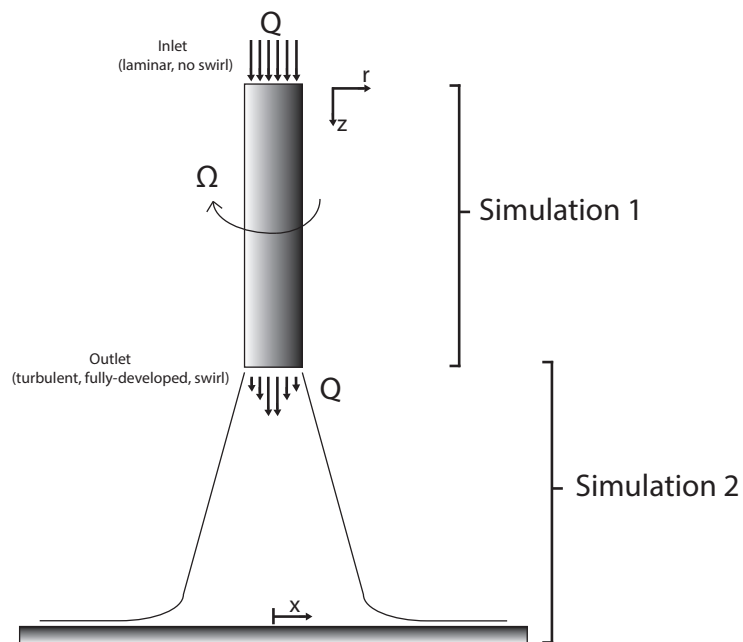


Figure 3.2 Sketch of *Simulation 1* & *2*. Note that the x and r axis are the same in practice and with origin in the axisymmetry axis, but for the sake of avoiding confusion in the following plots and data tables, r is used in *Simulation 1* and x for *Simulation 2*.

that do not take into account the anisotropy of the turbulence as the eddy viscosity ones.

3.2 Setting-Up the CFD Simulations

To overcome this problem, several turbulent model configurations and wall treatments were tested in this work to simulate the swirling flow confined in the rotating pipe with the computational mesh shown in Fig. 3.3. In CFD is common practice to test as many options as possible since there is not a general turbulence model that works for all case scenarios. The intention is, therefore, to see if remarkable differences and similarities are drawn and check at the same time the grid convergence, as relevant errors can be derived from the mesh as well. Specifically, the nodal distribution for the boundary layer and the wall treatment functions used make a strong difference since it is a complex thing to model in the physics of fluids. In computational fluid dynamics, the boundary layer cannot be exactly computed and wall approximations are always present.

The size of the computational grid has been chosen as $[n_r \times n_z] = 68 \times 450$ cells, with n_i the number of computational cells in the i direction, and being the first computational cell at a dimensionless wall distance of $y^+ < 1$ along the walls of the pipe. The uncertainty and convergence of the mesh are also analysed in Section 3.2.2.

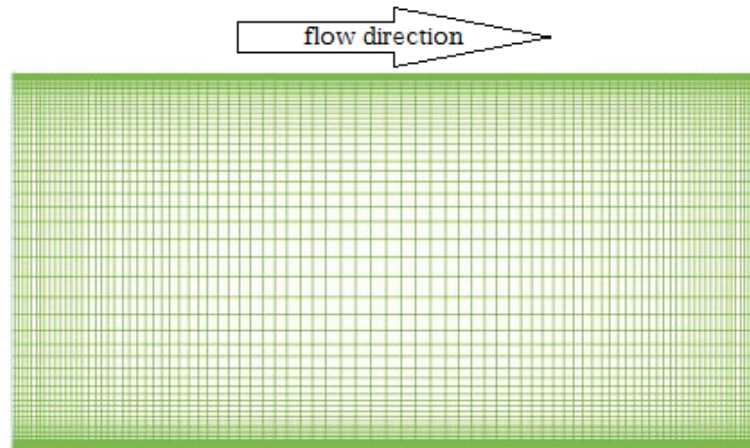


Figure 3.3 Computational grid for the pipe.

A detail of the evolution of the velocity profile along the pipe and the imposed boundary conditions can be seen in Fig 3.4. Note that, despite of the fact that in the figure the inlet axial velocity appears as constant profile, this profile becomes the same as the outlet one because of the use of the periodic boundary condition between the pipe inlet and outlet to obtain a fully-developed swirling turbulent flow.

The physics are governed by the Navier-Stokes Equations, solved numerically by the CFD code FLUENT in a 2D axisymmetric domain. For the tested turbulence models, the best results took place with variants of $k - \varepsilon$, $k - \omega$ and RSM, for which both axial and azimuthal

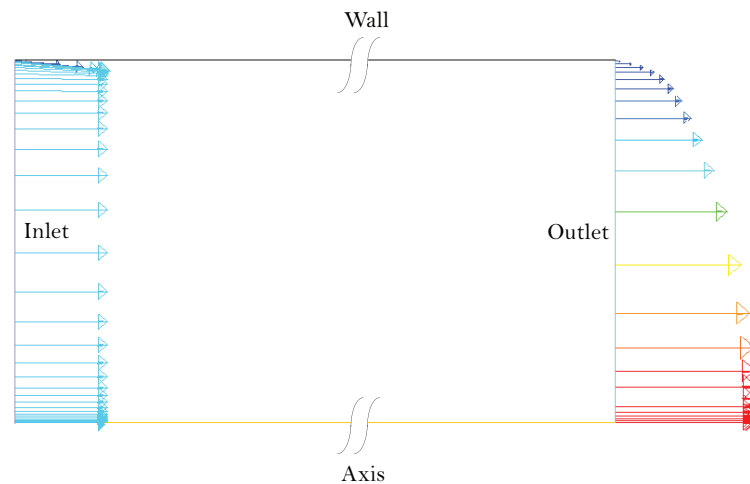


Figure 3.4 Detail of the evolution of the axial velocity profile along the pipe and boundary conditions imposed. The red colour scale stands for the radial distance with the maximum exit velocity and the blue colour scale stands for the lowest.

dimensionless velocity profiles have been validated with the experimental results by Imao et al [101], where $Re = 20000$ and $S = 1$ was used and thus, imposed now in our turbulent model validations. The corresponding turbulent model results, in terms of the axial (v_z) and azimuthal (v_r) velocities and the friction factor (λ) on the wall, will be compared with those from [101] and depicted in Figs. 3.5-3.7. The turbulent models used and their limitations are analysed in the following.

$k - \varepsilon$ turbulence model

After averaging the Navier Stokes equations, due to unknown velocity fluctuations, a turbulence model is required for the problem closure. The $k - \varepsilon$ is one of the most popular turbulence models. This model requires the use of only two closure equations: one for the turbulent kinetic energy, k , and another one for the rate of dissipation, ε .

There are three formulations of $k - \varepsilon$ turbulent models available in FLUENT: Standard, RNG and Realizable. Among them, the one that provided the better results was the Realizable one with Enhanced Wall Treatment.

The term "realizable" means that the model satisfies certain mathematical constraints on the Reynolds stresses, consistent with the physics of turbulent flows: the positivity of normal stresses and the Schwarz inequality for Reynolds shear stresses .

Enhanced wall treatment is an option to better solving the flow for a coarser mesh than the usually required to solve the laminar sublayer, thanks to a near-wall formulation. This would be equivalent to the implementation of a very fine mesh but with less computational cost and a small error difference. For further information, the author suggest to see [69] and

[73].

The model has been extensively validated for a wide range of flows [115, 212], including rotating homogeneous shear flows, free flows including jets and mixing layers, channel and boundary layer flows, and separated flows. The better performance of this model in our problem under study is not surprising, since it more accurately predicts flows involving rotation, boundary layers under strong adverse pressure gradients, separation, and recirculation. According to [69], for all these cases, the performance of the model has been found to be substantially better than the one with the standard $k - \varepsilon$ model. But unfortunately, this model provides a poor approximation to the velocity profiles when comparing with experimental data [101] in Figs. 3.5-3.7. with this model, the numerical axial velocity profile is notably deformed, and the numerical azimuthal velocity profile provides a solid rigid body rotation ($\frac{v_t}{U} = \Omega \frac{r}{R}$, with R the radius of the pipe), so for this high swirl the results show that, according to this model, the flow is behaving like a solid in the azimuthal direction, being obliged to discard this model.

$k - \omega$ turbulence model

The $k - \omega$ turbulence model has a similar computational cost than with respect to the $k - \varepsilon$, as again two closure equations are required to compute the turbulence: one to compute the turbulent kinetic energy, k , and another one to compute the specific turbulent dissipation rate, ω . In this work, both the Standard and Shear Stress Transport (SST) $k - \omega$ models have been tested.

The standard $k - \omega$ model in FLUENT is based on the Wilcox $k - \omega$ model [252], which provides an accurate formulation in the near-wall region being recommended for wall-bounded flows. The SST $k - \omega$ model was developed by Menter [151] to merge the standard $k - \omega$ goodness in the near-wall region with the $k - \varepsilon$ model goodness in the far field. The SST model is similar to the standard one, but it includes, besides the blending function for the $k - \omega/\varepsilon$ merging, a damped cross-diffusion derivative term in the ω equation and a modification to account for the transport of the turbulent shear stress.

Despite these features make the SST $k - \omega$ model more accurate and reliable for a wider class of flows than the standard one, for the simulations of the rotating pipe we obtain pretty similar results than with $k - \varepsilon$ for both the axial and azimuthal velocity profiles, as one can see in Fig. 3.5.

RSM turbulence model

In the case under study, as the Reynolds number is large and wall effects are present, the contribution of several physical mechanisms to turbulence processes changes with respect to

3.2 Setting-Up the CFD Simulations

the lower-Reynolds reliability case [194]. If engineers want to simulate the turbulence in the most reliable way, DNS would be the best. LES would be a cheaper option, but simulations still take a long time and this cannot be afforded for uncertainty quantification and modelling purposes in this work. For this reason, the RSM [79, 127] is the most reliable turbulence model that can be used in FLUENT with RANS. Its name is owed to the fact that Reynolds' stresses are used to obtain closure for the Reynolds' averaged momentum equation. RSM closes the RANS equations by solving the transport equations for the Reynolds stresses, together with an equation for the dissipation rate. Despite of this model is very accurate (specially for swirling flows as commented also below) the computational cost is larger, as five additional transport equations are required in 2D flow domains and seven additional transport equations must be solved in 3D.

Since RSM takes into account the anisotropy of turbulence generation (that is to say, directional effects of the Reynolds stress fields), it has greater potential to give accurate predictions for complex flows but the fidelity of predictions is still limited by the closure assumptions employed to model some terms in the exact transport equations for the Reynolds stresses.

While effective viscosity models have led to satisfactory predictions of many two-dimensional thin shear flows, their use in 3D flows and other flows with more than a single significant component of mean velocity gradient has achieved, at best, only moderate success. One may cite turbulence-driven secondary flows in non-circular ducts or the influence of high swirl as examples of phenomena which cannot satisfactorily be predicted with models of the effective-viscosity type [126]. This leads to making numerical calculations of such complex flows by carrying on the exact computation of Reynolds stresses.

The exact transport equations for the transport of the Reynolds stresses $\rho \overline{v'_i v'_j}$ (note that the sub-index ij is used in this section for the sake of simplicity, with i and j the coordinates, and v' stands for the fluctuations of velocity) may be written, in essence, as follows:

$$\text{Local Time Derivate} + C_{ij} = D_{T,ij} + D_{L,ij} + P_{ij} + G_{ij} + \phi_{ij} - \varepsilon_{ij} + F_{ij} + S_{user}, \quad (3.1)$$

where C_{ij} is the convection term, $D_{L,ij}$ equals the turbulent diffusion, $D_{T,ij}$ stands for the molecular diffusion, P_{ij} is the term for stress production, G_{ij} equals buoyancy production, ϕ_{ij} is for the pressure-strain, ε_{ij} stands for the dissipation and F_{ij} is the production by system rotation. As there is a vast literature to find the equations (see for instance [69] and [126]), no further descriptions of the equations will be developed here.

As mentioned above, the RSM includes the effect of anisotropy of turbulence, which yields it superior to models based on the Boussinesq approach (effective viscosity models) when simulating highly swirled flows and stress-driven secondary flows. However, as of the various terms in Eq. (3.1), C_{ij} , $D_{L,ij}$, P_{ij} , and F_{ij} do not require any modeling but, $D_{T,ij}$,

G_{ij} , ϕ_{ij} , and ϵ_{ij} do, the accuracy of the RSM is limited by these closure assumptions [60]. Particularly, the modeling of the pressure-strain and dissipation-rate terms is challenging, and often considered to be responsible for compromising the accuracy of RSM predictions [244].

There are many examples in literature where using RSM is recommended for swirling as cyclone flows, highly swirling flows in combustors, rotating flow passages, and the stress-induced secondary flows in ducts [69]. RSM is hence used for high swirl confined flows, as the case under study, and the plots in Fig. 3.6 reveal that it has been the only tested model able to properly catch up the curved shape of the azimuthal velocity profile.

In CFD, the validation of simulations has to be against analytical results, a benchmark study or experimental data. Sometimes, another simulation with a very fine mesh or DNS (no turbulent model required) can be sufficient if other sources are not available. As only experimental data is available in literature for validation purposes, the procedure is to compare both the computational and experimental results. Then, it is possible to check what configuration (turbulent model, solver, mesh, and wall functions) of the CFD problem offers the closest performance to the experiment. For a reliable validation, the values of the Reynolds and swirl intensity have to be the same for both the computational and experimental study, for obvious reasons.

In order to improve the quality of the simulation results, several options of RSM available in FLUENT were tried. The Linear Pressure-Strain (LPS) option refers to the modelling the pressure strain-term in Eq. (3.1) by a lineal sum of a slow-pressure strain, a rapid-pressure strain and a wall-reflection term. The Quadratic Pressure-Strain (QPS) option refers to an improved modelling of the pressure-strain that does not require a correction to account for the wall-reflection effect and use to provide better results for a wide range of flows.

From the wall treatment viewpoint, what is an important feature in our pipe, four options are available to combine with RSM:

- Standard Wall Functions (st.). This is the classic choice for industrial flows. The logarithmic law for mean velocity is known to be valid for $30 < y^* < 300$, where y^* is the dimensionless wall unit. In the CFD solver, the log-law is employed when $y^* > 11.225$. When the mesh is such that $y^* < 11.225$ at the wall-adjacent cells, the solver applies the laminar stress-strain relationship that can be written as $U^* = y^*$. The use of this near-wall treatment has provided the worst results for the axial velocity profile when the QPS is used, as can be seen in Figs. 3.5 and 3.6. However, this is because the QPS tends to overestimate the axial velocity profile values even if the boundary layer was well solved. With LPS, the numerical profiles were good.

3.2 Setting-Up the CFD Simulations

- Scalable Wall Functions (sc.). When using a very fine grid, the usage of wall functions may lead to misleading results due to the fact that what was suppose to be modelled by wall functions is refined until having the first point in the sublayer. The scalable wall function model avoids such problem on grids with $y^* < 11$. For coarser grids ($y^* > 11$), the results are identical to the ones from Standard Wall Functions. This option has been worst to solve the boundary layer by far, as in Fig. 3.5 and 3.6 can be appreciated that for both the LPS and QPS options the boundary layer has an inaccurate behaviour for the velocity profiles.
- Non-Equilibrium Wall Function (neq.). The key elements in the non-equilibrium wall functions are the use of Launder and Spalding's log-law for mean velocity sensitized to pressure-gradient effects and the two-layer-based concept is adopted to compute the budget of turbulence kinetic energy in the wall-neighboring cells [69]. For these reasons, this function is usually useful in cases where complex scenarios such as separation, impingement or sudden pressure changes appear. As this is not our case scenario, it is not wise to use such wall function. By using this option, it can be observed that for both the LPS and QPS options the axial velocity profile is not well validated, but for the QPS one, the azimuthal velocity profile provides good match. It is interesting to see that for the LPS case, it provides almost identical results than when Standard Wall Function is active and the biggest error of the friction factor with respect to experimental data (see Fig. 3.7).
- Enhanced Wall Function (enh.). This option has been already explained in Section 3.2.1. This was the option that has better performed when the LPS is used but when using the QPS, the CFD code convergence was slow and at a certain point even blew up. The good performance with LPS is not surprising since we used a very fine mesh ($y^+ < 1$) and for such, the Enhanced Wall Function allows to resolve the viscous sublayer [38]. The azimuthal velocity profile (Fig. 3.6) has a good match with experimental results, and the axial velocity profile (Fig. 3.5) has a perfect fit. Regarding the friction factor, in Fig. 3.7 can also be observed that is the one that has the closest to experiments.

Therefore, due to its better agreement with experimental data, the turbulent model finally chosen was the **RSM with Linear Pressure-Strain and Enhanced Wall Function**.

Regarding the solver configuration, as we are modelling an incompressible flow, a pressure based formulation is used. The pressure-velocity coupling is done by SIMPLE (Semi-Implicit Method for Pressure-Linked Equations) algorithm [184]. The spatial discretisation of convection terms was done with Second Order Upwind methods. When second-order accuracy is desired, quantities at cell faces are computed using a multidimensional linear

reconstruction approach [19]. In this approach, higher-order accuracy is achieved at cell faces through a Taylor series expansion of the cell-centered solution about the cell centroid.

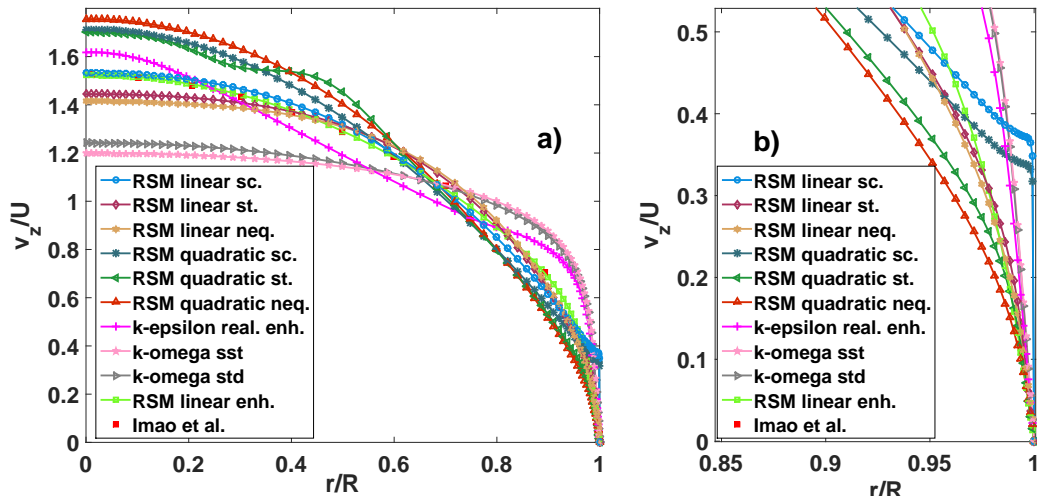


Figure 3.5 a) Plot of the axial velocity profiles of the fully-developed turbulent swirling flow for several turbulence models and validation with Imao et al [101]. b) Zoom of the boundary layer. $Re = 20000$ and $S = 1$.

3.2.2 Grid uncertainty

The uncertainty of the grid has been also analysed for the CFD simulation of the pipe and the impinging problem following the Grid Convergence Index (GCI) procedure described in [35], which has been developed from Richardson extrapolation. The parameter under study is the friction factor, λ , as it is a good measure for checking whether the boundary layer has been solved properly. Once the CFD simulations of the rotating pipe are ready, the GCI can be computed. Its value is shown in Fig. 3.8 for λ , where a discretization error of only a 0.2% is achieved with 200 iterations per minute in our $[n_r \times n_z] = 68 \times 450$ cells mesh shown in Fig. 3.3. Despite of the simulations of the impinging jet are described in the following section, it is worthy to mention here that their discretisation error has been studied already in [177], with a 0.4% of error.

3.2 Setting-Up the CFD Simulations

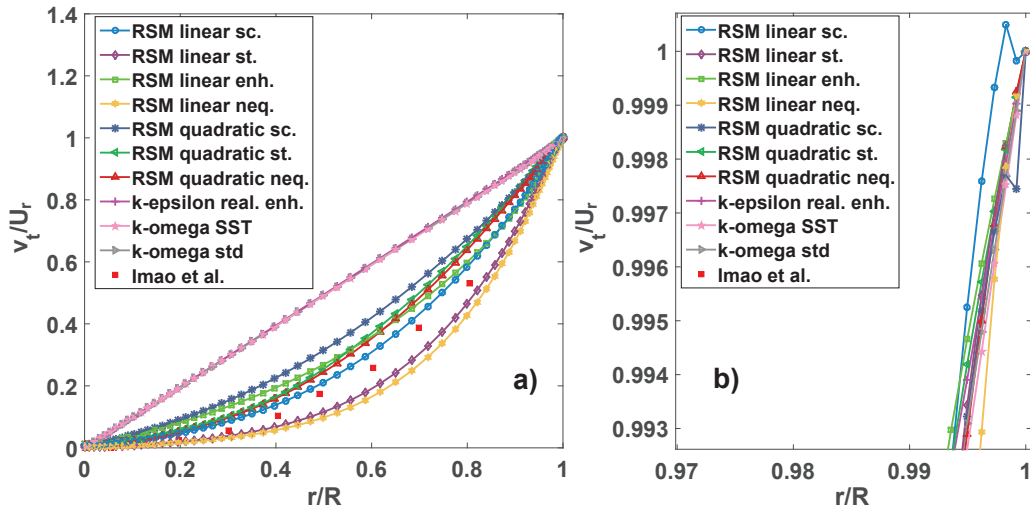


Figure 3.6 a) Plot of the azimuthal velocity profiles of the fully-developed turbulent swirling flow for several turbulence models and validation with Imao et al [101]. b) Zoom of the boundary layer. $Re = 20000$ and $S = 1$. U_r stands for the solid rigid body rotational velocity $U_r = \Omega R$.

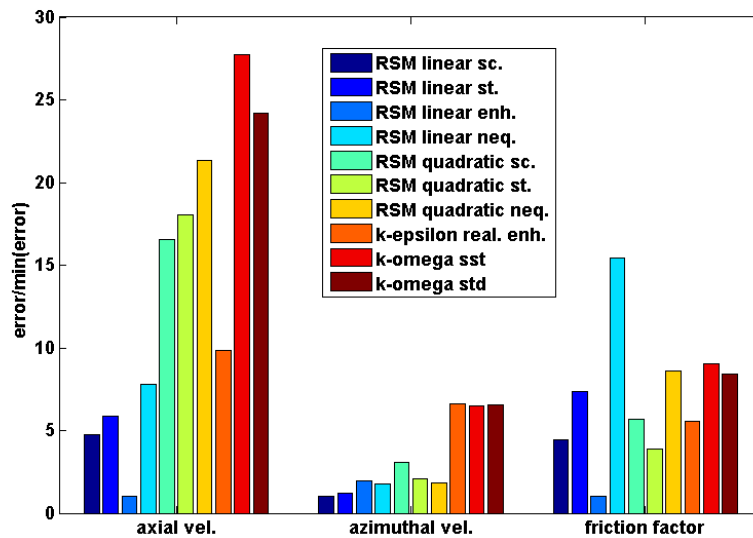


Figure 3.7 Plot of the errors of relevant parameters of the simulation for several turbulence models, with respect to the minimum value of the error (the RSM linear enh.). The error measure is the euclidean norm.

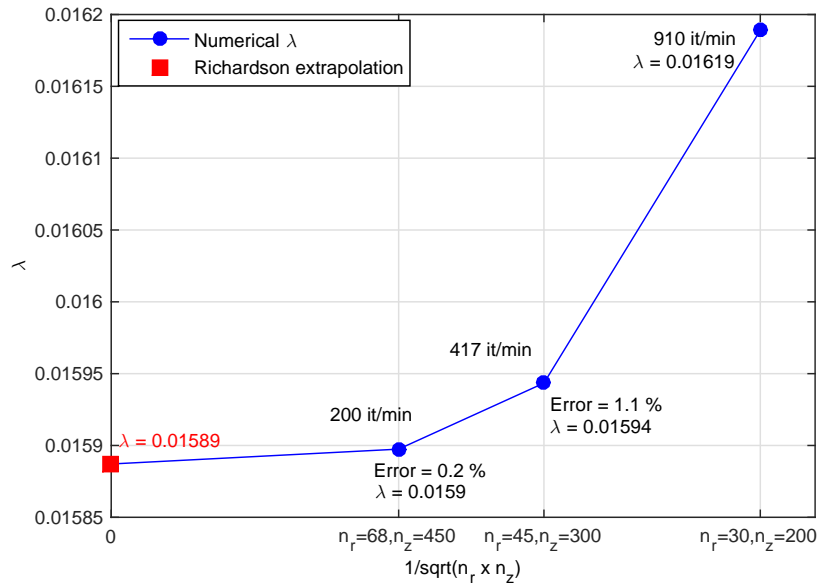


Figure 3.8 Grid Convergence Index to quantify the discretization errors and Richardson Extrapolation. The iterations per minute and the corresponding error are also included in the figure for each grid.

3.2.3 Simulation 2: CFD Simulations of the Heat Transfer to a Heated Solid Flat Plate from an Impinging Swirling Jet

Impinging jets for heat transfer have an extensive number of applications, as introduced in Section 4.1. The plate under consideration is fully flat (no roughness) and the distance between the exit of the pipe and the plate is constant at $H/D = 5$, although the validation of the simulations was done for $H/D = 2$, as it is a more unfavourable case and there are existing results from different authors in literature to compare with. The corresponding velocity and turbulent profiles at the exit of the rotating pipe are now used as inflow boundary conditions. The simulations have been developed as axisymmetric 2D RANS in FLUENT.

A detail of the meshed domain and the boundary conditions can be seen in Fig. 3.9. The size of the grid is $[n_x \times n_h] = 140 \times 250$ cells, with a $y^+ < 1$ along the plate. In practice, the x axis is the same as the r one when the pipe was analysed, but it is preferred to use different notation in order to avoid confusion between the parameters at the exit of the pipe and on the flat plate. Part of the rotating pipe was also incorporated in the computational domain of the impingement for a less abrupt coupling of the profiles from the pipe.

Regarding the turbulence model, the SST $k - \omega$ has been chosen. This choice, already demonstrated in [177] and [173], has been validated with the experimental data of impinging

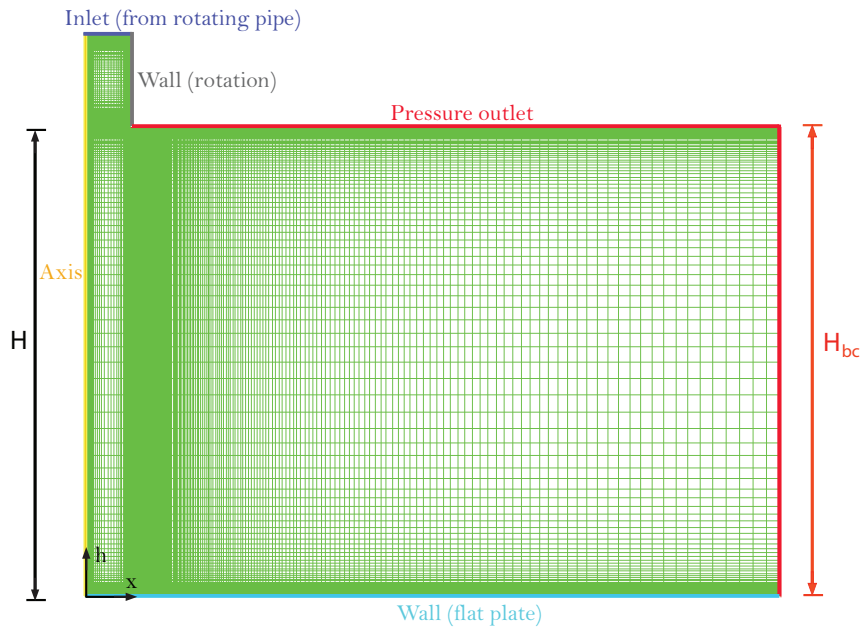


Figure 3.9 Computational grid for the CFD simulations of the impinging jet and boundary conditions imposed. H_{bc} stands for the height of the upper boundary condition, that can be different than H . The size of the pipe wall is kept fixed at a length D .

jets in [130] and [20], as can be also seen in Fig. 3.10, where the results obtained with different options for SST $k - \omega$ model have been included. For $H/D = 2$, it is known that there is a secondary peak in the Nusselt number. It can be guessed that this secondary peak is attributed to the transition from laminar to turbulent boundary layer in the spreading wall jet as suggested by [75, 131]. This transition seems to be triggered by disappearance of the pressure gradient which exists in the stagnation region. The pressure gradient serves to stabilize the laminar boundary layer, despite of high turbulence levels in the free jet stream [113]. By our numerical experiments this has in fact been validated with the results shown in Fig. 3.11, where it can be observed that there is a peak in the turbulent intensity on the plate coinciding with the position of such peak in the Nusselt. This peak is not captured when the transition option is not activated in the turbulent model (SST $k - \omega$ conf. 1 in Fig. 3.10). For further information about the computational features of the simulation, including the discretization error and the selection of the SST $k - \omega$ turbulence model, the author suggest to see [177]. In Fig. 3.12 is shown the velocity contour plot at $Re = 23000$ and $S = 1$ of the simulation with $H/D = 5$.

When simulating high Reynolds jets, it is common to have a pressure suction area that takes place because of the difference in velocity between the jet and the surrounding flow. This can affect somehow the jet development, and therefore, the heat transfer. For this

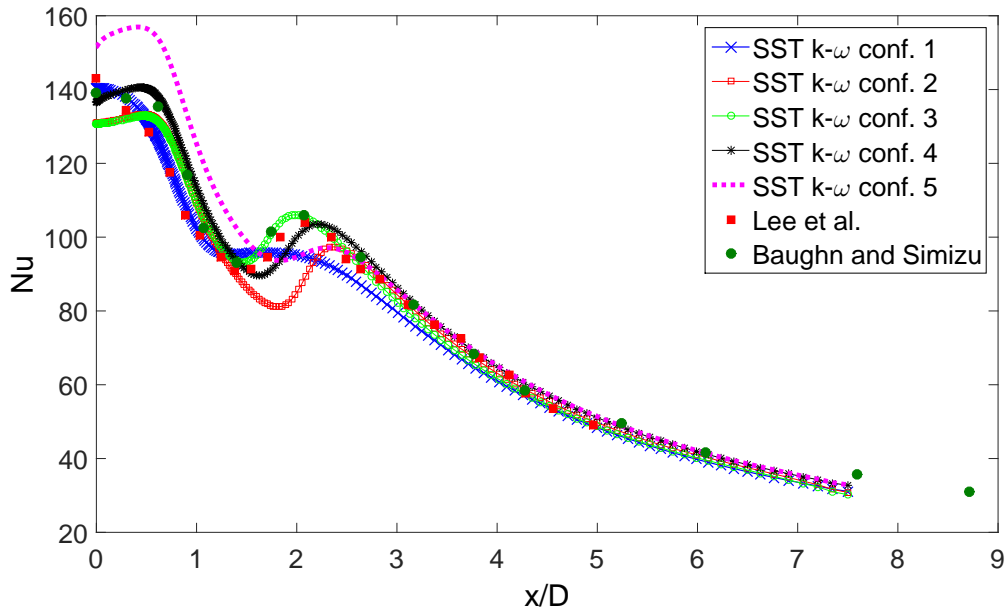


Figure 3.10 Validation of the turbulent model for $H/D = 2$. The different configurations of the SST $k - \omega$ turbulence model correspond to conf. 1: with transitional flow (old model in FLUENT version 6.3), conf. 2: with Low Reynolds correction, conf. 3: without Low Reynolds correction, conf. 4: Transition SST with the Production Kato-Launder option and conf. 4: Transition SST with the Production Limiter option. The chosen option was SST $k - \omega$ with the Production Kato-Launder option.

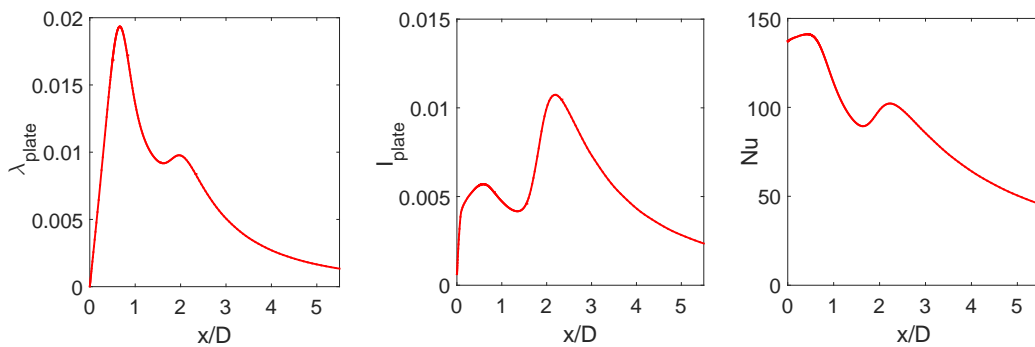


Figure 3.11 Graphs of the friction factor on the plate (left), turbulent intensity (centre) and Nusselt number (right).

reason, it is also interesting to see how the boundary conditions can affect the simulations. To that end, it was tested how the height of the upper boundary condition could affect the computation for different values of H_{bc} , as described in Fig. 3.9 . The effect is minimum

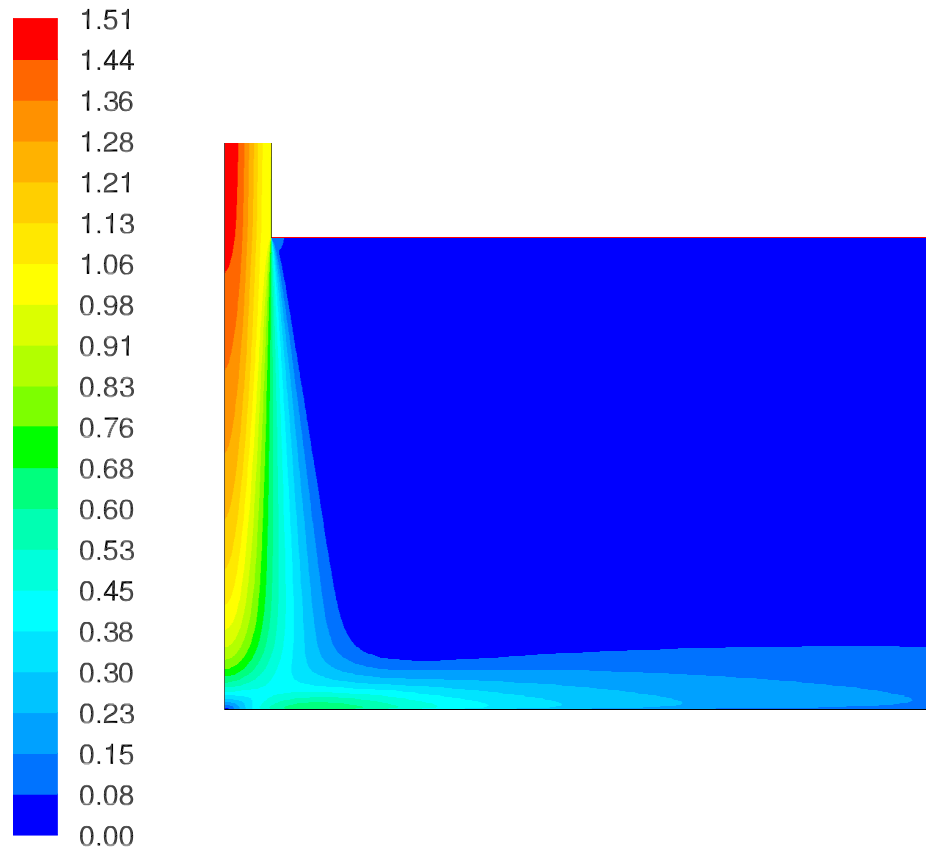


Figure 3.12 Velocity contour plots made dimensionless with the mean velocity U . $Re = 23000$, $S = 1$ and $H/D = 5$.

even for the unfavourable case of $H/D = 2$, as it can be observed in Fig. 3.13, where the evolution of the Nusselt number was plotted for three different values of H_{bc} . Because it makes no effect, the initial configuration in Fig. 3.9 with $H_{bc} = H$ is kept.

3.3 Coupling the Two-Step CFD Simulations

As the turbulence model used for the pipe and the one used for the impinging heat transfer problem are both different, a single simulation of the two-case scenario cannot be developed. Moreover, the complexity of the problem would be unnecessarily increased as the pipe may be long enough to guarantee the fully-developed flow, being necessary a massive domain to simulate.

To overcome this drawback, the two-step CFD simulations were coupled in the following

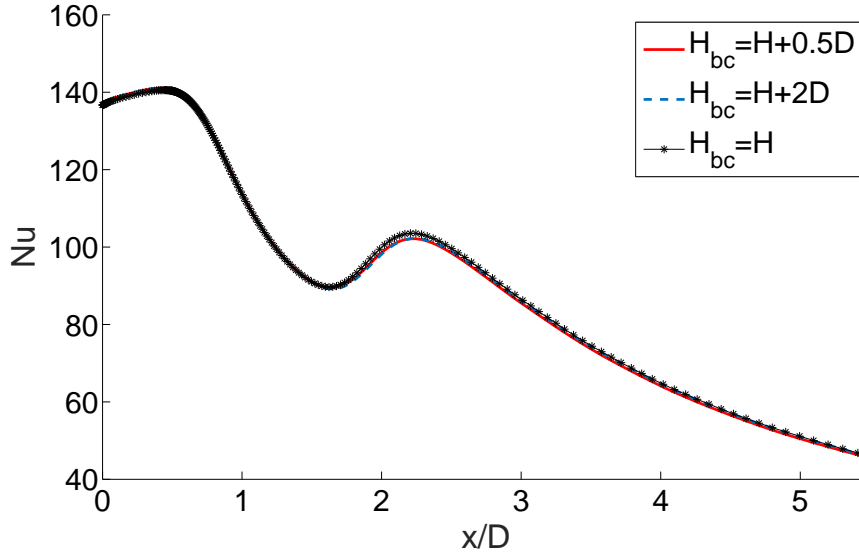


Figure 3.13 Effect of the position of the upper boundary condition in the Nusselt number.

way: firstly, the CFD simulations of the swirling flow confined in a rotating pipe with the RSM turbulent model were developed (*Simulation 1*), and secondly, the velocity and $k - \omega$ profiles at the exit of the pipe are imposed as inlet boundary conditions for the heat transfer simulation (*Simulation 2*). For the purpose, the turbulent parameters are defined as

$$k = \frac{2}{3}(UI)^2, \quad (3.2)$$

$$\omega = \rho \frac{k}{\mu} \left(\frac{\mu_t}{\mu}\right)^{-1} = \rho \frac{k}{\mu} \beta^{-1}, \quad (3.3)$$

where k is the turbulent kinetic energy, I is the turbulent intensity, U is the average velocity of the flow, ρ is the density of the fluid, ω is the turbulent dissipation rate and μ_t/μ is defined as the turbulent viscosity ratio, represented by β throughout this thesis. The turbulent kinetic energy is available from the RSM simulations, but the turbulent dissipation rate is not, therefore has to be evaluated by Eq. (3.3) in order to be a boundary condition for *Simulation 2*.

In order to couple the two simulations for modelling, two options have been tested in this work for the *Simulation 2* as shown in Fig. 3.14. The first one is to impose as inlet conditions the simulated profiles exiting the rotating pipe, what requires to perform both *Simulation 1* and *Simulation 2* for every required deterministic simulation for uncertainty quantification. The second option is to develop several mathematical models for different magnitudes at the exit of the pipe that let us avoid *Simulation 1*. For some further studies like uncertainty quantification, every time the accuracy of the uncertainty prediction is to be increased, new simulations are

3.4 Proposed Mathematical Models for the Dimensionless Profiles From the Rotating pipe

required, making the use of models very attractive. These models are introduced in the next section and applied to uncertainty quantification in Chapter 4.

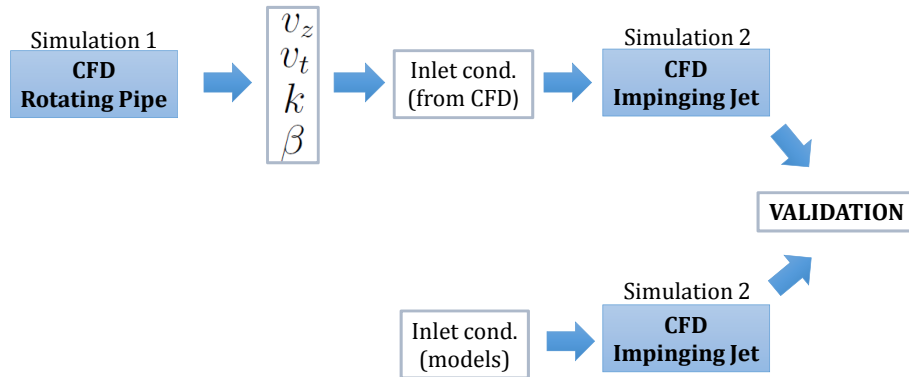


Figure 3.14 The two possibilities: by using the CFD profiles at the exit of the nozzle to impose, or by modelling them.

3.4 Proposed Mathematical Models for the Dimensionless Profiles From the Rotating pipe

In some applications involving expensive runs or complicated couplings, it is necessary to run CFD simulations or experiments for which lower cost models could be found in order to skip such tedious part of the study. In this section, four dimensionless models are given: for the axial velocity (v_z), azimuthal velocity (v_t), kinetic turbulent energy (k) and turbulent viscosity ratio (β) profiles, all of them for the fully-developed turbulent swirling flow case. Those models will approximate the response of the CFD RANS simulations for the different Q and Ω . In literature one may find that inlet boundary conditions for turbulence are simply modelled as a percentage, so to give also an equation for both the kinetic turbulent energy and viscosity ratio represents an accurate insight. It is certainly a cheap way to evaluate computationally cost codes in some fields as, e. g., CFD optimisation, prototyping or UQ, as it can be sampled almost costless.

The models have been designed following the same practice as in [175], and which were also successfully input in CFD simulations of impinging swirling jets in [173, 174, 177]. These models are composed of several functions chosen according to the features of the profiles and validated with CFD results as will be shown in this section and in Section 4.3. It is true that a very accurate model to fit the profiles could be obtained by interpolation. However, a new model should be built for each CFD simulation profile losing any possible generality. For this reason, a coefficient dependent approach is preferred, being possible to

3.4 Proposed Mathematical Models for the Dimensionless Profiles From the Rotating pipe

link the coefficients to the physical parameters Q and Ω as in Section 4.3. The coefficients are found by a MATLAB main custom code which calls Curve Fitting Toolbox functions that use a Non-Linear Square method with Trust-Region algorithm [44]. The introduced models in this thesis can be implemented to obtain quick dimensionless profiles in tasks like increasing the accuracy of surrogates models, as it has been done in [85], where it has been also demonstrated the validity of the models for wider intervals (needed for optimisation).

The process of finding the appropriate models for the velocity and turbulent profiles was developed as follows. First, an analytical solution based on physics ground was not considered and this is the main limitation of this approach, as the flow is turbulent and this makes a pure mathematical analysis very complex for the purpose. Here it is only intended to find mathematical models to avoid the repetition of *Simulation 1* every time Q and/or Ω is varied. Therefore, mathematical custom regression fit models were tried as done in [175] and successfully implemented in [177, 173, 174]. The use of such modelling is in fact a very popular approach in industrial practice, and one can find this often i.e. in technical engineering documentation sheets and predictive modelling in other fields such as finance.

Several options were tested for the axial and azimuthal velocities as shown in Fig. 3.15. For the axial velocity profile, it can be observed that the shape is non-linear with different piecewise curvatures. It is specially relevant the proper modelling of the boundary layer, since it plays an important role in the further development of the flow. This led to the modelling with a hyperbolic tangent in $v_z/U^{(1)}$, $v_z/U^{(2)}$, $v_z/U^{(best)}$. Despite that it is not clear under which conditions the hyperbolic tangent shape is taking place, it has been formerly observed by other researchers that the boundary layer flow profile looks close to this mathematical function [146, 175] in flows under rotation, and in jet flows this is also observed since a simple scenario of hyperbolic tangent profile takes place when two flows are in contact with different but constant velocities [153]. To model the flow velocity as a fully parabolic profile like in Hagen-Poiseuille flows (fully-developed, incompressible, newtonian and laminar flow in a non-rotating pipe) will be mistaken, since the shape is not parabolic at all. This was even tried with a cubic polynomial in $v_z/U^{(3)}$, which requires only three constants to estimate with a poor performance. Amongst $v_z/U^{(1)}$ and $v_z/U^{(2)}$ there are some clear differences. A power effect in $v_z/U^{(1)}$ is introduced to deal with the non linearity, which is not introduced in $v_z/U^{(2)}$, undergoing a bad fit. The combination of the power function featured in $v_z/U^{(1)}$ with the flexibility of the third order polynomial $v_z/U^{(3)}$ led to the selected model in Eq. (3.4), the $v_z/U^{(best)}$, which undergoes a very good match.

The procedure for the azimuthal velocity was simpler. It was already suggested in [101] that the profile is closely parabolic. However, due to its also possible exponential behaviour, this was also tried. In Fig. 3.15, it is shown that the power function fitted the best, and the predicted values of the constants are $a = 0.9709$ and $b = 2.0052$, thus $v_t/U_r \sim (r/R)^2$. The

3.4 Proposed Mathematical Models for the Dimensionless Profiles From the Rotating pipe

constants of the discarded models can be found in Table 3.1.

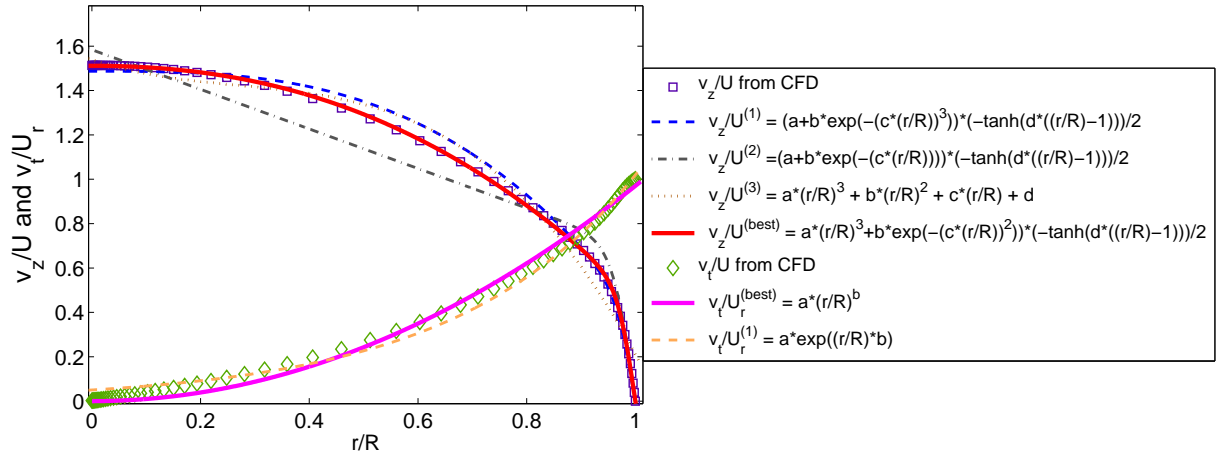


Figure 3.15 Axial and azimuthal velocity profiles from CFD and tested mathematical models.

Table 3.1 Fitting coefficients of the discarded mathematical models for the axial and azimuthal dimensionless velocity profiles.

Model	a	b	c	d
$v_z/U^{(1)}$	1051	-1048	-0.1276	32.230
$v_z/U^{(2)}$	-596.3	599.5	2.980E-03	24.710
$v_z/U^{(3)}$	-2.682	2.174	-0.819	1.539
$v_t/U_r^{(1)}$	5.032E-02	3.009	-	-

The modelling of k/U^2 was the most complicated of them all. The tried fits can be seen in Fig. 3.16. The procedure for this fitting search was similar to the one followed for v_z/U . Again, the best function for the region near to the wall was the hyperbolic tangent, although $k/U^{2(2)}$ did not undergo a bad fit over there without that term. However, its fit was too bad for the rest of the profile. For these reasons, some effort was focused on improving the exponential term of $k/U^{2(1)}$. Several tests were done on a function with the form of $k/U^{2(3)}$. As one can see in the Fig. 3.16, its graph is far from the training points. This is because the MATLAB curve fitting algorithm had problems to fit the k/U^2 data with four coefficients, being required to reduce the dimension in the search space. An accurate initial guess would solve this issue, but even with the $k/U^{2(best)}$ coefficients as initial guess, the fitting search

3.4 Proposed Mathematical Models for the Dimensionless Profiles From the Rotating pipe

was impossible. By tuning manually $k/U^2^{(3)}$, it was observed that the a coefficient tended to be a value close to 0.05327. Despite the fact that the fitting is very accurate, to fix the 0.05327 and 1.2 coefficients in the equation is reducing the flexibility of the model to adapt to changes in Q and Ω . This is going to be further tested in Section 4.3. The constants of the discarded models can be found in Table 3.2.

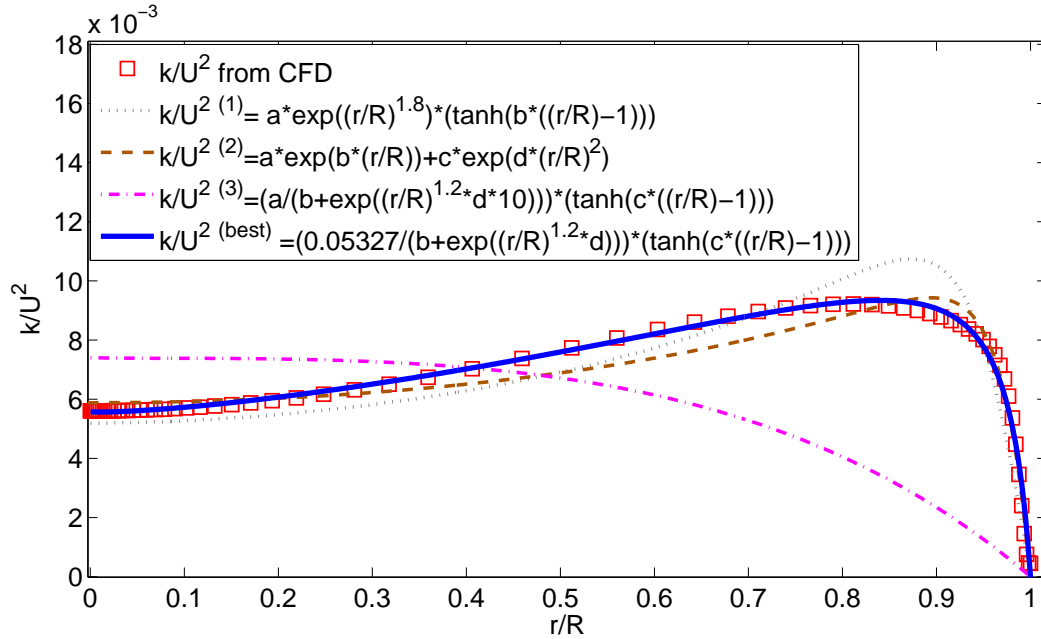


Figure 3.16 Dimensionless kinetic energy profile and tested mathematical models.

Table 3.2 Fitting coefficients of the discarded mathematical models for the kinetic energy dimensionless profile. $k/U^2^{(3)}$ does not appear because the search was not possible.

Model	a	b	c	d
$k/U^2^{(1)}$	5.190E-03	-14.090	-	-
$k/U^2^{(2)}$	-4.552E-17	33.140	5.883E-03	0.6341

The turbulent viscosity ratio, β , was also modelled with several custom functions and their performance can be seen in Fig. 3.17. The analysis firstly started with an exponential decay, $\beta^{(1)}$, which imitated well the shape of the profile. The power function inside helped to recreate the curvatures. As the shape in the intermediate region is similar to the shape experienced in the axial velocity profile, the same power functions were tried with a hyperbolic tangent in $\beta^{(2)}$, but the fit close to the wall was fully linear, with no curvature approaching $\beta = 0$.

3.4 Proposed Mathematical Models for the Dimensionless Profiles From the Rotating pipe

This happened even when changing the hyperbolic tangent by an exponential function, so this obliged to a different custom function. For this reason, in $\beta^{(3)}$ a set of exponentials were tried, as in $\beta^{(1)}$ this function showed a promising curve shape. Some difficulties in fitting the $r/R < 0.8$ region were noticed and the addition of a coefficient d in the power of the left hand exponential solved that successfully. In order to reduce the dimension in the search space, the former d coefficient in $\beta^{(3)}$ has been now manually controlled and fixed to 13, as it mainly controls the curvature approaching $\beta = 0$. The fitting coefficients of the discarded models are shown in Table 3.3.

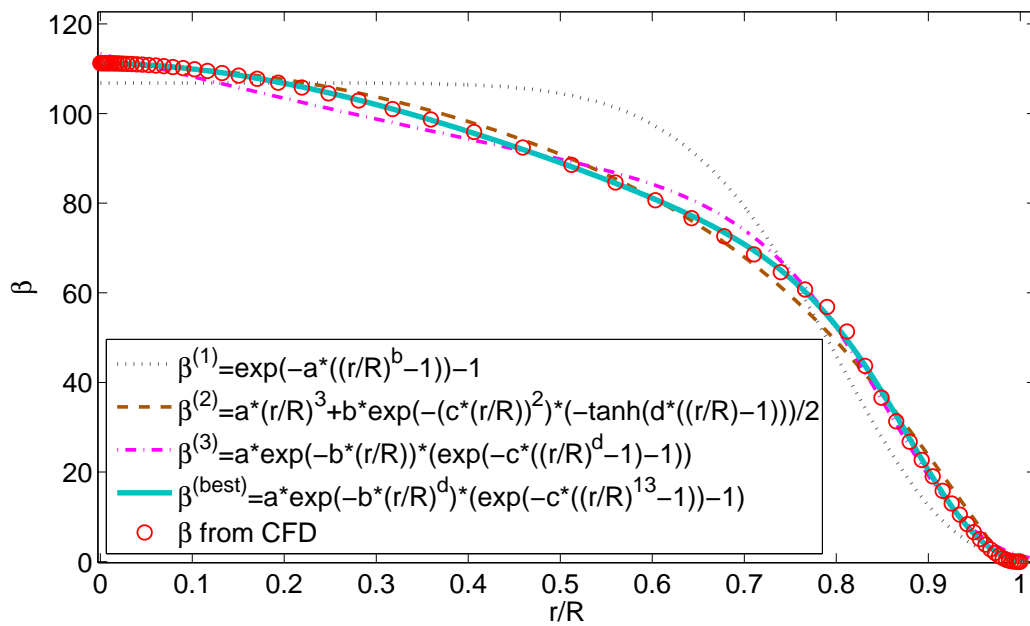


Figure 3.17 Viscosity ratio profile and tested mathematical models.

Table 3.3 Fitting coefficients of the discarded mathematical models for the turbulent viscosity profile.

Model	a	b	c	d
$\beta^{(1)}$	4.681	7.743	-	-
$\beta^{(2)}$	-4.561	221.5	0.8234	4.513
$\beta^{(3)}$	5.785	0.458	3.975	10.170

3.4 Proposed Mathematical Models for the Dimensionless Profiles From the Rotating pipe

After fitting the numerical profiles with different custom mathematical models as discussed above, the proposed ones are those labelled as best

$$\frac{v_z}{U} = \left(a_z \left(\frac{r}{R} \right)^3 + b_z e^{-(c_z (\frac{r}{R}))^2} \right) \frac{1}{2} \left(-\tanh \left(d_z \left(\frac{r}{R} \right) - 1 \right) \right), \quad (3.4)$$

$$\frac{v_t}{U_r} = a_t \left(\frac{r}{R} \right)^{b_t}, \quad (3.5)$$

$$\frac{k}{U^2} = \frac{0.05327 \tanh \left(b_k \left(\frac{r}{R} \right) - 1 \right)}{a_k + e^{c_k \left(\frac{r}{R} \right)^{1.2}}}, \quad (3.6)$$

$$\beta = a_\beta e^{-b_\beta \left(\frac{r}{R} \right)^{d_\beta}} \left(e^{-c_\beta \left(\left(\frac{r}{R} \right)^{13} - 1 \right)} - 1 \right). \quad (3.7)$$

The coefficients of the mathematical models, addressed for sake of notation as γ_i , where $\gamma = a, b, c, d$ and $i = z, t, k, \beta$, are shown in Table 3.4. In Figs. 3.18-3.20 the goodness of the models is revealed through the 95% prediction bound and goodness indicators described in the following. In addition to the fitting described here, the model with bigger uncertainty in the prediction is k/U^2 . The model for v_t/U has some slight uncertainty in the prediction as well, but we decided to keep it as simple as possible (with only two unknown coefficients). More coefficients could be added and the fitting could be improved, but the trend is clearly a power function and it would unnecessary complicate the model and the performance for wider intervals.

It is important to ensure that their values are enclosed in a short confidence bound. This means that the uncertainty in the prediction of the fitting coefficients is small, giving a sense of robustness and reliability (that can be a special need for the greater domains appearing in optimisation problems). The confidence bounds for the coefficients are calculated as

$$c_b = \gamma_i \pm t_{0.95, \nu} SE_{\gamma_i}, \quad (3.8)$$

where $t_{0.95, \nu}$ refers to the two-tailed value of the inverse of t-Student distribution for ν degrees of freedom and a 95% level of confidence, and SE_{γ_i} refers to the estimated standard error of γ_i .

The results can be seen in Table 3.4 for the deterministic base case ($Re = 23000$ and $S = 1$). These values, as well as those from Table 3.5, were monitored for all the fittings of the collocation points for the Sparse Grids required simulations in Chapter 4 when studying the propagation of uncertainty, showing almost identical results for the goodness and variance in the confidence bounds.

In Table 3.5 it can also be found the goodness indicators of the fit for the deterministic base case. As the coefficient of determination (defined in this thesis as \hat{R}^2 in order to not

3.4 Proposed Mathematical Models for the Dimensionless Profiles From the Rotating pipe

Table 3.4 Fitting coefficients of the dimensionless profiles for the deterministic base case.

Coefficient	Value, γ_i	95% confidence bound, c_b
a_z	-1.0474	(-1.1231, -0.9718)
b_z	3.0230	(3.0169, 3.0291)
c_z	-0.6538	(-0.6765, -0.6310)
d_z	34.1414	(32.6899, 35.5929)
a_t	0.9709	(0.9563, 0.9854)
b_t	2.0052	(1.9048, 2.1056)
a_k	-0.1708	(-0.1815, -0.1602)
b_k	-0.0880	(-0.0890, -0.0870)
c_k	-1.6985	(-1.7538, -1.6432)
a_β	1.9314	(1.7141, 2.1486)
b_β	0.7933	(0.7712, 0.8154)
c_β	4.0472	(3.9363, 4.1581)
d_β	1.8621	(1.8048, 1.9194)

confuse with the radius of the pipe) is not the best measure for the goodness of a fit, specially in non-linear cases or experiencing overfitting, the Sum of Squares due to Error (SSE), Adjusted- \hat{R}^2 and Root Mean Squared Error (RMSE) are also given. These are typically defined as

$$\hat{R}^2 = \frac{\text{Sum of Squares of Regression (SSR)}}{\text{Total Sum of Squares (TSS)}} = \frac{\sum_{i=1}^{N_t} (\hat{y}_i - \bar{y})^2}{\sum_{i=1}^{N_t} (y_i - \bar{y})^2} = 1 - \frac{SSE}{TSS}, \quad (3.9)$$

$$\text{Adjusted} - \hat{R}^2 = 1 - \frac{SSE}{TSS} \frac{(N_t - 1)}{v}, \quad \text{with } v = N_t - m, \quad (3.10)$$

$$SSE = \sum_{i=1}^{N_t} (y_i - \hat{y}_i)^2, \quad (3.11)$$

$$RSME = \sqrt{MSE} = \sqrt{\frac{SSE}{v}}. \quad (3.12)$$

In Eqs. (3.9)-(3.12), N_t stands for the number of training points ($N_t = 69$ from $r/R = 0$ to $r/R = 1$), v indicates the number of independent parts for N data points (also called degree of freedom for error), m the number of coefficients to calculate, y_i the values of the training points (CFD data), \hat{y} the values of the models at the training points and \bar{y} the mean value. When increasing the number of terms in the models, \hat{R}^2 is increasing despite of the model can be overfitted. It is hence important to consider the Adjusted- \hat{R}^2 , whose value in case of overfitting starts to decrease. As Adjusted- \hat{R}^2 is always less or equal to \hat{R}^2 , and in Table 3.5

3.4 Proposed Mathematical Models for the Dimensionless Profiles From the Rotating pipe

they are both very close each other, it has been accepted as an indicator of good fitting.

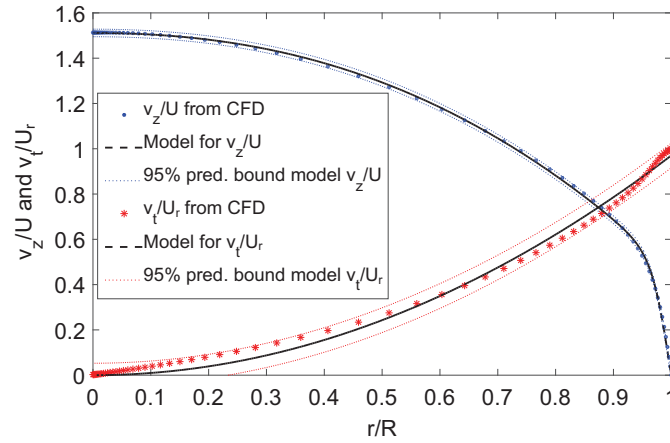


Figure 3.18 Axial and azimuthal velocity profiles from CFD and mathematical model fits with prediction bounds.

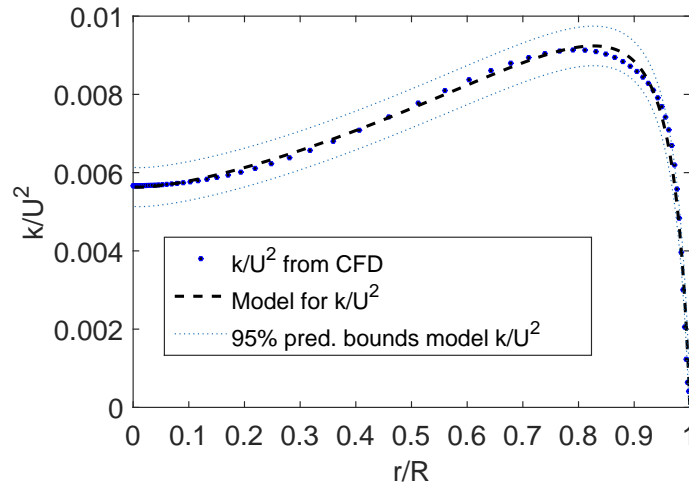


Figure 3.19 Dimensionless kinetic energy profile from CFD simulations and mathematical model fits with prediction bounds.

It can be noticed that the models do not directly depend on any input parameter, hence Eqs. (3.4)-(3.7) can be written as

$$(v_z/U, v_t/U_r, k/U^2, \beta)^T = \mathbf{F}(\gamma_i), \quad (3.13)$$

3.4 Proposed Mathematical Models for the Dimensionless Profiles From the Rotating pipe

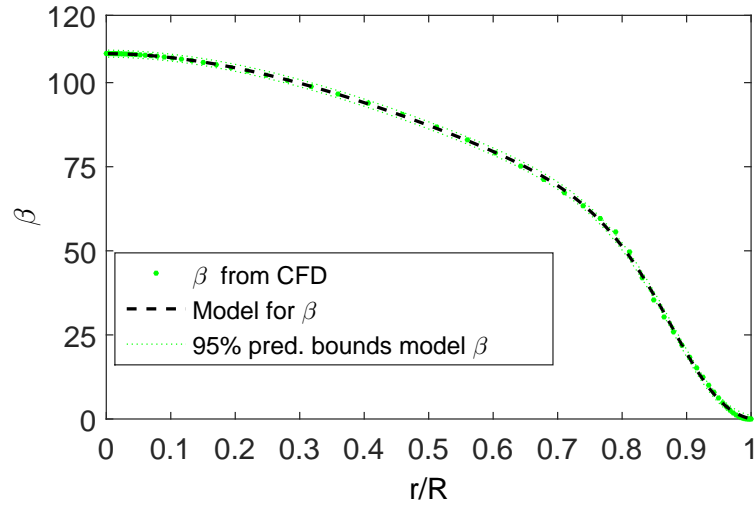


Figure 3.20 Turbulent viscosity ratio profile from CFD simulations and mathematical model fits with prediction bounds.

Table 3.5 Goodness fitting of the dimensionless profiles for the deterministic base case.

Profile	SSE	\hat{R}^2	Adjusted- \hat{R}^2	RMSE	m	ν
v_z/U	0.0044	0.9997	0.9997	0.0082	4	65
v_t/U_r	0.0536	0.9947	0.9946	0.0283	2	67
k/U^2	3.9766e-06	0.9865	0.9861	2.4546e-04	3	66
β	16.6794	0.9999	0.9999	0.5066	4	65

with T denoting transpose. In order to provide input-dependent mathematical models, polynomial regressions can be also built for the coefficients, so that γ_i would depend on Q and Ω . This can be found in Chapter 4, where an application to Uncertainty Quantification is given, as well as the dependency of the models on input uncertain parameters rather than coefficients γ_i .

For implementation of the models as boundary conditions in FLUENT, in Appendix A an User Defined Function (UDF) is given, in order to facilitate the use of these models in future works. This function is coded in C, but it could be easily exported to any other coding language.

In Fig. 3.21 a comparison of both the use of *Simulation 1* and the models as inlet boundary conditions is shown for the Nusselt number along the plate. It can be noticed that the errors are not very substantial and the models slightly overestimate the numerical Nusselt values.

3.5 Comparison and Discussion of Results

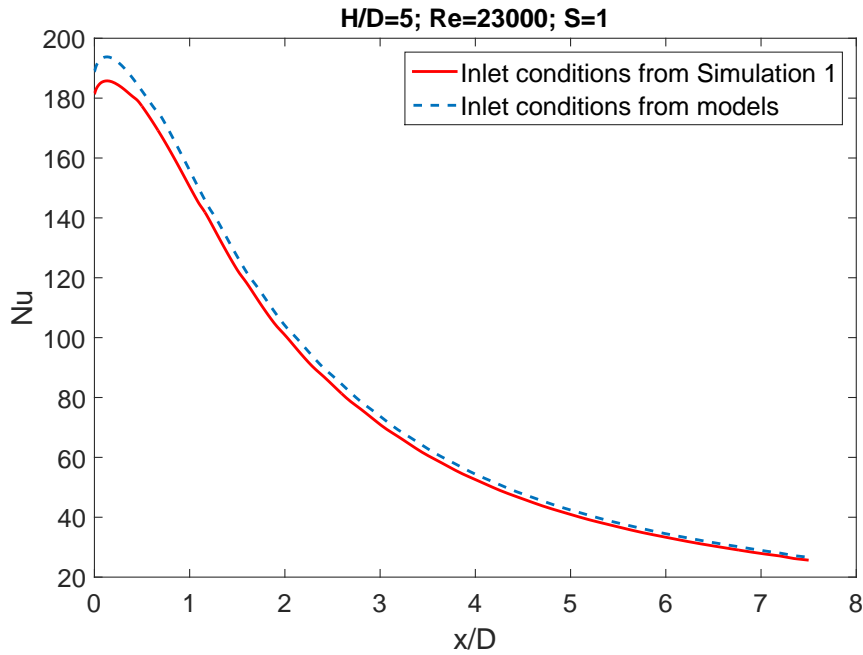


Figure 3.21 A comparison between the use of *Simulation 1* and the models as inlet boundary conditions. $Re = 23000$, $S = 1$ and $H/D = 5$.

3.5 Comparison and Discussion of Results

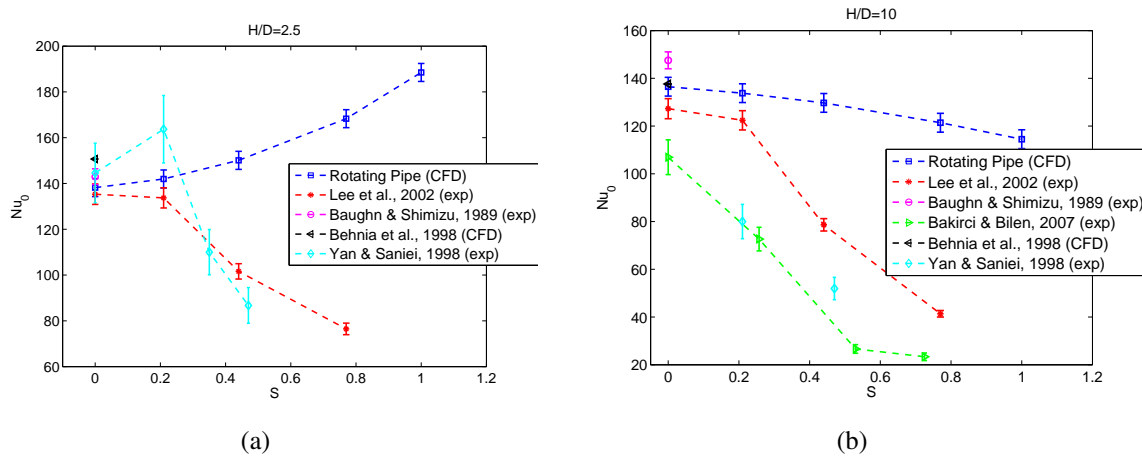


Figure 3.22 Comparison of Nusselt at stagnation point and various swirl numbers with other existing data in literature, with different swirl generation mechanisms for a) $H/D = 2.5$, and b) $H/D = 10$. In the legends, *exp* and *CFD* stands for experimental and computational, respectively.

3.5 Comparison and Discussion of Results

In literature, despite of several comparisons when using different positions of jets, shape of the nozzle or surface variations in the plate can be found, there is no comparison among the best mechanisms for swirling generation to enhance heat transfer results to author's knowledge. In this work, the addition of the swirling has been made by means of a rotating pipe but, as described in Section 3.1, the most popular mechanisms for swirl generation in impinging jet flows are the use of pipes with spirals or vane-type swirl generators [130], swirl strips in pipes [248], angled blades to force rotation [174, 173] and the use of tangential jets to impart the swirl [260].

In Fig. 3.22, the heat transfer at the stagnation point with the rotating pipe mechanism has been compared with these experimental mechanisms from literature, as well as computational ones². In such plot, both a near and a far H/D distance is under analysis, since its impact in the heat transfer is enormous, because it affects the jet development. Actually, it has been reported in literature that for $H/D > 10$ the effect of swirl is unseen [131]. The region of highest interest for comparison is the stagnation region (the quantity of interest to report is, thus, the Nusselt at the stagnation point Nu_0), since it is the region where the swirl effect is most noticeable [260]. Moreover, only the Nusselt at this point was checked since the Nusselt average on the plate depends on the length of the tested surface. For a clear and meaningful comparison, the plotted literature results will be also briefly explained. The comparisons are all made with air jets at a short ($H/D = 2.5$) and a far ($H/D = 10$) distances and $Re = 23000$ as benchmark, from the following papers:

- *Lee et al, 2002* [130]: $Re = 23000$ with swirl generated by pipes with spirals (vane-type swirl generators), whose swirl number is based on geometrical parameters [112] of the swirl generators independent of the Reynolds number. Data reported at different swirl intensities. The Nusselt is always decreasing, independently of H/D , when the swirl intensity is increased. The reported experimental uncertainty for the Nuselt is 3.3%. The results of this thesis for $S = 0$ match very well their experiments.
- *Baughn and Shimizu, 1989* [20]: The $Re = 23700$ is a bit higher than the benchmark one ($Re = 23000$), but as the Re uncertainty is 2.3%, it is still good for comparison. In this work only $S = 0$ is measured and that is the reason of having a single point in the figures. There is a greater discrepancy in $H/D = 10$ with respect to other works, perhaps because that small difference in Re is more sensitive for larger $H/D = 10$. The Nusselt uncertainty is 2.4%, as reported in the paper.
- *Bakirci, 2007* [18]: Only $H/D = 10$ experimental data reported with $Re = 20000$ and several swirl intensities generated by helical swirl generators (spirals inside the pipe) plus a conical tip. The Re is slightly smaller than the benchmark one, but useful for comparison, as Re uncertainty is 3.7%, so the real Re is in the range [19260, 20740].

²The uncertainty bars shown in the rotating pipe simulations have been obtained in Chapter 4, and the procedure to obtain them will be discussed throughout the chapter.

3.5 Comparison and Discussion of Results

The Nusselt uncertainty is a 6.8%. The swirl intensity has been obtained by the same equation from [112] utilised in *Lee et al., 2002*. In *Bakirci, 2007*, $r_1 = 1.25\text{mm}$, $R = 7.5\text{mm}$ and $l = 0.123 \cos \Theta$, following the notation in the paper. The experimental results have the lowest Nu_0 , with a large difference with respect to the others. Despite the devices are similar to the ones used in the also compared *Lee et al., 2002*, the hub was extended with a conical tip in order to avoid a sudden expansion, that is affecting the jet and then producing such a different behaviour in the heat transfer. It is important to point out that in both *Bakirci & Bilen, 2007* and *Lee et al., 2002* plotted results, the $S = 0$ case is consequence of a round jet, not the spirals with zero angle, because the idea is to compare the match with the non-rotating pipe simulations and experiments.

- *Behnia, 1998* [21]: Only $Re = 23000$ with $S = 0$ data available, as only non-swirling flows are under study. In this computational work, the turbulence model used is $V2f$ ($k - \varepsilon$ is employed too, but with a very poor performance). The greater discrepancy with the rotating pipe data is in $H/D = 2.5$, but in their paper can be observed that the turbulence model is not very accurate at such distance. With $H/D = 10$ the match is almost perfect. No uncertainty is reported on the simulation, and as it will be discussed in Chapter 4, this is a regular missing data in CFD, that is reported in this thesis for the rotating pipe approach.
- *Yan & Saniei, 1998* [260]: In this work, $Re = 23000$ and several swirl intensities imparted by tangential jets are reported. In these results, the Nu_0 decreases when S is increased, for a given H/D . However, is interesting to see the sudden peak in $S = 0.21$ for $H/D = 2.5$. These results have been tried to be simulated by other researchers too [231, 259].

Therefore, having a look at Fig. 3.22, some conclusions can be drawn from the rotating pipe option.

The suggested mechanism always provides the highest heat transfer and the best control of the swirl. It is relevant also the fact that for near distances between the nozzle and the plate, the higher the S , the greater the Nu_0 . This does not happen with other mechanisms compared. This is likely consequence of the jet spreading: the swirl generation mechanism plays a very relevant role on this. Depending on the employed mechanism, the generated jet will have different patterns and hence, the way it spreads downstream will be different. This spreading is influential for the impinging conditions affecting the heat transfer as in the swirling jet, the degrees of jet growth, entrainment of ambient air, and jet decay are affected by the degree of swirl [18, 195] and other perturbations from generation mechanisms. In [202] has been reported that even the addition of light swirl can change significantly the behaviour of the jet. In the rotating pipe, it would be expected to have a decay in the heat transfer at $H/D = 2.5$ if a certain value of S is surpassed, as the vortex breakdown and spreading angle would be highly influenced.

3.5 Comparison and Discussion of Results

The reason according to flow physics behind the improvement of the heat transfer by increasing S is not clear. A detailed experimental study of the flow structures should take place, comparing with the other methods too. However, there are some hints, according to detailed experimental results reported in [61, 62]. These results demonstrate that in a swirling jet flow from a rotating pipe at a similar Reynolds ($Re = 24000$) to the benchmark, the jet flow experiments:

- Increase in the spreading angle.
- Increase in the turbulent intensity.
- Increase of the turbulent intensity in both axial and orthogonal velocity components at the centreline,
- Entrainment increases with rotation as compared with the non-rotation case, since rotation makes the potential core break down faster.
- Azimuthal velocity changes sign in the core of the jet at $H/D > 5$.
- Interesting differences between the the non-swirling and swirling jets with regard to large scale structures inside the jet.

All these bullet-points represent special features of a swirling jet generated by a rotating pipe, and the behaviour of other mechanism can be completely different and be affected by the a short H/D distance. For example, the jet centreline development is different when spiral vanes are used as in *Lee et al., 2002* and *Bakirci & Bilen, 2007*. These two mechanisms have no flow in the centreline at the exit of the pipe, what dramatically affects the heat transfer at the stagnation point, which is at the centreline. This is an important effect in near distances such as $H/D = 2$.

For larger distance ($H/D = 10$), even having a negative slope in the evolution for higher S , the Nu_0 with a rotating pipe exhibits a weaker decay. The worst results took place in *Bakirci & Bilen, 2007* paper, where the Re was slightly lower than the benchmark ($Re = 20000$). In such piece of work, a conical tip was placed at the end of the helical generator in order to reduce the sudden expansion. That was not placed for the similar helical mechanism in *Lee et al., 2002*, so it would be interesting to explore whether is negatively affecting to heat transfer at far H/D distances. Moreover, in *Lee et al., 2002* eight grooved channels instead of four were used, so the gap may be also due to either the blockage at the centre of the swirl generator for larger swirl angle and/or the high spreading rate for high swirl angles, as specified in *Bakirci & Bilen, 2007*. In the generation of swirl by a rotating pipe,

These comparisons led to a further study to see the behaviour at different conditions. A helpful picture of this scenario can be seen in Fig. 3.23(a).

3.5 Comparison and Discussion of Results

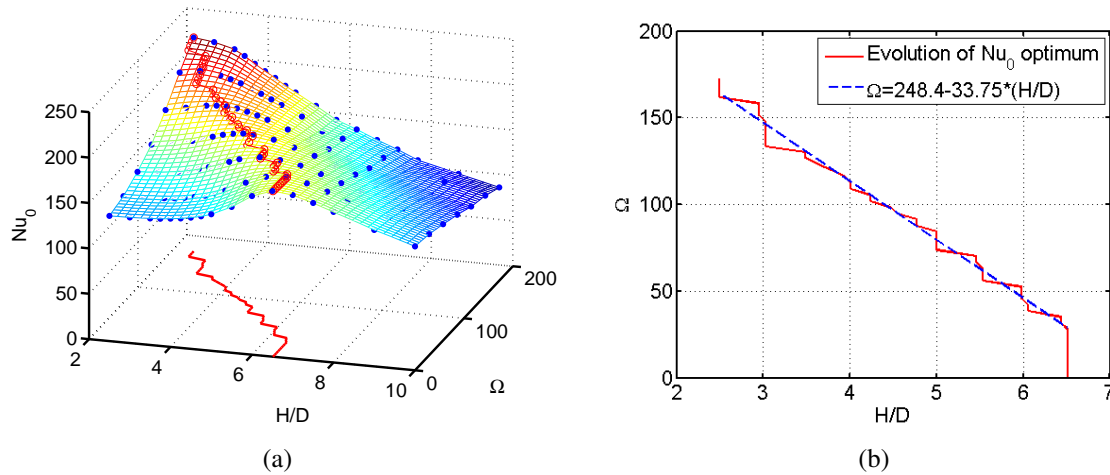


Figure 3.23 a) Evolution of the optimal Nu_0 with $Re = 23000$, and different Ω and H/D . b) Correlation fit $\Omega - H/D$.

This plot has been built from several simulations (each blue point stands for a CFD simulation). There, it can be observed that for $\Omega = 0$, the optimal value of the Nusselt is near $H/D = 6$, as reported in many literature sources. When Ω is increased, the best option is a very close nozzle-to-plate distance. It is also very interesting to see that the evolution of the optimal Nu_0 points have a very linear trend as shown in 3.23(b). From this plot, it is easy to get the best Ω for a specific H/D and vice versa, in order to get the highest Nu_0 .

To show the qualitative improvements of a rotating with respect to other methods in literature, the differences amongst mechanisms can be broken down as:

1. When using helical (or vane-type swirl) generators as in *Lee et al., 2002* and *Bakirci & Bilen, 2007* or longitudinal swirling strips as in [248], a new pipe device must be mechanised and it experiments always lower heat transfer than the rotating pipe. Moreover, as can be seen in the paper, it is important to remark that with this swirl generation mechanism the heat transfer at the stagnation point for small H/D decreases when increasing the swirl.
2. When using oriented blades as in [175, 174, 173] for a water jet flow, in non-swirl conditions (blades at zero angle but affecting the jet) the flow performs poorly the heat transfer. In the paper can be read that when increasing the Reynolds number, the heat transfer is enhanced but, as the swirl is strongly Reynolds number dependent ($S = S(Re)$), it cannot be controlled independently. A similar case is *Yan & Saniei, 1998*, where three tangential air mini-jets impart the swirl.
3. Taking into account the devices of the items above, some other issues are addressed by the rotating pipe option:

- If a single non-swirling round jet flow is desired in the experiments, the mechanisms at zero angle are still affecting the flow. This could only be avoided by dismantling.
- The helical guide-ways and the blades can be oriented for a desired swirl intensity, but there will be a maximum angle at which the swirl cannot be increased any more. With a rotating pipe, there is no limitation in principle and the pipe can spin at any desired angular velocity with a fixed Reynolds number. The big disadvantage is that the rotating pipe must be very long ($55 - 60D$), and not all the experimental rigs may allow such a long pipe.

To sum up, the use of a rotating pipe for impinging heat transfer provides some flexibility versus costs advantage (a motor would be needed for the rotation, but this would be less expensive than mechanising several spiral ducts and one can control more swirl intensities). Some future investigations can be linked to this swirl generation mechanism or even mixing this method with other existing in literature to enhance the swirl number ranges or swirl properties.

3.6 Conclusions

An intensive study of CFD simulations of a swirling impinging flow from a rotating pipe have been done in the presented chapter. A big emphasis has been laid on the proper simulation of the swirl of the flow confined in the pipe and on getting the mathematical models for both the velocity and turbulent profiles at the exit of the pipe, being the turbulent ones a repetitive lack in literature as researchers tend to impose a turbulent intensity value.

Regarding the simulations of the rotating pipe, the best performance was found with the Reynolds Stress turbulence Model, as eddy viscosity models tended to simulate the azimuthal velocity profile as solid rigid body rotation. This is because of this turbulence model takes into account the anisotropy in the generation of turbulence (directional effects of the Reynolds stress fields). Some RSM configurations did not properly mimic the experimental results and some were particularly problematic to solve the boundary layer. The best performance took place with Linear Pressure Strain and Enhanced Wall Function. This simulation was addressed as *Simulation 1* throughout the document.

Regarding the imposition of models as inlet conditions for *Simulation 2* (use of the swirling flow as impinging jet), four models have been found for the fully-developed state of the swirling flow confined in the rotating pipe (dimensionless profiles v_z/U , v_t/U_r , k/U^2 and β). These models mimic very accurately the computational and experimental results from bibliography.

For the simulations of the impingement, the Transition SST $k - \omega$ with the Production Kato-Launder option was the best one. This was not surprising since there are previous papers suggesting the good performance of this turbulent models in impingements. The Production Kato-Launder modification is very useful for this kind of problems since the regular $k - \omega$ and $k - \epsilon$ models tends to generate excessive turbulent energy in stagnation point overproducing turbulent viscosity. In this simulation, it has been also demonstrated that for small H/D distances, the secondary peak in Nusselt number is in fact product of laminar to turbulent transition, as a sudden increase in the turbulent intensity reveals. During these simulations it was also tested how the upper boundary condition of the domain affects the heat transfer, arriving to the conclusion that is not an influential factor.

A comparison between the use of former *Simulation 1* and the investigated models was done showing that the models are an interesting application. These models are undeniable useful for further studies requiring several evaluations of the CFD problem such as uncertainty quantification, sensitivity analysis or CFD optimisation, as *Simulation 1* is not required any more.

It has also been demonstrated that the use of this mechanism for swirling generation has several advantages with respect to other methods from literature, with the remarkable goodness of the possibility of increasing the swirl whilst keeping the Reynolds number fixed. This is particularly beneficial for close nozzle-to-plate distances, since increasing the swirl by increasing the rotation of the pipe, the heat transfer is also increased. Other methods in literature require an increase of Reynolds number, what might be impossible under some circumstances and/or increase the angle of blades/spirals of ducts, which is constrained to a maximum angle and manufacturing costs. On the other hand, the bigger disadvantages of the rotating pipe are that the pipe must be very long ($55 - 60D$) to achieve the fully-developed state, and not all the experimental rigs may allow such a long pipe. Also, a motor must be purchased, but this should be cheaper than designing and manufacturing the other existing devices in literature.

Despite in this chapter the CFD problem has been modelled and discussed, there is an important missing part: the addition of experimental uncertainty to CFD simulations. And this is an important regular lack in computational literature. To improve this is the objective in the next chapter, which completes the earlier computational runs by a dedicated stochastic approach to measure the impact of uncertainties in the performance of both *Simulation 1* and *Simulation 2*, as well as when the mathematical models are used to avoid the first simulation.

Chapter 4

A Swirling Flow Generated by a Rotating Pipe for Heat Transfer by Impingement Under Uncertainty. Part II: Uncertainty Quantification

The investigation in this chapter can be considered an extension of the work in Chapter 3, where the reader is redirected for the state-of-the-art literature review. In this part, the modelling under uncertainty is the core topic, with application to the CFD simulations and the impact with mathematical models. The structure is as follows.

In Section 4.2, the uncertainty quantification process is described, in order to better understand Stochastic Collocation Method and the usage of sparse grids. The decision on which UQ method can be chosen is also explained. In Section 4.3, the coupling between *Simulation 1* and *Simulation 2* and the found models was explained, for a further comparison between the resulting uncertainties with and without implementing the models for the profiles in Section 4.4 in this chapter. In this section, different probabilistic distributions for the inputs are also tested. Finally, in Section 4.5, the relevant conclusions of this piece of work are given. In Appendix A, expressions for the coefficient of the models are given, and in Appendix B a piece of code is available for implementation as User Defined Function in FLUENT, in order to facilitate the use of the models and reproducible research.

4.1 Introduction and Motivation for Uncertainty Quantification

In experimental work, uncertainty and error measurements are often given but, when performing CFD simulations, this is not a common practice. If one needs to provide reliable results, this should be a must to offer the most complete overview.

Generally speaking, in CFD simulations, boundary conditions and geometries are imposed, ignoring any fluctuation or inaccurate description that can be noted in real performance scenarios. This therefore rise the need of carrying out these tasks under stochastic analysis instead of a deterministic approach. For this reason, uncertain inputs are mathematically modelled by probabilistic distributions from experiments. This is often unavailable and modellers themselves tend to provide the assessment of input uncertainties by means of intervals as well as the study of this propagation, based on expertise.

The introduction of experimental uncertainties for a probabilistic approach to the computations let us know also how robust an experimental design can be prior the construction. In the present case scenario, there is a rotating pipe available at the University of Málaga, that may be used for heat transfer by impingement with swirl. **Prior the construction of the test rig, it is possible to develop computational simulations to see whether such rotating pipe is robust enough** or not, being necessary a better calibration or new devices. This is a reason why currently the **computational approaches under uncertainty are gaining popularity**, as discussed in Section 1.1 in Chapter 1.

4.1.1 Methodology and Challenges

In Uncertainty Quantification (UQ) the aim is to determine how likely the outputs of a model are when the inputs are not precisely defined. Once the input uncertainties are modelled under a probabilistic approach, it is necessary to find an appropriate UQ method.

The **uncertain inputs** in this study are the **volume flow-rate**, Q , and the **angular velocity**, Ω . Initially, it was intended to deal with both the Reynolds number, Re , and Swirl Intensity, S , as uncertain, but this would complicate the problem as these two parameters share Q in their formulas, being necessary to take into account the correlation between Re and S . Both the volume-flow rate and the angular velocity of the pipe are independent uncertain inputs. Uncertainties in these parameters of the pipe are translated into propagated uncertainties in both the exit of the pipe and heat transfer, which is quantified by the Nusselt number, Nu . Despite the fact that only two variables may seem a small size problem, in uncertainty analysis in CFD it is a common stochastic space dimension and the problem is computationally expensive already (a single two-steps CFD run takes around half a week, depending on the mesh size).

4.1 Introduction and Motivation for Uncertainty Quantification

In this work, the impinging swirling jet is created by a rotating pipe with the fully-developed flow at the exit and under the conditions discussed in Chapter 3. To remind the highlights, the inlet is a uniform flow with Reynolds number $Re = \frac{4\rho Q}{\pi D\mu} = 23000$, whilst the outflow is turbulent at the exit. The Swirl number is set to $S = \frac{\pi D^3 \Omega}{8Q} = 1$ with Q the volume-flow rate and Ω the angular velocity of the pipe. The simulations are developed as 2D steady Reynolds-Averaged Navier-Stokes (RANS) equations with a SST $k - \omega$ turbulence model.

In order to choose the most efficient method, one has to take into account the **knowledge about the random inputs** (can I construct the probabilistic distributions? are they uniform/normal/etc.?), **computational budget/computational cost** (how many simulations can I afford? how long does a deterministic run take?), **intrusiveness** (is it worthy to code inside the solver?), **desired accuracy** (is precision a crucial thing for my approach? can I use approximations?), and the **desired outputs** (is the mean and variance enough? sensitivity analysis? probabilistic distributions?).

Explaining in a nutshell the content in Chapter 2, the probabilistic methods can be either intrusive or non-intrusive. In this chapter, a non-intrusive approach is chosen since does not require to code inside the solver and can deal with any model as a black-box (FLUENT software in this case). On that basis, Monte-Carlo simulations [152] are the most popular approach in literature because of the easy implementation [168, 216, 59, 68]. This non-intrusive method is based on a random sampling on the input uncertainties in order to obtain enough outputs to build the desired probabilities. As the convergence of the method is slow, being of order $O(1/\sqrt{N_s})$, with N_s the number of samples, in order to reduce the number of model evaluations and increase the efficiency, some other sampling methods are available in literature such as Latin Hypercube [93] or quasi-random Halton [64] and Sobol sequences [29] amongst others. These sampling techniques optimise the Design of Experiment by taking also into account previous positions of the samples in the stochastic space, and the error can be essentially considered as a $O(1/N_s)$. It is important to point out that this efficiency is only really noticed for moderate dimensions of the stochastic space, as for high dimensional problems they behave similarly to Monte-Carlo (which is dimension independent).

Sampling based methods are then a reliable choice for UQ. However, they normally require many model evaluations. This is an enormous disadvantage in CFD, as each model evaluation takes too long, being often unaffordable. **To overcome this drawback, Stochastic Collocation Method (SCM) [149] is implemented** in this work. This method allows to calculate the statistical moments of the output by **quadrature rules with specific collocation schemes that require few CFD model evaluations**, outperforming sampling methods especially by choosing sparse grids for low dimensions in the stochastic space. When the dimension is high, the cost leads to the so-called Curse of Dimensionality, as the number of collocation points to evaluate increases exponentially, and it is preferable to keep

4.1 Introduction and Motivation for Uncertainty Quantification

a sampling-based approach.

As remarked above, an efficient way to mitigate the needs of using many collocation points is the usage of **sparse grids** [218], for which the accuracy (that is to say the number of collocation points) can be increased with great control until achieving convergence.

The use of SCM is not a brand new thing. Actually the non-intrusive method has been successfully applied in many problems such as elliptic partial differential equations with random input data [16], supersonic aircraft jets [84] or cardiovascular research [208]. However, there is no application to problems like the one presented in Chapter 3, and its **application in a two-step approach** is very interesting, since the output of *Simulation 1* becomes the input of *Simulation 2*, being uncertainty propagated. The choice of SCM obliges to discard other methods such as generalised Polynomial Chaos (gPC) or Kriging surrogates (KG). SCM is simpler than gPC, because the mean and variance can be computed simply by Eq. (4.2), and there are no expansion terms in the formulation to be computed, so the accuracy can be controlled just by the number of collocation points. The gPC would be recommended in test cases that sensitivity analysis is important too, but in this application is not necessary as by simple parameter exploration, one can see that Q is more influential than Ω . SCM is also preferred than KG because it is more accurate and surrogates can be also built by Eq. (2.6).

When using SCM, as discussed for KG, the exact response can be approximated and sampling techniques can be applied on it, recovering more statistical information such as probabilistic distributions of the outputs. For this reason, **two types of input probabilistic distributions were tested** for the random inputs: uniform and normal. As experimental uncertainty data is not available to build the approximate probabilistic functions, at least to try two different distributions based on expertise provide more information about the impact of uncertainty on the CFD simulation. The random variables are sampled to evaluate the SCM surfaces by means of LHS, as it was discussed in this section that it converges faster than brute-force Monte-Carlo. For more details about the choice of the methods, one can see Section 2.3 in Chapter 2.

A very important issue in UQ in CFD, and also in optimisation, is the computational cost of the deterministic runs. Since the swirling flow generation in *Simulation 1* is decoupled from *Simulation 2*, it would be very useful to find a way to quickly generate the flow profiles input in *Simulation 2*. That is the purpose in Sections 4.3 and 4.4.3, where the **mathematical models** introduced in Chapter 3 are used to avoid CFD *Simulation 1*, in order **to speed up the uncertainty analysis process**. The UQ results obtained by the application of the models will be compared with the direct CFD simulation ones.

4.2 Uncertainty Quantification

4.2.1 Stochastic Collocation Method and Sources of Uncertainty

The method here implemented for UQ is the Non-Intrusive Stochastic Collocation Method (SCM) developed by Mathelin and Hussaini [149] at NASA. SCM represents a very efficient option for lower dimension problems in comparison with sampling techniques such as Monte-Carlo. By means of this method, the aim is to compute the integral of the i -th statistical moment approximated as

$$\mu(\mathbf{x}, \hat{\alpha})_i^{\text{SC}} = \sum_{j=1}^{N_q} y_j(\mathbf{x})^i \int_{\Gamma} l_j(\hat{\alpha}) f_{\xi}(\hat{\alpha}) J(\hat{\alpha}) d\hat{\alpha}, \quad (4.1)$$

where $J(\hat{\alpha})$ is the Jacobian of the differential transformation, $\hat{\alpha}$ the alpha-space, $y_j(\mathbf{x})$ the deterministic CFD solutions from $y(\mathbf{x}, \xi_j)$ now transformed into $y(\mathbf{x}, \hat{\alpha}_j)$, N_q the number of collocation points and l_j the Lagrange interpolation polynomials. The integral in Eq. (4.1) can be numerically computed by quadrature:

$$\mu(\mathbf{x}, \hat{\alpha})_i^{\text{SC}} \simeq \sum_{j=1}^{N_q} y_j(\mathbf{x})^i \sum_{k=1}^{N_q} l_j(\hat{\alpha}_k) f_{\xi}(\hat{\alpha}_k) J(\hat{\alpha}_k) z_k, \quad (4.2)$$

with z_k and $\hat{\alpha}_k$ the quadrature weights and points respectively. Both the quadrature and collocation points can be chosen to coincide. Moreover, Lagrange interpolating polynomials are defined in the transformed space with the property of $l_i(\hat{\alpha}_j) = \delta_{ij}$ for $i, j = [1, 2, \dots, N_q]$, which states that at collocation points the values of y and \hat{y} coincides.

The choice of collocation points is an important matter. If tensor grids are chosen, the computational cost would be very high, especially when N_{ξ} is not low. A very efficient alternative is the use of sparse grids. In this analysis, the collocation points of the sparse grids have been determined according to the Clenshaw-Curtis (C-C) quadrature nested rule [238] and Smolyak construction [219]. With sparse grids, several levels of accuracy were tried in the problem, in order to test the convergence as it will be shown in the following chapters. For further information on these methods, the reader is kindly suggested to have a look at Chapter 2.

Regarding the sources of uncertainty, these have been based on a mix of literature review, conversation with experimentalists with conservative insights and the mechanical characteristics of a similar rotating pipe facility at University of Málaga. Depending on the facility and method used to measure, one may have different uncertainties in the experiments, but the idea of this research is to understand the propagation of uncertainties in the computational

4.3 Coupling the Two-Step CFD Simulations For UQ purposes

problem that mimic the physics of the flow in order to improve the deterministic simulations. This is an important thing when engineers need to provide reliable results of their computations, based on realistic uncertainties from literature in the case when uncertainties from experiments are not available. For that aim, have been taken under consideration papers as [43], where a 2.5% of variance in uniform distribution in the swirl number and inlet velocity was applied, that is a 2.5% of variance for Q ; [27], where a $\pm 3\%$ of variation as uniform inlet velocity was applied; or [17], where a maximum of a $\pm 1\%$ error for the velocity has been found for the described measurement techniques. For this reason, a conservative value of uncertainty for Q has been chosen as a 5% of variance. In addition, in the Fluid Mechanics laboratory at University of Málaga, the error of the available rotating pipe was analysed by engineers and it was found a 0.5% of variance as uncertainty for the angular velocity.

In the present problem, the Reynolds number under study is $Re = 23000$, as studied in [130], and the Swirl number is $S = 1$. For this situation, where the inflow is a uniform flow, the deterministic mean values of our two uncertain parameters are denoted by \bar{Q} and $\bar{\Omega}$. Within that framework, and trying to be conservative with respect to the literature results as explained in the paragraph above, the source of uncertainties have been determined as the uniform distributions $Q \sim Unif(0.95\bar{Q}, 1.05\bar{Q})$ and $\Omega \sim Unif(0.995\bar{\Omega}, 1.005\bar{\Omega})$. The motivation of modelling the inputs by this type of distribution is conservativeness. The same probability is assigned to every possible value in the ranges of the variables, so it is ensured that the worst performance scenario is analysed. This is a frequent approach when enough information about the probabilistic distribution is not given.

The turbulent intensity has been discarded from the uncertainty analysis as the flow confined in the pipe is fully-developed and the uncertainties in the turbulent intensity will not vary the results of the output parameters under study.

A good point of dealing with Q as stochastic input is that several uncertainties such those related to measurement tools tolerance, pipe diameter, loss of pressure or density variations can be accounted in only one parameter. That is why being conservative is a good viewpoint. If one wants to study each parameter separately, the dimension of the stochastic space would be unnecessarily increased and correlated sampling techniques must be used, and there is no correlation amongst the chosen random variables. That is, both the cost and difficulty would increase.

4.3 Coupling the Two-Step CFD Simulations For UQ purposes

The problem under analysis is the CFD simulation of an impinging swirling flow for heat transfer, generated by a rotating pipe as nozzle. A detailed description of the simulations and how to proceed can be found in Chapter 3 and it is not going to be taken into detailed

4.3 Coupling the Two-Step CFD Simulations For UQ purposes

consideration in this chapter. However, a sketch of this set up is shown in Fig. 4.1.

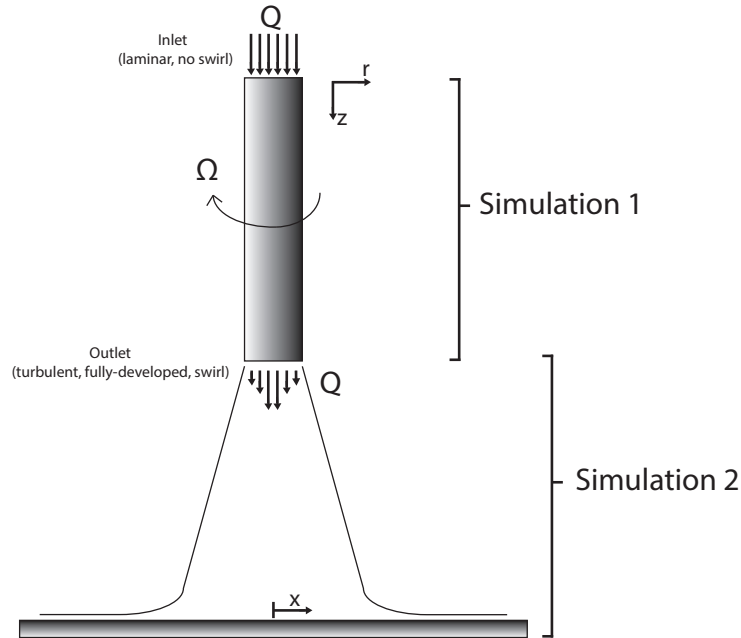


Figure 4.1 Sketch of *Simulation 1* & *2*. Note that the x and r axis are the same in practice and with origin in the axisymmetry axis, but for the sake of avoiding confusion in the following plots and data tables, r is used in *Simulation 1* and x for *Simulation 2*.

It is also important to point out prior to any uncertainty quantification that, as the turbulence model used for the pipe and the one used for the impinging heat transfer problem are both different, a propagation of uncertainty is taking place from one simulation to another. The two-step CFD simulations were coupled in the following way: firstly, the CFD simulations of the swirling flow confined in a rotating pipe with the RSM turbulent model were developed (*Simulation 1*), and secondly, both the velocity and some turbulent dimensionless profiles at the exit of the pipe are used as inlet boundary conditions for the heat transfer simulation (*Simulation 2*). This was explained already in Section 3.3, and the coupling of the turbulent models is taking place in the same way. Again, to couple the two simulations for the modelling, two options have been tested for the *Simulation 2* as shown in Fig. 3.14.

To develop UQ, the four dimensionless models given by Eqs (3.4)-(3.7) are used for the purpose. These models can be defined as *metamodels*. They conduct a cheap way to evaluate costly computations or experiments in some fields as, e. g., CFD optimisation, prototyping or UQ, as it can be sampled with no cost.

4.3 Coupling the Two-Step CFD Simulations For UQ purposes

A detailed description of the models has been given in Section 3.4, but the application to a more general case scenario (varying also the input conditions and then, the fitting coefficients) was not studied. For this reason, in this section is now shown the behaviour of the proposed models within the uncertainty space domain.

In Fig. 4.2, 4.3 and 4.4 the goodness of the models is revealed through the good fitting when Q and Ω are varied in the prescribed intervals. The model with greater uncertainty in the prediction is k/U^2 and for greater values of Ω (see Fig. 4.5) has been noted that its modelling is performing slightly worse than the others, thus future works can be linked to improve it. The model for v_t/U_r has some notable uncertainty in the prediction as well, but we decided to keep it as simple as possible.

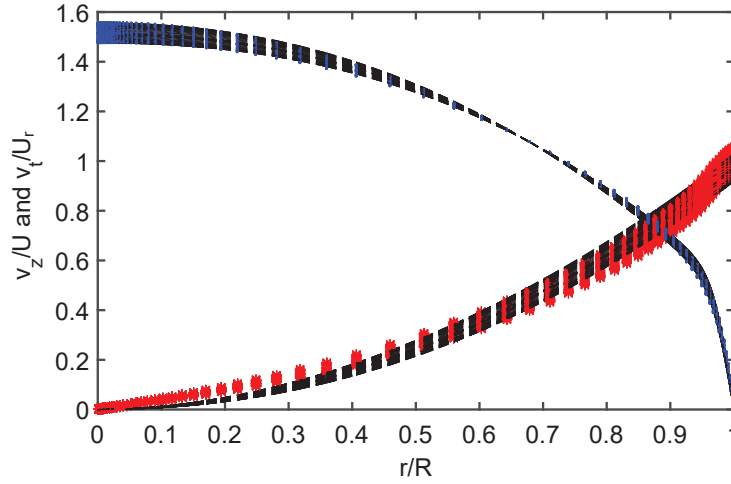


Figure 4.2 (•) Axial velocity profile from CFD. (*) Azimutal velocity profile from CFD. (-) Mathematical models for the Clenshaw-Curtis sparse grid with level 2 of accuracy. Each plot corresponds to a deterministic run and its fit.

One can notice that the models in Eqs. (3.4)-(3.7) do not directly depend on Q and Ω . To overcome this problem, new simple fitting models based on polynomial regression can be built. By means of these new models, now the original models for the profiles can be linked to the input uncertain variables and can be rewritten as

$$(v_z/U \ v_t/U_r \ k/U^2 \ \beta)^t = \mathbf{F}(\gamma_i) = \mathbf{G}(Q, \Omega). \quad (4.3)$$

These polynomial fits are shown in Appendix B, with the correspondent equations, fitting goodness and plots. In addition to this, it is recalled that in Appendix A the UDF for its implementation is given, in order to facilitate the task of using these models in future works

4.3 Coupling the Two-Step CFD Simulations For UQ purposes

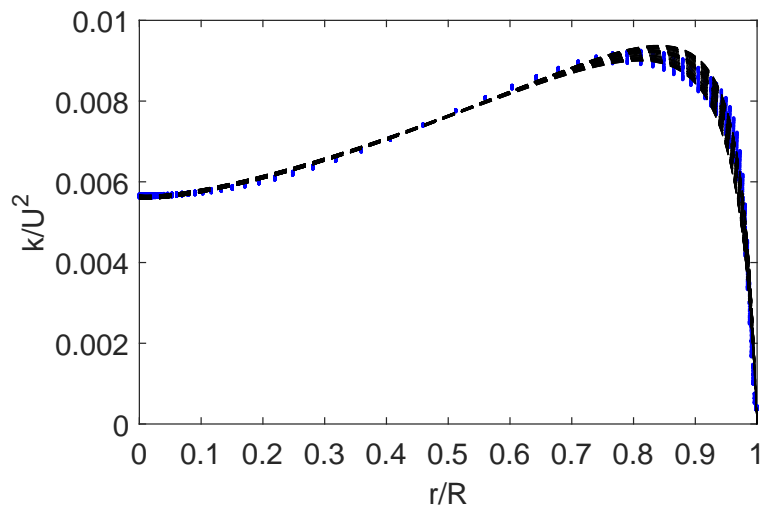


Figure 4.3 (●) Turbulent kinetic energy profile from CFD. (- -) Mathematical models for the Clenshaw-Curtis sparse grid with level 2 of accuracy. Each plot corresponds to a deterministic run and its fit.

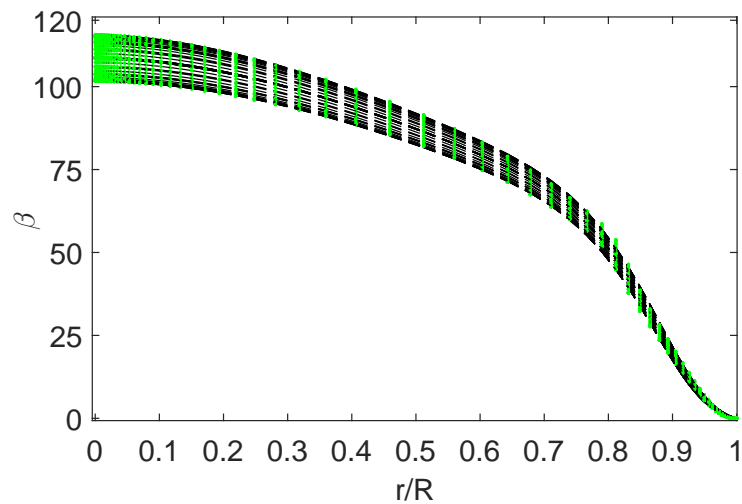


Figure 4.4 (●) Turbulent kinetic energy profile from CFD. (- -) Mathematical models for the Clenshaw-Curtis sparse grid with level 2 of accuracy. Each plot corresponds to a deterministic run and its fit.

for other researchers.

Despite a very accurate model to fit the profiles could be found by numerical interpolation, a new model should be built for each CFD simulation profile losing any possible

4.4 Uncertainty Quantification Results of the Two-Step CFD Simulation

generality. In other words, those original models could not be used for non-simulated cases of *Simulation 1*, as we would not have data to feed the predictor. On the other hand, the introduced models in this work can be implemented to obtain quick dimensionless profiles in tasks like increasing the accuracy of surrogates models, as it has been done in [85], where it has been also demonstrated the validity of the models for larger intervals than the ones in UQ (see Fig. 4.5). The domain of Eqs. (3.4)-(3.7) for the uncertainty analysis is constrained by $Q \in [0.95\bar{Q}, 1.05\bar{Q}]$ and $\Omega \in [0.995\bar{\Omega}, 1.005\bar{\Omega}]$, which is set by prescribed uniform input uncertainties and it is not guaranteed the good performance for greater domains, except for S varied from 0 up to 1.5 as demonstrated in Fig 4.5. As mentioned in Chapter 3, one of the advantages in the use of a rotating pipe to generate swirl is that by increasing the angular velocity one can obtain a wide range of values of S to test the models.

4.4 Uncertainty Quantification Results of the Two-Step CFD Simulation

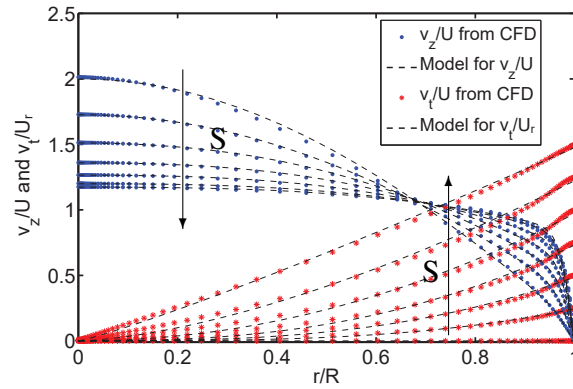
As for uncertainty analysis purposes several simulations are required, they were run at the computational clusters at University of Málaga, with the support and collaboration of Dr Joaquín Ortega-Casanova.

4.4.1 Simulation 1. Uncertainty Quantification on the Fully-developed Turbulent Swirling Flow Generated by the Rotation of a Pipe

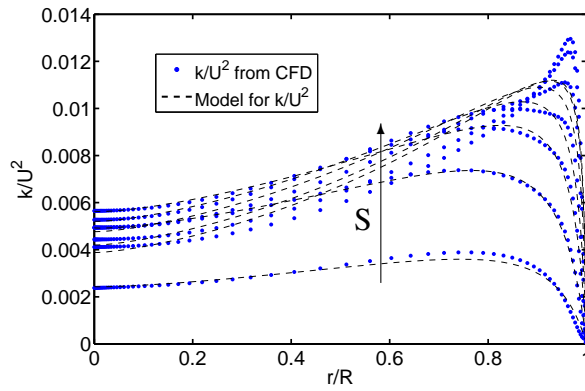
Simulation 1 comprises only the flow confined in the rotating pipe not simulating the impinging jet, as explained in Section 3.3. Further information in relation to the CFD simulations can be seen in Chapter 3 but, in order to provide a brief description in this work as well, it can be remarked that the computational grid is $[n_r \times n_z] = 68 \times 450$ cells, having a dimensionless wall distance of $y^+ < 1$ along the walls of the pipe.

Regarding the uncertainty quantification process, in Section 4.2 the Stochastic Collocation method's results from analysing *Simulation 1* are shown in Table 4.1 & 4.2. It can be observed that since using few points for the C-C Sparse Grid, the results are not changing that much. This is a common conclusion in uncertainty analysis when input uncertainties are based on experimental error, where, under good practice, they use to be very small and hence the interval under analysis has an almost linear behaviour. This makes unnecessary in practice to try many collocation points (or accuracy levels) from SG, but as the initial computational budget for the Design of Experiment (DoE) was established in 65 points (that is, 65 CFD simulations running for around a week and a half), it has been kept in this piece of work. The reason behind the 65 points is that a more remarkable non-linear behaviour

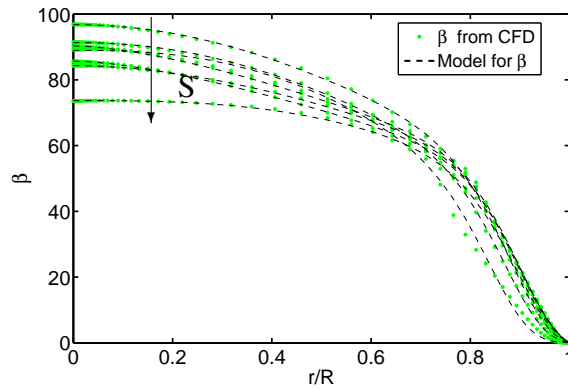
4.4 Uncertainty Quantification Results of the Two-Step CFD Simulation



(a)



(b)



(c)

Figure 4.5 Dimensionless profiles from CFD and their models for (a) axial and azimuthal velocity, (b) turbulent kinetic energy and (c) turbulent viscosity ratio, for optimisation purposes in [85], where S was varied from 0 up to 1.5.

was erroneously expected, dedicating a more ambitious DoE.

4.4 Uncertainty Quantification Results of the Two-Step CFD Simulation

Table 4.1 Stochastic means of the friction factor (λ), turbulent intensity (I), dimensionless axial (v_z/U) and azimuthal (v_t/U) velocity at $r/R = 0.5$, at the exit of the rotating pipe.

Level	Points	$\lambda_{r/R=1}$	$I(\%)_{r/R=0.5}$	$(v_z/U)_{r/R=0.5}$	$(v_t/U_r)_{r/R=0.5}$
1	5	0.01373401	8.45783368	1.28350388	0.26677295
2	13	0.01373399	8.45774137	1.28350593	0.26676999
3	29	0.01373404	8.45773429	1.28350567	0.26676957
4	65	0.01373401	8.45773957	1.28350436	0.26676961

Table 4.2 Stochastic variances of the friction factor (λ), turbulent intensity (I), dimensionless axial (v_z/U) and azimuthal (v_t/U) velocity at $r/R = 0.5$, at the exit of the rotating pipe.

Level	Points	$\lambda_{r/R=1}$	$I(\%)_{r/R=0.5}$	$(v_z/U)_{r/R=0.5}$	$(v_t/U_r)_{r/R=0.5}$
1	5	0.22152010E-06	0.72630289E-03	0.75705236E-04	0.22938667E-03
2	13	0.22059469E-06	0.72520829E-03	0.75256672E-04	0.22639809E-03
3	29	0.22066632E-06	0.72553382E-03	0.75245877E-04	0.22636540E-03
4	65	0.22067550E-06	0.72554659E-03	0.75261365E-04	0.22636600E-03

The most important outputs from *Simulation 1* are the dimensionless velocity and turbulent profiles at the exit of the pipe, as the pipe will become the nozzle for the impinging problem and these profiles will be used as inlet boundary conditions. For sake of convenience, a quantification of their uncertainties has been also done along the profile as can be seen in Fig. 4.6 and 4.7, where the mean and standard deviation envelopes of those profiles are shown.

4.4.2 Simulation 2. Uncertainty Quantification on the Impinging Swirling Jet for Heat Transfer: Boundary Conditions Imposed from Simulation 1.

In *Simulation 2*, a heat transfer process took place on a heated flat plate due to a jet impacting on it. For uncertainty quantification purposes, the so-called Stochastic Collocation method with Clenshaw-Curtis nested rule with sparse grid quadrature points is developed again, in order to be consistent with the deterministic simulations from the rotating pipe with relation to the Q and Ω uncertain parameters. For the deterministic simulations of the impinging jet domain, the correspondent velocity and turbulent profiles at the exit of the rotating pipe are used as inflow conditions. The CFD simulations have been conducted as axisymmetric 2D RANS in FLUENT.

4.4 Uncertainty Quantification Results of the Two-Step CFD Simulation

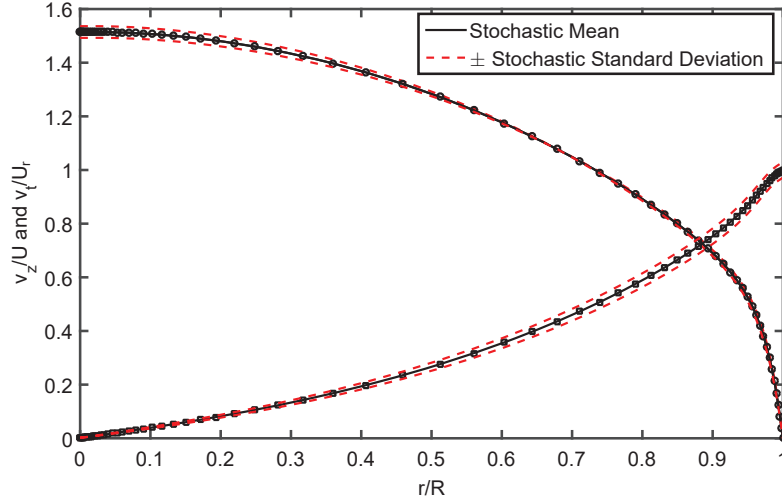


Figure 4.6 Radial distribution of the axial (\circ) and azimuthal (\square) dimensionless velocity profiles at the exit of the pipe for the level 4 of the C-C Sparse Grid.

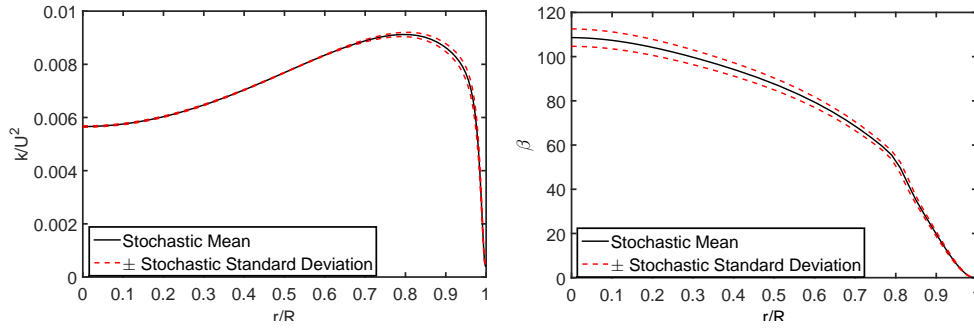


Figure 4.7 Radial distribution of the Turbulent Kinetic Energy, k , and the Turbulent Viscosity Ratio, β , at the exit of the pipe for the level 4 of the C-C Sparse Grid.

In Fig. 4.8, the detail of the mesh as well as the boundary conditions are depicted. The computational mesh for the Finite Volume code is $[n_x \times n_h] = 140 \times 250$ cells, ensuring an $y^+ < 1$ all along the plate. The dimensionless distance is $H/D = 5$ and the length of the wall boundary condition with rotation (rotating pipe) is D , in order to facilitate adaptation of the inlet flow from *Simulation 1*. In practice, the x axis is the same as the r one when the pipe was under study, but it is preferred to use different notation in order to avoid confusion between the parameters at the exit of the pipe and on the flat plate. Regarding the turbulence model, the SST $k - \omega$ has been chosen and validation has been carried out against experimental data of impinging jets in as in [177]. For further information about the computational features of the simulation, including the discretization error and the selection of the SST $k - \omega$ turbulence model, the authors suggest to see Chapter 3 and [177].

4.4 Uncertainty Quantification Results of the Two-Step CFD Simulation

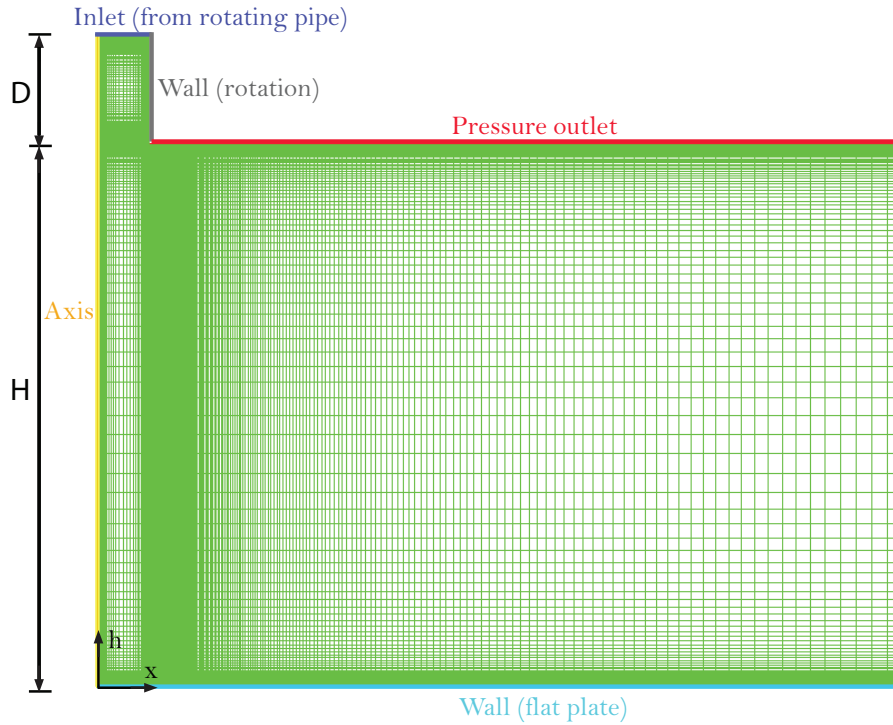


Figure 4.8 Computational grid for *Simulation 2* and boundary conditions imposed. Note that D is the diameter of the pipe but D is also the length of the wall pipe in the computational domain.

With this built-in framework, uncertainties are propagated from the pipe inputs until the development of the boundary layer on the flat plate responsible of the heat transfer quantified through the Nusselt number at the stagnation region and its averaged value on the plate, computed as

$$Nu_{avg} = \frac{1}{\pi R_{int}^2} \int_0^{R_{int}} Nu(x') 2\pi x' dx', \quad (4.4)$$

where R_{int} stands for the radius for integration of the Nusselt number on the plate and its value is set to $7.5D$. The mean and variance results for the SCM are presented in Tables 4.3 & 4.4. The evolution of the Nusselt number along the plate is shown in Fig. 4.9, where it is represented with its standard deviation as uncertainty measurement. It can be observed that the most sensitive part to the input uncertainties is the stagnation area, and for x/D values far from the stagnation, the input uncertainties are irrelevant.

As it happened when performing UQ on *Simulation 1*, it can be noted that since using few points for the C-C Sparse Grid, the results are practically converged. This is again due to the fact that input uncertainties are extracted from experimental error, that is very small and hence the interval under analysis has an almost linear behaviour, especially for the Nusselt

4.4 Uncertainty Quantification Results of the Two-Step CFD Simulation

average. This is something that not always happens, since small errors could lead to great changes in some case scenarios. Regarding the convergence, as the Nusselt average is an integrated quantity, it is normal to suffer light variations that are not really representing any oscillation in the convergence of the UQ technique but only small precision errors.

Table 4.3 Stochastic means of the Nusselt number at the stagnation point and its average value along the flat plate.

Level	Points	Nu_0	Nu_{avg}
1	5	187.8183333	51.45473951
2	13	187.7914166	51.45413825
3	29	187.8031984	51.45457487
4	65	187.7993255	51.45497083

Table 4.4 Stochastic variance of the Nusselt number at the stagnation point and its average value along the flat plate.

Level	Points	Nu_0	Nu_{avg}
1	5	15.24348189	1.50945541
2	13	15.56881637	1.50878302
3	29	15.47284719	1.50909036
4	65	15.47621431	1.50822473

In order to give a wider insight of the propagation of uncertainties, it is recommended to plot the Probabilistic Distribution Functions (PDF) of the outputs. One reason is that, if we focus only in the variance and the mean, two PDFs can be different but share the same mean and different variance, leading to wrong conclusions. This can be seen, e.g., in multimodal distributions. To obtain such information, Latin Hypercube Sampling (LHS), as can be seen in Fig. 4.10, has been applied on the construction from Eq. (2.6). With this technique, several number of samples have been tried up to achieve convergence ($N_s = 50, 100, 500, 1000, 2000$). The PDFs for the Nusselt average and at stagnation point are plotted in Fig. 4.11. The output PDFs accurately fit a $Nu_0 \sim Unif(180, 195)$ and $Nu_{avg} \sim Unif(49, 53.7)$ distribution. The reasons of having a uniform distribution for the output variables might be that we only have two uncertain parameters, small input uncertainties leading to linearity and uniform distributions for them. However, in order to gain more knowledge on the propagation of uncertainties and certify our guesses regarding the linearity, the input uncertain parameters have been also modelled as normal distributions to check their impact in the probabilistic

4.4 Uncertainty Quantification Results of the Two-Step CFD Simulation

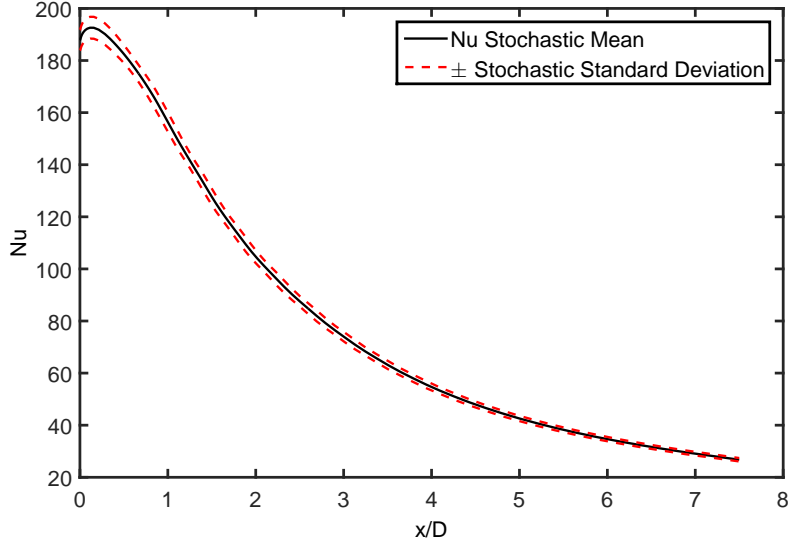


Figure 4.9 Evolution of the stochastic mean of the Nusselt number along the plate \pm its stochastic standard deviation for level 4 of the C-C sparse grid.

functions of the output. For such constructions, the definition of the input has been chosen as

$$Q = \bar{Q} + \sigma_Q \theta, \quad (4.5)$$

$$\Omega = \bar{\Omega} + \sigma_\Omega \theta, \quad (4.6)$$

with

$$\theta \sim N(0, 1), \quad (4.7)$$

$$\sigma_Q = CoV_Q \bar{Q}, \quad (4.8)$$

$$\sigma_\Omega = CoV_\Omega \bar{\Omega}, \quad (4.9)$$

where N refers to normal distribution, CoV the coefficient of variation (2.5% for Q and 0.25% for Ω), θ the chosen probabilistic distribution and σ_Q and σ_Ω the standard deviation of the variables. These values have been chosen as half of the variations used in the definitions of the uniform probabilistic distributions as otherwise many values in the sampling would be out of the domain on which the surrogate is defined (that is in fact the domain defined by the former uniform distributions). Even in such scenario some values, mostly at the tail of the normal distributions, are still out of the range. For such reason, the sampling has been done only in the region enclosed in the domain $Q \in [0.95\bar{Q}, 1.05\bar{Q}]$ and $\Omega \in [0.995\bar{\Omega}, 1.005\bar{\Omega}]$, as can be seen in Fig. 4.12. The values of N_s where chosen as $N_s = 100, 500, 1000, 2000, 4000$, but subtracting the points outside the ranges (in the tails), the sampling up to convergence became $N_s = 90, 453, 915, 1828, 4556$.

4.4 Uncertainty Quantification Results of the Two-Step CFD Simulation

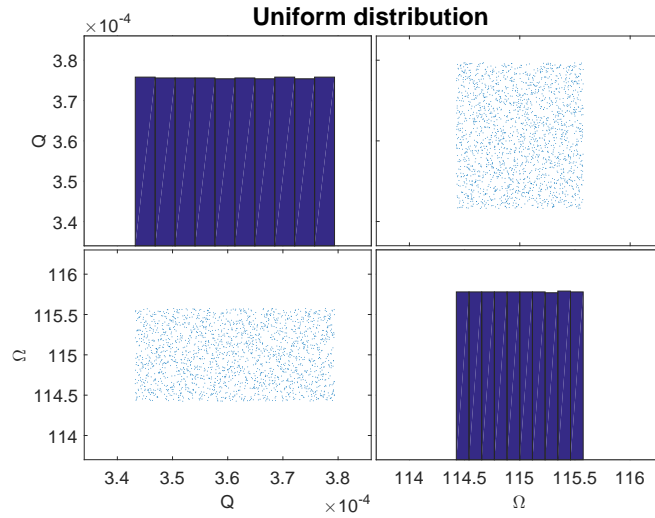


Figure 4.10 Sampling with $N_s = 2000$ samples.

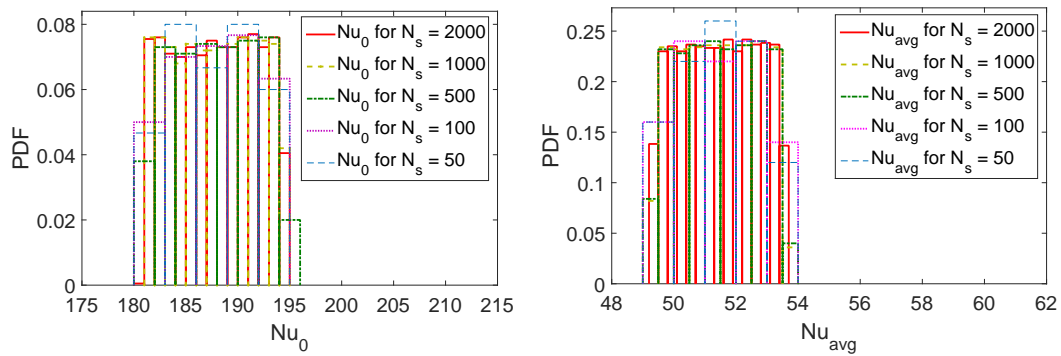


Figure 4.11 PDFs for Nu_0 (left) and Nu_{avg} (right). The greater the N_s , the better the uniformity in the PDF. However, as the problem under study has a notable linearity, since a low number of samples the shape of the PDF is not changing anymore.

The distributions of the output variables are plotted in Fig. 4.13 for different number of samples in order to achieve convergence in LHS method. The output variables are now, approximately, following the distributions $Nu_0 \sim N(187.841, 8.9155)$ and $Nu_{avg} \sim N(51.4658, 0.863819)$. One can see in Table 4.5 and 4.6 a comparison on using uniform and gaussian input uncertainties and it can be noticed in Table 4.6 that variances are almost the half than for the uniform case. As half of the coefficient of variance used for the uniforms was used for the gaussian ones, this is suggesting us that, due to the linearity, the features are preserved.

4.4 Uncertainty Quantification Results of the Two-Step CFD Simulation

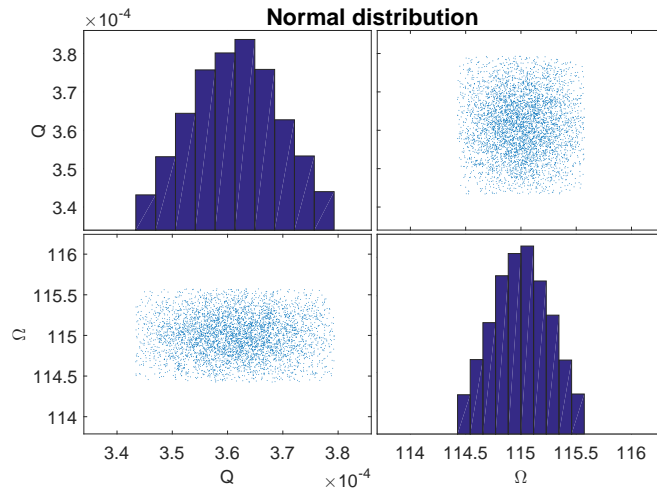


Figure 4.12 Sampling with $N_s = 4556$ samples.

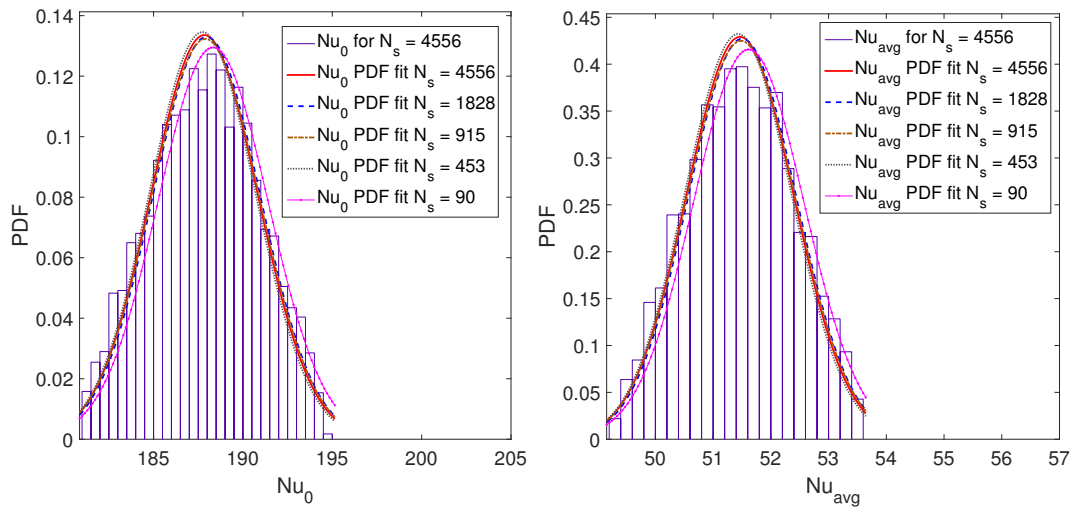


Figure 4.13 PDFs for Nu_0 (left) and Nu_{avg} (right) when sampling the normal probabilistic distributions.

Table 4.5 Stochastic means of the Nusselt number at the stagnation point and its average value along the flat plate for the two different input uncertainties tested on the construction of the surrogate.

Input uncertainties	Nu_0	Nu_{avg}
Uniform	187.7993255	51.4549708
Gaussian	187.8407596	51.4657798

4.4 Uncertainty Quantification Results of the Two-Step CFD Simulation

Table 4.6 Stochastic variance of the Nusselt number at the stagnation point and its average value along the flat plate for the two different input uncertainties tested on the construction of the surrogate.

Input uncertainties	Nu_0	Nu_{avg}
Uniform	15.47621431	1.50822473
Gaussian	8.91549584	0.86381887

4.4.3 Simulation 2. Uncertainty Quantification on the Impinging Swirling Jet for Heat Transfer: Use of Models for Outputs from Simulation 1.

To quantify the propagation of uncertainties when implementing the models given by Eqs. (3.4)-(3.7) in a User-Defined Function code in FLUENT, SCM has been applied again for levels 1 and 2 in the Clenshaw-Curtis sparse grid, in order to compare with the CFD inlet condition case (coupling between *Simulation 1* and *Simulation 2*). Proceeding this way, the results will show not only the propagation of the experimental uncertainties, but also of the modelling errors. The obtained results are shown in Tables 4.7 and 4.8. Notice that negative values in the relative error reveal an increase of the Nusselt number in the modelled case. It can be seen that, despite the models have fitted very accurately with CFD data profiles in the modelling phase, the small fitting errors are propagated through the simulation having a relative error of almost an 8.7% in the Nusselt number at the stagnation point by using the CFD inlet condition case as reference result. This error could seem large, however, if both the results of the simulation of the Nusselt number with the CFD profiles and the models as inlet conditions are plotted (Fig. 4.14), it can be noted that the results are not that different and the 8.7% of variation in the variance is not that relevant. This difference is even smaller than any other taking place in these computational simulations with a slightly coarser but valid mesh, for instance. In CFD validation against experimental data, errors usually are remarkably greater. Other relative errors in the tables can be considered negligible according to the same reference. It has been hence demonstrated that the use of the mathematical models is not introducing a dramatical source of errors as well as reducing the computational budget at the same time. It is therefore recommended its implementation in further works involving swirling flows generated by rotating pipes when initialisation of RANS/LES/DES/DNS simulations, prototyping, optimisation, uncertainty quantification or sensitivity analysis purposes are desired.

4.5 Conclusions

Table 4.7 Stochastic means of the Nusselt number case at the stagnation point and its average value along the flat plate. Relative error (in %) between the CFD and model input results.

Level	Points	Nu_0	Nu_{avg}	$Nu_{0,model}$	$Nu_{avg,model}$	$\epsilon_{r,Nu_0}(\%)$	$\epsilon_{r,Nu_{avg}}(\%)$
1	5	187.81833	51.454739	188.886500	51.245621	-0.5687	0.4064
2	13	187.79141	51.454138	188.859827	51.244494	-0.5689	0.4074

Table 4.8 Stochastic variances of the Nusselt number case at the stagnation point and its average value along the flat plate. Relative error (in %) between the CFD and model input results.

Level	Points	Nu_0	Nu_{avg}	$Nu_{0,model}$	$Nu_{avg,model}$	$\epsilon_{r,Nu_0}(\%)$	$\epsilon_{r,Nu_{avg}}(\%)$
1	5	15.243481	1.509455	16.467074	1.521298	-8.026989	-0.784601
2	13	15.568816	1.508783	16.930460	1.521590	-8.745970	-0.848853

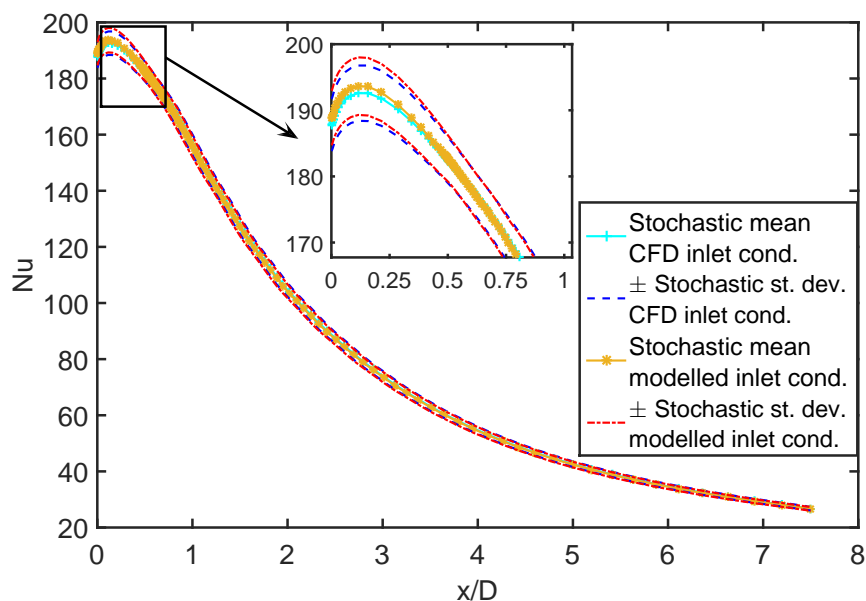


Figure 4.14 Comparison between Nusselts when using the CFD profiles and models for the inlet boundary conditions.

4.5 Conclusions

CFD simulations of a two-step heat transfer process have been carried out for modelling and uncertainty quantification purposes. The outflow from *Simulation 1* (generation of

a fully-developed swirling turbulent flow due to the rotation of a circular pipe) has been mathematically modelled, in order to provide reliable equations without the needs of simulating the physics when requiring new profiles to impose in *Simulation 2* (application of the swirling flow as impinging jet onto a heated flat plate). These models have been also used for uncertainty quantification purposes as they require several runs of the simulations whose computational cost would be reduced.

The key contribution of this chapter is to complete the deterministic CFD simulations in Chapter 3 by a quantification of physical uncertainties. This analysis has been extended not only to the simulations, but also to the application of suggested mathematical models to avoid the so-called *Simulation 1*. This chapter is a very usual lack in computational research in heat transfer and fluid dynamics, since these studies tend to develop just deterministic simulations.

The Stochastic Collocation Method with Clenshaw-Curtis nested rule has been applied for uncertainty quantification to the two-step CFD simulation, reducing the number of collocation points with sparse grids. The main purpose of this study is to improve the deterministic approach presented in Chapter 3. The input uncertainties have been the angular velocity Ω and the volume flow rate Q . An advantage in studying Q as uncertain is that several uncertainties such those related to measurement tools tolerance, pipe diameter, loss of pressure or density variations can be accounted in only one factor. If one wants to study each parameter separately, the dimension of the problem under study would unnecessarily be increased and also correlations would complicate the problem not being a simple Stochastic Collocation approach feasible.

From the UQ study on *Simulation 1*, results have shown that the physical uncertainties in Q and Ω slightly vary the friction factor, λ , and the turbulent intensity, I . In the dimensionless velocity profiles, it was noticed that the most sensitive part of the dimensionless axial velocity profile is $r/R = 0$, and $r/R = 1$ for the azimuthal one. For the dimensionless turbulent kinetic energy, k/U^2 , the most sensitive area is the one located at the beginning of the decay, due to the strong effect of the wall. For the laminar to turbulent viscosity ratio, β , the sensitivity trend is pretty similar to the dimensionless axial velocity one, having around the axis the largest variances. This is the most sensitive profile to the input uncertainties.

The UQ study on the heat transfer process in *Simulation 2* was developed in two different ways: by imposing the dimensionless outflow profiles from *Simulation 1* and by imposing its models by User Defined Functions as inlet boundary conditions.

In both cases it has been observed that the input uncertainties have some impact on the Nusselt number along the plate, but not very remarkable. It was also noticed that Q was the most influential parameter, as Ω had a very light contribution to uncertainty, so this is revealing that in an experimental facility the engineers have to put more effort in reducing the variance in the volume-flow rate by i. e. avoiding pressure loss or mechanical tolerances manufacturing the nozzle. It has been also studied how the output of the problem changes when using two different probabilistic distributions: uniform and gaussian. These results have shown that the probabilistic distribution of the Nusselt number is almost uniform when both input uncertainties are uniform, and gaussian when both input uncertainties are gaussian as well, and this conclusion is product of the linearity existing under the uncertain conditions. In all the uncertainty studies presented in this work can be observed that since using few points for the C-C sparse grid, the statistical moments are not changing dramatically. This is a common conclusion in uncertainty analysis when input uncertainties are based on experimental errors, which under good practice, usually are pretty small and hence the response under analysis has the commented linear-like behaviour. This is often an advantage in problems where other approaches such as sensitivity-based uncertainty are carried out, since exact sensitivities can be calculated from an adjoint approach and costless Taylor expansions can be built for sampling purposes.

Regarding the imposition of models as inlet conditions for *Simulation 2*, four models have been given for the fully-developed state of the swirling flow confined in the rotating pipe (dimensionless profiles v_z/U , v_t/U , k/U^2 and β). These models fit very well with the computational results and a study of the propagated errors when implementing them in the uncertainty quantification by Stochastic Collocation Method has been given. It has been demonstrated that the evolution of the Nusselt number is almost insensitive to the modelling uncertainty and one can avoid to run the CFD solver for *Simulation 1* every time a deterministic case is required for higher levels in the sparse grid.

In Chapters 3 and 4 it has been addressed the modelling under uncertainty of a swirling flow generated by a rotating pipe for heat transfer by impingement. As earlier said in Chapter 1, there is another industrial jet flow of interest in this thesis: an aircraft under-expanded jet. In the next chapter, a framework for the propagation of uncertainties in the research modelling of these jets involving several stages will be shown.

Chapter 5

A Framework for Uncertainty Propagation in Under-expanded Single Jet Simulations

A classic approach to computational fluid dynamics is to perform simulations with fixed parameters and boundary conditions in order to model a specific case-scenario. However, this is not accurate enough, due to the fact that under realistic conditions, some parameters may vary. In recent years, the interest of undertaking the simulations under uncertainty is increasing, but is not yet a common rule and ‘incomplete’ simulations are still taking place. This procedure could be missing information such as whether mechanical tolerances are influential in dramatic parts of the flow or the relevancy in accurate tuning of turbulence models. Taking this knowledge into consideration, Non-Intrusive Uncertainty Quantification has been applied to 3D Reynolds-Averaged Navier-Stokes simulations of an under-expanded jet, in order to understand the impact of input uncertainties. Results show that some regions of the jet plume simulations are very sensitive to a combination of both physical and turbulence model variance, obtaining an visualisation of the propagation of uncertainties in the computational domain.

The last part of the framework deals with the Parabolised Stability Equations, which are considered for an approach under uncertainty. As these equations do not deal with turbulence nor stagnation pressure as inputs, this framework provides a new way to quantify the impact of earlier stages uncertainty on jet instability.

Breaking down this chapter into sections, Non-Intrusive UQ methods have been applied to 3D steady Reynolds-Averaged Navier-Stokes (RANS) simulations with *elsA* solver [32], whose set-up is described in Section 5.3. Due to the fact that common sampling methods such as Monte-Carlo are impractical in terms of computational cost, UQ will be deployed with two different approaches. First, generalised Polynomial Chaos [258] is applied in order to quantify the uncertainty in Section 5.4.2. Second, in order to have another method for

comparison, Kriging surrogates are built to ensure the quality of the analysis. In Section 5.5, a sensitivity analysis is conducted with both methods, in order to assign to each input uncertainty its contribution to the total variance. In Section 5.6, Stochastic Collocation is applied to PSE to quantify the impact of framework's input uncertainties on jet stability.

5.1 Introduction and Motivation

A framework for propagation of uncertainties in the research of under-expanded jet flows is presented in this chapter. The analysis begins with the experimental uncertainty agreed with experts and its propagation through 3D CFD simulations. A latter use of the base-flows for Parabolised Stability Equations (PSE) in order to perform a stochastic analysis on stability is also developed. Experimentalists tend to provide error analysis in their research but computationalists do not normally. This study aims to offer an alternative to this lack, especially missed in stability analysis literature. This framework is developed to show an approach to the common deterministic one in computational research of jets, due to the fact that sampling-based approaches on the simulations are computationally expensive and time demanding. Thus, this approach is specially interesting in the current trend, as computational approaches are becoming more and more relevant, even changing the former classical approach in design of aircraft engines. Formerly these designs used to require a 90% of experimental tests and 10% of computational approach, but nowadays the situation has been inverted [157].

5.2 Literature Review

There are many papers dealing with UQ in CFD and other computational problems, where sampling approaches are not practical. However, there are few references on applications closely related to this work. The Non-Intrusive UQ methods used in this chapter were the so-called generalised Polynomial Chaos (gPC) and Kriging surrogates, as well as the Stochastic Collocation method, already introduced in previous chapters of this thesis.

Interesting literature about gPC whose application can serve as guidance for this work are the sensitivity analysis of the impact of impurities in CO_2 pipeline failure [26], uncertainty analysis of the effect of inlet uncertainties in pipes [43], comparisons with other UQ methods such as Stochastic Collocation [58, 2], uncertainty in hot gas turbines [183] or sensitivity analysis for parametric uncertainty in turbulent computations [142].

On the other hand, several works can also be found where Kriging surrogates are conducted such as in CFD optimization of combustion chambers [55] and aerodynamic optimisation of civil structures via CFD and Kriging surrogates [24], variance-based sensitivity analysis in structural failure [242], and of course UQ [56, 108, 137], but in general trend is

not as popular for uncertainty analysis as gPC.

To the knowledge of the author, **there is no literature about UQ on aircraft thrust jet flows in the presence of shock-cells**, despite that it has been already applied to CFD simulations of synthetic jets as in [1], by means of polynomial chaos, and underexpanded jet in a crossflow for turbulent mixing [82], to quantify physical uncertainties in transonic airfoils to point out the importance of the sensitivity of shocks [253] or to uncertainties in the turbulence models for transonic wall-bounded flows [211]. All these works have similarities with the one here treated in terms of the stochastic approach in CFD. Some of them are even dealing with the well-known uncertainty implicit in turbulence modelling as it is going to be done here with the laminar to turbulent viscosity ratio. In [157] one can also find several approaches to aircraft engines, which might seem closer to this work in thematic, but different as it focuses on the turbomachinery side.

In compressible supersonic jet flows, UQ is a particularly interesting analysis, as the imperfectly expanded conditions generate shock-cells. **It is also a concern that small changes in input parameters may lead to sensitive variations in shock-cell position and then to noise emission** [227, 180, 182], which currently represents a major concern in robust design because of environmental regulations and the challenge of perceived noise reduction of 65% by 2050 with respect to the values dated from the year 2000 [42].

In the under-expanded condition, the flow exits with a pressure p_e greater than the ambient one, p_{amb} and obliges the flow to adapt to the ambient pressure. This adaptation is carried out through series of expansion fans and oblique shocks, originating the so-called shock-cell pattern as shown in Fig 5.1. In the figure, (+) stands for the regions where $p_e > p_{amb}$, (+) refers to the regions where $p_e = p_{amb}$ and (-) where $p_e < p_{amb}$. The pressure mismatch leads to expansion fans attached to the lip of the nozzle. These are refracted at the jet mixing layer as compression waves, which collapse forming an oblique shock. Both oblique shocks, one corresponding to the upper side of the nozzle and the other to the lower side, will meet at an interception point P . This point indicates the end of the expansion zone in the cell. The oblique shock will impinge on the jet boundary at the reflection point Q , marking the end of a shock-cell [86, 33].

The last part of the framework is about using the stochastic base-flow from the former UQ on RANS to stretch the propagation of uncertainty up to the latest design phase of Parabolised Stability Equations (PSE) [95] for stability analysis. As stability analysis, in this work is interpreted the study of the evolution of the growth rate and spatial wavelength of Kelvin-Helmholtz instabilities [237, 154]. This type of instability is a growth of perturbations at the interface between two fluids due to shear. Such perturbations grow and become unstable typically by forming waves, powered by the kinetic energy of the shearing motion and difference in velocities. In the absence of viscosity and gravity, only inertia can exert a

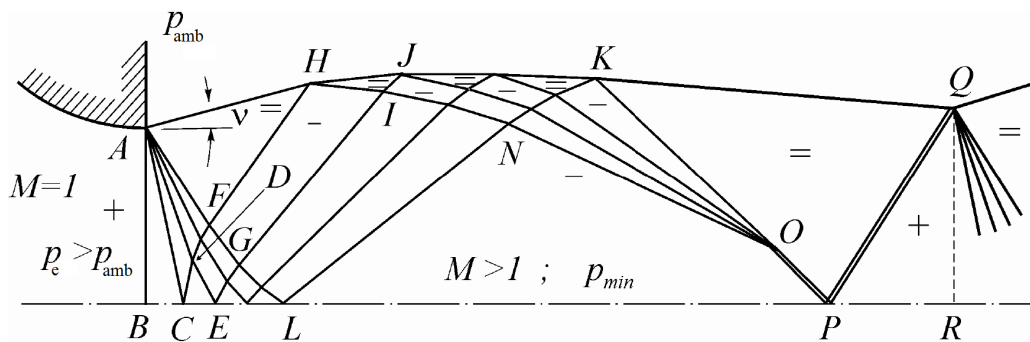


Figure 5.1 Shock-cell pattern [33].

stabilizing influence on perturbations and damp oscillations before growth commences [200]. A detail of their generation is depicted in Fig. 5.2.

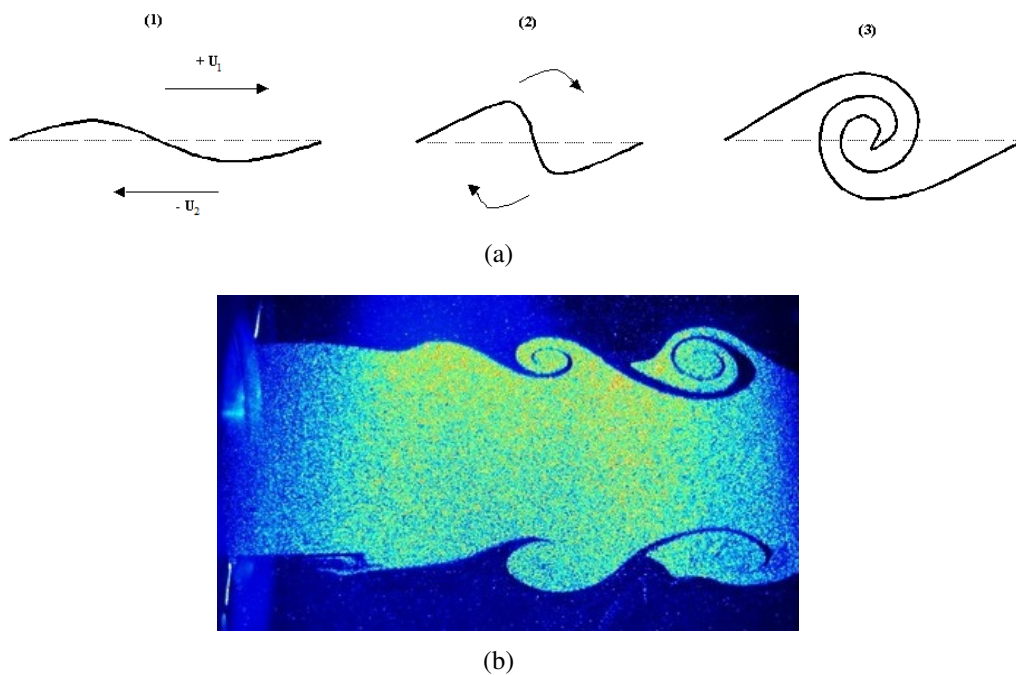


Figure 5.2 a) Generation of Kelvin-Helmholtz instabilities (Image from [165]). b) Detail of shear-layer Kelvin-Helmholtz instabilities in a round jet (Image from [122]).

There are several works on the use of PSE for stability analysis as in optimisation in control of Tollmien-Schlichting waves [240] or the to be presented case of jet flow instability [261, 13, 12, 11]. However, to the knowledge of the author, **there is no stochastic approach for PSE on jets in literature**, despite the fact that one can find few papers on the application of UQ on PSE such as in roughness modelling in crossflow disturbance generation [161] and assessing the boundary layer instability [147].

This approach is therefore a light step beyond in the field and it can be repeated for more

exhaustive analysis by practitioners in order to develop more robust designs. This can also become in an interesting initial contribution to determine the impact of uncertainty in the noise emission, since **it has been demonstrated that instability plays an important role in noise emission** [227, 193, 135].

5.2.1 Methodology and Challenges

The current trend in industry and academia related to under-expanded jets is to focus on deterministic simulations, either in CFD or PSE, as noticed in the literature review. When UQ is applied to CFD simulations, **in industry** is also frequent to see **mostly surrogate-based approaches**, being Kriging the most applied method. Surrogates have the advantage of flexibility, since they can be randomly sampled, and if the dimension is increased (that is, more variables are added to the stochastic space), the new samples does not require special needs as in quadrature rules. If not only UQ but also optimisation is a purpose in the industrial problem, surrogates are then a quite flexible tool, but less accurate than collocation rules. It is nowadays also frequent to see industrial research on the application of **polynomial chaos expansions**, possibly because **in academia became very popular (even trendy)** and some codes, toolboxes and packages are available for any purpose.

To develop a framework for the propagation of uncertainties in modelling of under-expanded jet flows is a multi-step task that was not handled before, but certainly has a great both industrial and academic interest. The tested procedure is summarised in Fig. 5.3.

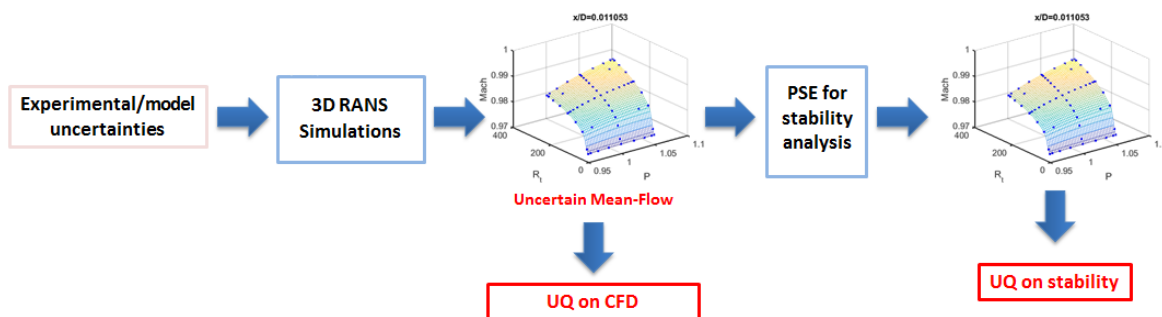


Figure 5.3 Sketch of the uncertainty propagation through experiments, CFD simulations and PSE equations.

The **first step** is to **model the experimental and turbulence model uncertainty**. One of the greatest sources of uncertainty that one can recognise in these jet flows is the mass-flow rate, which is in fact related to other variables such as the nozzle diameter or stagnation pressure, being such pressure a chosen random input. As the test rig was not yet built to measure the stagnation pressure (p_s) uncertainty, it was agreed with the experts to set a specific value based on a range to p_s to compute the input uncertainty by a conservative uniform distribution. The same approach was followed for the second source of uncertainty, the

laminar viscosity ratio (R_t), which was identified by computational tests.

The **second step** involves the computation of **UQ and sensitivity analysis in the CFD simulations of the jet flow**. As earlier discussed in the literature, **there is no previous bibliography on the analysis of uncertainties in aircraft under-expanded jet flow computations**, despite the fact that helpful information regarding the quality of the simulations can be extracted, since some regions are critical to be accurately computed if reliable conclusions based on the simulations are desired. This analysis hence pretend to fill the gap with some contributions, providing metrics to measure the impact of uncertainty.

Non-Intrusive UQ methods have been applied to 3D steady Reynolds-Averaged Navier-Stokes (RANS) simulations with *elsA* solver [32], whose set-up is described in Section 5.3. Due to the fact that common sampling methods such as Monte-Carlo are impractical in terms of computational cost, UQ will be deployed with two different approaches. First, **generalised Polynomial Chaos** [258] is applied in order to quantify the uncertainty in Section 5.4.2. Second, in order to have another method for comparison, **Kriging surrogates** are built to ensure the quality of the analysis. The **Stochastic Collocation Method (SCM)** could also be applied, but it was **discarded** since its results would be quite similar to the ones with gPC, but without the possibility of computing a sensitivity analysis instantaneously. The **direct sampling methods were discarded** because they are unaffordable: their convergence rate is too slow and it is not possible to have such a large computational budget in this problem. Each CFD simulation takes half a week with the advanced available computational resources at CERFACS.

Kriging surrogates were also tried because in Section 5.5, a sensitivity analysis is conducted with gPC and results looked misleading. Then, to try a second approach was important to figure out what is happening, and the Kriging surrogates were sampled by Latin Hypercube Sampling (LHS). With the sensitivity analysis, the objective is to assign to each input uncertainty its contribution to the total variance at each point of the domain.

The **third step** deals with the impact of the prescribed **uncertainty in jet stability**. In Section 5.6, SCM is applied to PSE to quantify the impact of framework's input uncertainties on jet stability. This method is chosen because this third part of the analysis depends on the computational budget in the second step, and SCM tends to require the same or less collocation points than gPC to exactly compute the integrals, and it is not necessary to tune the order of an expansion. **Since the PSE formulation does not deal with turbulence, there is no approach in literature to measure the impact of turbulence modelling in stability**, and to fill this gap is an interesting motivation. Turbulence is a crucial part of fluid dynamics simulations and, as PSE uses their output as input (or rather, as starting point), the accuracy of the stability computations is undoubtedly linked to the accuracy of the base-flows.

5.3 CFD simulations

5.3.1 Numerical formulation

The full three-dimensional compressible Reynolds-Averaged Navier-Stokes equations have been solved by using the Finite Volume multi-block structured solver *elsA* (Onera's software [32]) at the Centre Européen de Recherche et de Formation Avancée en Calcul Scientifique (CERFACS) in Toulouse (France) by Carlos Pérez Arroyo [189–191], and will be briefly explained here. The turbulence model used in the computations of this work is the one-equation Spalart-Allmaras standard model [224]. Other popular turbulence models were tried in *elsA*, but for fluids with shocks, $k - \omega$ is not a recommended practice [81]. By using the $k - \omega$ turbulence model, the convergence was extremely slow and finally the simulation did not even converge. With $k - \varepsilon$ convergence was achieved, but only the first shock was captured, obtaining therefore an inaccurate simulation. According to these results, the Spalart-Allmaras model had the best performance, as it was able to accurately simulate the first three shock-cells, known as the most interesting ones in jet analysis [180]. Spalart-Allmaras is in fact a recommended turbulence model in cases with shocks and less demanding in near-wall resolution [81]. Some examples of the application of the chosen turbulence model in supersonic/transonic flows can be found in [256, 72, 186, 145]. The convective flux is computed using an upwind approach based on the Roe's approximate Riemann solver [201]. The scheme's accuracy is increased by the use of either a second order MUSCL extrapolation [233] coupled with the minmod limiter or a third order extrapolation technique [36]. The implicit system is solved at $CFL = 100$ with a $LU - SSOR$ algorithm with four sweeps [246]. In order to accelerate the convergence for all the conditions, a converged deterministic base case solution has been used as initial solution.

5.3.2 Simulation set-up

The case of study is the cold supersonic under-expanded single jet that was tested experimentally by André [9]. The jet is produced from a convergent nozzle with an exit diameter of $D = 38.0\text{mm}$ and a modelled nozzle lip thickness of $t = 0.125D$. The nozzle is operated under-expanded at the stagnation to ambient pressure ratio $NPR = p_s/p_{amb} = 2.27$, with p_s the stagnation pressure and p_{amb} the ambient one. The Reynolds number, Re , based on the jet exit diameter is 1.25×10^6 and the fully expanded jet Mach number is $M_j = 1.15$. The perfectly expanded Mach number, *i.e.* the Mach number that would be reached if the jet was able to expand further to ambient conditions, is related to the total pressure by

$$NPR = \frac{p_s}{p_{amb}} = \left(1 + \frac{\gamma - 1}{2} M_j^2\right)^{\gamma/(\gamma - 1)}. \quad (5.1)$$

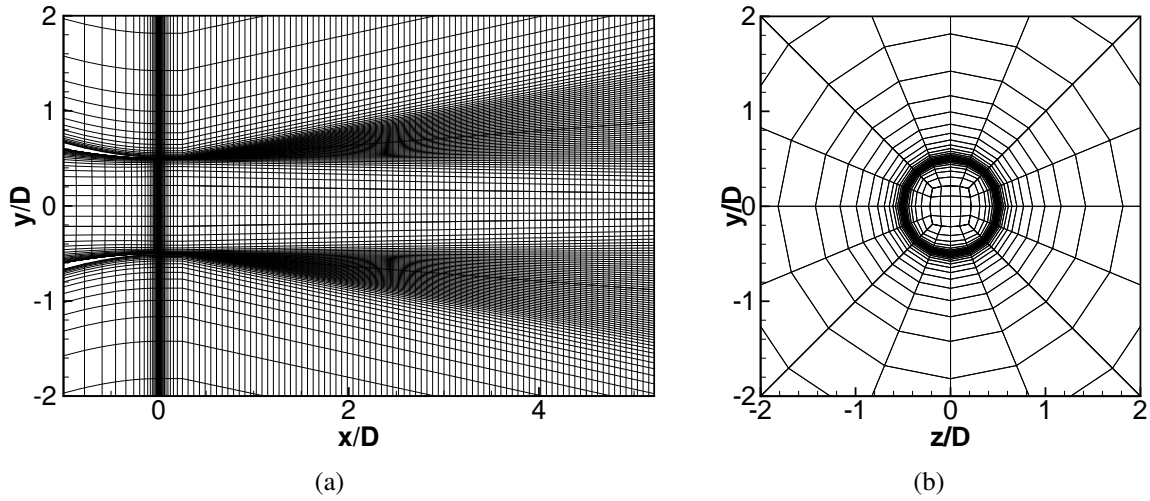


Figure 5.4 Mesh cuts representing every fourth cells in the plane (a) $z/D = 0$ and the plane (b) $x/D = 0$. Image courtesy of CERFACS.

For the boundary conditions used in the computations, the interior/exterior and lip walls of the nozzle are computed with adiabatic no-slip wall conditions. A characteristic approach is chosen to define the inflow conditions outside the nozzle. Such a condition works for all configurations (inflow/outflow, subsonic/supersonic): the number of fields to impose (1, 4 or 5) is chosen according to the local analysis of the waves that travel across the interface. The remaining lateral and outlet boundary conditions are set to a subsonic characteristic one, where the reference ambient pressure is defined.

The computational domain used for the RANS simulations extends $100D$ in the axial direction and $50D$ in the radial direction. The interior of the nozzle is modeled up to $6D$ while the exterior up to $9D$.

5.3.3 Mesh generation

The converged mesh developed in CERFACS consists of a butterfly type mesh to avoid the singularity at the axis as shown in Fig. 5.4 (b). It contains 20×10^6 cells with roughly $(900 \times 300 \times 64)$ cells in the axial, radial and azimuthal directions respectively forward to the nozzle exit plane, $(220 \times 120 \times 64)$ inside the nozzle and $(170 \times 100 \times 64)$ outside.

The nozzle is wall-resolved for all the conditions with $y^+ \approx 1$ and radially stretched up to the end of the domain at a rate of 10% as can be seen in Fig. 5.4 (a). Axially, the mesh is uniform at the exit of the nozzle, then it is stretched at 6% up to $0.25D$. Next, it is kept constant up to $10D$, in order to have a minimum of around 40 cells per shock-cell (measured at the last cell, which due to the flow physics, it is the most shortened shock-cell). The mesh is axially stretched again up to the end of the domain at a rate of 10%.

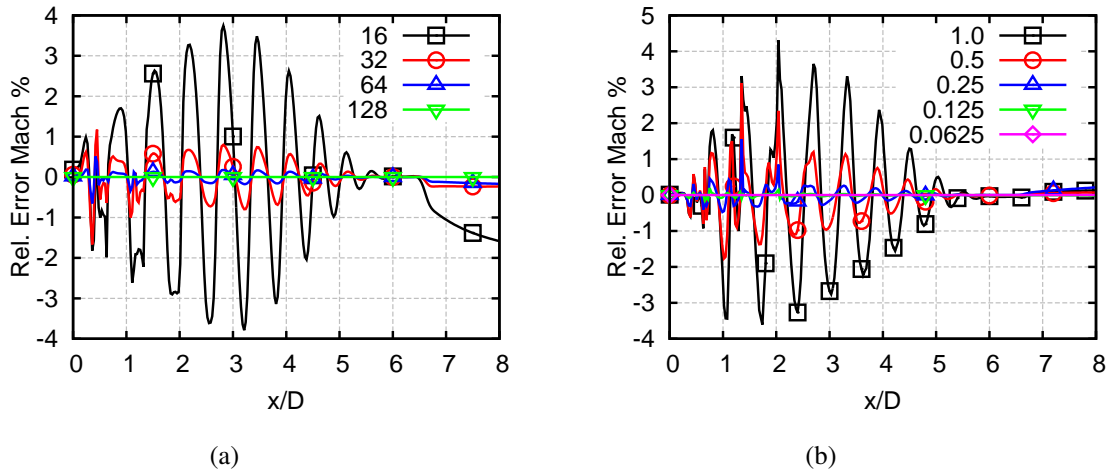


Figure 5.5 Mach number profile relative error of the deterministic base case at the centreline for **(a)** different azimuthal discretizations, where each line represents the number of azimuthal nodes, and **(b)** different axial discretizations, where each line represents the starting position where the mesh is uniform. The refined mesh has been used as converged solution. *Image courtesy of CERFACS.*

To have a converged mesh for all deterministic simulations required for uncertainty quantification is a must. This need is specially important for flows containing shocks. In this under-expanded jet, the shock-cells are actually a series of expansion and compression waves that look like widen shocks. The above mentioned mesh has been thoroughly obtained with the following convergence procedure using as reference parameter the Mach number profile at the axis for the deterministic base case and conditions with a higher NPR . First, the mesh has been converged azimuthally with 64 cells, obtaining a relative error with respect to a refined mesh of less than 0.15% as shown in Fig. 5.5 (a). Second, the axial discretization is taken into account by varying the starting position, where the mesh topology is uniform. Axial convergence is obtained with an error of 0.2% with respect to the most refined mesh for the position of $0.25D$ as shown in Fig. 5.5 (b). Finally, the y^+ has been checked so that it still lays in the range smaller than unity for the range of working conditions. The validation with the available experimental results of the jet centreline is also showing that the first three shock-cells, which are the most influential ones in the jet physics features such as noise emission [180], are accurately reproduced (see Fig. 5.8). Also a contour plot of the definitive CFD simulation can be seen in Figs. 5.6 and 5.7, where only a region of the extensive computational domain is shown.

5.4 Uncertainty Quantification on 3D RANS simulations

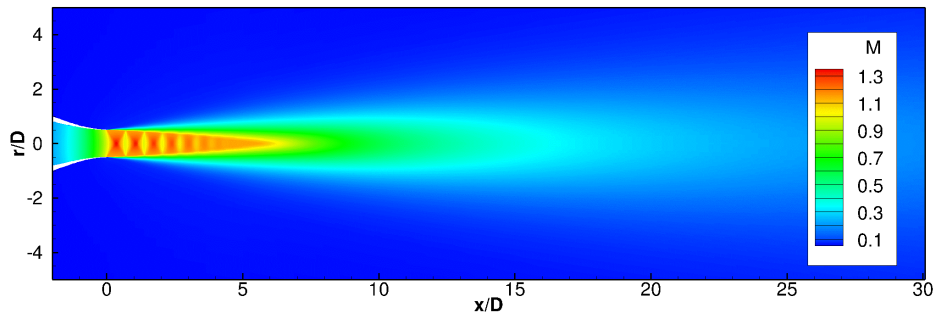


Figure 5.6 CFD RANS simulation of the Mach number from the deterministic base case of the under-expanded jet in *elsA*. Image courtesy of CERFACS.

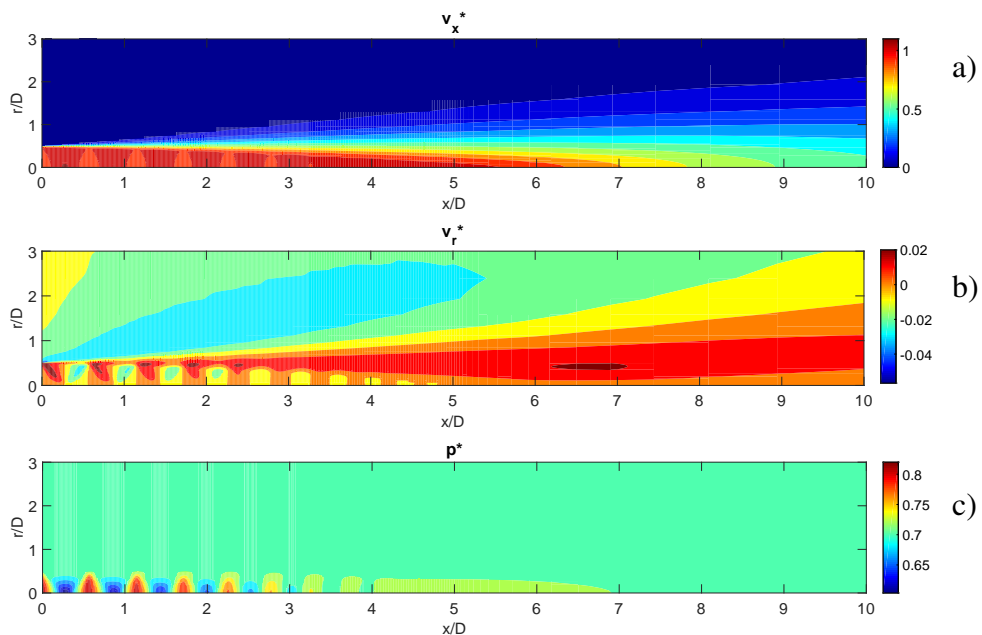


Figure 5.7 CFD RANS simulations of the deterministic base case of the under-expanded jet in *elsA*. The shown parameters are (a) the dimensionless axial velocity profile, $v_x^* = v_x/c_{ref}$, (b) dimensionless radial velocity profile, $v_r^* = v_r/c_{ref}$ and (c) dimensionless static pressure, $p^* = \frac{p}{\gamma_{ref} p_{ref}}$, with $\gamma = 1.4$ the specific heat ratio, $p_{ref} = 98000 Pa$ the reference pressure and $c_{ref} = 340.26 m/s$ the reference speed of sound.

5.4 Uncertainty Quantification on 3D RANS simulations

The main purpose of this work is to compute both the impact of uncertainty from a jet facility and the computational injection of turbulence, that give a stochastic point of view to the problem, rather than the classical deterministic one. This leads to the concepts of Uncertainty Quantification and Sensitivity Analysis, which involves the study of how uncertainty in the output of a model (numerical or otherwise) can be apportioned to different sources of uncertainty in the model input [206]. In this section, the input uncertainties are described as

well as the mathematical methods used for their handling.

5.4.1 Tests and Prescription of Uncertainties

The parameters treated as stochastic inputs for uncertainty quantification are the stagnation pressure, p_s , and the turbulent to laminar viscosity ratio, $R_t = \mu_t/\mu$, that are both imposed at the inlet of the nozzle. These parameters have been selected because of their stochastic behaviour in nature. Other parameters could also be selected, but these are the most relevant ones according to our experience and quick tests.

The stagnation pressure is used to model the uncertainty in the mass-flow rate. Such decision is based on suggestions from the experimentalists at von Karman Institute for Fluid Dynamics. For them, during a single run, notable pressure variations are not yet expected due to emptying of the tanks. However, these are expected during repeated tests. This is because of the membranes of the valves are opening and closing several times, and the displacements of these membranes can be slightly different for each run, leading to variations in the mass-flow rate. Moreover, we have to take into account the uncertainty of the measurement devices (pressure sensors). Consequently, a conservative range of $\pm 5\%$ has been agreed with experimentalists. To sum up, the chosen probabilistic distribution is $p_s \sim U(0.95\bar{p}_s, 1.05\bar{p}_s) = U(211337, 233583) Pa$, where \bar{p}_s refers to the deterministic base value $\bar{p}_s = 222460 Pa$.

The second parameter is the laminar to turbulent viscosity ratio, $R_t = \mu_t/\mu$, used for the injection of turbulence in the Spalart-Allmaras model [224], which is in fact a computational input for the turbulence at the exit of the nozzle. This parameter stays fixed when simulating the operating conditions of an experimental facility. However, treating it as a deterministic parameter is not appropriate, as the flow properties can be sensitive. Thus to quantify the change in the simulations is relevant. Therefore, the variation of the parameter has been carefully chosen based on several tests on the CFD solver, for which the solution is close to experimental results. By increasing this parameter at the inlet, it increases also the maximum non dimensional turbulent wall unit, y^+ , achieved at the wall near the exit. Nevertheless, the y^+ remains of order unity changing from 1 to 6 for the highest R_t value. Figs. 5.8 and 5.9 show the Mach and R_t profiles for different R_t inlet values, respectively. Fig. 5.10 shows the impact on the axial velocity profile at $x = 2mm$, and it is compared with the available experimental data. The values are non-dimensionalized by the maximum values due to the fact that the experimental data corresponds to a subsonic test case with a Mach number at the exit of the nozzle of $M_e = 0.9$. The chosen probabilistic distribution is $R_t \sim Unif(2.2, 220)$. This is because for smaller values of R_t the change in the injection of turbulence is too small and there is no need to include it in the study. The deterministic base value is $R_t = 2.2$, as this was the value used by the authors in the initialisation of the flow for a Large Eddy Simulation

[191, 190].

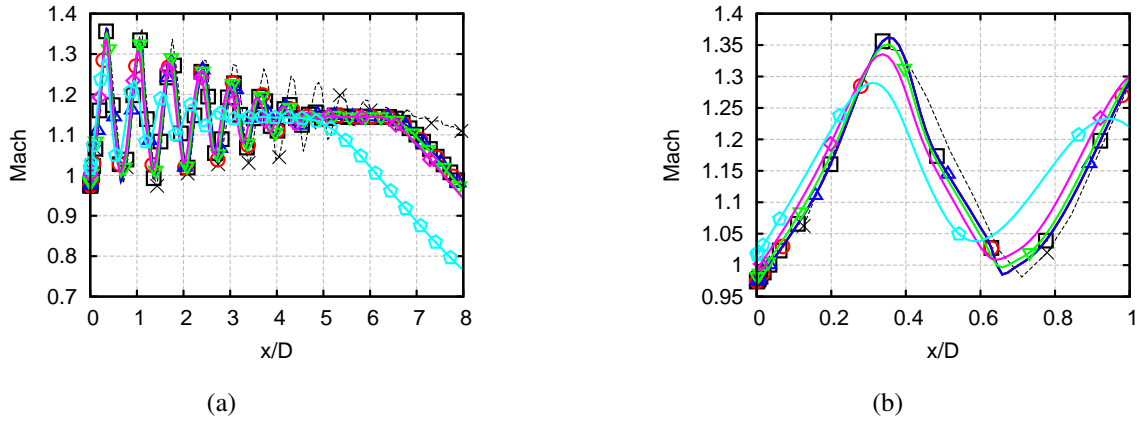


Figure 5.8 Mach number profile of the deterministic base case at the axis for different R_t inlet values in a (a) general and a (b) detailed view. Experimental \times , $R_t = 0.022$ \square , $R_t = 0.22$ \circ , $R_t = 2.2$ \triangle , $R_t = 22$ ∇ , $R_t = 220$ \diamond , $R_t = 2200$ \diamond . Results by *elsA* software, run at CERFACS facilities.

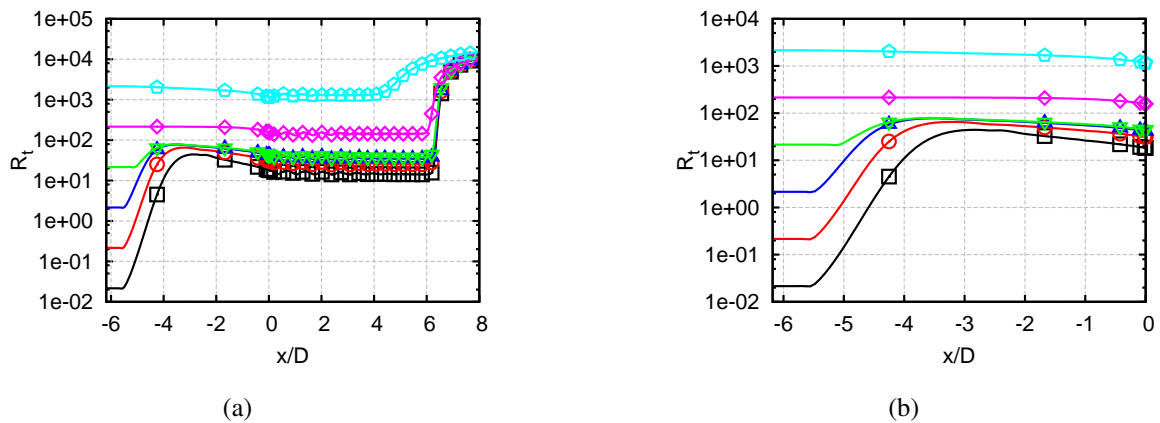


Figure 5.9 R_t profile of the deterministic base case at the axis for different R_t inlet values in a (a) general and a (b) detailed view. $R_t = 0.022$ \square , $R_t = 0.22$ \circ , $R_t = 2.2$ \triangle , $R_t = 22$ ∇ , $R_t = 220$ \diamond , $R_t = 2200$ \diamond . Results by *elsA* software, run at CERFACS facilities.

5.4.2 Uncertainty Quantification Methods: Generalised Polynomial Chaos and Kriging Surrogates

Uncertainty quantification (UQ) has become a very influential field, due to the fact that methods developed in recent years bring the possibility of understanding how the behaviour of expensive (normally in terms of computation) mathematical models can be affected by imprecisely defined inputs.

5.4 Uncertainty Quantification on 3D RANS simulations

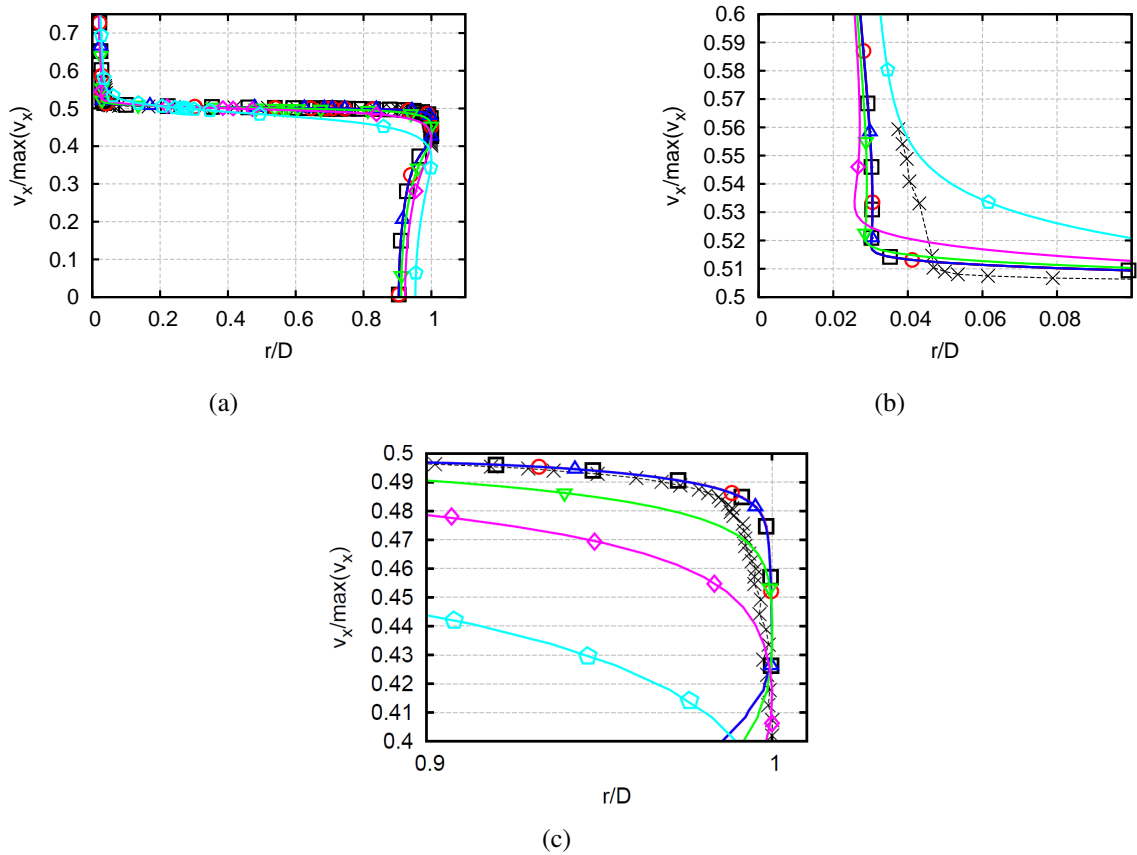


Figure 5.10 Axial velocity profile of the deterministic base case at the axis for different R_t inlet values in a (a) general and a (b)&(c) detailed view. Experimental \times , $R_t = 0.022$ \square , $R_t = 0.22$ \circ , $R_t = 2.2$ \triangle , $R_t = 22$ ∇ , $R_t = 220$ \diamond , $R_t = 2200$ \diamond . Results by *elsA* software, run at CERFACS facilities

The first approach implemented in this section is the Polynomial Chaos method. This method has been developed to solve Stochastic Differential and Partial Equations (SDE and SPDE, respectively)[225]. Xiu & Karniadakis extended the original version of Wiener [251] to a wide family of basis functions leading to the known concept of generalised Polynomial Chaos (gPC) [258]. Polynomial Chaos is a spectral method and as such, an important advantage is that one can decompose a random representation into deterministic and stochastic components. Moreover, from a Polynomial Chaos Expansion a global sensitivity analysis is straightforward from its results at zero cost. This will be discussed in Section 5.5. The scripts for gPC utilised in this thesis were coded in MATLAB. For detailed information regarding the gPC method, please see Chapter 2.

The second approach is Kriging interpolation. Kriging (also known as Gaussian Process interpolation, and in this chapter under the acronym KG) is an interpolation surrogate method to approximate sets of data and it has been widely used in literature, specially for tasks involv-

5.4 Uncertainty Quantification on 3D RANS simulations

ing costly computational analysis that by other methods would be expensive. Examples of this are sensitivity analysis [245], topography [133] or prototyping [97]. Despite of the fact that surrogates can be also constructed with the Polynomial Chaos Expansion, the main idea of using Kriging is to try another method for a quick comparison in this chapter with the available budget. For Kriging interpolation, the MATLAB code[140] used by the first author in [85] has been utilised here. For further information on the method, it is suggested to see Chapter 2.

In order to generate an accurate Kriging surrogate, it is important to pay attention to the correlation function. The generalised exponential worked very well and was the final choice. From Eq. (2.41), exponential and gaussian correlations were not appropriate for the complicated surrogates since during tests these gave some bumped areas in the spaces between collocation nodes. Because the shock-cells could create abrupt changes in some features, the generation of surrogates has been carefully tested. The best performance was observed for the general exponential correlation, whose results for complicated data sets to be interpolated can be seen in Fig. 5.11. It can be noticed that the surrogates have a smooth shape, so it is not expected to have substantial erratic contributions in uncertainty quantification when sampling across inter nodal areas. Once the Kriging surrogates are available, sampling techniques are affordable. Latin Hypercube Sampling [92] and Random Sampling Monte Carlo are widely used non-intrusive methods for propagation of uncertainty in models. These methods have been used for many applications in science and a vast literature can be found.

In Sections 5.4.3 and 5.5, the application of sampling techniques for UQ and sensitivity analysis on Kriging surrogates is developed and a comparison between both Kriging and gPC results is discussed.

5.4.3 Comparison and Discussion of Uncertainty Quantification Results

The first step for uncertainty quantification was to test the convergence of each method with our computational budget. The idea behind using two different methods with different procedures (Kriging surrogate by sampling and gPC by quadrature on collocation points) is to provide a comparison. When focusing only on one method, any incoherent feature in the analysis or the codes could be taken as a conclusion that cannot be contrasted with any other result. However, if a second approach is giving similar outputs, a more consistent feedback can be extracted.

For this purpose, several samplings were tried on KG surrogates by Latin Hypercube Sampling (LHS) and the results were compared with the gPC expansion of 4th order (as $N_{\xi} = 2$, only 21 terms are required in the expansion). The accuracy of the methods has been

5.4 Uncertainty Quantification on 3D RANS simulations

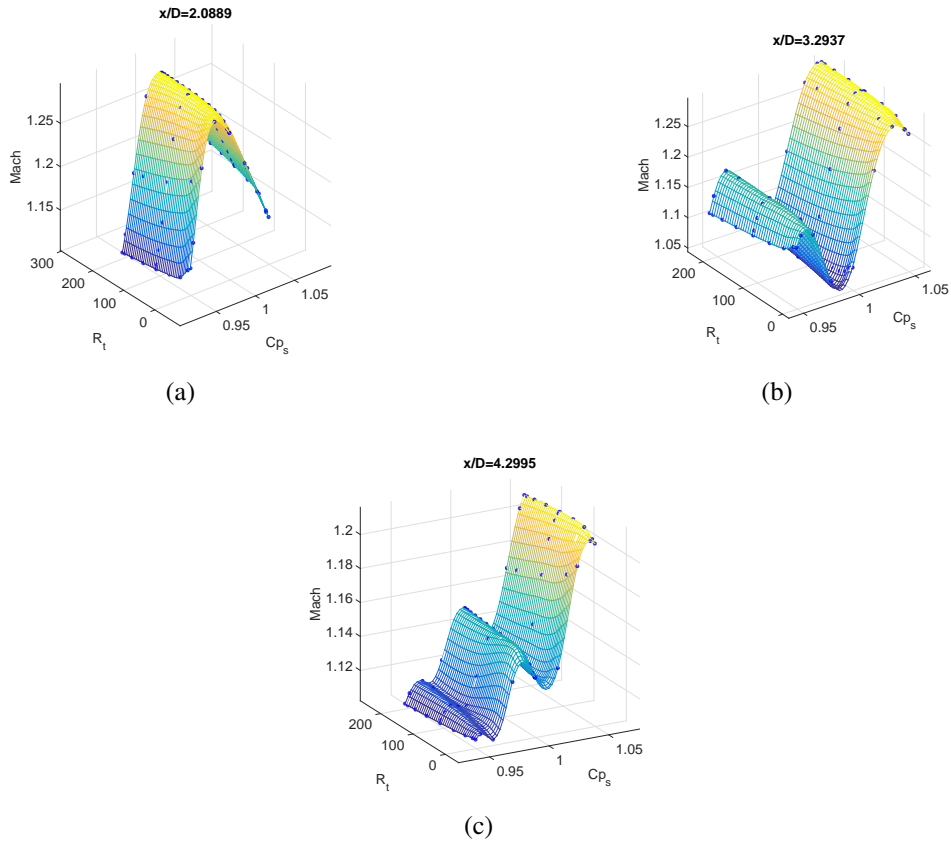


Figure 5.11 Examples of Kriging surrogates at several x/D distances on data sets with challenging shape. The blue points correspond to the deterministic CFD solutions from the fourth level of accuracy in the Clenshaw-Curtis sparse grid. In the plots Cp_s stands for the coefficient of variation for p_s ($\pm 5\%$).

tested along the lipline for the dimensionless axial velocity, v_x^* , and along the centreline for the Mach number, as these are the most relevant parts of the jet (along the centreline the shock-cells are strong and preliminary tests revealed that the nozzle lipline could be sensitive for v_x^*). To compute the integrals for the statistical moments of gPC, a sparse grid of 65 collocation points based on Clenshaw-Curtis (C-C) nested rule was used (the 65 collocation points correspond to the fourth level of accuracy), having a good match with Kriging sampled surrogates as shown in Figs. 5.12 and 5.13. The required number of collocation points was tested in [83], computing the convergence of statistical moments with Stochastic Collocation Method, so that level of accuracy of the sparse grid was intended here for gPC.

For convergence of gPC, the order of the expansion, P , and the number of collocation points, N_q , have to be controlled. If N_q is fixed to the fourth level of accuracy ($lv/4$) as aforementioned, it is now necessary to focus on the order of the expansion, P , to compute the statistical moments. These undergo convergence up to $P = 4$. However, if $P > 4$, there is divergence and this is due to the fact that more collocation points are needed to compute the

5.4 Uncertainty Quantification on 3D RANS simulations

integrals. This has been tested numerically by means of generating artificial deterministic solutions from Kriging surrogates (see Fig. 5.14). With this procedure, the extra deterministic solutions of the sparse grid required for the fifth and sixth level of accuracy (*lvl5 artif* and *lvl6 artif* in the legend of the plots) are artificially generated and higher orders in the gPC expansion are tested. These plots are revealing that in fact in the region of $3 < x/D < 4$ more collocation points would be required with higher P . As for *lvl5* and *lvl6* are required 145 and 321 collocation points respectively with a not very relevant improvement in the accuracy, it is not worthy to perform such a large number of simulations with the CFD code and *lvl4* is assumed to be enough. Moreover, an adaptive refinement method[254] would not be worthy since the surrogates are different at each point of the domain.

Regarding the convergence of sampling on Kriging surrogates, even with a reduced number of samples, converged statistical moments can be obtained. This is because LHS is a sampling strategy more efficient than Monte-Carlo and also due to the fact that the stochastic dimension is low, requiring to sample less dimensions. Absolute errors are shown in the comparisons with gPC.

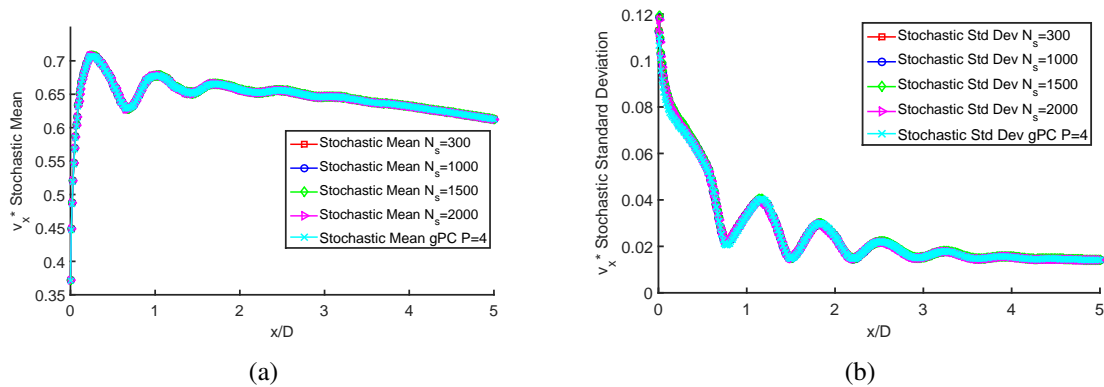


Figure 5.12 Evolution of the v_x^* stochastic means (a) and standard deviations (b) along the lipline for LHS on Kriging surrogates with different number of samples, N_s , and its comparison with gPC results. Even for a small number of samples, LHS is undergoing very good convergence.

For the purpose of visualising uncertainty, the contour plots of the stochastic mean and variance are represented for both methods. In Figs. 5.15, 5.16 and 5.17 these values are plotted for v_x^* , v_r^* and p^* for Kriging surrogates only, as well as the absolute error with respect to gPC, which is showing the small difference in the results between both methods.

Despite the absolute error in the variance can seem slightly notable, it is just illustrative. If attention is paid, i.e. on v_x^* along the lipline close to the nozzle in Fig. 5.15.d, the absolute error seems to be notable, but in Fig. 5.12 the difference is practically negligible.

5.4 Uncertainty Quantification on 3D RANS simulations

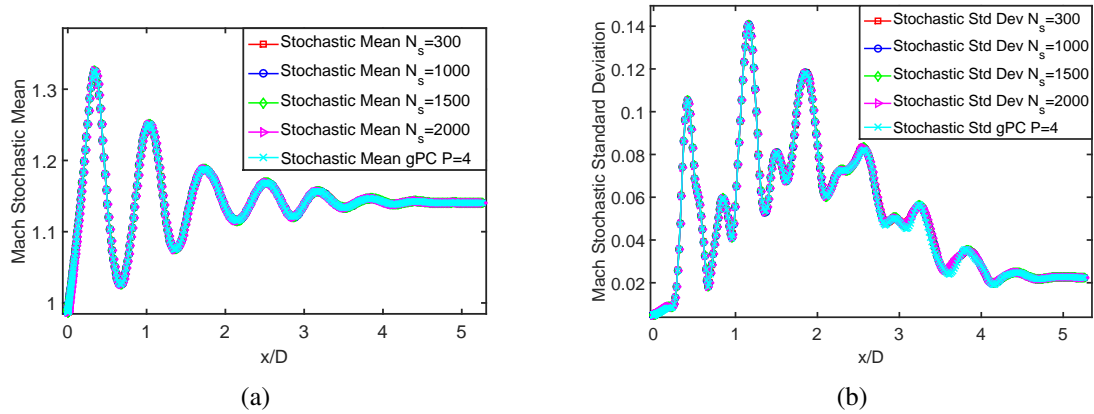


Figure 5.13 Evolution of the Mach stochastic means (a) and standard deviations (b) along the centreline for LHS on Kriging surrogates for different number of samples and its comparison with gPC results. Even for a small number of samples, LHS is undergoing very good convergence.

The objective of the analysis is to determine the regions of the jet which are more sensitive to the input uncertainties in the CFD simulation. From the task of understanding the physical meaning of the plots above, one can extract the following relevant information:

- For the dimensionless axial velocity, v_x^* , the most sensitive region is along the lipline, close to the nozzle lip (see Fig. 5.15.b). This uncertainty is in fact very high, as can be more clearly observed in Fig. 5.18.b. Such large sensitivity nearby the nozzle lip makes sense due to the fact it is well-known that small variations in the nozzle diameter (in this work uncertainty in stagnation pressure and turbulence vary the mass-flow rate similarly) modifies features that takes places in the nozzle lip/lipline regions, such as a consequence of the perturbations in the shear layer that leads to the feedback loop for screech noise [181]. Along the centreline some uncertain regions can also be detected, but they can be better explained when describing the variance in p^* .
- Regarding the dimensionless radial velocity, v_r^* , the most sensitive region is immediately below the lipline (see Fig. 5.16.b). It can also be observed that the second and third shock-cell compression are notoriously the most sensitive to input uncertainty, where screech jet noise is usually generated [180].
- For the dimensionless static pressure, p^* , the most sensitive region is along the centreline (see Fig. 5.17.b). This is also observed for the Mach number in Fig. 5.18.a, where can also be noticed relevant uncertainty in the position of the shocks. The envelopes show a variation in both the amplitude and position of the shock-cell which makes sense due to the fact that shocks have a strong relation with the variations in stagnation pressure, according to basic fluid dynamics of compressible flows. The prescribed

5.4 Uncertainty Quantification on 3D RANS simulations

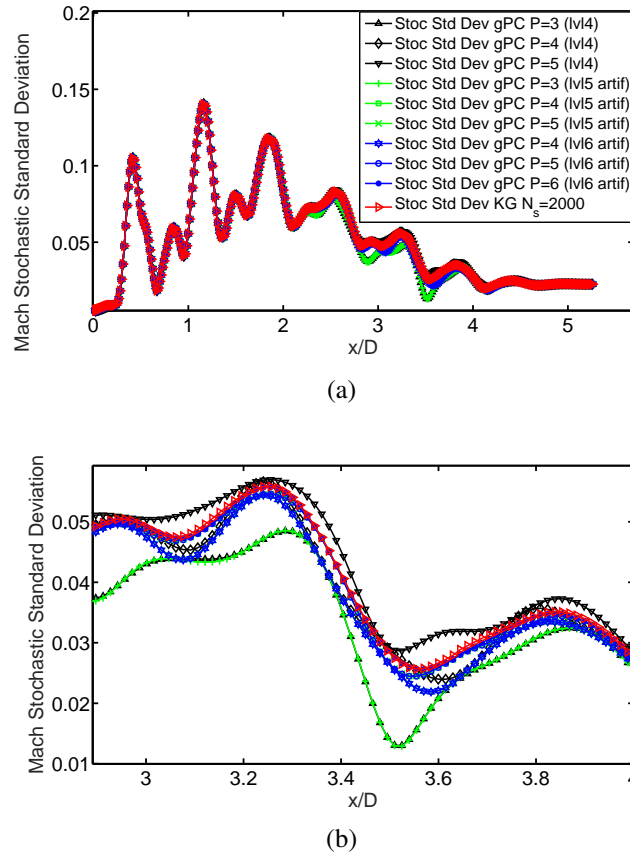


Figure 5.14 Evolution of (a) Mach stochastic standard deviation for different P and levels of the sparse grid and (b) a zoom of the hardest part in the convergence analysis. These results are compared with Kriging surrogates sampled by means of LHS with $N_s = 2000$.

uncertainties would therefore, as expected, be affecting the robustness of the simulated case scenario.

- As one of the major purposes of this type of studies is also to check how the input of uncertainty would make the simulation be closer to real performance, one can also look at Fig. 5.19, where the first shock-cells are shown. In this figure, the standard deviation envelopes show that, despite the fact that the CFD RANS with Spalart-Allmaras (deterministic simulation) was accurate, and the addition of uncertainty (deterministic simulation \pm std) perfectly wraps the experimental data, the stochastic plot envelopes (stoch mean \pm std) are not able to cover all the experimental data after the first peak. This is not surprising, since CFD simulations are rarely able to undergo a perfect match with experiments (especially in high-speed flows with shocks), and the most relevant peaks are more or less captured or close to the envelopes, not being remarkable outliers. On the other hand, the feature that they cover accurately is how the position of the shock-cell is being varied by uncertainty in p_s and R_t . In fact, it can be observed that the

5.4 Uncertainty Quantification on 3D RANS simulations

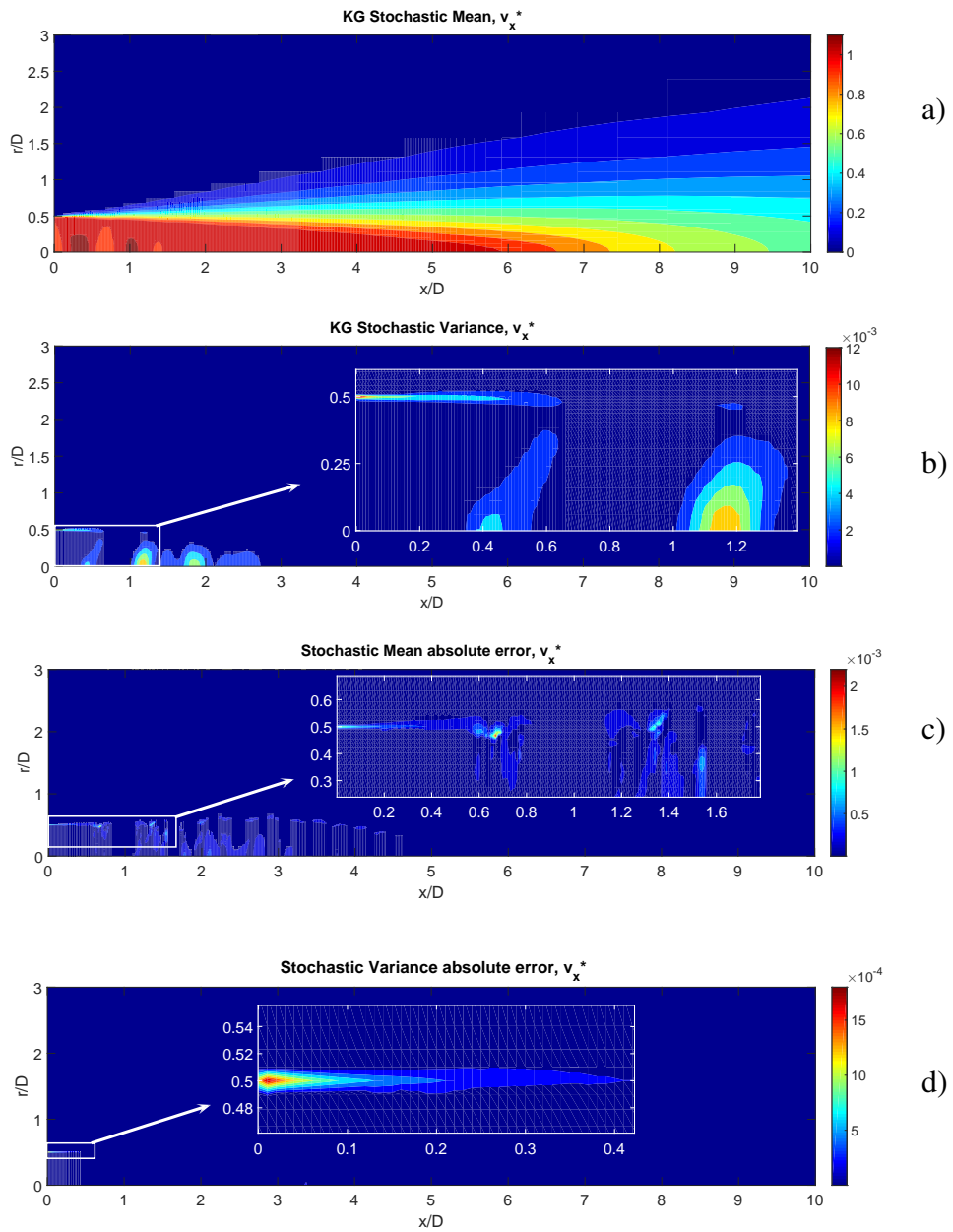


Figure 5.15 Contour plots of v_x^* (a) stochastic mean and (b) variance by means of LHS on KG surrogates. Contour plots of the absolute error between (c) stochastic mean and (d) variance between KG and gPC methods.

bigger the input uncertainty, the more disturbed the oscillatory pattern is downstream, as consequence of the variations in the shock-cell positions and dissipation. Obviously, the aim is not to always wrap the experimental data in any case (as otherwise very large input uncertainties would be desired), but to show a more complete description

5.4 Uncertainty Quantification on 3D RANS simulations

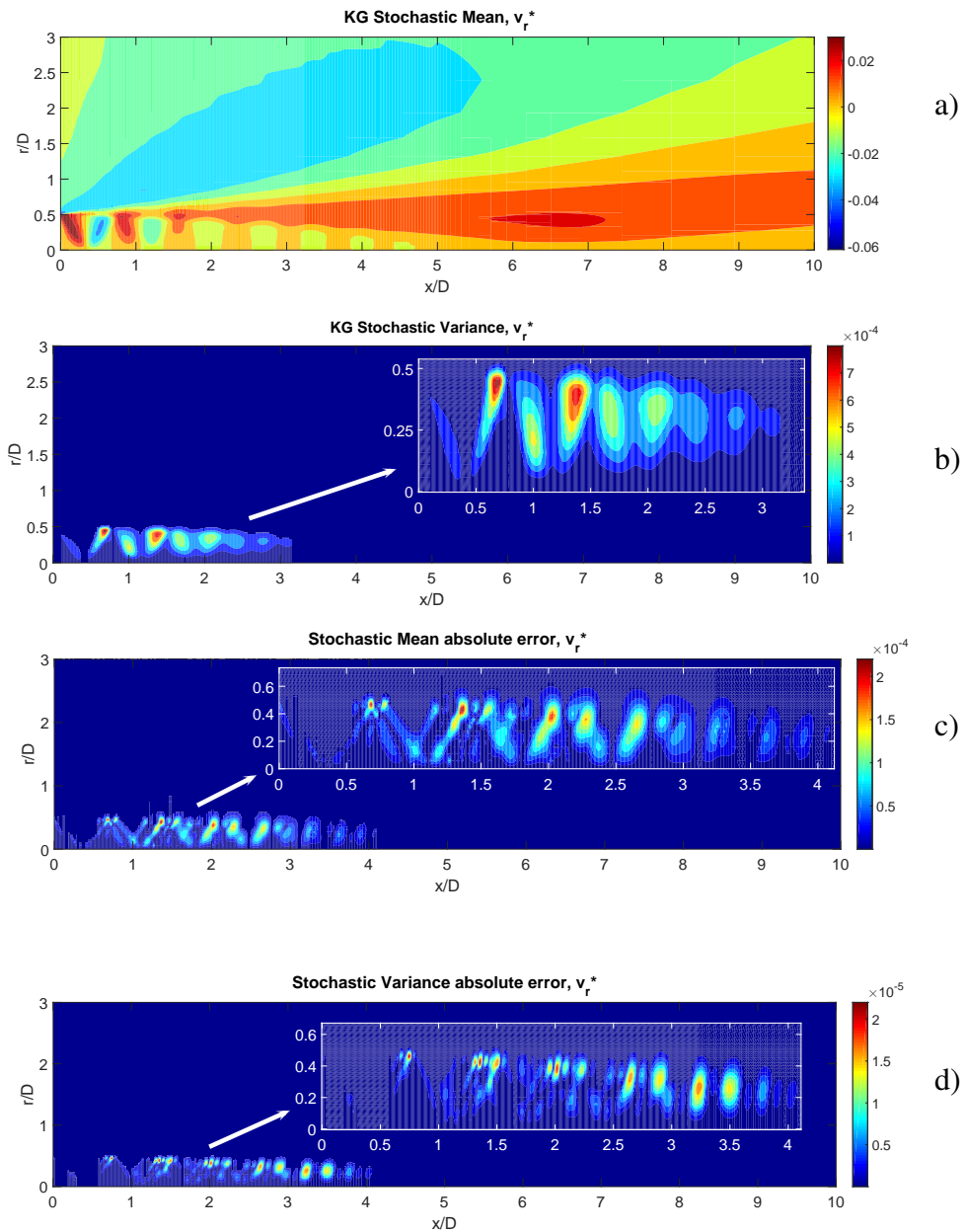


Figure 5.16 Contour plots of v_r^* (a) stochastic mean and (b) variance by means of LHS on KG surrogates. Contour plots of the absolute error between (c) stochastic mean and (d) variance between KG and gPC methods.

for validation of the CFD simulation and how sensitive to relevant input uncertainty is.

5.5 Global Sensitivity Analysis by Means of Generalised Polynomial Chaos and Kriging Surrogates

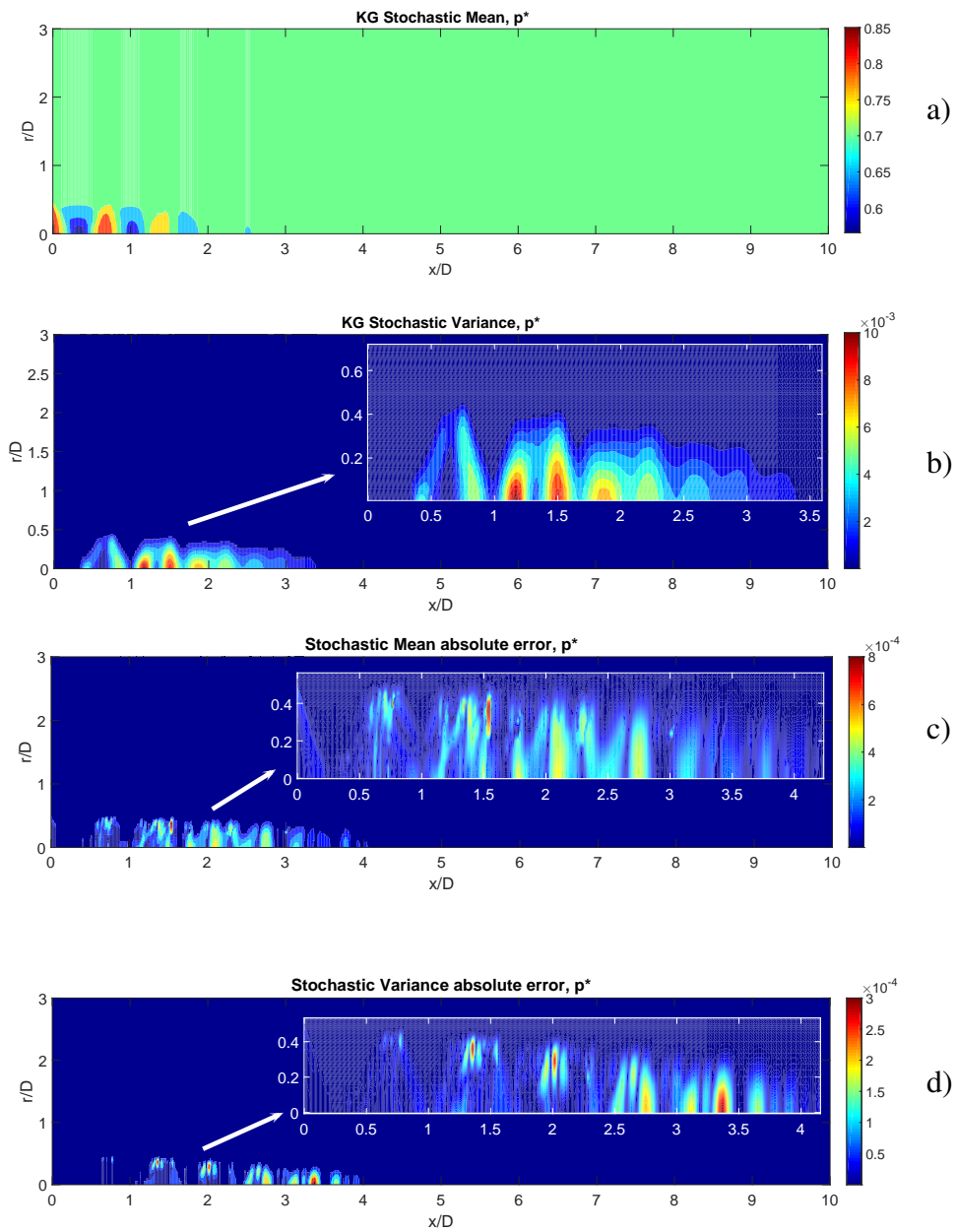


Figure 5.17 Contour plots of p^* (a) stochastic mean and (b) variance by means of LHS on KG surrogates. Contour plots of the absolute error between (c) stochastic mean and (d) variance between KG and gPC methods.

5.5 Global Sensitivity Analysis by Means of Generalised Polynomial Chaos and Kriging Surrogates

As explained in Chapter 2, an extension of UQ is the global sensitivity analysis. There are different methods for global sensitivity analysis, such as Screening Method, Derivate

5.5 Global Sensitivity Analysis by Means of Generalised Polynomial Chaos and Kriging Surrogates

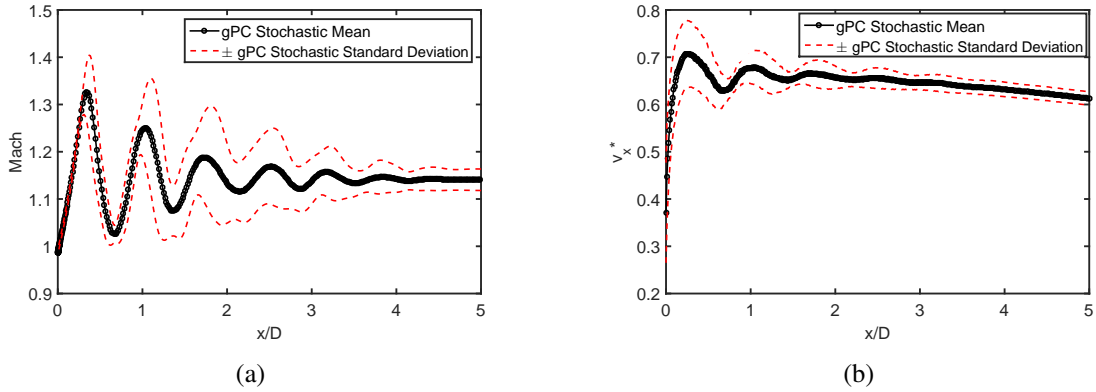


Figure 5.18 Stochastic mean and standard deviation envelopes with gPC for (a) Mach along centreline and (b) dimensionless axial velocity, v_x^* along the lipline.

Based Sensitivity Analysis or Variance-Based Analysis [230]. The analyst should choose the appropriate one depending on the computational cost, dimension of the problem or the expected output, among others. For the purposes of this work, a Variance-Based Analysis has been chosen [204]. One of the main reasons of using this method is the possibility of ranking the influence of the input factors by sensitivity indices.

As the sensitivity indexes have relation with UQ, the approaches from Section 5.4 have been used in this section as well. Particularly, the Kriging surrogates are sampled according to [105] and the coefficients from gPC are used to compute the sensitivity indexes. Despite that sampling could also be done on the Polynomial Chaos Expansion, it is worthy to remind that a second objective in this work is to have two different methodologies to compare results (sampling and quadrature based approaches).

We have proceeded in this way due to the fact that one of the interesting features of gPC is the possibility of performing sensitivity analysis straightforward after uncertainty quantification. For such task, it is not difficult to realise that there is a clear relation between Eqs. (2.25), (2.49) and (2.50), as commented in Chapter 2.

Regarding the Kriging surrogates, \hat{y}^{KG} , as they are available from the former uncertainty analysis, it is now possible to compute the sensitivity indices from Eqs. (2.52) and (2.53). A very efficient method has been coded in MATLAB by following the suggested procedure in [105], which can be extended to any other surrogate or mathematical model as it is based on a sampling. With this method, the first order sensitivity with Kriging surrogates, S_i^{KG} , and the total effect, S_{Ti}^{KG} , can be computed as already explained in detail in Chapter 2.

5.5 Global Sensitivity Analysis by Means of Generalised Polynomial Chaos and Kriging Surrogates

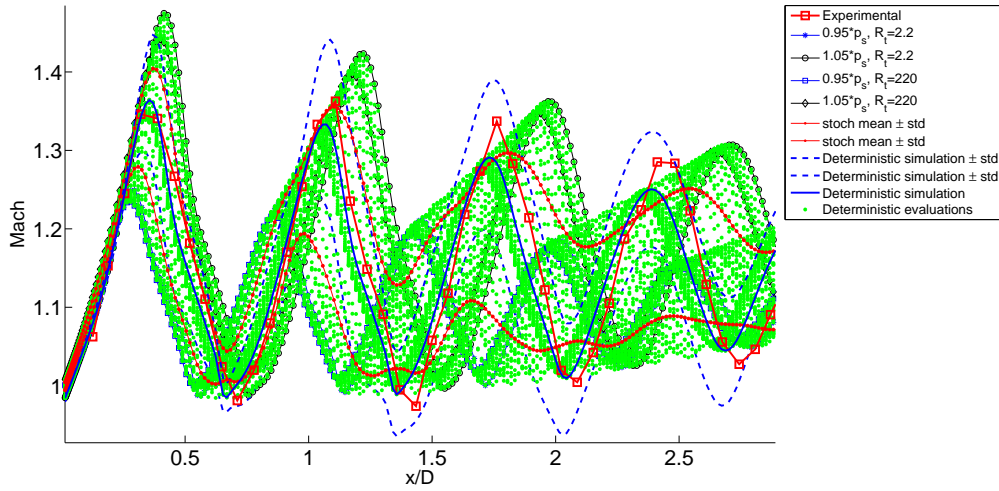


Figure 5.19 Validation of computations with the Mach number along the centreline. The green dots are the deterministic evaluations required for the fourth level of accuracy of the Clenshaw-Curtis sparse grid.

5.5.1 Comparison and Discussion of Global Sensitivity Analysis Results

As uncertainty quantification results were compared by means of Kriging surrogates and Polynomial Chaos in Section 5.4, attention is now focused on the sensitivity contours with both methods for the dimensionless static pressure, p^* , plotted in Figs. 5.20 and 5.21.

One of the motivations of using two methods for sensitivity analysis purposes is that the resulting contours for the sensitivity indices were not intuitive, which could be product of errors when implementing the codes. Fortunately, both methods provided similar solutions, discarding that. The explanation behind the contours appearance can be that, when performing sensitivity analysis, all the sensitivities of the domain are quantified simply providing a ‘ratio’ of contribution of uncertainty at every cell of the CFD domain.

A solution to provide a more intuitive and useful insight is to show the contribution to the total uncertainty by each parameter as shown in Figs. 5.22-5.24. To the knowledge of the author, there are not previous works showing such pictures to visualise the impact of each uncertainty in each area of the computational domain, despite how helpful is it for engineers.

For representation of the quantities of interest, now only gPC results will be shown, as the errors between the implemented methods were checked in Section 5.4 and they were practically negligible.

In a similar manner than for uncertainty quantification, in this section several interesting patterns have been found linked to apportions to the input uncertainties:

5.5 Global Sensitivity Analysis by Means of Generalised Polynomial Chaos and Kriging Surrogates

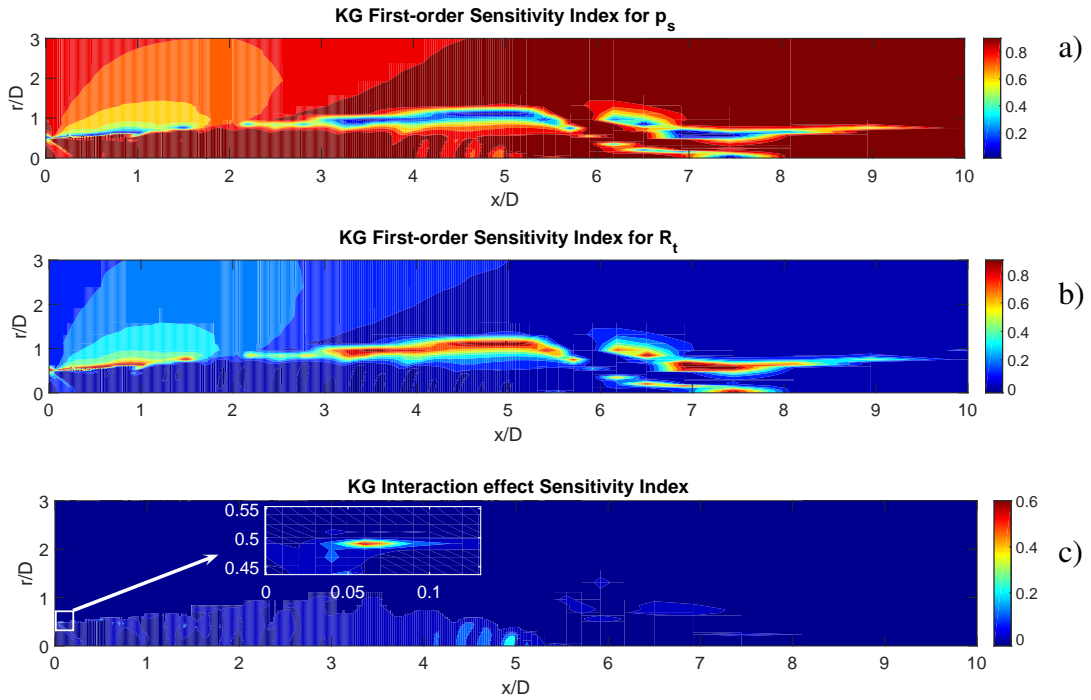


Figure 5.20 Sensitivity indices contour plots by means of Kriging for p^* . a) and b) are the first-order sensitivities and c) the higher-order interaction.

- For the dimensionless axial velocity, v_x^* , the most sensitive region was detected along the lipline, close to the nozzle lip (see Fig. 5.15.b). This uncertainty is mainly due to uncertainty in the laminar to turbulent viscosity ratio, R_t , from the Spalart-Almaras turbulent model (see Fig. 5.22.b). The stagnation pressure uncertainty, p_s , is also playing an influential role (Fig. 5.22.a), but its impact is not as high as by R_t in the area immediately at the exhaust exit. The contribution to uncertainty in the shock-cell areas is done only by means of p_s uncertainty.
- Regarding the dimensionless radial velocity, v_r^* , the most sensitive region is immediately below the lipline (see Fig. 5.16.b). This uncertainty is undoubtedly linked to p_s as seen in Fig. 5.23.a.
- For the dimensionless static pressure, p^* , the most sensitive region is along the centreline (see Fig. 5.17.b). As can be seen in Fig. 5.24.a, p_s uncertainty is again the most influential one and the influence of R_t uncertainty is practically null. Closer to the lipline, R_t uncertainty is greater, but not very significant.

This analysis suggests that p_s uncertainty is a common factor in the three analysed uncertain flow parameters (dimensionless axial velocity, radial velocity and static pressure) and espe-

5.6 Uncertainty Quantification on Parabolised Stability Equations (PSE) Applied to Stability Analysis

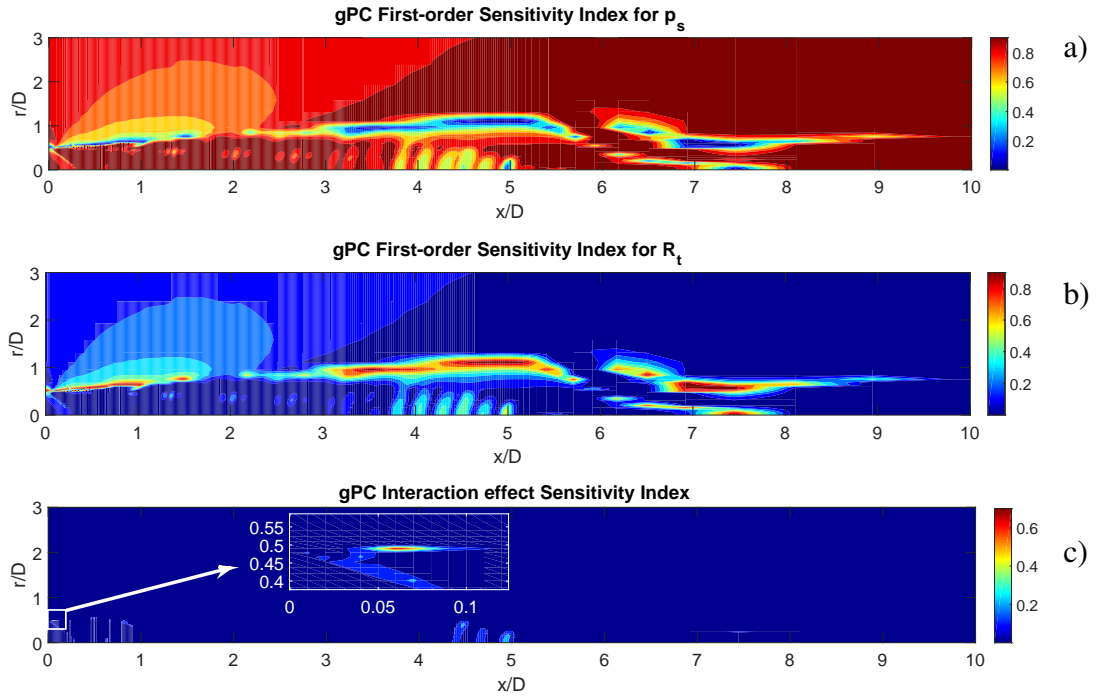


Figure 5.21 Sensitivity indices contour plots by means of gPC for p^* . a) and b) are the first-order sensitivities and c) the higher-order interaction.

cially influential in the area where the shock-cells are located.

5.6 Uncertainty Quantification on Parabolised Stability Equations (PSE) Applied to Stability Analysis

The last part in the uncertainty quantification framework is the PSE analysis. Here, the earlier introduced Stochastic Collocation Method (see Chapter 2.1) will be applied. The main idea behind this approach is to use a previously generated stochastic base-flow from CFD as input for PSE. So that, the contribution of the input uncertainties can be artfully accounted in the PSE approach for stability analysis. This can be a useful tool in order to understand how noise emission is being affected by uncertain flow instability when an acoustic analogy is available [227, 135].

The Parabolized Stability Equations [95] approach (PSE) consists of solving a set of Partial Differential Equations (PDE) mostly parabolic in the streamwise direction. Contrary to Linear Stability Theory (LST), where local parallel flow is assumed, PSE take into account also the small streamwise variations of the base flow and of the disturbances directly in the formulation.

5.6 Uncertainty Quantification on Parabolised Stability Equations (PSE) Applied to Stability Analysis

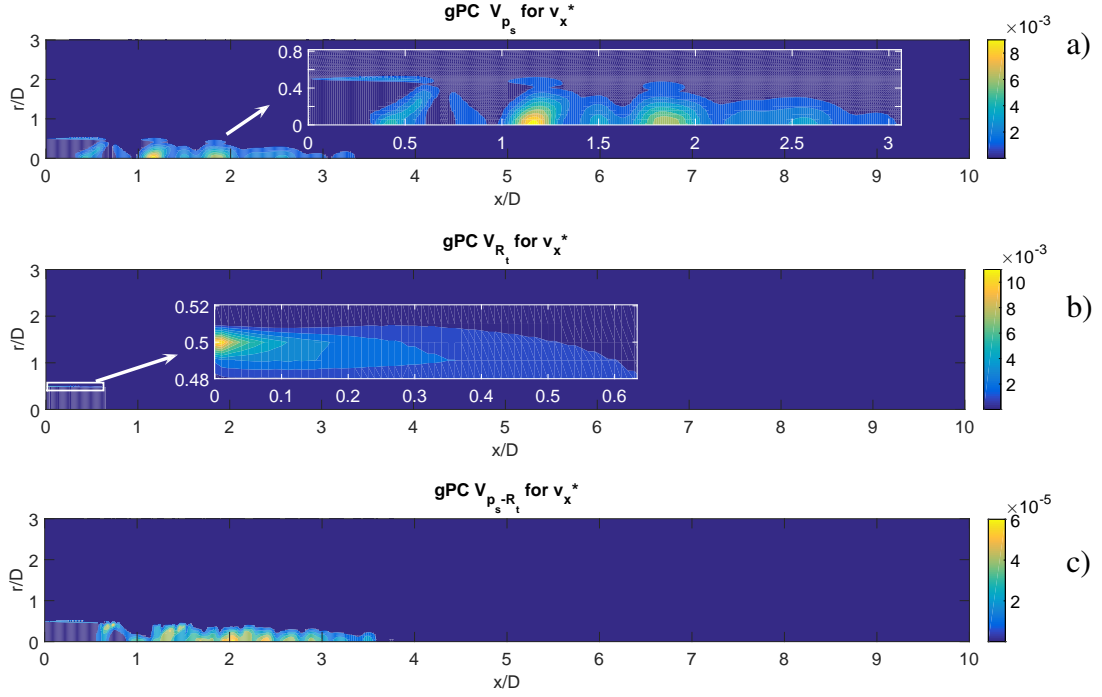


Figure 5.22 Contribution to the total variance of a) stagnation pressure, b) laminar to turbulent viscosity ratio and c) their interaction, for v_x^* .

For this analysis, the PSE are derived from the Linearized Euler Equations (LEE) in cylindrical coordinates (x, r, θ) . The total flow field \mathbf{q}^0 is built by the superposition of two parts: a base flow $\bar{\mathbf{q}} = (\bar{u}_x, \bar{u}_r, \bar{u}_\theta, \bar{\rho}, \bar{p})^t$ and a small perturbation quantity $\mathbf{q}' = (u'_x, u'_r, u'_\theta, \rho', p')^t$, and the t exponent denoting transpose. Any perturbation is assumed to have a like-wave exponential term $\chi(x) \exp(i(m\theta - \vartheta t))$ and a x -slowly amplitude function $\mathbf{q}(x, r)$:

$$\mathbf{q}' = \mathbf{q}(x, r) \chi(x) \exp(i(m\theta - \vartheta t)), \quad \text{with} \quad \chi(x) = \exp\left[i \int_{x_0}^x \alpha(s) ds\right], \quad (5.2)$$

where $\alpha(x)$ is the complex axial wavenumber. The imaginary part, $\alpha_i(x)$, can be defined as a growth rate and $2\pi/\alpha_r(x)$ corresponds to a spatial wavelength. m is the fixed integer azimuthal wavenumber ($m = 0$ in our application), the real number ϑ is the fixed angular frequency of the disturbance and x_0 is the inlet of the computational domain. Substituting Eq. (5.2) into LEE we obtain the so-called Parabolized Stability equations (PSE):

$$L_{PSE} \mathbf{q} = \mathbf{0}. \quad (5.3)$$

From Eq. (5.2) it can be noticed that the streamwise change of the disturbance can be described by the product of the amplitude function and the exponential term. This ambiguity

5.6 Uncertainty Quantification on Parabolised Stability Equations (PSE) Applied to Stability Analysis

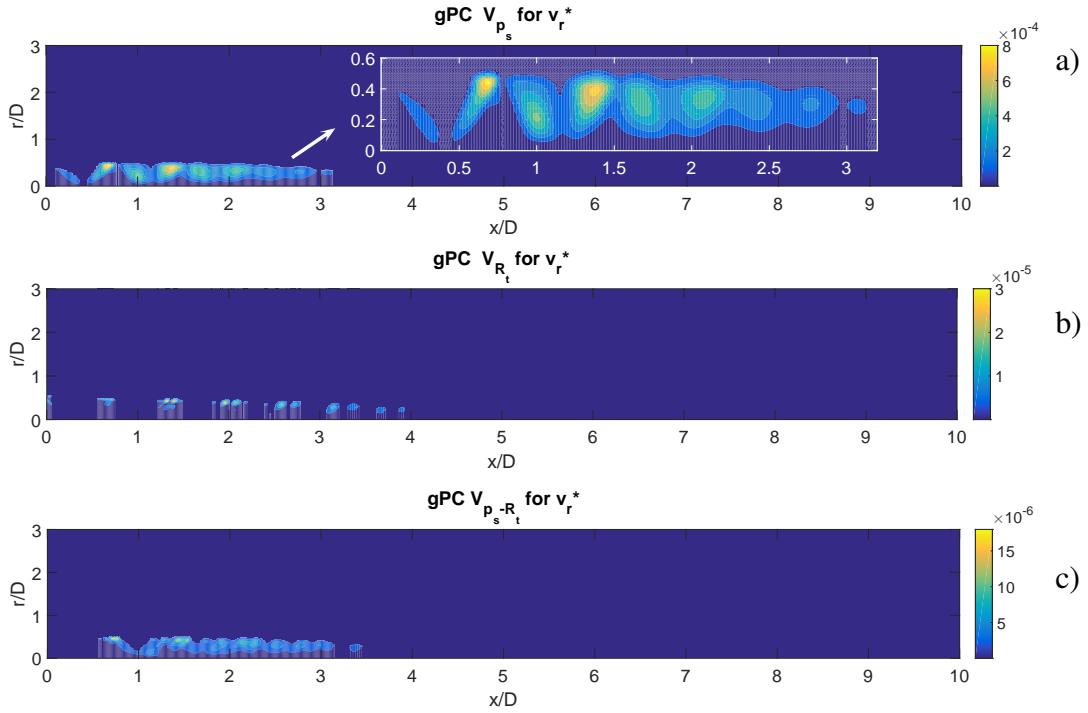


Figure 5.23 Contribution to the total variance of a) stagnation pressure, b) laminar to turbulent viscosity ratio and c) their interaction, for v_r^* .

must be resolved by the introduction of an additional equation, called normalization or closure relationship, which imposes that the growth of the disturbance is absorbed by the wave function part of the decomposition $\chi(x)$, making sure that the shape function $\mathbf{q}(x, r)$ stays slowly varying in x [95]. It is then set

$$N_{imp}(\mathbf{q}, x) = \int_0^\infty \bar{\bar{\mathbf{q}}}^t \frac{\partial \mathbf{q}}{\partial x} r dr = 0, \quad (5.4)$$

where t denotes transpose and double over-bar, complex conjugate. Eqs. (5.3) and (5.4) are solved using a streamwise marching solution starting from the initial condition at $x = x_0$ which is the solution of the local approach (LST). The PSE solver 'Pasteq' designed by the ONERA stability team [134] is used by Tobias Ansalidi at the partner Institute de Mecanique de Fluides in Toulouse (IMFT) for the required deterministic simulations for uncertainty quantification presented in the next section. For further information regarding the theory behind PSE, the reader is suggested to see [11], where the theoretical description here shown can also be found. The theory introduced in this section is merely informative as the PSE is entirely handled as a black-box model.

5.6 Uncertainty Quantification on Parabolised Stability Equations (PSE) Applied to Stability Analysis

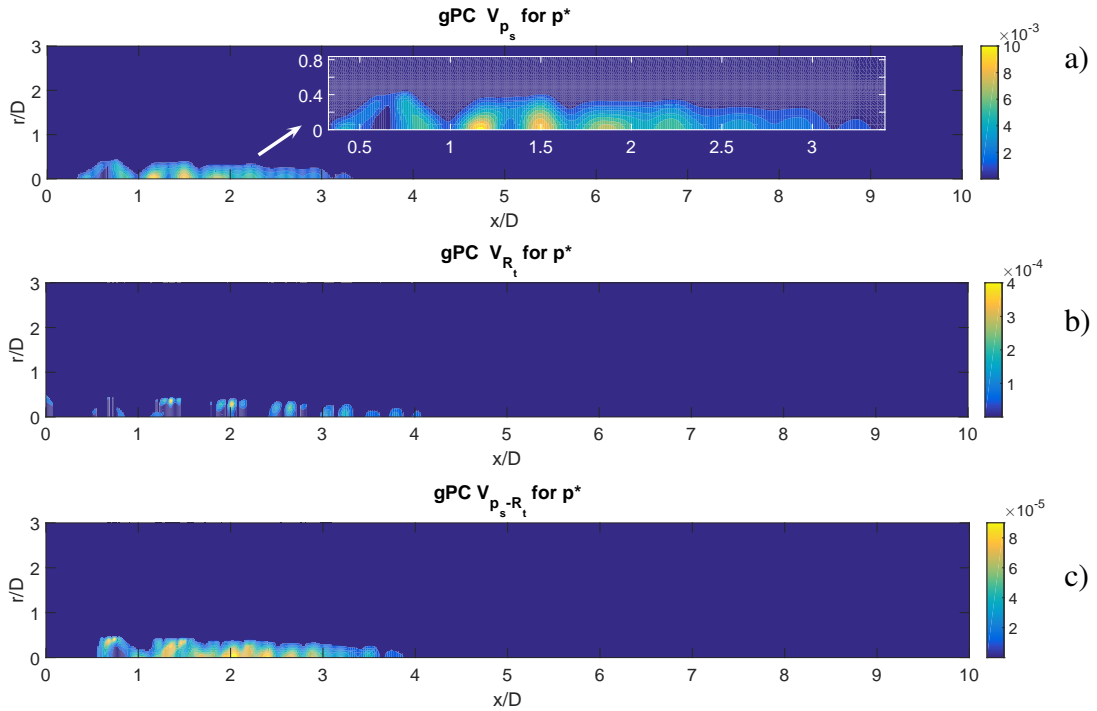


Figure 5.24 Contribution to the total variance of a) stagnation pressure, b) laminar to turbulent viscosity ratio and c) their interaction, for p^* .

5.6.1 Results from Uncertainty Quantification on PSE from a Stochastic CFD Base-flow

Without the framework presented in this part of the thesis, it would be impossible to quantify the experimental and turbulent uncertainties on PSE analysis, as it is not possible to directly deploy the mentioned random inputs on the PSE formulation. The quality of the results depends not only on the correct development of the PSE analysis, but also on how the base flow from CFD is. So that, if the base flow is stochastic, the deterministic approach of PSE can be turned into stochastic as well.

An approach similar to the one presented for the CFD simulations is deployed here. In Section 5.4, some deterministic simulations (collocation points) were run based on the input uncertainties, and the deterministic outputs were used to compute the statistics for the stochastic analysis. Such deterministic base-flows from CFD are used as input for PSE, so that, several deterministic PSE outputs are generated. Then, Stochastic Collocation (see Chapter 2 for a theoretical definition and Chapter 2.4 or 4 for applications) can be applied for this continuation of the propagation of uncertainties, in order to obtain the statistical moments. With this approach it is possible to quantify how the experimental and turbulent uncertainties affect not only the CFD simulations, but also the development of Kelvin-Helmholtz (K-H) instabilities (see Fig. 1.6). The converged results of the uncertainty analysis on PSE with the

fourth level of the Clenshaw-Curtis sparse grid (from the CFD design of experiment) can be seen in Fig. 5.25.

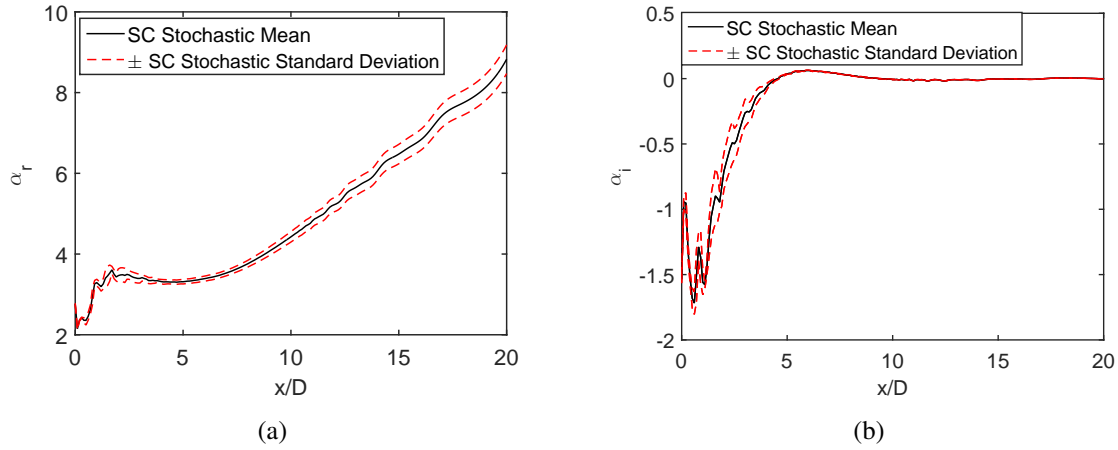


Figure 5.25 Impact of input uncertainties on $\alpha(x)$ for $St = 0.4$. The real part, α_r , is related to the spatial wavelength of the instabilities and the imaginary part, α_i is related to the growth rate.

In these plots can be observed that, for the Strouhal number under consideration $St = fD/U = 0.4$, with f the frequency at which there is a maximum in the noise emission (a shock-cell noise peak in fact) [8] and U the mean velocity of the flow, the spatial wavelength of the K-H instabilities is starting to be affected by uncertainties after $x/D = 7$. This uncertainty is increasing the farther one goes along x/D , together with the natural increase of α_r . For the results of α_i under uncertainty, it can be noticed a ‘noisy’ behaviour for $x/D < 5$, where results present some variance because of a high sensitivity to input uncertainty in the birth area of K-H instabilities. For $x/D > 5$, the flow becomes stable and input uncertainties are not affecting at all on the instability growth rate. As the RANS simulation started to be dissipative after the fourth shock, the jet flow after $x/D = 3$ still have some greater influence of the shock-cells and in this stability analysis the ‘noisy’ behaviour for $x/D < 5$ might be present up to a further x/D value. Also the stability of the flow could be delayed. This could be only demonstrated with higher-quality CFD simulations unaffordable here.

5.7 Conclusions

The main objective of this analysis has been to assess computationally the propagation of uncertainties in the computation of under-expanded jet flows in order to improve the popular deterministic approach. This represents a novel study in jets in the presence of shock-cells and the framework here introduced determines the only possible way to quantify the impact of experimental and turbulent model uncertainty on stability analysis through PSE. This

study can lead to a better understanding about how uncertainty at different design stages can affect to the analysis to be validated against experimental results, to improve the current trend of deterministic approaches in simulations and to create more robust designs in jet flows and aeroacoustics research.

Non-Intrusive Uncertainty Quantification techniques have been applied to 3D RANS CFD simulations of a supersonic under-expanded jet, accurately simulating the most relevant shock-cells, in order to understand the impact of input uncertainty (experimental and in turbulence modelling) affects to flow properties. A global sensitivity analysis was also carried out to understand the relevance of each random input in the output uncertainty. The results from the application of both methods (generalised Polynomial Chaos and Kriging with Latin Hypercube Sampling) have undergone a good match in the shown comparisons.

It has been relevant to extend this study to the whole CFD domain instead of relevant points, since some interesting regions such as the centre and lipline are sensitive and this study can lead to a more detailed understanding of the CFD simulations of jet flows to motivate future investigations or paying more attention to development of more robust designs. Especially if in a near future Large Eddy or Direct Numerical Simulations are affordable for uncertainty analysis in shock-cell noise, since more trustworthy conclusions regarding the physics of the flows could be summarised. From the analysis on the CFD simulations, the following conclusions can be drawn:

- Despite the fact that shock-cells could be problematic in catching the features in uncertainty quantification, **convergence was achieved with only 65 collocation points**. The shape of the Kriging surrogates looks appropriate to interpolate the training data, as convergence was achieved, providing also the same results as Polynomial Chaos.
- **Shock-cell position and amplitude is highly sensitive to input uncertainty**. The evolution of the Mach number was checked and its standard deviation has clearly revealed that fact. This effect was also noticed in the contour plots of the variance in v_x^* , p^* and v_r^* . Under a sensitivity analysis it has been observed that the uncertainty below the lipline (where the shock-cells are located) is mostly due to the uncertainty in the stagnation pressure.
- **The area immediately after the nozzle lip is highly sensitive to input uncertainty**. This outcome can be observed in the variance of v_x^* , where this interesting behaviour can be product of the pressure suction effect. The uncertainty in that region is something interesting to take into account, since this is the location of the jet where the screech feedback loop takes place, and uncertainties in the simulations can have influence in computational approaches. However, from a steady RANS simulation this cannot be concluded and future work would be necessary on LES with this drawback in mind. From sensitivity analysis, it has been also demonstrated that both the injection

of turbulence and stagnation pressure imprecisions are actively contributing to that feature in the computational simulations. Besides that, it can be observed in v_r^* a high uncertainty immediately below the lipline and in this, the variance of stagnation pressure is the most influential parameter. This shows that the simulated stochastic behaviour of the jet is affecting the uncertainty spreading in the radial velocity at the lipline in the presented computational simulations.

- As one of the aims of UQ is also to check how the input of uncertainty would make the difference in the deterministic simulation, the analysis along the Mach centreline (the hardest part to be validated due to the shock-cells) has been **checked against the experimental data**. The standard deviation envelopes show that, despite the fact that the CFD RANS with Spalart-Allmaras was accurate for the first shock-cells, the stochastic plot envelopes do not cover all the experimental data after the first peak. This is not surprising, since CFD simulations are rarely able to undergo a perfect match with experiments (especially in high-speed jet flows), and the most relevant peaks are more or less captured or close to the envelopes, not being considered far outliers. However, the position of the shock-cell is being varied by uncertainty in p_s and R_t , having such effect now covered in the simulations, and then providing a more trustworthy validation of computational results. Obviously these results could be improved with high-fidelity simulations such as LES, unaffordable yet for such computationally demanding task.

In addition, the stochastic base-flows generated are also employed for uncertainty quantification on Parabolised Stability Equations, that model the jet flow instabilities. Once a stochastic base-flow is available, it can be used as input for stability analysis. The results have shown that for the Strouhal number $St = 0.4$, the spatial wavelength of K-H instabilities is sensitive in far x/D distances, but it is slightly influenced by input uncertainties closer to the nozzle. With respect to the growth rate of the instabilities, the region near the nozzle is showing a ‘noisy’ behaviour where input uncertainties are influencing the growth rate. But when the flow becomes stable, uncertainties are not influencing anymore. However, as the CFD RANS simulation was not very accurate after the fourth peak, this stability analysis might be slightly changed. This could imply a longer noisy area for α_r and α_i , and a light delay of the stability in the α_i plot.

These results support the utility of the presented framework for propagation of uncertainties, since it has been possible to measure the contribution of uncertainties from experiments and turbulence modelling on Parabolised Stability Equations for the K-H instabilities study, with an extensive analysis on CFD simulations in between. From this work, future research is encouraged based on the unavoidable drawbacks here commented, as discussed in the final

chapter on conclusions and future work (Chapter 6). This framework is specially interesting for industrial design life cycles in aeronautical or aerospace thrusts involving computational simulations of flows.

Regarding the engineering applications under study in this thesis, this is the last chapter, where a framework for propagation of uncertainties in under-expanded jets has been investigated. In the next chapter, the most relevant conclusions in this thesis and suggestions for future work will be discussed.

Chapter 6

Conclusions and Suggested Future Work

This chapter aims to synthesise the most important conclusions drawn from the investigations in this thesis, as well as to suggest future work based on the limitations of the followed methodology, other possible applications or extensions of the approaches. Few details on the methodology can be discussed here, but the reader is suggested to see Chapter 2 for mathematical descriptions on the UQ/SA methods, and the sections ‘Methodology and Challenges’ in Chapters 3, 4 and 5 for the industrial jet investigations.

6.1 CFD Simulations and UQ for Incompressible Swirling Impinging Jet Flows with Heat Transfer Purposes.

6.1.1 Conclusions and Contribution to Knowledge

The work presented in Chapter 3 addresses a novel computational approach for swirling impinging jet flows. There is no literature on such flows generated by rotating pipes for heat transfer, despite the fact that the addition of swirl has been noticed as beneficial for heat transfer enhancing in both experimental [248, 18, 130] and computational [174, 177, 3] studies.

The novelty of the approach mainly relies on the two-step simulation developed. Regarding the computational simulations of swirling flows (*Simulation 1*), there is a vast literature [98, 104, 117, 60, 80, 166] about the turbulent models to be used for confined swirling flows when the RANS equations are used, and the general viewpoint is that the RSM performs the better, as concluded in an extensive numerical test in this work with several turbulent models. However, RSM is too expensive for *Simulation 2*, and also to have such a large picture as the two simulations together in the same computational domain requires a very long pipe to achieve the fully developed flow. These are the main motivations to split in two parts, and it has been proven that is suitable.

6.1 CFD Simulations and UQ for Incompressible Swirling Impinging Jet Flows with Heat Transfer Purposes.

By this suggested approach, it was possible to use a short pipe for *Simulation 1* imposing periodic conditions and validating these results with [101]. Also, the $k - \omega$ turbulent model was employed in *Simulation 2*, having an enormous computational cost saving in both simulations.

The generation of swirl with a rotating pipe for impingement jets has not been addressed before, but other methods were tested in literature. Depending on the system, the jet has different patterns and hence, the spreading will be different. This is influential for the impinging conditions affecting the heat transfer as in the swirling jet, the degrees of jet growth, entrainment of ambient air, and jet decay are affected by the degree of swirl [18, 195] and other perturbations from generation mechanisms. In [202] it has been reported that even the addition of light swirl can change significantly the behaviour of the jet. However, as seen in the aforementioned papers, this is also influenced by the nozzle-to-plate distance. In this work, the closer the nozzle-to-plate distance, the most influential the swirl is to enhance the heat transfer, as can be seen in Fig. 3.23.

By comparing this mechanism with other methods from literature, there are some advantages that demonstrates that this can be simpler but efficient. There is a remarkable benefit in the possibility to increase the swirl when keeping the Reynolds number fixed. Other methods in literature require an increase in Reynolds number, which might be impossible under some circumstances and/or increase the angle of blades/spirals of ducts, what is constrained to a maximum angle and manufacturing costs.

The second part of the analysis is presented in Chapter 4. This chapter complements Chapter 3 by the addition of experimental uncertainty, that is not yet a popular add-on to CFD analysis. Experimental random variables are taken into consideration, leading to a complete computational analysis, not assessing the quality of the approach only under a deterministic framework. This chapter addresses the quantification of uncertainties by means of the so-called Stochastic Collocation Method, which is applied on the two-steps numerical simulation.

To carry out an UQ study is very expensive, since several simulations are compulsory. For less computational cost, some mathematical models are also suggested for velocity and turbulent profiles, in order to avoid running *Simulation 1* when increasing the number of collocation points for uncertainty quantification.

To make these models also available to other researchers, User Defined Function (UDF) codes in *C* are given ready to be imposed in FLUENT. The quality of the given models for the velocity and turbulent profiles has been tested by stretching also the values of S from 0 up to 1.5, with quite accurate performance.

Uncertainty is always present in test rigs and it is not a standard thing to implement them into Computational Fluid Dynamic simulations. An advantage in studying the volume flow rate, Q , as uncertain is that several uncertainties such as those related to measurement tools

6.1 CFD Simulations and UQ for Incompressible Swirling Impinging Jet Flows with Heat Transfer Purposes.

tolerance, pipe diameter, loss of pressure or density variations can be accounted in only one factor.

In both cases (with and without imposed models) it has been observed that the input uncertainties have a light impact on the Nusselt number along the plate, something expected for a robust experimental facility. It was also noticed that Q was the most influential parameter, as the angular velocity Ω had a very light contribution to uncertainty, so this concludes that in an experimental facility, engineers must put more effort into reducing the variance in the volume-flow rate by *e. g.* avoiding associated pressure losses.

Industrial applications of this type of jets are cooling of electronic components [99, 129] or impinging gases and flame jets [148, 236] for instance, but it is not a very extended method and most of the applications that can be found are in academic research. To show the possibility of using such a simple device in this thesis, aims to encourage the use of jets in industrial practice too. From a practical viewpoint, in order to make the presented mechanism suitable for more industrial applications, some future research is suggested and discussed.

6.1.2 Suggested future work

- **Beating the size of design.** Depending on the application, this approach might or might not be eligible. This study is dimensionless (Re and S are chosen for dimension independence), but the reader needs to remember that the pipe must be long enough to achieve a fully-developed flow, and *e. g.* for small electronic devices this method may not be convenient. Then, suggested work would be, for instance, to investigate small rotating pipes, use of fans to induce swirl effects or the mix of rotation, blades and fans, to produce a similar (or enhanced) swirl flow pattern.

Although electronics is not the particular scope of this work, this method could have a nice impact in cooling electronics community, challenging other popular mechanisms. The use of microjets/jets has been shown to be comparable to commercially available electronic cooling fans [111] and sprays [264], so suggested improvements could help for better developments. Jet impingement has been reported formerly as a great alternative to other cooling electronic methods, thanks to the also commented parametric dependence: by flexibly controlling some parameters it is possible to optimise the performance, making this approach very promising in the field [264].

- **The impinging shape and distribution of jets.** It is well-known in the heat transfer field that the greater the surface, the greater the heat that can be exchanged. Also, changes in shape can vary the flow behaviour (affecting the boundary layer separation or turbulence energy, for instance), and this leads to variations in the Nusselt number [177]. Very often, to change the impingement surface will not be possible, but other

6.2 Framework for Uncertainty Propagation in Aircraft Under-expanded Jet Flows Research

plausible options to research could be to make use of forced convection by swirl flows travelling in-between objects. To the knowledge of the author, there is no literature on a swirl approach in cooling electronics without fans.

A popular tested mechanism to improve the heat transfer by impingement is the use of several jets together (jet arrays). The benefits are clear: the jet can impinge on the desired points of the surface, where an enhanced heat transfer is desired. Some work as guidance can be [76, 107, 247, 37].

- **The shape of the nozzle.** This feature has been formerly reported as influential in the way the jet spreads and the heat transfer [235, 249, 217]. The addition of swirl to different nozzle shapes or shape optimisation can be interesting and studies are highly encouraged.
- **Use of high-fidelity simulations and experimental research.** To reproduce the CFD simulations by LES, DES or DNS would provide better computational results. Also, these numerical analysis could give more information not only about heat transfer, but also flow physics, such as the evolution of vortical structures [88]. It would certainly be very interesting to see how the vortex breakdown and spreading angle is affected at a very high angular velocity. The impinging jet flows are a complex physics problem, and there are still unknowns to solve, such as why the azimuthal velocity changes the sign in the core for $H/D > 5$, as reported by [61, 62].
- **Heat transfer optimisation.** It would be possible to improve the mechanism here presented by finding the optimal problem set-up (nozzle-to-plate distance, surface variations, angular velocity, jet-to-jet distance in arrays, etc.) as initially suggested in [85], and these steps have already led to further recent optimisation studies such as [177, 176, 178].

6.2 Framework for Uncertainty Propagation in Aircraft Under-expanded Jet Flows Research

6.2.1 Conclusions and Contribution to Knowledge

The main objective of the analysis in Chapter 5 has been to study the propagation of uncertainties (from experiments and turbulent modelling) in computational research of under-expanded jet flows, in order to improve the deterministic scenario, a common practice even in the current state-of-the-art approaches. This framework represents a novel study in this type of jet in the presence of shock-cells and the approach here introduced determines the only possible way to quantify the impact of experimental and turbulent model uncertainties on stability analysis through Parabolised Stability Equations, which can lead to more complete

6.2 Framework for Uncertainty Propagation in Aircraft Under-expanded Jet Flows Research

practices in the field, as presented in [83, 13].

In relation to the 3D Reynolds-Averaged Navier Stokes simulations, non-Intrusive Uncertainty Quantification techniques (generalised Polynomial Chaos and Kriging interpolation) have been applied in order to understand the impact of input uncertainty in the computed flow properties. It has been very interesting to extend this study to the whole CFD domain instead of relevant points or lines in the domain as most literature papers do, since some interesting areas have been identified as sensitive and then it is possible to provide much more complete information on the behaviour of the CFD simulation, which is pretending to mimic the flow physics. Moreover, a global sensitivity analysis was also carried out after the uncertainty quantification in order to understand the relevance of each random input in the output uncertainty as presented in [84].

Generally speaking, to perform uncertainty quantification and sensitivity analysis is not a new contribution itself, but one can conclude that the framework approach here presented improves the common deterministic approach that researchers tend to develop in computational studies of high-speed jet flows, omitting the impact of uncertainties in a realistic computational performance. This is the reason why uncertainty and global sensitivity analysis are both very relevant topics nowadays.

6.2.2 Suggested Future Work

From this work, future research is highly encouraged. A suggested improvement can be linked to the fact that the stochastic behaviour of the vortical structures that generate noise when interacting with shock-cells cannot be captured by RANS method. It is well-known that the interaction of the vortical structures and shock-cells drives acoustics and unfortunately this can only be analysed by LES or DNS simulations (the noise emission models existing for RANS are too empiric and poor to perform uncertainty analysis on them). That was the main reason for not carrying out the analysis not only on the jet flow but also on jet noise emission, which is a concern especially in aircraft cabin noise. Moreover, despite the fact that shock-cells after the third one are not very relevant in the under-expanded jet flow features, and with RANS they are difficult to be reproduced, LES would be suggested. Nowadays, the computational resources to perform uncertainty quantification with such high-fidelity simulations of flows in the presence of shock-cells are very limited, but can be something achievable in a near future.

Other suggested improvements to the presented analysis would be to include more sources of uncertainty or more realistic probabilistic distributions, that were not available during the writing of this thesis. For this reason, a conservative approach with uniform probabilistic distributions was applied to the random inputs.

6.3 Dissemination of Work to Date

Publications

- F.-J. Granados-Ortiz, J. Ortega-Casanova, C.-H. Lai: “Uncertainty Quantification and Modelling of CFD simulations of a Swirling Turbulent Jet created by a Rotating Pipe for Application to Heat Transfer from a Heated Solid Flat Plate“. 1st International Conference on Uncertainty Quantification in Computational Sciences and Engineering. 25-27 May 2015. Crete Island, Greece (SCOPUS published paper).
- F.-J. Granados-Ortiz, J. Ortega-Casanova, C.-H. Lai. “A Swirling Flow Generated by a Rotating Pipe for Impingement Heat Transfer Under Uncertainty. Part I: CFD Set-up“. International Journal of Heat and Mass Transfer. (Submitted).
- F.-J. Granados-Ortiz, J. Ortega-Casanova, C.-H. Lai. “A Swirling Flow Generated by a Rotating Pipe for Impingement Heat Transfer Under Uncertainty. Part II: Uncertainty Quantification and Use of Models“. International Journal of Heat and Mass Transfer. (Submitted).
- F.-J. Granados-Ortiz, C.-H. Lai, C. Perez-Arroyo, G. Puigt, C. Airiau. “Uncertainty Quantification and Sensitivity Analysis of an Under-expanded Jet“. AIAA Aviation 2016, 13-17 June 2016. Washington D. C., USA (AIAA paper).
- F.-J. Granados-Ortiz, C.-H. Lai. “A Novel Framework for Uncertainty Propagation in Multidisciplinary Design Life Cycle in Shock-cell Noise Research“. 22nd AIAA/CEAS Aeroacoustics Conference, 30 May - 1st June, Lyon, France (AIAA paper).
- T. Ansaldi, F.-J. Granados-Ortiz, C. Airiau, C.-H. Lai. “Sensitivity Analysis and Uncertainty Quantification for jet noise analysis“. Congrès Français de Mécanique 2015, organised by L’Association Française de Mécanique. 24-28th August 2015, Lyon (France) (Congress paper).

Presentations, Posters and Public Addresses

- F.-J. Granados-Ortiz, J. Ortega-Casanova, C.-H. Lai. Contributed paper talk: “Modelling for Computational Cost Reduction and Optimisation of an Impinging Swirling Jet created by a Rotating Pipe with Application to Heat Transfer from a Heated Solid Flat Plate“. The 8th International Congress on Industrial and Applied Mathematics. 10-14 August 2015. Beijing, (China).
- F.-J. Granados-Ortiz, C.-H. Lai. “An optimisable jet noise design life-cycle“. One-Day Workshop on Aircraft Noise and Aeroacoustics Research in the UK, 2nd April, 2014. Manchester (UK).

- F.-J. Granados-Ortiz, C.-H. Lai, K. Pericleous. “Identification and assessment of the impact of parameters in computer-based engineering processes“. One-Day Workshop on Applied and Numerical Mathematics, 6th June, 2014. University of Greenwich (UK).
- F.-J. Granados-Ortiz, C.-H. Lai, S. Davis. Presentation: “Uncertainty Quantification in jet-noise design life-cycle“. Aircraft Noise and Aeroacoustics Research in the UK. University of Greenwich. 20th April 2015.
- F.-J. Granados-Ortiz. “What can I do when data is expensive?”. Data Natives 2016. 6th May 2016, City University London, London, UK.
- F.-J. Granados-Ortiz, C.-H. Lai. Uncertainty Quantification in Jets. Aircraft Noise and Aeroacoustics Research in the UK/EU 2016. 2nd June 2016, Lyon (France).

Posters:

- F.-J. Granados-Ortiz, J. Ortega-Casanova, C.-H. Lai. “Propagation of uncertainty in jets (I)“, NASA Langley Uncertainty Quantification Challenge – UK Reception. Pullman St Pancras, London, 11th November 2015.
- F.-J. Granados-Ortiz, C.-H. Lai. “Propagation of uncertainty in jets (II)“, NASA Langley Uncertainty Quantification Challenge – UK Reception. Pullman St Pancras, London, 11th November 2015.

Public address:

F.-J. Granados-Ortiz. “Data analysis in the aerodynamic design industry“. 5th May 2016. University of Greenwich, London, UK.

Bibliography

- [1] Adya, S., 2011. Uncertainty quantification integrated to computational fluid dynamic modeling of synthetic jet actuators.
- [2] Ahlfeld, R., Belkouchi, B., Montomoli, F., 2016. Samba: Sparse approximation of moment-based arbitrary polynomial chaos. *Journal of Computational Physics* 320, 1–16.
- [3] Ahmed, Z. U., 2016. An experimental and numerical study of surface interactions in turbulent swirling jets.
- [4] Ahmed, Z. U., Al-Abdeli, Y. M., Matthews, M. T., 2015. The effect of inflow conditions on the development of non-swirling versus swirling impinging turbulent jets. *Computers & Fluids* 118, 255–273.
- [5] Aichinger, C., 2013. A sparse grid stochastic collocation fem for uncertainty quantification in a nanowire sensor model. Ph.D. thesis, University of Wien.
- [6] Alefeld, G., Herzberger, J., 2012. Introduction to interval computation. Academic press.
- [7] Amini, Y., Mokhtari, M., Haghshenasfard, M., Gerdroodbary, M. B., 2015. Heat transfer of swirling impinging jets ejected from nozzles with twisted tapes utilizing CFD technique. *Case Studies in Thermal Engineering* 6, 104–115.
- [8] André, B., 2012. Etude expérimentale de l’effet du vol sur le bruit de choc de jets supersoniques sous-détendus. Ph.D. thesis, L’École Centrale de Lyon.
- [9] André, B., Castelain, T., Bailly, C., 2013. Broadband shock-associated noise in screeching and non-screeching underexpanded supersonic jets. *AIAA Journal* 51 (3), 665–673.
- [10] Angioletti, M., Nino, E., Ruocco, G., 2005. CFD turbulent modelling of jet impingement and its validation by particle image velocimetry and mass transfer measurements. *International Journal of Thermal Sciences* 44 (4), 349–356.
- [11] Ansaldi, T., Airiau, C., 2015. Sensitivity analysis for subsonic jet using adjoint of non local stability equations. In: 21st AIAA/CEAS Aeroacoustics Conference, Dallas TX, USA.
- [12] Ansaldi, T., Airiau, C., Pérez Arroyo, C., Puigt, G., 2016. PSE-based sensitivity analysis of turbulent and supersonic single stream jet. In: 22nd AIAA/CEAS Aeroacoustics Conference. p. 3052.

- [13] Ansaldi, T., Granados-Ortiz, F.-J., Airiau, C., Lai, C.-H., 2015. Sensitivity and Uncertainty Quantification for Jet Noise Analysis. In: 22ème Congrès Français de Mécanique 2015, organised by L' Association Française de Mécanique. Lyon (France). 24-28th August 2015.
- [14] Askey, R., Wilson, J., 1985. Some basic hypergeometric polynomials that generalize Jacobi polynomials, vol. 319. Mem. Amer. Math., Providence, RI.
- [15] Asmussen, S., Glynn, P. W., 2007. Stochastic simulation: algorithms and analysis. Vol. 57. Springer Science & Business Media.
- [16] Babuška, I., Nobile, F., Tempone, R., 2007. A stochastic collocation method for elliptic partial differential equations with random input data. *SIAM Journal on Numerical Analysis* 45 (3), 1005–1034.
- [17] Bailey, S., Hultmark, M., Monty, J., Alfredsson, P. H., Chong, M., Duncan, R., Fransson, J., Hutchins, N., Marusic, I., McKeon, B., et al., 2013. Obtaining accurate mean velocity measurements in high reynolds number turbulent boundary layers using pitot tubes. *Journal of Fluid Mechanics* 715, 642–670.
- [18] Bakirci, K., Bilen, K., 2007. Visualization of heat transfer for impinging swirl flow. *Experimental thermal and fluid science* 32 (1), 182–191.
- [19] Barth, T. J., Jespersen, D. C., 1989. The design and application of upwind schemes on unstructured meshes.
- [20] Baughn, J., Shimizu, S., 1989. Heat transfer measurements from a surface with uniform heat flux and an impinging jet. *Journal of Heat Transfer* 111 (4), 1096–1098.
- [21] Behnia, M., Parneix, S., Durbin, P. A., 1998. Prediction of heat transfer in an axisymmetric turbulent jet impinging on a flat plate. *International Journal of Heat and Mass Transfer* 41 (12), 1845–1855.
- [22] Bellman, R., 1961. Adaptive control processes.
- [23] Benhamou, F., Older, W. J., 1997. Applying interval arithmetic to real, integer, and boolean constraints. *The Journal of Logic Programming* 32 (1), 1–24.
- [24] Bernardini, E., Spence, S. M., Wei, D., Kareem, A., 2015. Aerodynamic shape optimization of civil structures: A CFD-enabled Kriging-based approach. *Journal of Wind Engineering and Industrial Aerodynamics* 144, 154–164.
- [25] Bradford, J., Montomoli, F., D' Ammaro, A., 2014. Uncertainty quantification and race car aerodynamics. *Proceedings of the Institution of Mechanical Engineers, Part D: Journal of Automobile Engineering*, 0954407013514396.
- [26] Brown, S., Beck, J., Mahgerefteh, H., Fraga, E., 2013. Global sensitivity analysis of the impact of impurities on CO2 pipeline failure. *Reliability Engineering & System Safety* 115, 43–54.

- [27] Brugière, O., Balarac, G., Corre, C., Métais, O., Flores, E., et al., 2012. Numerical prediction of a draft tube flow taking into account uncertain inlet conditions. In: IOP Conference Series: Earth and Environmental Science. Vol. 15. IOP Publishing, p. 032039.
- [28] Buhmann, M. D., 2000. Radial basis functions. *Acta Numerica* 2000 9, 1–38.
- [29] Burhenne, S., Tsvetkova, O., Jacob, D., Henze, G. P., Wagner, A., 2013. Uncertainty quantification for combined building performance and cost-benefit analyses. *Building and Environment* 62, 143–154.
- [30] Burkardt, J., 2010. Sparse grids: Mixed families, growth rules, anisotropy: <http://people.sc.fsu.edu/burkardt/presentations/icms2010.pdf>. In: Accessed 16th May 2015. Virginia Tech.
- [31] Butchers, M., 2015. Annual report in uncertainty quantification and management in high value manufacturing special interest group. In: Knowledge Transfer Network and Innovate UK.
- [32] Cambier, L., Heib, S., Plot, S., 2013. The Onera elsA CFD software: input from research and feedback from industry. *MI* 14 (03), 159–174.
- [33] Carlomagno, G., Astarita, T., 2009. *Slides from the course on Gasdynamics, University of Naples Federico II*. Università degli Studi di Napoli Federico II.
- [34] Carr, J. C., Beatson, R. K., Cherrie, J. B., Mitchell, T. J., Fright, W. R., McCallum, B. C., Evans, T. R., 2001. Reconstruction and representation of 3D objects with radial basis functions. In: Proceedings of the 28th annual conference on Computer graphics and interactive techniques. ACM, pp. 67–76.
- [35] Celik, I. B., Ghia, U., Roache, P. J., et al., 2008. Procedure for estimation and reporting of uncertainty due to discretization in CFD applications. *Journal of fluids. Engineering-Transactions of the ASME* 130 (7).
- [36] Chakravarthy, S., 1988. High resolution upwind formulations for the Navier-Stokes equations. In: Computational Fluid Dynamics, VKI Lecture Series 1988-05, March 7–11.
- [37] Chang, S. W., Jan, Y. J., Chang, S. F., 2006. Heat transfer of impinging jet-array over convex-dimpled surface. *International Journal of Heat and Mass Transfer* 49 (17), 3045–3059.
- [38] Chmielewski, M., Gieras, M., 2013. Three-zonal wall function for k- ϵ turbulence models. *Computational Methods in Science and Technology* 19 (2), 107–114.
- [39] Choi, S.-K., Grandhi, R. V., Canfield, R. A., Pettit, C. L., 2004. Polynomial chaos expansion with latin hypercube sampling for estimating response variability. *AIAA journal* 42 (6), 1191–1198.
- [40] Clenshaw, C. W., Curtis, A. R., 1960. A method for numerical integration on an automatic computer. *Numerische Mathematik* 2 (1), 197–205.

- [41] Colyvan, M., 2008. Is probability the only coherent approach to uncertainty? *Risk Analysis* 28 (3), 645–652.
- [42] Commission, E., 2012. Flightpath 2050. Europe’s vision for aviation. Report of the High Level Group on Aviation Research, Publications Office of the European Union, Luxembourg.
- [43] Congedo, P. M., Duprat, C., Balarac, G., Corre, C., 2011. Effects of inlet uncertainties on prediction of turbulent flows using RANS and LES simulations. In: 20th AIAA Computational Fluid Dynamics Conference. p. 3869.
- [44] Conn, A. R., Gould, N. I., Toint, P. L., 2000. Trust region methods. Vol. 1. SIAM.
- [45] Constantin, P., Foias, C., 1988. Navier-stokes equations. University of Chicago Press.
- [46] Constantine, P. G., 2015. Active subspaces: Emerging ideas for dimension reduction in parameter studies. SIAM.
- [47] Constantine, P. G., Emory, M., Larsson, J., Iaccarino, G., 2015. Exploiting active subspaces to quantify uncertainty in the numerical simulation of the HyShot II scramjet. *Journal of Computational Physics* 302, 1–20.
- [48] Cox, R. T., 1946. Probability, frequency and reasonable expectation. *American Journal of Physics* 14 (1), 1–13.
- [49] Cukier, R., Levine, H., Shuler, K., 1978. Nonlinear sensitivity analysis of multiparameter model systems. *Journal of computational physics* 26 (1), 1–42.
- [50] Datta, D., 2011. Non-probabilistic uncertainty analysis of analytical and numerical solution of heat conduction. *International Journal of Energy, Information and Communications* 2 (4), 143–156.
- [51] De Baar, J., Scholcz, T. P., Verhoosel, C. V., Dwight, R. P., van Zuijlen, A. H., Bijl, H., 2012. Efficient uncertainty quantification with gradient-enhanced Kriging: Applications in fsi. ECCOMAS Vienna.
- [52] De Luca, A., Termini, S., 1972. A definition of a nonprobabilistic entropy in the setting of fuzzy sets theory. *Information and control* 20 (4), 301–312.
- [53] Derksen, J., 2002. Confined and agitated swirling flows with applications in chemical engineering. *Flow, turbulence and combustion* 69 (1), 3–33.
- [54] Dessombz, O., Thouverez, F., Lainé, J.-P., Jézéquel, L., 2001. Analysis of mechanical systems using interval computations applied to finite element methods. *Journal of Sound and Vibration* 239 (5), 949–968.
- [55] Duchaine, F., Morel, T., M. Gicquel, L., 2009. Computational-fluid-dynamics-based kriging optimization tool for aeronautical combustion chambers. *AIAA journal* 47 (3), 631–645.
- [56] Dwight, R. P., Han, Z.-H., 2009. Efficient uncertainty quantification using gradient-enhanced kriging. AIAA paper 2276, 2009.

- [57] Eggels, J., 1994. Direct and large eddy simulation of turbulent flow in a cylindrical pipe geometry. Ph.D. thesis, Delft University of Technology, The Netherlands.
- [58] Eldred, M., Burkardt, J., 2009. Comparison of non-intrusive polynomial chaos and stochastic collocation methods for uncertainty quantification. AIAA paper 976 (2009), 1–20.
- [59] Erkoyuncu, J. A., 2011. Cost uncertainty management and modelling for industrial product-service systems. Ph.D. thesis, Cranfield University.
- [60] Escue, A., Cui, J., 2010. Comparison of turbulence models in simulating swirling pipe flows. *Applied Mathematical Modelling* 34 (10), 2840–2849.
- [61] Facciolo, L., 2006. A study on axially rotating pipe and swirling jet flows. Ph.D. thesis, KTH.
- [62] Facciolo, L., Tillmark, N., Talamelli, A., Alfredsson, P. H., 2007. A study of swirling turbulent pipe and jet flows. *Physics of Fluids* 19 (3), 035105.
- [63] Fang, H., Rais-Rohani, M., Liu, Z., Horstemeyer, M., 2005. A comparative study of metamodeling methods for multiobjective crashworthiness optimization. *Computers & Structures* 83 (25), 2121–2136.
- [64] Faure, H., Lemieux, C., 2009. Generalized Halton sequences in 2008: A comparative study. *ACM Transactions on Modeling and Computer Simulation (TOMACS)* 19 (4), 15.
- [65] Feiz, A., Ould-Rouis, M., Lauriat, G., 2003. Large Eddy Simulation of turbulent flow in a rotating pipe. *International journal of heat and fluid flow* 24 (3), 412–420.
- [66] Fernández-Martínez, J., Tompkins, M., Mukerji, T., Alumbaugh, D., 2010. Geometric sampling: An approach to uncertainty in high dimensional spaces. *Combining Soft Computing and Statistical Methods in Data Analysis*, 247–254.
- [67] Fesanghary, M., Damangir, E., Soleimani, I., 2009. Design optimization of shell and tube heat exchangers using global sensitivity analysis and harmony search algorithm. *Applied Thermal Engineering* 29 (5), 1026–1031.
- [68] Fiorentini, G., Lisi, E., Sarkar, S., Villante, F., 1998. Quantifying uncertainties in primordial nucleosynthesis without Monte Carlo simulations. *Physical Review D* 58 (6), 063506.
- [69] Fluent, 2005. *Fluent 6.3 User's Guide*. Fluent Incorporated, Centerra Resource Park, 10, Cavendish Court, Lebanon (NH) 03766 USA.
- [70] Franzelin, F., Diehl, P., Pflüger, D., 2015. Non-intrusive uncertainty quantification with sparse grids for multivariate peridynamic simulations. In: *Meshfree Methods for Partial Differential Equations VII*. Springer, pp. 115–143.
- [71] Friedman, J. H., Roosen, C. B., 1995. An introduction to multivariate adaptive regression splines. *Statistical Methods in Medical Research* 4 (3), 197–217.

- [72] Gacherieu, C., Weber, C., Coriolis, G., 1998. Assessment of algebraic and one-equation turbulence models for the transonic turbulent flow around a full aircraft configuration. AIAA paper, 98-32457.
- [73] Galván, S., Reggio, M., Guibault, F., 2011. Assessment study of k-epsilon turbulence models and near-wall modeling for steady state swirling flow analysis in draft tube using fluent. *Engineering Applications of Computational Fluid Mechanics* 5 (4), 459–478.
- [74] Garcke, J., Griebel, M., Thess, M., 2001. Data mining with sparse grids. *Computing* 67 (3), 225–253.
- [75] Gardon, R., Akfirat, J. C., 1965. The role of turbulence in determining the heat-transfer characteristics of impinging jets. *International Journal of Heat and Mass Transfer* 8 (10), 1261–1272.
- [76] Geers, L. F., Tummers, M. J., Hanjalić, K., 2004. Experimental investigation of impinging jet arrays. *Experiments in fluids* 36 (6), 946–958.
- [77] Gerstner, T., Griebel, M., 1998. Numerical integration using sparse grids. *Numerical algorithms* 18 (3-4), 209–232.
- [78] Gerstner, T., Griebel, M., 2003. Dimension-adaptive tensor-product quadrature. *Computing* 71 (1), 65–87.
- [79] Gibson, M., Launder, B., 1978. Ground effects on pressure fluctuations in the atmospheric boundary layer. *Journal of Fluid Mechanics* 86 (03), 491–511.
- [80] Gibson, M., Younis, B., 1986. Calculation of swirling jets with a Reynolds Stress closure. *Physics of Fluids (1958-1988)* 29 (1), 38–48.
- [81] Gicquel, L., 2016. *Slides from the course Turbomachinery: Basic principles of turbulence*. CERFACS.
- [82] Gorle, C., Emory, M., Iaccarino, G., 2011. Epistemic uncertainty quantification of RANS modeling for an underexpanded jet in a supersonic cross flow. CTR Annual Research Briefs, Center for Turbulence Research, Stanford University, Stanford, CA.
- [83] Granados-Ortiz, F.-J., Lai, C.-H., 2016. A Novel Framework for Uncertainty Propagation in Multidisciplinary Design Life Cycle for Shock-Cell Noise Research. In: 22nd CEAS/AIAA Aeroacoustics 2016, Lyon, France.
- [84] Granados-Ortiz, F.-J., Lai, C.-H., Perez Arroyo, C., Puigt, G., Airiau, C., 2016. Uncertainty Quantification and Sensitivity Analysis applied to an under-expanded single jet. In: AIAA Aviation 2016, Washington D.C., USA.
- [85] Granados-Ortiz, F.-J., Ortega-Casanova, J., Lai, C.-H., 2015. Modelling for Computational Cost Reduction and Optimisation of an Impinging Swirling Jet created by a Rotating Pipe with Application to Heat Transfer from a Heated Solid Flat Plate. In: 8th International Congress on Industrial and Applied Mathematics. Beijing, (China). 10-14 August 2015.

- [86] Guariglia, D., 2016. Shock-cell noise investigation on a subsonic/supersonic coaxial jet. Ph.D. thesis, Universita di Roma La Sapienza.
- [87] Gulati, P., Katti, V., Prabhu, S., 2009. Influence of the shape of the nozzle on local heat transfer distribution between smooth flat surface and impinging air jet. *International Journal of Thermal Sciences* 48 (3), 602–617.
- [88] Hadžiabdić, M., Hanjalić, K., 2008. Vortical structures and heat transfer in a round impinging jet. *Journal of Fluid Mechanics* 596, 221–260.
- [89] Halton, J. H., 1970. A retrospective and prospective survey of the Monte Carlo method. *Siam review* 12 (1), 1–63.
- [90] Han, Z.-H., Zimmermann, R., Görtz, S., 2010. A new cokriging method for variable-fidelity surrogate modeling of aerodynamic data. *AIAA Paper* 1225, 2010.
- [91] Hegland, M., 2003. Adaptive sparse grids. *Anziam Journal* 44, 335–353.
- [92] Helton, J., Davis, F., 2003. Latin hypercube sampling and the propagation of uncertainty in analyses of complex systems. *Reliability Engineering and System Safety* 81, 23–69.
- [93] Helton, J. C., Davis, F. J., 2003. Latin hypercube sampling and the propagation of uncertainty in analyses of complex systems. *Reliability Engineering & System Safety* 81 (1), 23–69.
- [94] Hengwei, L., Zhonggliang, L., Yongxun, F., Keyu, G., Tingmin, Y., 2005. Characteristic of a supersonic swirling dehydration system of natural gas. *Chinese Journal of Chemical Eng* 13 (1), 9–12.
- [95] Herbert, T., 1997. Parabolized stability equations. *Annu. Rev. Fluid Mech.* 29, 245–283.
- [96] Hestenes, M. R., Stiefel, E., 1952. *Methods of conjugate gradients for solving linear systems*. Vol. 49. NBS.
- [97] Hiemstra, P. H., Pebesma, E. J., Twenhöfel, C. J., Heuvelink, G. B., 2008. Automatic real-time interpolation of radiation hazards: prototype and system architecture considerations. *International Journal of Spatial Data Infrastructures Research* 3, 58–72.
- [98] Hirai, S., Takagi, T., Matsumoto, M., 1988. Predictions of the laminarization phenomena in an axially rotating pipe flow. *Journal of fluids engineering* 110 (4), 424–430.
- [99] Hollworth, B., Durbin, M., 1992. Impingement cooling of electronics. *Journal of heat transfer* 114 (3), 607–613.
- [100] Homma, T., Saltelli, A., 1996. Importance measures in global sensitivity analysis of nonlinear models. *Reliability Engineering & System Safety* 52 (1), 1–17.
- [101] Imao, S., Itoh, M., Harada, T., 1996. Turbulent characteristics of the flow in an axially rotating pipe. *International journal of heat and fluid flow* 17 (5), 444–451.

- [102] Iooss, B., Lemaître, P., 2015. A review on global sensitivity analysis methods. In: *Uncertainty Management in Simulation-Optimization of Complex Systems*. Springer, pp. 101–122.
- [103] Iooss, B., Popelin, A., Blatman, G., Ciric, C., Gamboa, F., Lacaze, S., Lamboni, M., 2012. Some new insights in derivative-based global sensitivity measures. In: *Proceedings of PSAM*. Vol. 11. pp. 1094–1104.
- [104] Jakirlic, S., Hanjalic, K., Tropea, C., 2002. Modeling rotating and swirling turbulent flows: a perpetual challenge. *AIAA journal* 40 (10), 1984–1996.
- [105] Jansen, M. J., 1999. Analysis of variance designs for model output. *Computer Physics Communications* 117 (1), 35–43.
- [106] Jaspreet, S., Rakesh, K., Parampreet, S., 2016. CFD analysis of investigation of heat transfer using single swirling jet air impingement with twisted tapes. *International Advanced Research Journal in Science, Engineering and Technology* 3-6.
- [107] Kanokjaruvijit, K., Martinez-botas, R. F., 2005. Jet impingement on a dimpled surface with different crossflow schemes. *International journal of heat and mass transfer* 48 (1), 161–170.
- [108] Kawai, S., Shimoyama, K., 2013. Kriging-model-based uncertainty quantification in computational fluid dynamics. In: *32nd AIAA Applied Aerodynamics Conference*.
- [109] Kaya, F., Karagoz, I., 2008. Performance analysis of numerical schemes in highly swirling turbulent flows in cyclones. *Current science* 94 (10), 1273–1278.
- [110] Kent, E., Neumann, S., Kummer, U., Mendes, P., 2013. What can we learn from global sensitivity analysis of biochemical systems? *PLoS ONE* 8(11): e79244. doi:10.1371/journal.pone.0079244.
- [111] Kercher, D. S., Lee, J.-B., Brand, O., Allen, M. G., Glezer, A., 2003. Microjet cooling devices for thermal management of electronics. *IEEE Transactions on Components and Packaging Technologies* 26 (2), 359–366.
- [112] Kerr, N., Fraser, D., 1965. Swirl part 1: Effect on axisymmetrical turbulent jets. *J. Inst. Fuel* 38 (299), 519.
- [113] Kestin, J., Maeder, P., Wang, H., 1961. Influence of turbulence on the transfer of heat from plates with and without a pressure gradient. *International Journal of Heat and Mass Transfer* 3 (2), 133–154.
- [114] Kikuyama, K., Murakami, M., Nishibori, K., 1983. Development of three-dimensional turbulent boundary layer in an axially rotating pipe. *Journal of Fluids Engineering* 105 (2), 154–160.
- [115] Kim, S.-E., Choudhury, D., Patel, B., 1999. Computations of complex turbulent flows using the commercial code fluent. In: *Modeling complex turbulent flows*. Springer, pp. 259–276.

- [116] Klimke, A., Willner, K., WOHLMUTH, B., 2004. Uncertainty modeling using fuzzy arithmetic based on sparse grids: applications to dynamic systems. *International Journal of Uncertainty, Fuzziness and Knowledge-based Systems* 12 (06), 745–759.
- [117] Kobayashi, T., Yoda, M., 1987. Modified k-epsilon model for turbulent swirling flow in a straight pipe. *JSME international journal* 30 (259), 66–71.
- [118] Koziel, S., Leifsson, L., 2013. Surrogate-based modeling and optimization. *Applications in Engineering*.
- [119] Krommer, A. R., Ueberhuber, C. W., 1994. *Numerical Integration: On Advanced Computer Systems*. Vol. 848. Springer Science & Business Media.
- [120] Kronrod, A. S., 1965. Nodes and weights of quadrature formulas.
- [121] Kucherenko, S., Sobol, I., 2009. Derivative based global sensitivity measures and their link with global sensitivity indices. *Mathematics and Computers in Simulation* 79 (10), 3009–3017.
- [122] K.U.Leuven, 2016. Shear-layer Kelvin-Helmholtz instabilities in a round jet. <http://www.mech.kuleuven.be/en/tme/research/Thermotech/FlowCombust/Images/vortex.jpg>, [Accessed on 21st July 2016].
- [123] Kurowicka, D., Cooke, R. M., 2006. *Uncertainty analysis with high dimensional dependence modelling*. John Wiley & Sons.
- [124] Kwanten, B., 2014. *Bayesian Inference Uncertainty Quantification of RANS Turbulence Models*. Ph.D. thesis, TU Delft.
- [125] Laffan, S. W., Nielsen, O. M., Silcock, H., Hegland, M., 2005. Sparse grids: a new predictive modelling method for the analysis of geographic data. *International Journal of Geographical Information Science* 19 (3), 267–292.
- [126] Launder, B., Reece, G. J., Rodi, W., 1975. Progress in the development of a Reynolds-Stress turbulence closure. *Journal of fluid mechanics* 68 (03), 537–566.
- [127] Launder, B. E., 1989. Second-moment closure: present... and future? *International Journal of Heat and Fluid Flow* 10 (4), 282–300.
- [128] Laurenceau, J., Meaux, M., 2008. Comparison of gradient and response surface based optimization frameworks using adjoint method. *AIAA Paper 1889*, 2008.
- [129] Lee, D., Chung, Y., Ligrani, P., 2007. Jet impingement cooling of chips equipped with multiple cylindrical pedestal fins. *Journal of Electronic Packaging* 129 (3), 221–228.
- [130] Lee, D. H., Won, S. Y., Kim, Y. T., Chung, Y. S., 2002. Turbulent heat transfer from a flat surface to a swirling round impinging jet. *International Journal of Heat and Mass Transfer* 45 (1), 223–227.
- [131] Lee, J., Lee, S.-J., 2000. The effect of nozzle configuration on stagnation region heat transfer enhancement of axisymmetric jet impingement. *International Journal of Heat and Mass Transfer* 43 (18), 3497–3509.

- [132] Lee, J. H.-M., Van Emden, M. H., 1993. Interval computation as deduction in chip. *The Journal of Logic Programming* 16 (3-4), 255–276.
- [133] Legleiter, C. J., Kyriakidis, P. C., 2008. Spatial prediction of river channel topography by kriging. *Earth Surface Processes and Landforms* 33 (6), 841–867.
- [134] Léon, O., Brazier, J. P., 2011. Application of linear parabolized stability equations to a subsonic coaxial jet. In: 17th AIAA/CEAS Aeroacoustics Conference, May 5–8, 2011, Portland, Oregon, USA.
- [135] Leon, O., Brazier, J.-P., 2013. Investigation of the near and far pressure fields of dual-stream jets using an Euler-based PSE model. In: 19th AIAA/CEAS Aeroacoustics Conference. p. 2280.
- [136] Li, W., Lin, G., Li, B., 2016. Inverse regression-based uncertainty quantification algorithms for high-dimensional models: Theory and practice. *Journal of Computational Physics* 321, 259–278.
- [137] Lockwood, B. A., Rumpfkeil, M. P., Yamazaki, W., Mavriplis, D. J., 2011. Uncertainty quantification in viscous hypersonic flows using gradient information and surrogate modeling. AIAA Paper 885, 2011.
- [138] Loeven, G., Bijl, H., 2009. Probabilistic collocation used in a two-step approach for efficient uncertainty quantification in computational fluid dynamics. *CMES Computer modeling in engineering and sciences*, 36 (3), 2009.
- [139] Loeven, G., Witteveen, J., Bijl, H., 2007. Probabilistic collocation: an efficient non-intrusive approach for arbitrarily distributed parametric uncertainties. In: Proceedings of the 45th AIAA Aerospace Sciences Meeting and Exhibit, AIAA paper. Vol. 317.
- [140] Lophaven, S. N., Nielsen, H. B., Søndergaard, J., 2002. Dace: A MATLAB Kriging Toolbox. version 2.0. Tech. rep., DTU, tech. Report NASA/CR-2003-212153, NASA Langley Research Center.
- [141] Loukrezis, D., Römer, U., Casper, T., Schöps, S., De Gerssem, H., 2017. High-dimensional uncertainty quantification for an electrothermal field problem using stochastic collocation on sparse grids and tensor train decompositions. *International Journal of Numerical Modelling: Electronic Networks, Devices and Fields*.
- [142] Lucor, D., Meyers, J., Sagaut, P., 2007. Sensitivity analysis of large-eddy simulations to subgrid-scale-model parametric uncertainty using polynomial chaos. *Journal of Fluid Mechanics* 585, 255–279.
- [143] Lukaczyk, T., Palacios, F., Alonso, J. J., Constantine, P., 2014. Active subspaces for shape optimization. In: Proceedings of the 10th AIAA Multidisciplinary Design Optimization Conference. pp. 1–18.
- [144] Mahaffy, J., Chung, B., Song, C., Dubois, F., Graffard, E., Ducros, F., Heitsch, M., Scheuerer, M., Henriksson, M., Komen, E., et al., 2007. Best practice guidelines for the use of CFD in nuclear reactor safety applications. Tech. rep., Organisation for Economic Co-Operation and Development.

- [145] Mani, M., Babcock, D., Winkler, C., Spalart, P., 2013. Predictions of a supersonic turbulent flow in a square duct. AIAA Paper 860, 2013.
- [146] Manneville, P., 2016. Transition to turbulence in wall-bounded flows: Where do we stand? *Mechanical Engineering Reviews* 3 (2), 15–00684.
- [147] Marek, C., 2012. Assessing uncertainties in boundary layer transition predictions for hifire-1 at non-zero angles of attack. AIAA Paper 1015.
- [148] Martin, H., 1977. Heat and mass transfer between impinging gas jets and solid surfaces. In: *Advances in heat transfer*. Volume 13. New York, Academic Press, Inc., 1977, p. 1-60. Vol. 13. pp. 1–60.
- [149] Mathelin, L., Hussaini, M. Y., 2003. A stochastic collocation algorithm for uncertainty analysis.
- [150] McDaniel, D., Cummings, R., Bergeron, K., Morton, S., Dean, J., 2007. Comparisons of cfd solutions of static and maneuvering fighter aircraft with flight test data. Tech. rep., DTIC Document.
- [151] Menter, F. R., 1994. Two-equation eddy-viscosity turbulence models for engineering applications. *AIAA journal* 32 (8), 1598–1605.
- [152] Metropolis, N., Ulam, S., 1949. The Monte Carlo method. *Journal of the American statistical association* 44 (247), 335–341.
- [153] Michalke, A., 1964. On the inviscid instability of the hyperbolic-tangent velocity profile. *Deutsche Versuchsanstalt f. Luft-u. Raumfahrt*.
- [154] Miles, J. W., 1959. On the generation of surface waves by shear flows. Part 3. Kelvin-Helmholtz instability. *Journal of Fluid Mechanics* 6 (04), 583–598.
- [155] Moens, D., Vandepitte, D., 2005. A survey of non-probabilistic uncertainty treatment in finite element analysis. *Computer methods in applied mechanics and engineering* 194 (12), 1527–1555.
- [156] Moens, D., Vandepitte, D., 2007. Interval uncertainty quantification in numerical models using dynamic fuzzy finite element analysis. In: *Proceedings of the NATO AVT-147 Symposium on Computational Uncertainty in Military Vehicle Design*.
- [157] Montomoli, F., Carnevale, M., D’Ammaro, A., Massini, M., Salvadori, S., 2015. Uncertainty quantification in computational fluid dynamics and aircraft engines. Springer.
- [158] Montomoli, F., Massini, M., 2013. Gas turbines and uncertainty quantification: Impact of PDF tails on UQ predictions, the Black Swan. In: *ASME Turbo Expo 2013: Turbine Technical Conference and Exposition*. American Society of Mechanical Engineers, pp. V03CT18A002–V03CT18A002.
- [159] Morris, M. D., 1991. Factorial sampling plans for preliminary computational experiments. *Technometrics* 33 (2), 161–174.
- [160] Mouda, A., Alaa, N., 2011. Sensitivity analysis of TSEB model by one-factor-at-a-time in irrigated olive orchard. *International Journal of Computer Science Issues*.

- [161] Mughal, M. S., Ashworth, R., 2013. Uncertainty quantification based receptivity modelling of crossflow instabilities induced by distributed surface roughness in swept wing boundary layers. In: 43rd AIAA Fluid Dynamics Conference. No. 2013-3106.
- [162] Mulligan, M., Wainwright, J., 2004. Modelling and model building. *Environmental modelling: Finding simplicity in complexity*, 7–73.
- [163] Murakami, M., Kikuyama, K., 1980. Turbulent flow in axially rotating pipes. *Journal of Fluids Engineering* 102 (1), 97–103.
- [164] Musavi, M. T., Ahmed, W., Chan, K. H., Faris, K. B., Hummels, D. M., 1992. On the training of radial basis function classifiers. *Neural networks* 5 (4), 595–603.
- [165] Nack, L., Maas, L., 2016. Generation of Kelvin-Helmholtz instabilities. <http://laurent.nack.pagesperso-orange.fr/kh/theo.htm>, [Accessed on 21st July 2016].
- [166] Najafi, A., Saidi, M., Sadeghipour, M., Souhar, M., 2005. Boundary layer solution for the turbulent swirling decay flow through a fixed pipe: Sbr at the inlet. *International journal of engineering science* 43 (1), 107–120.
- [167] Nobile, F., Tempone, R., Webster, C. G., 2008. An anisotropic sparse grid stochastic collocation method for partial differential equations with random input data. *SIAM Journal on Numerical Analysis* 46 (5), 2411–2442.
- [168] Noorkami, M., Robinson, J. B., Meyer, Q., Obeisun, O. A., Fraga, E. S., Reisch, T., Shearing, P. R., Brett, D. J., 2014. Effect of temperature uncertainty on polymer electrolyte fuel cell performance. *international journal of hydrogen energy* 39 (3), 1439–1448.
- [169] Nygård, F., Andersson, H., 2010. DNS of swirling turbulent pipe flow. *International Journal for Numerical Methods in Fluids* 64 (9), 945–972.
- [170] Oberkampf, W. L., DeLand, S. M., Rutherford, B. M., Diegert, K. V., Alvin, K. F., 2002. Error and uncertainty in modeling and simulation. *Reliability Engineering & System Safety* 75 (3), 333–357.
- [171] Olsson, A. M., Sandberg, G. E., 2002. Latin Hypercube Sampling for stochastic finite element analysis. *Journal of Engineering Mechanics* 128 (1), 121–125.
- [172] Orlandi, P., Fatica, M., 1997. Direct simulations of turbulent flow in a pipe rotating about its axis. *Journal of Fluid Mechanics* 343, 43–72.
- [173] Ortega-Casanova, J., 2011. Numerical simulation of the heat transfer from a heated solid wall to an impinging swirling jet. INTECH Open Access Publisher.
- [174] Ortega-Casanova, J., 2012. CFD and correlations of the heat transfer from a wall at constant temperature to an impinging swirling jet. *International Journal of Heat and Mass Transfer* 55 (21), 5836–5845.
- [175] Ortega-Casanova, J., Campos, N., Fernandez-Feria, R., 2011. Experimental study on sand bed excavation by impinging swirling jets. *Journal of Hydraulic Research* 49 (5), 601–610.

- [176] Ortega-Casanova, J., Castillo-Sanchez, S., 2017. On using axisymmetric turbulent impinging jets swirling as Burger's vortex for heat transfer applications. single and multi-objective vortex parameters optimization. *Applied Thermal Engineering* 121, 103–114.
- [177] Ortega-Casanova, J., Granados-Ortiz, F., 2014. Numerical simulation of the heat transfer from a heated plate with surface variations to an impinging jet. *International Journal of Heat and Mass Transfer* 76, 128–143.
- [178] Ortega-Casanova, J., Molina-Gonzalez, F., 2017. Axisymmetric numerical investigation of the heat transfer enhancement from a heated plate to an impinging turbulent axial jet via small vortex generators. *International Journal of Heat and Mass Transfer* 106, 183–194.
- [179] Ove-Andersen, B., Hjorth-Jensen, M., 2012. Vortex formation in free jet caused by kelvin-helmholtz instability: <https://www.youtube.com/watch?v=elaz2x42dku>. In: Accessed 5th July 2016. Technical University of Denmark.
- [180] Panda, J., 1998. Shock oscillation in underexpanded screeching jets. *JFM* 363, 173–198.
- [181] Panda, J., 1999. An experimental investigation of screech noise generation. *JFM* 378, 71–96.
- [182] Panda, J., Raman, G., Zaman, K., 2003. Underexpanded screeching jets from circular, rectangular, and elliptic nozzles. Tech. rep., NASA.
- [183] Panizza, A., Bonini, A., Innocenti, L., 2015. Uncertainty quantification of hot gas ingestion for a gas turbine nozzle using polynomial chaos. In: *ASME Turbo Expo 2015: Turbine Technical Conference and Exposition*. American Society of Mechanical Engineers, pp. V02CT45A009–V02CT45A009.
- [184] Patankar, S. V., Spalding, D. B., 1972. A calculation procedure for heat, mass and momentum transfer in three-dimensional parabolic flows. *International Journal of Heat and Mass Transfer* 15 (10), 1787–1806.
- [185] Patterson, T. c., 1968. The optimum addition of points to quadrature formulae. *Mathematics of Computation* 22 (104), 847–856.
- [186] Payne, J. L., Roy, C. J., Beresh, S. J., 2001. A comparison of turbulence models for a supersonic jet in transonic cross flow. In: *39th AIAA Aerospace Science Meeting and Exhibit*. pp. 2001–1048.
- [187] Peart, P., 1982. The dispersion of the Hammersley sequence in the unit square. *Monatshefte für Mathematik* 94 (3), 249–261.
- [188] Perez, R. A., 2008. Uncertainty analysis of computational fluid dynamics via polynomial chaos. Ph.D. thesis, Virginia Tech.
- [189] Perez Arroyo, C., 2016. Large eddy simulations of a dual stream jet with shock-cells and noise emission analysis. Ph.D. thesis, University of Toulouse.

- [190] Pérez Arroyo, C., Daviller, G., Puigt, G., Airiau, C., 2015. Modal structure of a supersonic under-expanded jet. In: 22^{ème} Congrès Français de Mécanique, 24 – 28 August, Lyon, France.
- [191] Pérez Arroyo, C., Daviller, G., Puigt, G., Airiau, C., 29-30 March - 1 April 2015. Shock-cell noise of supersonic under expanded jets. In: 50th 3AF International Conference on Applied Aerodynamics. Toulouse, France, conf.
URL http://www.cerfacs.fr/~cfdbib/repository/TR_CFD_15_18.pdf
- [192] Pflüger, D., 2010. Spatially adaptive sparse grids for high-dimensional problems. Verlag Dr. Hut.
- [193] Piot, E., Casalis, G., Muller, F., Bailly, C., 2006. Investigation of the PSE approach for subsonic and supersonic hot jets. detailed comparisons with LES and linearized Euler equations results. *International Journal of Aeroacoustics* 5 (4), 361–393.
- [194] Poroseva, S., 2001. Wall corrections in modeling rotating pipe flow. *Annual Research Briefs—2001*, 385.
- [195] Pratte, B. D., Keffer, J., 1972. The swirling turbulent jet. *Journal of Basic Engineering* 94 (4), 739–747.
- [196] Pruvost, J., Legrand, J., Legentilhomme, P., 2004. Numerical investigation of bend and torus flows, Part I: effect of swirl motion on flow structure in U-bend. *Chemical engineering science* 59 (16), 3345–3357.
- [197] Rao, S. S., Berke, L., 1997. Analysis of uncertain structural systems using interval analysis. *AIAA journal* 35 (4), 727–735.
- [198] Regis, R. G., Shoemaker, C. A., 2005. Constrained global optimization of expensive black box functions using radial basis functions. *Journal of Global optimization* 31 (1), 153–171.
- [199] Riley, M. E., Grandhi, R. V., 2011. Quantification of model-form and predictive uncertainty for multi-physics simulation. *Computers & Structures* 89 (11), 1206–1213.
- [200] Robertson, B. E., Kravtsov, A. V., Gnedin, N. Y., Abel, T., Rudd, D. H., 2010. Computational eulerian hydrodynamics and galilean invariance. *Monthly Notices of the Royal Astronomical Society* 401 (4), 2463–2476.
- [201] Roe, P. L., 1981. Approximate Riemann solvers, parameter vectors and difference schemes. *Journal of Computational Physics* 43 (2), 357–372.
- [202] Rose, W., 1962. A swirling round turbulent jet: Part 1. mean-flow measurements. *Journal of Applied Mechanics* 29 (4), 615–625.
- [203] Sagot, B., Antonini, G., Christgen, A., Buron, F., 2008. Jet impingement heat transfer on a flat plate at a constant wall temperature. *International Journal of Thermal Sciences* 47 (12), 1610–1619.

- [204] Saltelli, A., Annoni, P., Azzini, I., Campolongo, F., Ratto, M., Tarantola, S., 2010. Variance based sensitivity analysis of model output. design and estimator for the total sensitivity index. *Computer Physics Communications* 181 (2), 259–270.
- [205] Saltelli, A., Ratto, M., Andres, T., Campolongo, F., Cariboni, J., Gatelli, D., Tarantola, S., 2008. *Global sensitivity analysis: the primer*. John Wiley & Sons.
- [206] Saltelli, A., Tarantola, S., Campolongo, F., Ratto, M., 2004. *Sensitivity Analysis in Practice: A Guide to Assessing Scientific Models*. John Wiley & Sons, Ltd.
- [207] Saltelli, A., Tarantola, S., Chan, K.-S., 1999. A quantitative model-independent method for global sensitivity analysis of model output. *Technometrics* 41 (1), 39–56.
- [208] Sankaran, S., Marsden, A. L., 2011. A stochastic collocation method for uncertainty quantification and propagation in cardiovascular simulations. *Journal of biomechanical engineering* 133 (3), 031001.
- [209] Santoyo, E., Guevara, M., Verma, S. P., 2006. Determination of lanthanides in international geochemical reference materials by reversed-phase high-performance liquid chromatography using error propagation theory to estimate total analysis uncertainties. *Journal of Chromatography A* 1118 (1), 73–81.
- [210] Satake, S.-i., Kunugi, T., 2002. Direct numerical simulation of turbulent heat transfer in an axially rotating pipe flow: Reynolds shear stress and scalar flux budgets. *International Journal of Numerical Methods for Heat & Fluid Flow* 12 (8), 958–1008.
- [211] Schaefer, J., West, T., Hosder, S., Rumsey, C., Carlson, J.-R., Kleb, W., 2015. Uncertainty quantification of turbulence model closure coefficients for transonic wall-bounded flows. In: *22nd AIAA Computational Fluid Dynamics Conference*. p. 2461.
- [212] Shih, T.-H., Liou, W., Shabbir, A., Yang, Z., Zhu, J., 1994. A new k-epsilon eddy viscosity model for high reynolds number turbulent flows: Model development and validation.
- [213] Silva, R., Perez, M., Berenguel, M., Valenzuela, L., Zarza, E., 2014. Uncertainty and global sensitivity analysis in the design of parabolic-through direct steam generation plants for process heat applications. *Applied Energy* 121, 233–244.
- [214] Simpson, T. W., Poplinski, J., Koch, P. N., Allen, J. K., 2001. Metamodels for computer-based engineering design: survey and recommendations. *Engineering with computers* 17 (2), 129–150.
- [215] Sin, G., Gernaey, K. V., Neumann, M. B., van Loosdrecht, M. C. M., Gujer, W., 2011. Global sensitivity analysis in waste water treatment plant model applications: Prioritizing sources of uncertainty. *Water Research* 45 (2), 639–651.
- [216] Sin, G., Lantz, A. E., Gernaey, K. V., 2009. Good modeling practice for pat applications: Propagation of input uncertainty and sensitivity analysis. *Biotechnology progress*. DOI 10.1021/bp.166.

- [217] Singh, D., Premachandran, B., Kohli, S., 2015. Effect of nozzle shape on jet impingement heat transfer from a circular cylinder. *International Journal of Thermal Sciences* 96, 45–69.
- [218] Smolyak, S., 1963. Quadrature and interpolation formulas for tensor products of certain classes of functions. *Soviet Math. Dokl.*, 240–243.
- [219] Smolyak, S. A., 1963. Quadrature and interpolation formulas for tensor products of certain classes of functions. In: *Dokl. Akad. Nauk SSSR*. Vol. 4. p. 123.
- [220] Sobol', I. M., 1990. On sensitivity estimation for nonlinear mathematical models. *Matematicheskoe Modelirovanie* 2 (1), 112–118.
- [221] Sobol, I. M., 2003. Theorems and examples on high dimensional model representation. *Reliability Engineering & System Safety* 79 (2), 187–193.
- [222] Sobol, I. M., 2007. Global sensitivity indices for the investigation of nonlinear mathematical models. *Matematicheskoe Modelirovanie* 19 (11), 23–24.
- [223] Song, W., Keane, A., Eres, H., Pound, G., Cox, S., 2003. Two dimensional airfoil optimisation using cfd in a grid computing environment. In: *European Conference on Parallel Processing*. Springer, pp. 525–532.
- [224] Spalart, P., Allmaras, S., 1992. A one-equation turbulence model for aerodynamic flows. *AIAA Paper 92-0439*, 30th Aerospace Sciences Meeting and Exhibit, Reno, Nevada (1992).
- [225] Spanos, P. D., Ghanem, R., 1989. Stochastic finite element expansion for random media. *Journal of engineering mechanics* 115 (5), 1035–1053.
- [226] Sundén, B., Larocque, J., Wu, Z., 2014. Numerical simulation of heat transfer from impinging swirling jets. *Impingement Cooling In Gas Turbines: Design, Applications, And Limitations*, 185–203.
- [227] Tam, C. K., Burton, D. E., 1984. Sound generated by instability waves of supersonic flows. Part 2. Axisymmetric jets. *Journal of Fluid Mechanics* 138, 273–295.
- [228] Taylor, S., Galea, E., Patel, M., Petridis, M., Knight, B., Ewer, J., 1997. Smartfire: an integrated computational fluid dynamics code and expert system for fire field modelling. *Fire Safety Science* 5, 1285–1296.
- [229] Temam, R., 2001. *Navier-Stokes equations: theory and numerical analysis*. Vol. 343. American Mathematical Soc.
- [230] Tian, W., 2013. A review of sensitivity analysis methods in building energy analysis. *Renewable Sustainable Energy Rev* 20, 4–119.
- [231] Uddin, N., 2008. Turbulence modeling of complex flows in CFD. Ph.D. thesis, University of Sturrgart.
- [232] Van Gelder, L., Das, P., Janssen, H., Roels, S., 2014. Comparative study of meta-modelling techniques in building energy simulation: Guidelines for practitioners. *Simulation Modelling Practice and Theory* 49, 245–257.

- [233] van Leer, B., 1979. Towards the ultimate conservative difference scheme. V. A second-order sequel to Godunov's method. *Journal of Computational Physics* 32 (1), 101–136.
- [234] Verma, S. P., Andaverde, J., Santoyo, E., 2006. Application of the error propagation theory in estimates of static formation temperatures in geothermal and petroleum boreholes. *Energy Conversion and Management* 47 (20), 3659–3671.
- [235] Vinze, R., Chandel, S., Limaye, M., Prabhu, S., 2016. Effect of nozzle configuration on heat transfer on impinging compressible air jet on a smooth plate.
- [236] Viskanta, R., 1993. Heat transfer to impinging isothermal gas and flame jets. *Experimental thermal and fluid science* 6 (2), 111–134.
- [237] von Helmholtz, H., 1868. über discontinuirliche Flüssigkeits-Bewegungen. Akademie der Wissenschaften zu Berlin.
- [238] Von Winckel, G., 2008. Fast clenshaw-curtis quadrature. Tech. rep., The Mathworks Central File Exchange, Mar. 2008. URL <http://www.mathworks.com/matlabcentral/fileexchange/19063-sparse-grid-quadrature/content/spquad.m>.
- [239] Walters, R., Huyse, L., 2001. Stochastic methods for fluid mechanics-an introduction. Tech. rep., Tech. Rep. in preparation, ICASE, NASA Langley Research Center, Hampton, VA.
- [240] Walther, S., Airiau, C., Bottaro, A., 2001. Optimal control of Tollmien–Schlichting waves in a developing boundary layer. *Physics of Fluids* 13 (7), 2087–2096.
- [241] Walz, N.-P., Hanss, M., 2013. Fuzzy arithmetical analysis of multibody systems with uncertainties. *Archive of Mechanical Engineering* 60 (1), 109–125.
- [242] Wang, P., Lu, Z., Tang, Z., 2013. An application of the Kriging method in global sensitivity analysis with parameter uncertainty. *Applied Mathematical Modelling* 37 (9), 6543–6555.
- [243] Wang, Y., Chirikjian, G. S., 2008. Nonparametric second-order theory of error propagation on motion groups. *The International journal of robotics research* 27 (11-12), 1258–1273.
- [244] Wang, Y., Yan, L., 2008. CFD studies on biomass thermochemical conversion. *International journal of molecular sciences* 9 (6), 1108–1130.
- [245] Warnes, J. J., 1986. A sensitivity analysis for universal Kriging. *Mathematical Geology* 18 (7), 653–676.
- [246] Weber, C., 1998. Développement de méthodes implicites pour les équations de Navier-Stokes moyennes et la simulation des grandes échelles : Application à l'aérodynamique externe. Ph.D. thesis, Institut National Polytechnique de Toulouse, France. URL http://www.cerfacs.fr/~cfdbib/repository/TH_CFD_98_63.pdf
- [247] Weigand, B., Spring, S., 2011. Multiple jet impingement- a review. *Heat Transfer Research* 42 (2).

- [248] Wen, M.-Y., Jang, K.-J., 2003. An impingement cooling on a flat surface by using circular jet with longitudinal swirling strips. *International Journal of Heat and Mass Transfer* 46 (24), 4657–4667.
- [249] Whelan, B. P., Robinson, A. J., 2009. Nozzle geometry effects in liquid jet array impingement. *Applied Thermal Engineering* 29 (11), 2211–2221.
- [250] White, A., 1964. Flow of a fluid in an axially rotating pipe. *Journal of Mechanical Engineering Science* 6 (1), 47–52.
- [251] Wiener, N., 1938. The homogeneous chaos. *American Journal of Mathematics* 60 (4), 897–936.
- [252] Wilcox, D. C., et al., 1998. *Turbulence modeling for CFD*. Vol. 2. DCW industries La Canada, CA.
- [253] Witteveen, J. A., Doostan, A., Chantrasm, T., Pecnik, R., Iaccarino, G., 2009. Comparison of stochastic collocation methods for uncertainty quantification of the transonic rae 2822 airfoil. In: *Proceedings of workshop on quantification of CFD uncertainties*.
- [254] Witteveen, J. A., Iaccarino, G., 2013. Simplex stochastic collocation with ENO-type stencil selection for robust uncertainty quantification. *Journal of Computational Physics* 239, 1–21.
- [255] Witteveen, J. A., Loeven, A., Sarkar, S., Bijl, H., 2008. Probabilistic collocation for period-1 limit cycle oscillations. *Journal of sound and vibration* 311 (1), 421–439.
- [256] Wong, H. Y., 1999. One-equation turbulence model of Spalart and Allmaras in supersonic separated flows. *AIAA journal* 37 (3), 391–393.
- [257] Wood, R., Jones, T., Miles, N., Ganeshalingam, J., 2001. Upstream swirl-induction for reduction of erosion damage from slurries in pipeline bends. *Wear* 250 (1), 770–778.
- [258] Xiu, D., Karniadakis, G. E., 2003. Modeling uncertainty in flow simulations via generalized polynomial chaos. *Journal of computational physics* 187 (1), 137–167.
- [259] Yan, X., Kalvakota, R. S., 2006. Numerical analysis of local heat transfer from a flat plate to a swirling air impinging jet. In: *Proceedings of IMECE2006 2006 ASME International Mechanical Engineering Congress and Exposition*.
- [260] Yan, X., Saniei, N., 1998. Heat transfer measurements from a flat plate to a swirling impinging jet. *International Heat Transfer Conference August 23-28, Kyongju, Korea* 5, 497–502.
- [261] Yen, C., Messersmith, N., 1998. Application of parabolized stability equations to the prediction of jet instabilities. *AIAA journal* 36 (8), 1541–1544.
- [262] Zadeh, L. A., 1968. Fuzzy algorithms. *Information and control* 12 (2), 94–102.
- [263] Zadeh, L. A., 1997. Toward a theory of fuzzy information granulation and its centrality in human reasoning and fuzzy logic. *Fuzzy sets and systems* 90 (2), 111–127.

- [264] Zhang, H., Pinjala, D., Wong, T., Toh, K., Joshi, Y., 2005. Single-phase liquid cooled microchannel heat sink for electronic packages. *Applied Thermal Engineering* 25 (10), 1472–1487.
- [265] Zuckerman, N., Lior, N., 2006. Jet impingement heat transfer: physics, correlations, and numerical modeling. *Advances in heat transfer* 39, 565–631.

Appendix A

User-Defined Functions to Implement the Models

The models have been implemented in FLUENT through a User-Defined Function (UDF) coded in C. In this appendix, a piece of code is given to show how to implement the UDF.

```
/****** UDF FOR THE PROFILES *****/
#include "udf.h"

#define az -1.0474
#define bz 3.0230
#define cz -0.6538 /* These are the constants for v_z/U */
#define dz 34.1414

#define at 0.9709
#define bt 2.0052 /* These are the constants for v_t/U */

#define ak -0.1708
#define bk -0.0880 /* These are the constants for k/U^2 */
#define ck -1.6985

#define avr 1.9314
#define bvr 0.7933
#define cvr 4.0472 /* These are the constants for \beta */
#define dvr 1.8621

#define rho <input_value> /* Density */
#define mu <input_value> /* Viscosity */
```

```

#define D <input_value> /* Diameter */
#define Re <input_value> /* Reynolds number */

DEFINE_PROFILE(vz,t,i) /* Function for the v_z/U profile */
{
  real x[ND_ND];          /* this will hold the position vector */
  real r;
  face_t f;

  real U=Re*mu/(D*rho); /* Calculates the velocity from the Reynolds */

  begin_f_loop(f,t)
  {
    F_CENTROID(x,f,t);
    r = x[1]/(D/2);
    F_PROFILE(f,t,i) = U*(az*pow(r,3)+bz*exp(-pow(cz*r,2)))*(-tanh(dz*(r-1.0)))/2.0;
  }
  end_f_loop(f,t)
}

DEFINE_PROFILE(vt,t,i) /* Function for the v_t/U profile */
{
  real x[ND_ND];
  real r;
  face_t f;

  real U=Re*mu/(D*rho);

  begin_f_loop(f,t)
  {
    F_CENTROID(x,f,t);
    r = x[1]/(D/2);
    F_PROFILE(f,t,i) = U*at*pow(r,bt);
  }
  end_f_loop(f,t)
}

DEFINE_PROFILE(k,t,i) /* Function for the k/U^2 profile */
{
  real x[ND_ND];
  real r;

```

```

face_t f;

real U=Re*mu/(D*rho);

begin_f_loop(f,t)
{
F_CENTROID(x,f,t);
r = x[1]/(D/2);
F_PROFILE(f,t,i) = U*U*(0.05327/(ak+exp(pow(r,1.2)*ck)))*(tanh(bk*(r-1)));
}
end_f_loop(f,t)
}

DEFINE_PROFILE(omega,t,i) /* Function for the \omega profile from k and
* \beta profiles, as the turbulence model to be used is k-\omega */
{
real x[ND_ND]; /* this will hold the position vector */
real r,k,tvr;
face_t f;

real U=Re*mu/(D*rho);

begin_f_loop(f,t)
{
F_CENTROID(x,f,t);
r = x[1]/(D/2);
k=U*U*(0.05327/(ak+exp(pow(r,1.2)*ck)))*(tanh(bk*(r-1)));
tvr=avr*exp(-bvr*pow(r,dvr))*(exp(-cvr*(pow(r,13)-1))-1);
F_PROFILE(f,t,i) = rho*k/(tvr*mu);
/* This is the expression to obtain \omega */
}
end_f_loop(f,t)
}

```

Appendix B

Models for the Fitting Coefficients

As mentioned in Eq. (3.4)-(3.7) and in Section 4.4.3, the parameters γ_i , where $\gamma = a, b, c, d$ and $i = z, t, k, \beta$, are modelled by the following expressions Eqs. (B.1) - (B.13). The goodness of the fits can be seen in Fig. B.1-B.4.

From these results, the equations to model $\frac{v_z}{U}, \frac{v_t}{U_r}, \frac{k}{U^2}$ and β are only dependent on Q and Ω , and ready to be used for any purpose. Note the equations are normalised via $Q_n = \frac{Q - \bar{Q}}{\sigma_Q}$ and $\Omega_n = \frac{\Omega - \bar{\Omega}}{\sigma_\Omega}$, where overbar denotes mean values and σ' stands for the standard deviation. In Table B.1 can also be found goodness indicators of the fit. As the coefficient of determination (\hat{R}^2) is not the best measure for the goodness of a fit, specially in non-linear cases, the Sum of Squares due to Error (SSE), Adjusted- \hat{R}^2 and Root Mean Squared Error (RMSE) are also given. Over-fitting has been avoided for all the fits by using the minimum order polynomial that reasonably satisfied the goodness.

$$\begin{aligned} a_z = & -1.048 + 0.001532\Omega_n - 0.01444Q_n - (4.147e - 05)\Omega_n^2 - 0.0009388\Omega_nQ_n \\ & + 0.01183Q_n^2 - (5.997e - 05)\Omega_n^3 + (3.648e - 05)\Omega_n^2Q_n - 0.0005627\Omega_nQ_n^2 \\ & + 0.005394Q_n^3, \end{aligned} \quad (\text{B.1})$$

$$\begin{aligned} b_z = & 3.023 + 0.004779\Omega_n - 0.05368Q_n + (5.742e - 06)\Omega_n^2 - 0.0005031\Omega_nQ_n \\ & + 0.003906Q_n^2, \end{aligned} \quad (\text{B.2})$$

$$\begin{aligned} c_z = & -0.6536 - 0.002857\Omega_n + 0.03038Q_n + (1.346e - 05)\Omega_n^2 + 0.0003585\Omega_nQ_n \\ & - 0.004234Q_n^2, \end{aligned} \quad (\text{B.3})$$

$$\begin{aligned} d_z = & 34.16 + -0.05319\Omega_n + 1.362Q_n + 0.0008092\Omega_n^2 + 0.02154\Omega_nQ_n - 0.3225Q_n^2 \\ & + 0.002316\Omega_n^3 + 0.0001007\Omega_n^2Q_n + 0.01276\Omega_nQ_n^2 - 0.1631Q_n^3, \end{aligned} \quad (\text{B.4})$$

$$a_t = 0.9708 + 0.003415\Omega_n - 0.03677Q_n - 0.0001444\Omega_n Q_n + 0.001342Q_n^2, \quad (\text{B.5})$$

$$b_t = 2.005 - 0.006083\Omega_n + 0.06979Q_n + 0.0004104\Omega_n Q_n - 0.004283Q_n^2, \quad (\text{B.6})$$

$$\begin{aligned} a_k = & -0.1709 - 0.0001532\Omega_n - 0.000986Q_n + (7.86e - 05)\Omega_n Q_n + 0.0007671Q_n^2 \\ & - 0.0001781\Omega_n Q_n^2 - (6.527e - 05)Q_n^3 - (3.653e - 05)\Omega_n Q_n^3 - 0.0003428Q_n^4 \\ & + (8.297e - 05)\Omega_n Q_n^4 + 0.0001397Q_n^5, \end{aligned} \quad (\text{B.7})$$

$$\begin{aligned} b_k = & -1.698 + 0.001364\Omega_n - 0.002698Q_n + (3.023e - 05)\Omega_n^2 - 0.0002644\Omega_n Q_n \\ & - 0.002849Q_n^2 + (3.223e - 05)\Omega_n^2 Q_n + 0.0001315\Omega_n Q_n^2 - 0.001438Q_n^3 \\ & - (6.665e - 05)\Omega_n^2 Q_n^2 + (7.724e - 05)\Omega_n Q_n^3 + 0.001602Q_n^4, \end{aligned} \quad (\text{B.8})$$

$$\begin{aligned} c_k = & -0.08801 + (5.075e - 05)\Omega_n + 0.0005716Q_n + (3.703e - 06)\Omega_n^2 \\ & - (2.574e - 05)\Omega_n Q_n + 0.0001155Q_n^2, \end{aligned} \quad (\text{B.9})$$

$$a_\beta = 1.932 - 0.01402\Omega_n + 0.4053Q_n - 0.0006922\Omega_n Q_n + 0.02551Q_n^2, \quad (\text{B.10})$$

$$\begin{aligned} b_\beta = & 0.7933 + 0.001219\Omega_n + 0.003093Q_n - (7.063e - 06)\Omega_n Q_n + 0.001437Q_n^2 \\ & + (1.968e - 06)\Omega_n Q_n^2 - 0.0002586Q_n^3, \end{aligned} \quad (\text{B.11})$$

$$c_\beta = 1.862 - 0.000533\Omega_n - 0.04129Q_n - 0.0002055\Omega_n Q_n + 0.005018Q_n^2, \quad (\text{B.12})$$

$$d_\beta = 4.047 + 0.008784\Omega_n - 0.1622Q_n - 0.0009475\Omega_n Q_n + 0.00729Q_n^2. \quad (\text{B.13})$$

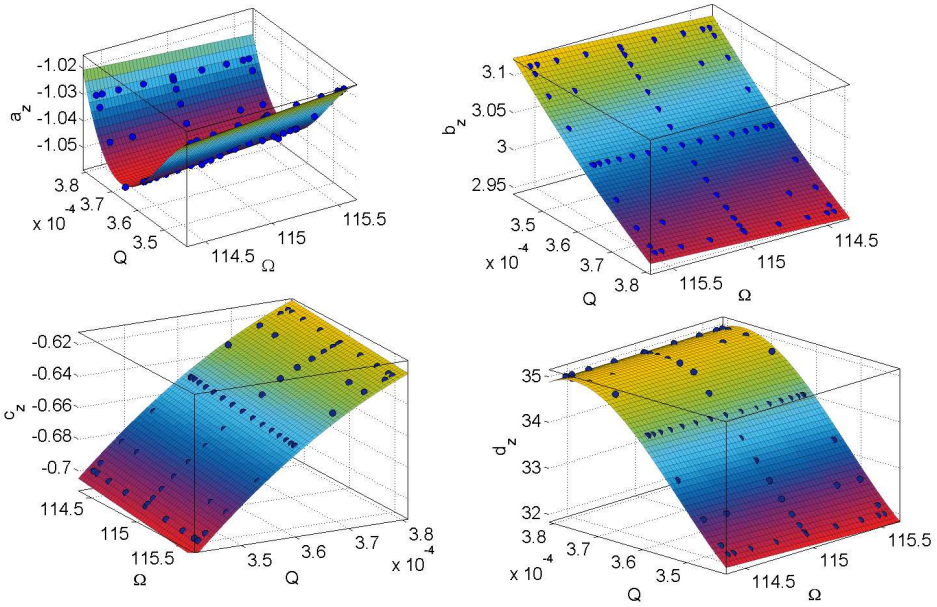


Figure B.1 Models for the $\frac{v_z}{U}$ coefficients.

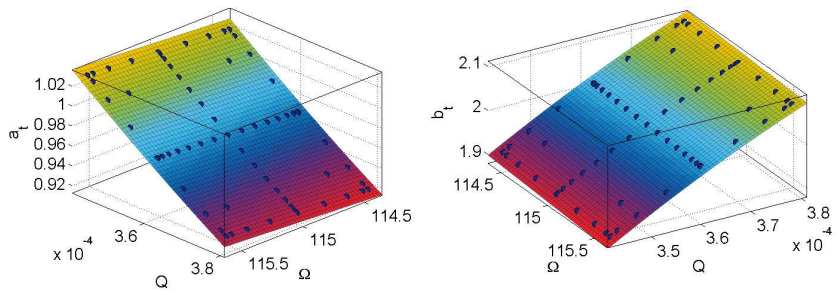


Figure B.2 Models for the $\frac{v_r}{U_r}$ coefficients.

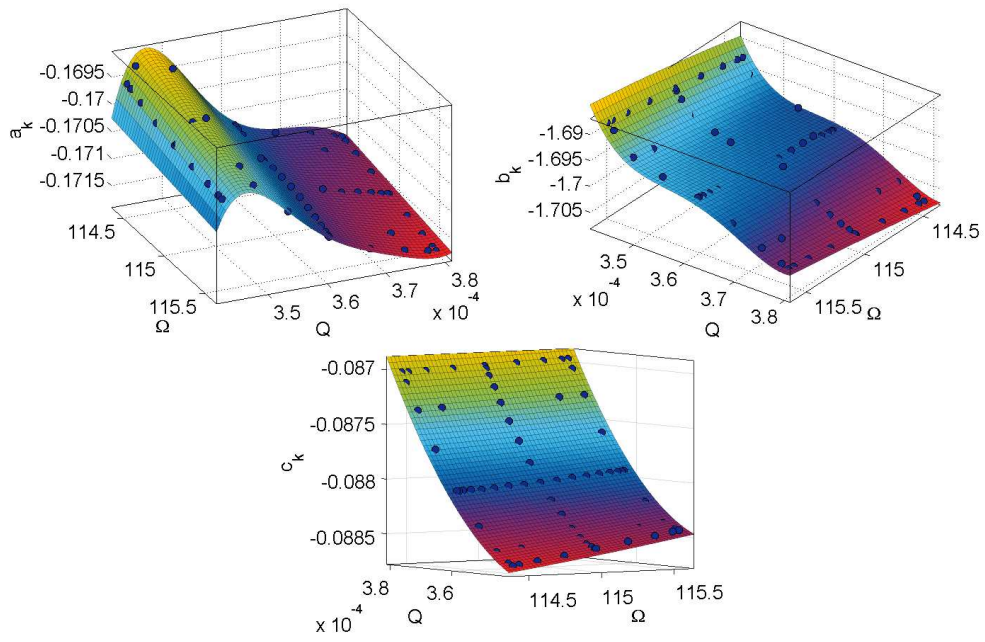


Figure B.3 Models for the $\frac{k}{U^2}$ coefficients.

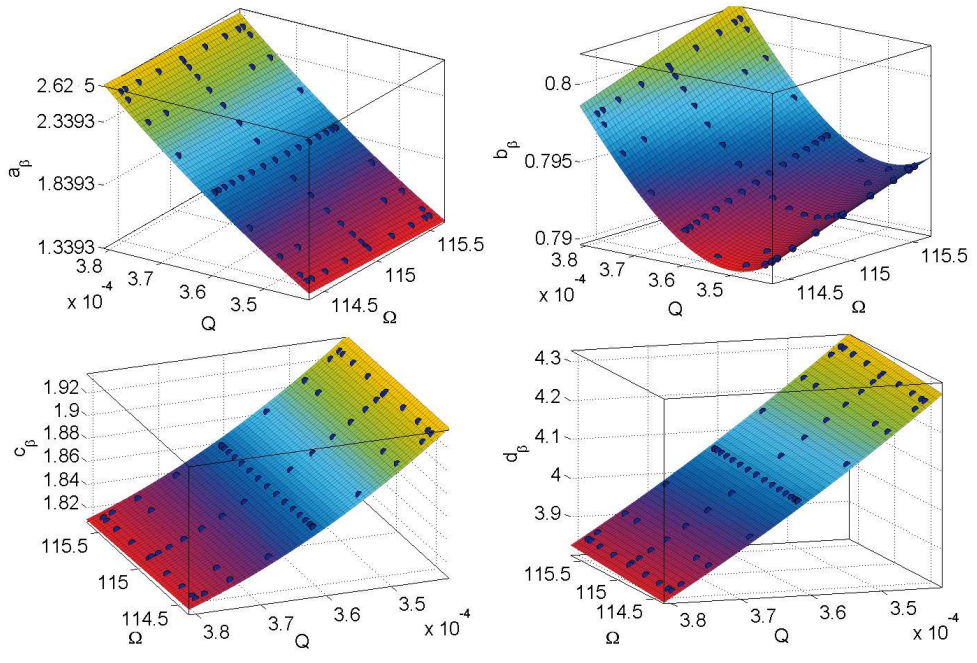


Figure B.4 Models for the β coefficients.

Coefficient	SSE	\hat{R}^2	Adjusted \hat{R}^2	RMSE
a_z	8.206e-05	0.9903	0.9887	0.001221
b_z	4.892e-07	1	1	9.105e-05
c_z	3.278e-05	0.9995	0.9994	0.0007453
d_z	0.07246	0.9991	0.999	0.0363
a_t	6.173e-08	1	1	3.208e-05
b_t	4.583e-07	1	1	8.74e-05
a_k	3.357e-07	0.9904	0.9887	7.884e-05
b_k	1.371e-05	0.9925	0.991	0.0005086
c_k	1.238e-08	0.9994	0.9994	1.448e-05
a_β	4.878e-06	1	1	0.0002851
b_β	2.248e-08	1	1	1.969e-05
c_β	1.954e-06	1	1	0.0001805
d_β	7.532e-06	1	1	0.0003543

Table B.1 Goodness of the fitting for the coefficients of the models.